A Combinatorial Study of Pt-Based Oxygen Reduction Electrocatalysts for Hydrogen Fuel Cells

by

Arman Bonakdarpour

Submitted in partial fulfilment of the requirements
for the degree of Doctor of Philosophy

at

Dalhousie University
Halifax, Nova Scotia
July 2007

Your file Votre référence
ISBN: 978-0-494-31495-1
Our file Notre référence
ISBN: 978-0-494-31495-1

DALHOUSIE UNIVERSITY

To comply with the Canadian Privacy Act the National Library of Canada has requested that the following pages be removed from this copy of the thesis:

Preliminary Pages

Examiners Signature Page (pii)

Dalhousie Library Copyright Agreement (piii)

Appendices

Copyright Releases (if applicable)

Table of Contents

List of Tables

List of Figures

Abstract

This thesis presents measurements of the stability and activities of Pt-based oxygen reduction reaction (ORR) electrocatalysts for proton exchange membrane fuel cells (PEMFC). Because more than 70% of electrochemical losses originate from the cathodic reduction of oxygen, research on ORR catalysts remains very active.

Numerous combinatorial libraries of $Pt_{1-x}M_x$ (M = Fe, Ni, Mn; $0 \leq x \leq 1$) and $Pt_{1-x-y}M_xM_y'$ (M, M' = Co, Ni, Mn, Fe) were prepared by magnetron sputtering using high surface area nano-structured thin film (NSTF) supports as substrates. The libraries were studied for the corrosion stability of the transition metal elements by acid leaching experiments. The results show that after exposing these libraries to 0.5M H_2SO_4 (or $HClO_4$) at 80°C for several days, significant amounts of transition metals leach off. When the transition metal content was about 60% or less mostly surface leaching occurred and for more than 60% surface and bulk leaching were observed. The composition of these libraries after acid treatment was very close to the electrocatalysts tested in hydrogen fuel cells, thus showing that acid treatment can mimic the fuel cell environment very well. Alloys of Pt-Ta, on the other hand, showed no dissolution of Ta. However, the presence of more than 10% Ta in the alloy, significantly reduces the ORR activity.

The rotating ring-disk electrode technique was used to measure the ORR activity of sputtered $Pt_{1-x}Co_x$ ($0 < x < 0.5$) films. After heat treatment a 1.7× gain in the specific current densities were observed. There are claims in the literature that very high activities (about 10×) can be achieved by Pt alloys such as Pt-Co with similar preparation methods. Poor experimental setups are most likely the sources of these observations.

High surface area Pt and Pt-Co-Mn catalysts, sputtered onto NSTF supports were studied using the RRDE technique. The Pt-Co-Mn alloy showed a kinetic gain of about 20 mV over Pt for ORR. This is in agreement with the FC results.

The impact of catalyst loading in RRDE experiments on the production of H_2O_2 during ORR, is discussed. It was found that lower loadings of both Pt-based and non-noble metal catalysts generate more H_2O_2 during the oxygen reduction reaction. These observations have important implications for both fundamental studies and applications.

List of Abbreviations and Symbols Used

2θ	scattering angle in diffraction
(hkl)	miller indices of crystallographic planes
Å	angstrom, 0.1 nm
a	lattice constant
A	frequency factor
AA	atomic absorption
AC	alternating current
AE	advanced energy
AFC	alkaline fuel cell
α	charge transfer coefficient
bcc	body centred cubic
BOP	balance of plant
C	analyzer constant in XPS
CAN	clean air now
CCM	catalyst coated membrane
CE	counter electrode
C^i	mass percentage
CMS	combinatorial material science
CNT	carbon nano-tube
CV	cyclic voltammetry
CVC	Corona Vacuum Coaters
χ	surface potential
$D_{grain\text{-}size}$	grain size
D	diffusion constant
D(E)	XPS detector efficiency
d	lattice spacing
DFT	density functional theory
dia.	diameter
DMFC	direct methanol fuel cell
DOE	department of energy

DOS	density of states
E	potential difference
E^a	activation energy
E_B	binding energy of electrons
E_{kin}	kinetic energy of electrons
E_o	analyzer's potential
E^o	equilibrium potential
e^-	elementary charge
E_{corr}	corrosion potential
ECS	the electrochemical society
ECSA	electrochemical surface area
EDS	energy dispersive spectroscopy
E_f	Fermi energy
EM	electron microprobe
ESCA	electron spectroscopy for chemical analysis
EtOH	ethanol
eV	electron volt
$E_{\sigma=0}$	potential of zero charge
F	Faraday constant
FC	fuel cell
F_{AB}	matrix factor of the two elements in XPS
fcc	face centred cubic
FWHM	full width at half maximum
ϕ	work function
GC	glassy carbon
GDL	gas diffusion layer
GM	General Motors
η	overpotential
h	Planck's constant
$\hbar$	$h/2\pi$
hcp	hexagonal close packed

HER	hydrogen evolution reaction
HOR	hydrogen oxidation reaction
IMFP	inelastic mean free path
INRS	Institut national de la recherche scientifique
IPCC	intergovermental panel on climate change
I	intensity in electron microprobe analysis
I_{Ring}	ring current
I_{Disk}	disk current
j	current density
$j_{diffusion-limited}$	diffusion-limited current density
jk	kinetic current density
J	flux of species
j_o	exchange current density
$\lambda(E)$	inelastic mean free path of electrons in solids
λ	wave length
k_B	Boltzman constant
KE	kinetic energy
LANL	Los Alamos National Laboratory
LBNL	Lawrence Berkley National Laboratory
KL	Koutecky-Levich
M	transition metal
M'	transition metal
M''	transition metal
M	molarity
M^+	metal ion
MCFC	molten carbonate fuel cell
MEA	membrane electrode assembly
MeOH	methanol
ML	mono layer
MMS	mercury-mercurus sulfate
ν	kinematic viscosity

n	number of electrons
$n_{integer}$	integer
N	ring efficiency factor
NIST	National Institute of Standards and Technology
NNMC	non-noble metal catalysts
NPW	nano-pure water
NREL	National Renewable Energy Laboratory
NSERC	National Science and Engineering Research Council
NSTF	Nano-structured thin film
OCV	open circuit voltage
OER	oxygen evolution reaction
ORR	oxygen reduction reaction
PAFC	phosphoric acid fuel cell
PE	potential energy
PEEK	poly-arylene-etheretherketone
PEM	proton exchange membrane
PEMFC	proton exchnge membrane fuel cell
PFSA	perfluorosulfonic acid
PGM	platinum group metal
ppb	parts per billion
ppm	parts per million
PR	perylene red
PV	photovoltaics
PVD	physical vapour deposition
PZC	point of zero charge
RDE	rotating disk electrode
R	ideal gas constant
rds	rate determining step
REF	reference electrode
RF	radio frequency
RHE	reversible hydrogen electrode

rpm	rotation per minute
RRDE	rotating ring-disk electrode
ρ_A	number density of atom A in the sample
θ	half the scattering angle
$\theta_{coverage}$	surface coverage
σ	cross section
$SA_{geometric}$	geometric surface area
SAX	small angle scattering
SCCM	standard cubic centimetre per minute
SEF	surface enhanced factor
SEM	scanning electron microscope
SF	sensitivity factor
SHE	standard hydrogen electrode
SOFC	solid oxide fuel cell
SPEEK	sulfonated polyetheretherketone
SWB	Solar-Wasserstoff Bayren
T	temperature
TEM	transmission electron microscope
TM	transition metal
TOF	turn over frequency
T(E)	transmission probability of XPS analyzer
υ	fluid velocity
υ	reaction rate
UHV	ultra high vacuum
UN	United Nations
UNEP	United Nations Environment Programme
UPD	under potential deposition
UPS	ultraviolet photoemission spectroscopy
UTC	united technologies
V	potential
V_{pr}	potential of peak reduction

ω	angular velocity in rotating disk experiments
WDS	wavelength dispersive spectroscopy
WE	working electrode
WMO	World Meteorological Organization
x, y	atomic concentration
XPS	X-ray photoelectron spectroscopy
XRD	X-ray diffraction
ZAF	atomic number, absorption, fluoresence factor in electron microprobe
ZEV	zero emission vehicle

Acknowledgements

I would like to thank all the members of Dahn lab over the past few years for their help and their friendship. In particular I would like to express my thanks to Prof. Jeff Dahn, my PhD supervisor, for his support, enthusiasm and the patience he showed during these past few years. Jeff, your teachings have had a great impact on my career. I also thank many post-doctoral fellows for many helpful discussions and their close collaboration in many projects. They are: Drs. David Stevens, Brad Easton, Ruizhi Yang, Thorsten Buhrmester, Arnd Garsuch and Philippe Westreich. Many undergraduate students assisted in RRDE measurements and materials characterizations over the past few years. They are: Joel Wenzel, Robert Löbel, Kerry Lake, Krystal Stevens, Hannah Dahn and Tara Dahn. I have had many interesting scientific and non-scientific discussions and learned a lot from my fellow thesis writers: Dr. Hubert Fortier, Gary Liu, Lee Moshurchak, Robbie Sanderson, Adam Timmons, Vincent Chevrier, Ye Tian and Peng Liao.

Many people in the department helped with numerous aspects of my work. I especially like to thank Simon Trussler for making many RRDE parts without which research would have been impossible or very slow. I thank Barbara Gauvin for placing orders, Andy George for helping with RRDE parts and Jürgen Müller for making glass cells used in the experiments. For the XPS experiments I had many helpful discussions with Drs. Ted Monchesky, Shuran Sheng and Zeynel Bayindir. Dr. Patricia Stoffyn assisted with the electron microprobe measurements. The fuel cell project at Dalhousie has been a close collaboration with the 3M Fuel Cell Program. 3M has provided funding, support and their wonderful NSTF technology for our research. In particular I thank three scientists from 3M who had the most impact: Drs. Mark Debe, Radoslav Atanasoski and Ms. Alison Schmoeckel.

I am indebted to NSERC, the Killam Foundation and the Sumner Foundation for providing scholarship support during the past four years.

Chapter 1

Introduction

This chapter provides a general introduction to the current state of the world's energy supplies, the need for renewable and clean energy resources, a discussion of some clean energy resources and a short background on fuel cells. For fuel cells, emphasis is placed on proton exchange membrane fuel cells (PEMFC), their basic electrochemistry and the current status of the catalyst materials used in them. Throughout this chapter, wherever needed, ample relevant citations from the most recent literature sources are provided. It is hoped that these references will help the reader to learn more about the material provided here, should he or she be interested.

1.0 World's Current Energy Problems

Today, more than 85% of global power consumption, which is about 13 TW, is based on non-renewable fossil fuel energy resources [1]. The fossil, or carbon-based fuels-oil, coal and natural gas--account for 35%, 23% and 21%, respectively of the world's power consumption. The remainder of the power is obtained from different sources such as: biomass (9%), nuclear energy (6%), hydroelectricity (2%) and renewable resources like wind, solar and geothermal (2%) [1]. The use of non-renewable carbon-based forms of energy, which are responsible for the production of greenhouse gases, is a decades old concern for both scientific and non-scientific communities.

Increasing energy demand, which results from population increase and the rapid industrialization of developing countries, makes the energy nightmare a more pronounced reality. In particular, it is estimated that current oil reserves and resources will last only 50-80 and 50-150 more years, respectively, based on 1998 consumption rates [1]. Of the three main fossil fuels, (oil, gas and coal), the most attention is usually paid to oil, which is refined to produce gasoline, the fuel of choice for transportation and which is also used for heating in many parts of the world. The demand for oil is increasing and its reserves/resources are more limited than both natural gas and coal. Furthermore, it is

believed that the global rate of oil production is reaching a peak – the much talked-about Hubbert oil peak. The Hubbert Oil Peak theory states that for any given geographical area, the rate of petroleum production follows a bell-shaped curve, i.e. it peaks at a given epoch in time [2, 3]. The initial rise in the bell curve is due to field discovery and infrastructure expansion, while the decline after the peak results from resource depletion. When first posed in the mid 1950's, the theory predicted that the rate of oil production in US (the lower 48 states) would reach a maximum by about 1970. This prediction was initially faced with significant disbelief; however around 1971, US oil fields reached their production peak and their production rate has been declining ever since [3]. Figure 1.1 shows both the original Hubbert calculations and actual observations of US oil production.

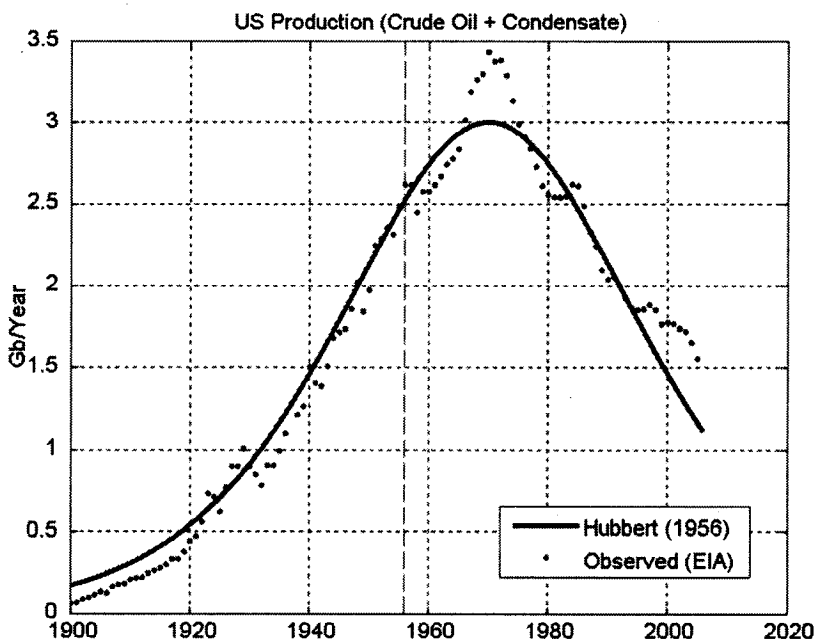

Figure 1.1 *US oil production (crude oil only) and Hubbert high estimate. (Taken from reference [3])*

In the meantime, other oil-rich countries have also reached their peaks: Iran in 1974, Russia in 1987, Saudi Arabia probably in 2006, Kuwait in 1971 and Canada (conventional oil only) in 1973 [3]. The model, when applied to the planet as a whole, predicts that the rate of global petroleum production will reach a maximum by around 2007. Figure 1.2 shows the oil production trends for the world's countries, excluding

OPEC and the former Soviet Union. For these countries, oil production has clearly reached its peak.

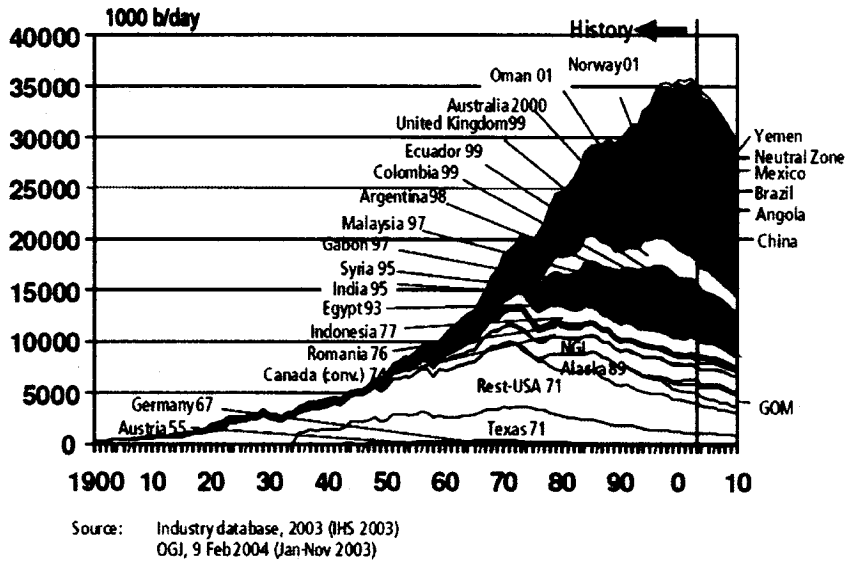

***Figure 1.2** World oil production for countries excluding OPEC and former Soviet Union countries. (Taken from reference [3])*

Figure 1.3 shows the trends in the oil production world-wide. A global peak in oil production is expected to be reached by the year 2010 or so.

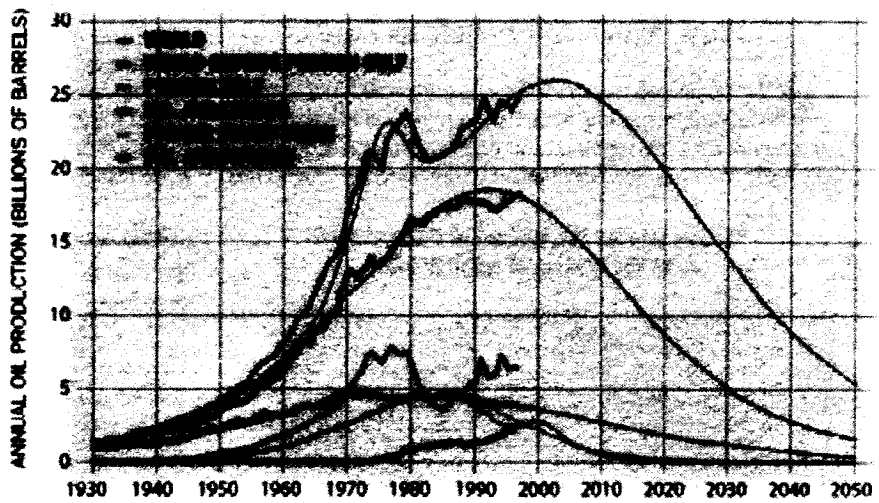

***Figure 1.3** Global production of oil, both conventional and unconventional (red), recovered after falling in 1973 and 1979. However, a more permanent decline is less than 10 years away, according to the authors' model, based in part on multiple Hubbert curves (lighter lines). US and Canadian oil (brown) topped out in 1972; production in the former Soviet Union (yellow) has fallen 45 percent since 1987. A crest in the oil produced outside the Persian Gulf region (purple) now appears imminent. (Taken from reference [2])*

Matt Simmons, one of the world's leading experts on the topic of peak oil and author of *Twilight in the Desert: The Coming Saudi Oil Shock and the World Economy [4]*, argues that Saudi Arabia's oil production and in particular that of Ghawar field, the world's largest field, will peak soon if it has not already done so.

Note that the Hubbert model does not state anything about global (or local) resources, but only the rate of petroleum production. The area under the Hubbert curve is a measure of world's total oil resources; judging from the model, there will be oil well into the future, albeit at a reduced production rate. It should also be noted that there are many who oppose the 'Hubbertists' and argue that this model is too simple to be applied to the planet as a whole [3]. Time will certainly tell; however, it is hard to argue that fossil fuel based energy resources are finite and will run out one day.

The consumption of energy by industrial nations and especially by rapidly developing countries, is increasing. Thus, there has been significant research into resources which could potentially substitute for oil as a source of energy. Coal is another fossil fuel that has been used as a source of energy for many years. Proven oil reserves, based on the 1998 global consumption rate, will last 50-80 years and additional undiscovered resources will probably extend this to 50-150 years. For coal, current estimates for the reserves and resources are 200 and 2000 years, respectively [1]. Furthermore, technology that can convert natural gas and coal into liquid fuel has been at least partially developed and can be, at least in principle, be further developed to produce liquid type fuel like gasoline [1]. However, the negative aspects of fossil fuels, especially the production of greenhouse gases, are increasingly being considered as major contributions to global warming. In recent years, many books, technical and non-technical, have been published on the subject of oil, its limitations and the economic and political consequences that a shortage of oil will cause [4-13].

1.1 Fossil Fuels and Global Warming

The negative consequences of the combustion of fossil fuels and the release of greenhouse gases such as CO_2 in the atmosphere have become increasingly pointed to as the main cause of the global warming. Currently, there is much debate in both the

scientific community and in the general public on the issue of global warming. Here, direct quotes are provided from the 4th assessment of the IPCC (Intergovernmental Panel on Climate Change) report which is being released in several parts during 2007. The IPCC was formed in 1988 by the World Meteorological Organization (WMO) and the United Nations Environment Programme (UNEP), both of which are United Nations organizations. The goal of the IPCC has been to study and evaluate the risks of human-made changes in the climate using peer reviewed and published scientific literature. The first part of the IPCC's 4th assessment, entitled *Climate Change 2007: The Physical Science Basis*, essentially a summary for policymakers, was formally approved at the 10th Session of Working Group I (covering the scientific basis) of the IPCC in Paris and was released in February 2007.

According to the IPCC report, "Global atmospheric concentrations of carbon dioxide, methane and nitrous oxide have increased markedly as a result of human activities since 1750 and now far exceed pre-industrial values determined from ice cores spanning many thousands of years [see Figure 1.4]. The global increases in carbon dioxide concentration are due primarily to fossil fuel use and land-use change, while those of methane and nitrous oxide are primarily due to agriculture [14]."

Figure 1.4, taken from the IPCC report (4th assessment), shows the variations in the concentration of three of the most important greenhouse gases (CO_2, N_2O and CH_4) and their corresponding radiative forcings over the last 10, 000 years [14]. Radiative forcing is, in simple terms, the difference between the incoming and the outgoing radiation energy. It is an index where positive values indicate the warming of a system and negative values mean a cooling effect. There is no doubt about the rapid and alarming increase of these greenhouse gases.

The report further concludes that the major source of these greenhouse gases has been human activities: "The understanding of anthropogenic warming and cooling influences on climate has improved since the Third Assessment Report (TAR), leading to very high confidence that the globally averaged net effect of human activities since 1750 has been one of warming, with a radiative forcing of +1.6 [+0.6 to +2.4] $W \cdot m^{-2}$ [14]." The 'very high confidence' level, mentioned here, translates to a 90% chance of being correct. The IPCC report further breaks down the contributions of the radiative forcing, from the

greenhouse gases CO_2, N_2O and CH_4, aerosols and various other sources, all of which contain a significant human contribution.

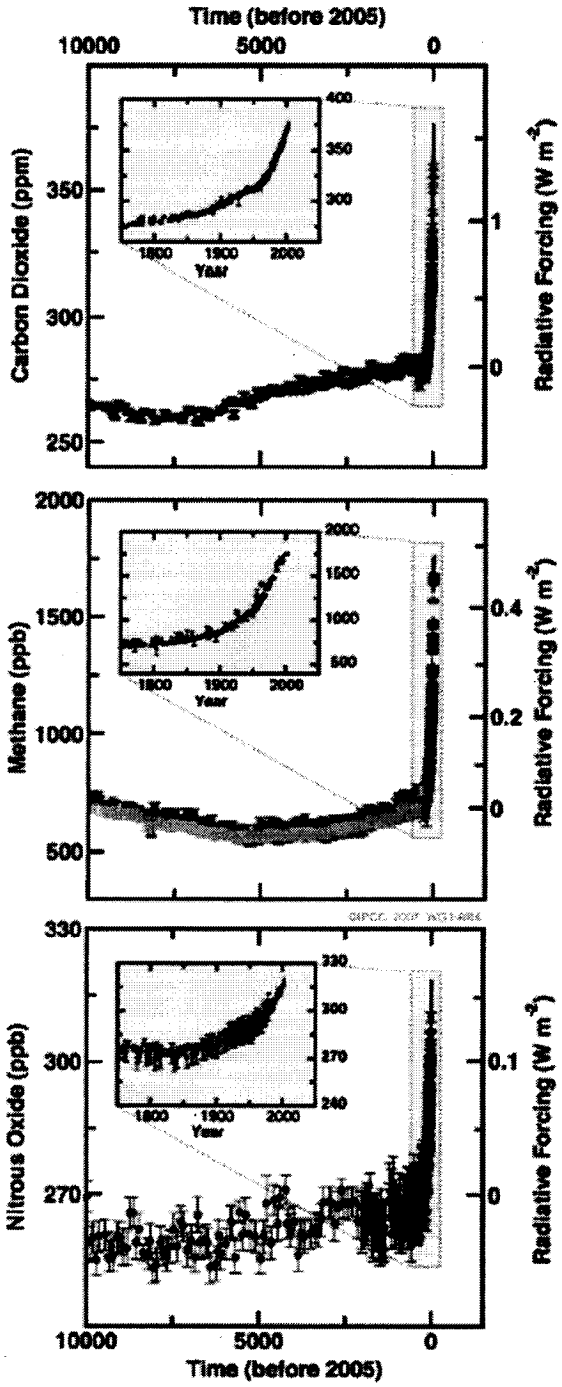

Figure 1.4 *Atmospheric concentrations of carbon dioxide, methane and nitrous oxide over the last 10,000 years (large panels) and since 1750 (inset panels). Measurements are shown from ice cores (symbols with different colors for different studies) and atmospheric samples (red lines). The corresponding radiative forcings are shown on the right hand axes of the large panels. (Taken from reference [14])*

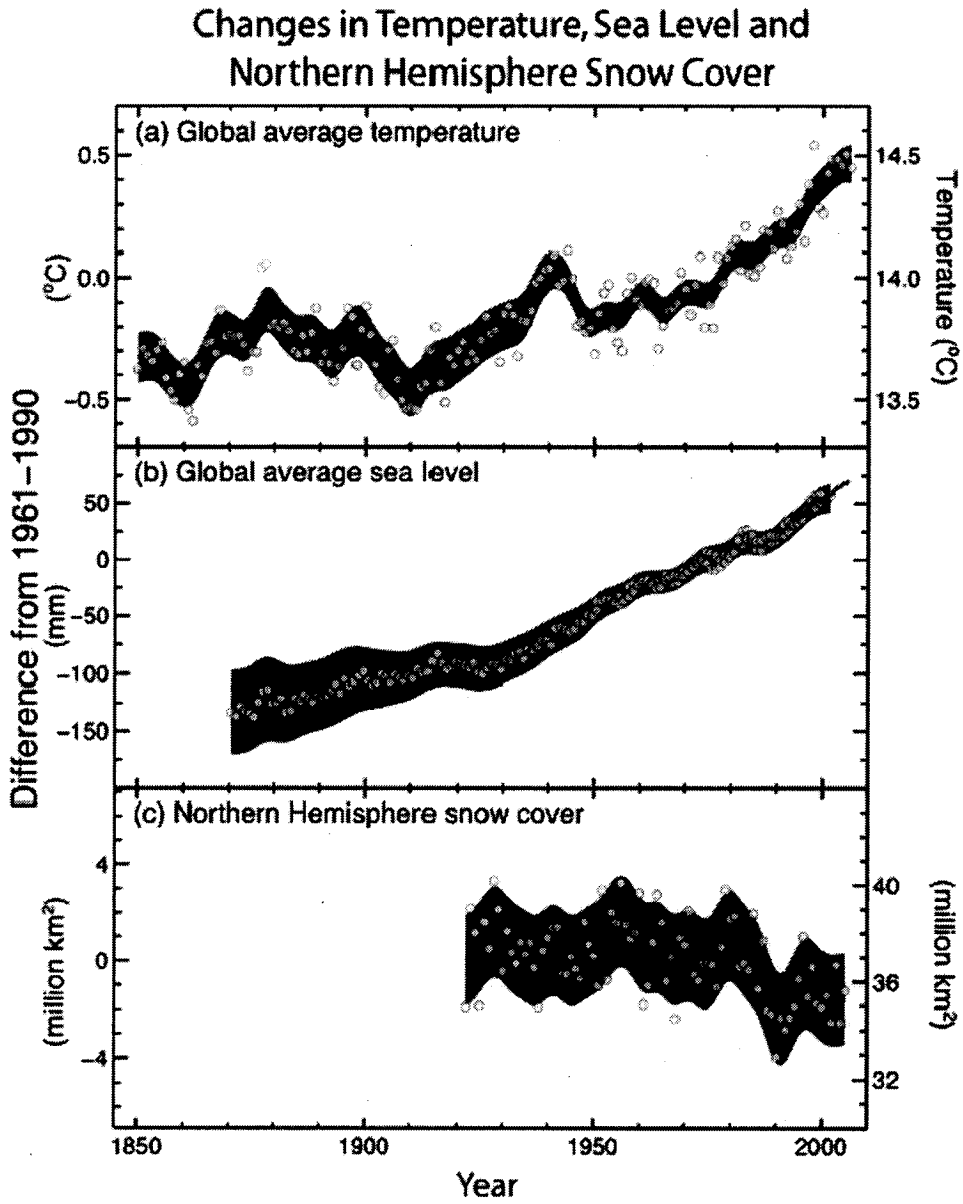

Figure 1.5 *Observed changes in (a) global average surface temperature; (b) global average sea level rise from tide gauge (blue) and satellite (red) data and (c) Northern Hemisphere snow cover for March-April. All changes are relative to corresponding averages for the period 1961-1990. The left y-axis in (a) and (b) show these changes. Smoothed curves represent ten-year averages while circles show yearly values. The shaded areas are the uncertainty intervals estimated from a comprehensive analysis of known uncertainties (a and b) and from the time series (c). (Taken from reference [14])*

On global warming, IPCC argues that "Warming of the climate system is unequivocal, as is now evident from observations of increases in global average air and ocean temperatures, widespread melting of snow and ice and a rising global average sea level. (See Figure 1.5) At continental, regional and ocean basin scales, numerous long-

term changes in climate have been observed. These include changes in Arctic temperatures and ice, widespread changes in precipitation amounts, ocean salinity, wind patterns and aspects of extreme weather including droughts, heavy precipitation, heat waves and the intensity of tropical cyclones [14]."

Figure 1.5, taken from 4th assessment IPCC report, shows the rapid increase in global temperature, sea level and a decrease of snow-covered land in the past 50 years. The phenomenon of global warming is manifested in numerous observable phenomena; for example, in increases in the: a) global average temperature, b) global average sea level, c) average atmospheric water vapor content, d) average temperature of the global ocean, e) f) temperatures at the top of the permafrost layer and g) two-fold increase in the average Arctic temperature change. The same warming effect is responsible for a decline in mountain glaciers, snow cover and losses in the ice sheets of Greenland and Antarctica. The IPCC report discusses the impact of global warming on climate, both regional and global, proposes possible scenarios and essentially forms a guideline, which is generally considered the most scientific report of its kind for policymakers.

In more recent years, the subject of fossil fuel shortages, global warming and their consequent geo-political and socio-political impacts have attracted a lot of attention in the media and in popular books [15-18]. Needless to say, the amount of technical and scientific literature on the topic of climate change and its consequences is also vast; see for example [19-27].

1.2 Alternate Energy Resources

Major alternative energy resources include solar energy, wind, geothermal, nuclear, hydroelectricity and biomass. These resources are not carbon based, are sometimes abundant and are generally considered clean. However, each of these resources faces a multitude of challenges, both technical and economical, which hinders their widespread use. Figure 1.6 shows the current fractional use of alternative energy resources.

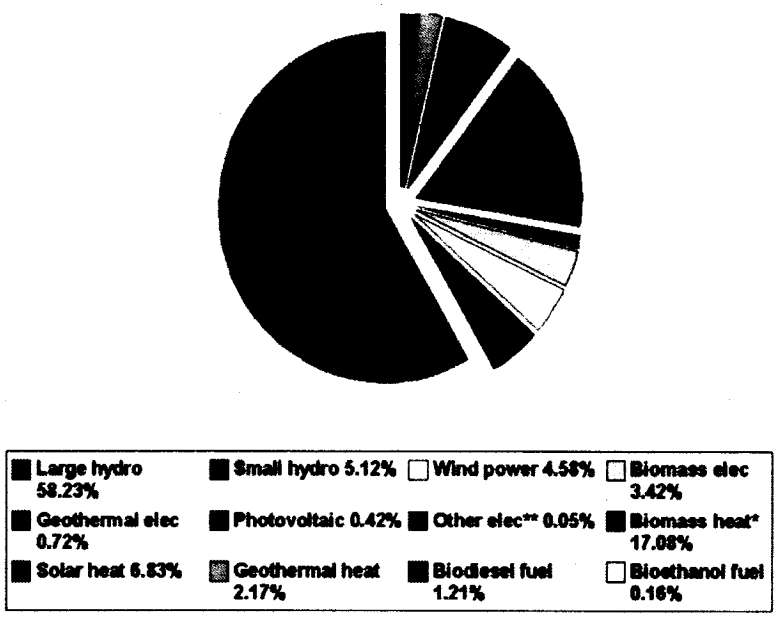

Figure 1.6 *World renewable energies in 2005. (Taken from reference [28])*

Hoffert *et al.* review possible future CO_2-free energy sources, like solar, wind, biomass, nuclear fission, nuclear fusion and fossil fuels from which CO_2 has been sequestered [29]. The authors explain the severe deficiencies that these technologies currently are facing and conclude that to make these technologies economically feasible, a broad range of intensive research and development is urgently needed. Only solar and wind energies and their prospects are briefly discussed here. Additional recent references on renewable energy include those of Twidell and da Rosa [30, 31].

Solar energy is the most abundant of all energy resources. The amount of solar radiation that hits the Earth's surface in one hour provides more than enough energy for all the energy consued by humans in one year [32]. This energy can be used to generate electricity, or more directly to heat buildings and water and for cooking. Solar cells, or photovoltaic (PV) cells, use light-absorbing materials which can use incident photons to produce electron-hole pairs and thus an electric current [33, 34]. They are widely used in low power applications such as calculators, LCDs and for powering Earth orbiting satellites. More recent applications of PV cells include grid connected solar panel power systems for buildings. Using these integrated power systems, the user draws power from the grid when the solar-produced power is insufficient and exports power to the grid when PV panels produce excess power. The high cost and low energy conversion

efficiency (about 15%) of PV cells are factors which have hindered their wider usage; however, their price has been decreasing in the past few years. As of 2005, the total world-wide peak power of PV panels was about 5,300 MW. In terms of installed PV power plants, Germany, Japan and the US are the forerunners in this field and together they account for more than 90% of the worldwide installed PV plants [35]. The total off-grid and grid-connected PV capacity of Germany, Japan and the US in 2005 was about 1,429, 1,421 and 479 MW, respectively [35]. According to Lewis *et al.* higher efficiency and a 10 times reduction in the cost of current solar energy conversion systems is needed for economically viable solar PV cells. For various aspects of solar energy, see a good recent review article by Sen [36].

Wind energy, which is converted to electricity using turbines, is the fastest growing of the renewable energy technologies. Commercial turbines typically produce about 1-5 MW of power. The world's wind power output grew from 2,500 MW in 1992 to about 40,000 MW in 2003, doubling every three years, at an annual growth rate of about 30% [28, 37]. Wind power was the fastest growing energy technology in the 1990s. Of course, wind power use is limited to areas where the speed and duration of the wind are sufficiently high. Offshore winds are particularly interesting because wind speeds are on average 90% higher than winds over land. The global theoretical potential of wind power is thought to be five times current production global energy consumption or 40 times current electricity demand [38]. However, mostly because of the intermittency issues, the scalability and feasibility of wind power for large scale power generation remains questionable. Germany, Spain, the US, India and Denmark have the largest investment in wind power technology [37]. Denmark and Germany produce 20% and 6% of their electricity needs, respectively, through wind power [28]. Ackermann provides a good review of wind energy by covering the historical background, current usage and the basic science and technology that is involved [37]. Other good technical review papers on wind energy are those of Sahin, Landberg, Tande, Singh and Bolinger [39-43].

Intermittency is a problem for both wind and solar energy. Storing the energy, for example in rechargeable batteries, is considered a partial solution. Another solution is to store the energy originating from the wind or sun in chemical bonds which can be later broken to release energy on demand. An example here would be splitting of water into

O_2 and H_2, where H_2 can later be used as a clean fuel in devices such as hydrogen fuel cells. Nathan Lewis discusses ways of storing solar energy in chemical forms, and makes clear and objective arguments for basic science needs, the development of more efficient photovoltaic materials and the direct splitting of water using solar radiation to achieve this goal [32, 44]. Sherif discusses the possibilities of utilizing wind energy to produce H_2 [45]. Levene *et al.* discuss the production of hydrogen from wind and solar energies [46].

1.3 Fuel Cells – A Brief Background

Fuel cells are devices which generate electricity from an electrochemical reaction between a fuel and oxidant. The efficiencies of fuel consumption are generally (but not necessarily) higher than combustion engines and green house gas emissions can be as low as zero. However, complications with fuel cell engineering, the production and storage of fuel, and most importantly the cost, availability and durability of the materials used in fuel cells, have been some of the major factors hindering the successful production and mass commercialization of fuel cells.

Fuel cells are targeted for a wide range of applications. Although automotive applications are currently the most important application, other applications like submarines and even aerospace are currently being considered. Stationary power supplies are also very important. In fact, phosphoric acid fuel cell (PAFC) systems have been commercialized by United Technologies (UTC) as back-up power systems in places like hospitals, police stations and remote areas [47]. In addition to automotive applications and stationary power supplies, fuel cells for portable electronics have also attracted a lot of attention. Many companies, for example Toshiba, Sanyo and Panasonic, have shown interest in FC powered cell phones and laptop computers. They hope to achieve significant energy density gains over current batteries, providing that they can overcome existing technical and economical hurdles [48, 49].

The current "Bible" of fuel cells, published by John Wiley & Sons in 2003, is the *Handbook of Fuel Cells* (in 4 volumes) edited by Vielstich, Lamm and Gasteiger. This work is the most extensive recent reference on fuel cells and covers nearly all aspects of fuel cell science and technology. The second volume of this work, *Electrocatalysis*,

focuses entirely on fundamental and applied aspects of catalysts and catalytic reactions of interest in the fuel cells. Another very recent and authoritative book on fuel cells is that by Srinivasan [50]. Srinivasan was one of the pioneers of fuel cell technology and spent decades researching in this field. His first fuel cell book, published in the 1960's, was a long time reference in this field. Other useful books on fuel cells are those of Hooger and Dicks & Larminie [47, 51].

1.4 Fuel Cells – Various Types

There are different kinds of fuel cells currently under research and development. They are sometimes grouped as low-temperature or high temperature fuel cells and usually they are named after their electrolyte. Table 1.1 presents a summary of various types of fuel cells.

In all fuel cells a hydrocarbon-based fuel (like hydrogen, methanol, ethanol, etc.) is catalytically dissociated (oxidized) to provide an electric current. The fuel is oxidized by oxygen and the by-product of the reaction (water in the case of hydrogen fuel) is released.

Table 1.1 *Summary of various kinds of fuel cells.*

Fuel Cell type	Electrolyte	Operating Temperature	Overall Reaction
Proton exchange Membrane Fuel Cell (PEMFC)	Solid polymer (Nafion)	40 – 100°C	$H_2 + ½ O_2 \rightarrow H_2O$
Direct Methanol Fuel Cell (DMFC)	Solid polymer (Nafion)	< 120°C	$CH_3OH + 3/2\ O_2 \rightarrow CO_2 + 2H_2O$
Alkaline FC (AFC)	35 / 85 wt% KOH in water	60 – 120°C	$H_2 + ½ O_2 \rightarrow H_2O$
Phosphoric acid Fuel Cell (PFC)	concentrated H_3PO_4	150 – 220 °C	$H_2 + ½ O_2 \rightarrow H_2O$
Molten Carbonate FC (MCFC)	Li/K carbonate	600 – 700°C	$H_2 + ½ O_2 \rightarrow H_2O$
Solid Oxide FC (SOFC)	metal oxide (ZrO_2)	650 – 1000°C	$H_2 + ½ O_2 \rightarrow H_2O$

High temperature fuel cells include molten carbonate and solid oxide fuel cells and low temperature fuel cells include phosphoric acid and proton exchange membrane fuel

cells. Proton exchange membrane fuel cells (or PEM, PEMFC) use different fuels. The most common are hydrogen and methanol. Of these fuel cells, phosphoric acid fuel cells are perhaps the most mature. UTC has commercialized these types of fuel cells for stationary power sources (250 kW). Since 1990, a few dozen units are currently in service. Solid oxide fuel cells are the most common high temperature fuel cells. PEM fuel cells are the most common low temperature fuel cells. Carrette *et al.* provide a good review of the various types of fuel cells, their principles and applications [52]. The *Handbook of Fuel Cells* also provides good coverage of different types of fuel cells like hydrazine, phosphoric acid, aqueous carbonate, direct methanol, other direct-alcohol, solid oxide and biochemical [53-59].

1.5 Proton Exchange Membrane Fuel Cells (PEMFC)

Among the different kinds of fuel cells, the low temperature hydrogen fuel cells, also called proton exchange membrane fuel cells, after the polymeric (Nafion) membrane used as the electrolyte, receive the most attention. The PEMFC were successfully used in Apollo space missions. In the 1970s research focused on PAFC. Since the mid 1980s PEMFC began to receive more attention when the groups at Los Alamos National Labs and Ballard Power Systems showed significant improvement in energy densities which made them suitable for transportation applications like cars and buses. Figure 1.7 compares the PEM fuel cell (UTC) which was used on the Apollo mission in 1965 and a portable power generator introduced by Ballard in 2003. Today, there are major governmental, industrial and academic research programs on different types of fuel cells and also on fuel processing, storage and infrastructure [60-63].

Koppel provides an exciting read of the story of Ballard Power Systems and their early success, in *Powering the Future: The Ballard Fuel Cell and the Race to Change the World* [64]. Ballard Power Systems, founded by Geoff Ballard in Vancouver, British Columbia, Canada in the 1980s, has been a leader in PEMFC technology for the past twenty years.

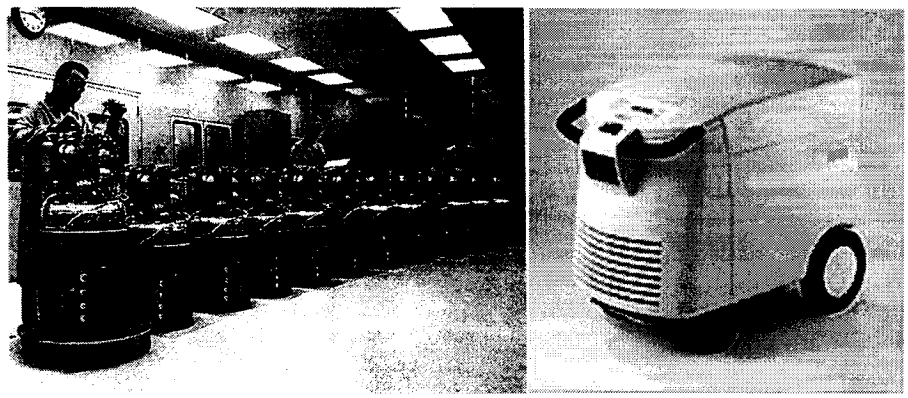

Figure 1.7 *Left: UTC's hydrogen fuel cell systems which were used aboard the Apollo spacecraft are shown (era 1965). Each individual cell in a system operated at 0.68 V and 168 mA·cm^{-2}, each system provided 600 W at 30 V and weighed 110 kg. (Taken from Hooger [47]). Right: AirGen, world's first indoor portable fuel cell power generator from Ballard Power Systems (2003). The unit weighs 49 kg and delivers 1000 W power at 120 V and is comprised of individual cells which operate at 0.75 V and 400 mA·cm^{-2}. (Taken from reference [65])*

1.6 PEMFC Components

Figure 1.8 shows a schematic drawing of a proton exchange membrane fuel cell. The anode and cathode electrodes of the cell are fed by hydrogen and air, respectively.

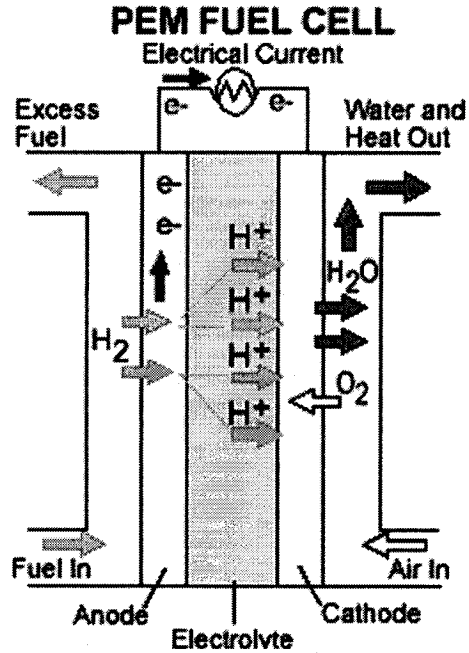

Figure 1.8 *A schematic drawing of a PEMFC. Oxidation of hydrogen and formation of water occur at the anode and cathode of the cell, respectively. The membrane, which separates the two electrodes, is permeable to protons. The flow of electrons, through an external circuit, provides electric power output. (Taken from reference [66])*

Hydrogen oxidation at the anode provides electrons, which power an external load and protons which are transferred through the membrane to the cathode side. At the cathode, oxygen is reduced to water. It is also possible for oxygen molecules to be reduced to H_2O_2, a potentially harmful species for fuel cells components. More on this will be discussed in later chapters.

Figure 1.9 illustrates a more detailed, cross-sectional schematic of a PEM fuel cell. Both the cathode and anode sides contain nano-particles of Pt catalyst supported on very fine carbon black particles. A mixture of catalyst powder and Nafion ionomer forms an ink which then is loaded onto the gas diffusion layer (GDL), typically some type of carbon cloth or paper. H_2, on the anode, and O_2, on the cathode sides permeates the GDLs and reaches the catalytic sites, where the corresponding oxidation and reduction reactions occur. The total change in the free energy of the $O_2 + 2H_2 \rightarrow 2H_2O$ reaction is negative, which means energy is released; however, the reaction is said to be kinetically-activated: that is, it does not occur spontaneously fast enough. Therefore a mixture of hydrogen and oxygen gases is stable and will not spontaneously combust. The presence of a catalyst at the two electrodes provides alternative paths (lower activation energy) for the reactions to proceed.

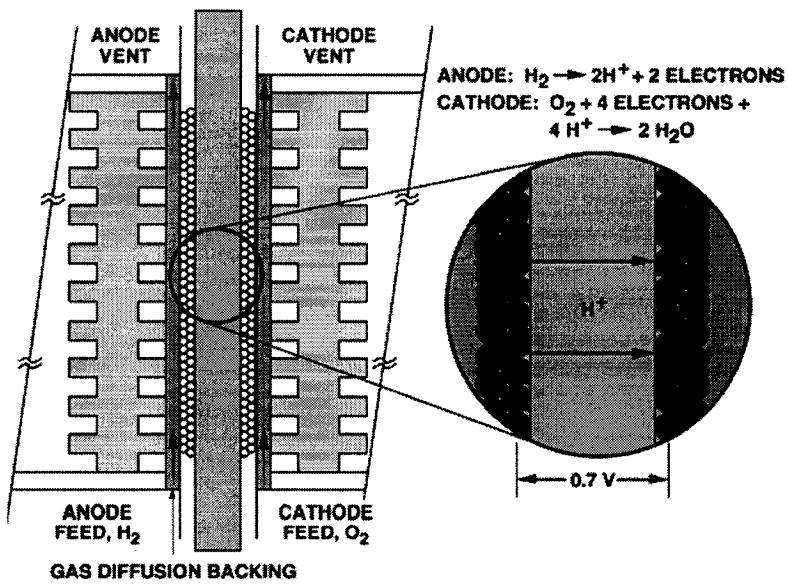

Figure 1.9 *A schematic drawing showing the internal structure of a hydrogen fuel cell. Hydrogen and oxygen (or air) flow in the respective anode and cathode flow fields. Hydrogen break up occurs at the anode side and water forms on the cathode. The magnified inset shows the chemical reactions that occur and transfer of protons across the Nafion membrane. (Taken from reference [67])*

Currently the preferred catalyst for both anode and cathode is Pt or an alloy of Pt. Limited sources of Pt and its high cost are major reasons to look for alternate (non Pt-based) catalysts. The membrane is essentially the electrolyte of the cell. It is ideally permeable to protons (and water) and electronically separates the two electrodes. The sandwich of two electrodes and the separating membrane is called the membrane electrode assembly or MEA and forms the active part of a PEMFC.

The basic properties of good membranes are: good proton conductivity, poor electron conductivity, good chemical and mechanical strength, low gas permeability, low fuel permeability and low cost. The most common and the industry-standard PEM material to date has been Nafion, a sulphonated fluoropolymer, which Dupont invented in the late 1960s. The chemical structure of Nafion is shown in Figure 1.10. The backbone is basically a modified polyethylene polymer, where fluorine is substituted for the hydrogen by a perfluorination process. The modified polymer is the well known polytetrafluoroethylene (PTFE) or Teflon.

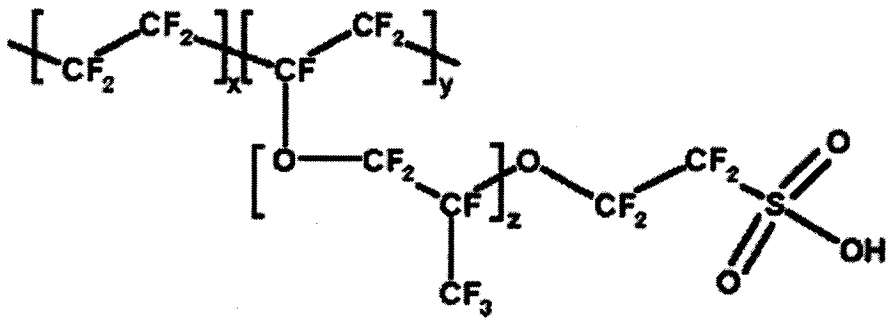

Figure 1.10 *Example structure of a sulphonated fluoroethylene. (Taken from reference [68])*

To make PTFE conductive, sulphonic acid containing $-SO_3H$ side chains are added to the polymer. The $-SO_3H$ group is acidic ($-SO_3^-H^+$) and thus the polymer is also called an ionomer. These sulphonic acid groups are hydrophilic; hence, the ionomer is able to absorb large amounts of water (up to 20 water molecules per $-SO_3H$ group). The H^+ ions are weakly attracted to the SO_3^- groups and are able to move, or hop, along the length of the molecule. This makes the Nafion a dilute solid acid.

There has been tremendous research on improving the PEM. Lowering the cost, improving the performance, durability and increasing the working temperature of membranes are the current focuses of research. Banerjee *et al.* discuss Nafion from a

Dupont point of view [69]. The authors describe the history and development of Nafion at Dupont, discuss current production levels and projected future manufacturing goals. Banerjee *et al.* point out that, at present, chloroalkali cells, which are used in chlorine production, are the biggest users of Nafion membranes. Hamrock *et al.* discuss the current membrane materials used for PEM and the key requirements for fuel cell applications [70]. These authors discuss materials and performance issues, the role of additives in increasing the conductivity, alternate acidic groups, sulfonated hydrocarbon based membranes and PEM durability. Schiraldi discusses the durability aspects of proton exchange membranes [71]. Schrialdi mentions that the main reason for membrane degradation is the release of H_2O_2, which is a possible product of oxygen reduction at the cathode side. H_2O_2 in the presence of metals breaks down into $OH^{\cdot}$ radicals, highly reactive species close in reactivity to fluorine. These radicals attack the acidic groups and initiate a chain oxidation which results in release of fluoride in the effluent water. Perpall *et al.* and Herrring discuss alternative approaches such as alternate fluoropolymer and carbon composite materials and role of inorganic additives in PEMs [72, 73]. Furthermore, and from the standpoint of fuel cell operation and balance of plant, there is a great desire to operate the fuel cell at higher (great than 100°C) temperatures. Higher temperatures lead to enhanced electrochemical kinetics, simpler water management and improved heat recovery. Zhang *et al.* provide a recent review of high temperature membranes [74].

The hardware components of fuel cells also create considerable complications and challenges. Efficient reactant (or fluid) flow fields, removal of water, temperature control, etc. are a few of these issues. Other important segments of fuel cells include current collectors and gas feeds. Stack engineering, balance of plant, water management issues and heat transfer are of paramount importance in making fuel cell stacks efficient. Stack modeling and computational fluid dynamics are widely used for theoretical studies of mass transport effects [75-79]. These engineering aspects will not be discussed here, however more information can be found elsewhere [80-85].

1.7 Basic FC Electrochemistry

In this section, the basic electrochemical operation of a fuel cell is introduced. The following material and examples are taken primarily from Dicks and Larminie [51].

1.7.1 Free Energy and the Equilibrium Potential of a PEMFC

As mentioned before, the PEM fuel cell reaction can be thought of as a slow combustion of fuel. The net change in the free energy of the reaction is negative; thus. it is thermodynamically favorable. The change in the molar Gibbs free energy of the reaction is expressed by the following equation:

$$\Delta g_f = (g_f)_{H2O} - (g_f)_{H2} - 0.5(g_f)_{O2}. \quad (1.1)$$

The free energy of each of the reactants H_2 and O_2 and the product H_2O is given by:

$$\Delta g_f = \Delta h_f - T\Delta s_f, \quad (1.2)$$

where h and s are the molar enthalpy and molar entropy, respectively. Both enthalpy and entropy are temperature dependent; hence, the change in the free energy of the reaction is also temperature dependent. The Gibbs free energy of the reaction is a measure of the maximum work that can be done by the conversion of reactants to products and is related to the cell electrochemical potential by:

$$\Delta g_f = -nFE, \quad (1.3)$$

where n (=2) refers to the number of electrons transferred for equation 1.1, F is Faraday's constant and E is the cell's equilibrium (also called open circuit voltage or OCV) potential. Larminie and Dicks provide the expressions for enthalpy and entropy of H_2, O_2 and water (steam) at different temperatures [51]. Although the magnitude of enthalpy increases at higher temperatures, the entropy factor makes the free energy smaller and as a result the cell OCV decreases as temperature increases. Table 1.2 shows the values of Δg_f, OCV and efficiencies of the H_2/O_2 reaction at different temperatures. The efficiencies reported in Table 1.2 are based on

$$\text{eff} = \Delta g_f/\Delta h_f * 100 \quad (1.4)$$

or in other words, the maximum possible electrical energy obtainable (i.e. Gibbs free energy) divided by the heat of reaction released from burning the fuel. Note that these values refer to the state of equilibrium, where no current is delivered. The concept of

efficiency is not so simple and is always a matter of controversy because one has to consider many different parameters.

Table 1.2 *Δg_f, maximum OCV and efficiency limit for hydrogen fuel cell.*

Form of water	Temperature (°C)	Δg_f (kJ/mole)	Maximum OCV (V)	Efficiency Limit
Liquid	25	-237.2	1.23	83%
Liquid	80	-228.2	1.18	80%
Gas	100	-225.3	1.17	79%
Gas	200	-220.4	1.14	77%
Gas	400	-210.3	1.09	74%
Gas	600	-199.6	1.04	70%
Gas	800	-188.6	0.98	66%
Gas	1000	-177.4	0.92	62%

Adapted from reference [51].

The free energy change also depends on the concentration of reactants and products. In a PEMFC, the concentrations are just partial pressures. This implies that the equilibrium potential of the cell will also depend on the partial pressures. The relationship is the well-known Nernst equation, here applied to the H_2/O_2 reaction:

$$E = E^{\circ} + \frac{RT}{2F} \ln\left(\frac{P_{H_2} . P_{O_2}^{\frac{1}{2}}}{P_{H_2O}}\right), \qquad (1.5)$$

where E° is the potential at standard pressure and temperature while P refers to the pressure (or partial pressure in the case of a gas mixture) of the respective gases. It should be noted that the theoretical open circuit potential of a hydrogen fuel cell, i.e. 1.23 V at 25°C, is not measured in a fuel cell. Special electrochemical cells and experimental setups are needed to observe the equilibrium potential of oxygen reduction. This has to do with the adsorbed species on the electrode surface which are said to poison the catalyst and corrosion of Pt. This will be discussed more in the next chapter.

1.7.2 Losses and the Non-Equilibrium Potential of a Fuel Cell

The potential of a fuel cell drops when current is drawn and the magnitude of the potential drop depends on the current. In general there are three or four types of losses associated with the voltage of the fuel cell. Minimizing these losses is crucial for obtaining higher power density. The loss in the potential is often called overpotential,

overvoltage, polarization, voltage drop, voltage loss or irreversibility. They all mean the same thing: the potential is not the equilibrium value.

Figure 1.11 shows a calculated plot of fuel cell voltage versus the current density that it generates.

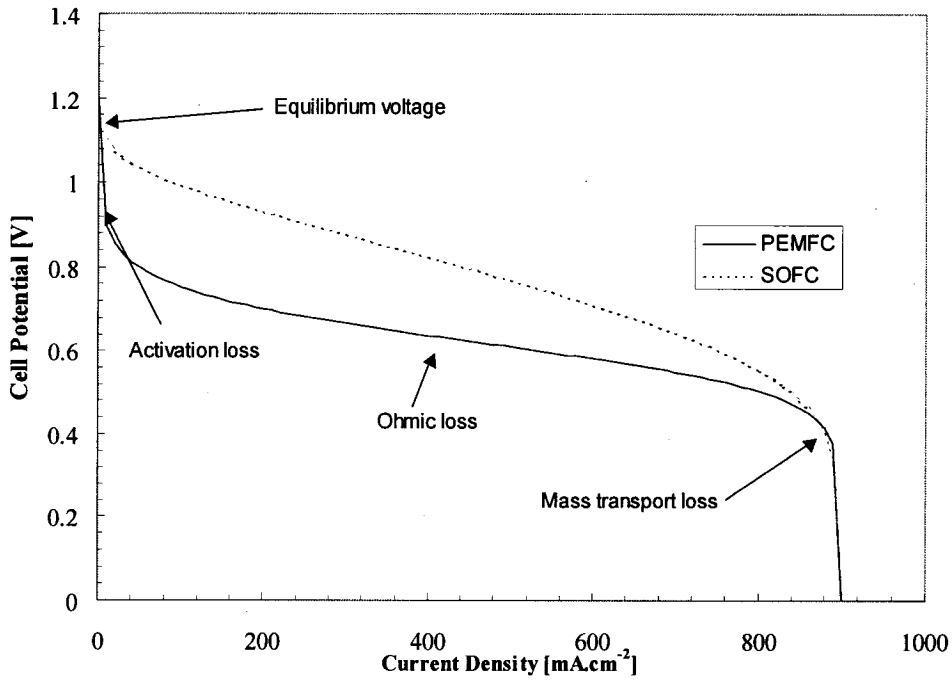

Figure 1.11 *Typical polarization curves are shown for a) PEMFC and b) SOFC.*

This kind of graph is referred to as a polarization curve and its measurement provides the first test of fuel cell performance. Notice that the potential drops along the curve are grouped into three main regions. The sudden initial drop is referred to as the activation drop and is governed by the performance of the catalyst. The linear region is due to Ohmic losses in the cell caused by the dissipative impedance of the cell components. The drop at high currents, or mass-transfer drop, is caused by the finite transfer rate of reactant to and product away, from the electrodes. These losses need to be discussed in some detail.

1.7.3 Activation Losses

After many experiments on different electrodes, Tafel in 1904 obtained the following empirical overpotential relation between the potential and current of a metal immersed in a solution like an acid:

$$\eta^{activation} = A\ln\frac{j_o}{j}, \qquad (1.6)$$

where j is the current density drawn from the cell, j_o is called the exchange current density (the equilibrium "current" at OCV) and $A = RT/\alpha nF$, where α is a material dependent constant. n refers to the number of electrons transferred during the reaction and is 4 for reduction of one oxygen molecule to water. This activation overpotential is dominant for small values of current density j_o, i.e. for a case where the potential is not perturbed too much from the equilibrium value. At equilibrium (really dynamic equilibrium), oxidation and reduction reactions of a molecule (e.g. $H_2 \leftrightarrows 2H^+ + 2e^-$) do occur, but at equal rates. The exchange current density is a measure of the rate of the equilibrium reactions (e.g. $H_2 \leftrightarrows 2H^+ + 2e^-$), which occur at the metal surface and is a surface-dependent quantity. The exchange current cannot be measured directly because there is no net current at equilibrium. The Tafel equation was later derived on basis of thermodynamics and derivations can be found elsewhere [86]. Values of exchange current densities for H_2 on the surface of several metals are shown in Table 1.3.

Table 1.3 *j_o for hydrogen oxidation/reduction on various metals with an acid electrolyte.*

METAL	*J_O ($A \cdot CM^2$)*
Pb	2.5×10^{-13}
Zn	3×10^{-11}
Ag	4×10^{-7}
Ni	6×10^{-6}
Pt	5×10^{-4}
Pd	4×10^{-3}

Adapted from reference [51].

The potential of a fuel cell, then, in the presence of only activation losses will be:

$$V = E^o - \eta^{activation}, \qquad (1.7)$$

where E^o is the equilibrium potential and its value is given by (1.5). Figure 1.12 shows the impact of exchange current density on the voltage of a cell. Increasing the exchange current density significantly lowers the activation losses. The activation overpotential is the only significant voltage loss at low current densities.

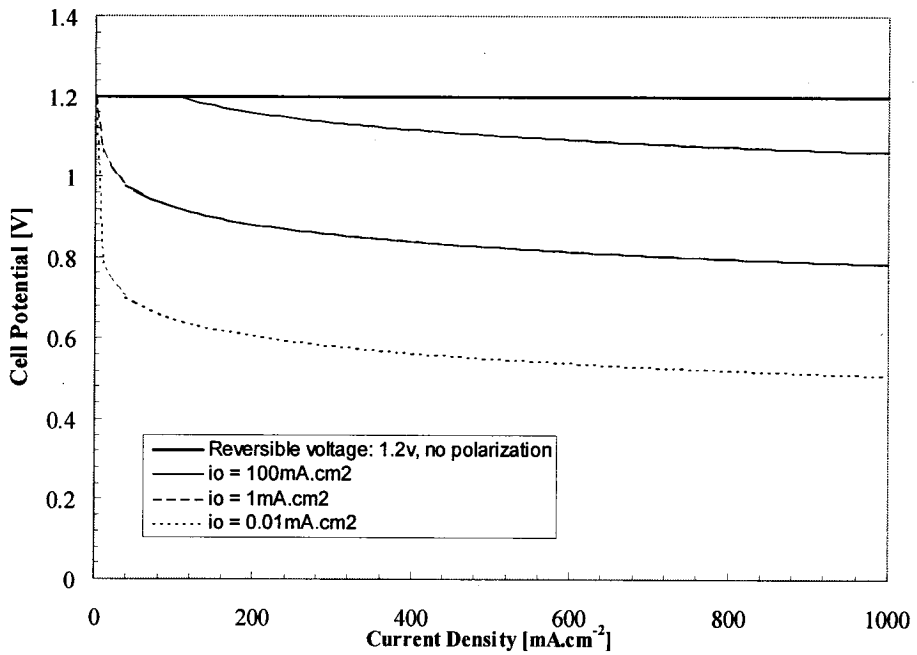

Figure 1.12 *Calculated polarization curves using equation 1.7 for a H_2/O_2 PEMFC reaction shown for different values of the exchange current density. The calculations assume that other voltage losses are not present.*

An optimum choice of materials and careful design of electrodes can increase j_o and lower the activation losses. Increasing the exchange current density can be achieved in several ways:

1) Increasing the temperature increases the rate of reactions and hence increases j_o.
2) Better catalysts have higher activity and thus improve j_o.
3) Increasing the surface area or the roughness of the electrodes to provide more reaction sites. This will increase the exchange current or j_oA.
4) Increasing the pressure increases the catalyst site occupancy and hence increases j_o. This also increases the equilibrium potential (1.5).

The Tafel relation will be again revisited in chapters 2 and 3 in the contexts of electrocatalysis and corrosion, respectively.

1.7.4 Ohmic Losses

Electronic resistance in the parts of the fuel cell and ionic resistance of the membrane electrolyte represent Ohmic losses in a fuel cell. The Ohmic potential drop is given by:

$$\eta^{Ohmic} = jr, \qquad (1.8)$$

where j is the current density and r is the area specific resistance.

1.7.5 Mass Transfer (concentration) Losses

The (partial) pressures of fuel and oxygen gradually decrease as the current increases. A pressure drop at the electrode translates into a potential drop whose magnitude can be approximated by the Nernst equation:

$$\Delta V = \frac{RT}{2F} \ln\left(\frac{P_2}{P_1}\right). \qquad (1.9)$$

At some maximum flow rate, the current density reaches its maximum level j_l. The partial pressure just reaches zero, the overpotential increases greatly and the current density cannot be increased above this level. If P_1 is the partial pressure at zero current density and assuming the pressure drops linearly to zero as the current density increases, then the partial pressure at any given current density, j, is given by:

$$P_2 = P_1\left(1 - \frac{j}{j_l}\right). \qquad (1.10)$$

The mass-transfer overpotential thus becomes:

$$\eta^{\text{MassTransport}} = B\ln\left(1 - \frac{j}{j_l}\right), \qquad (1.11)$$

where B = RT/4F for oxygen.

Now putting all the losses discussed so far together, a general equation for the polarization curve of a fuel cell is:

$$V = E - \eta^{\text{Activation}} - \eta^{\text{Ohmic}} - \eta^{\text{Mass Transport}}, \qquad (1.12)$$

where, E is the equilibrium potential of the cell and is given by (5). Substituting the expressions for the three losses discussed above, one obtains:

$$V = E - A\ln\left(\frac{j}{j_o}\right) - jr - B\ln\left(1 - \frac{j}{j_l}\right). \qquad (1.13)$$

Table 1.4 shows values of the parameters used in (1.13) for a typical PEMFC and a SOFC. These values were used to calculate the polarization curve shown earlier in Figure 1.11.

Table 1.4 *Example constants for equation 1.13.*

Constant	Low Temperature (e.g. PEMFC)	High Temperature (e.g. SOFC)
E / V	1.2	1.0
R / $k\Omega \cdot cm^2$	30×10^{-6}	300×10^{-6}
j_o / $mA \cdot cm^{-2}$	0.067	300
A / V	0.06	0.03
B / V	0.05	0.08
i_l / $mA \cdot cm^{-2}$	900	900

Adapted from reference [51].

Figure 1.13 shows the polarization curves of a state-of-the-art PEMFC from General Motors (GM). Various losses are approximated and it can be seen that the activation overpotential for oxygen reduction accounts for the most significant part of the voltage loss.

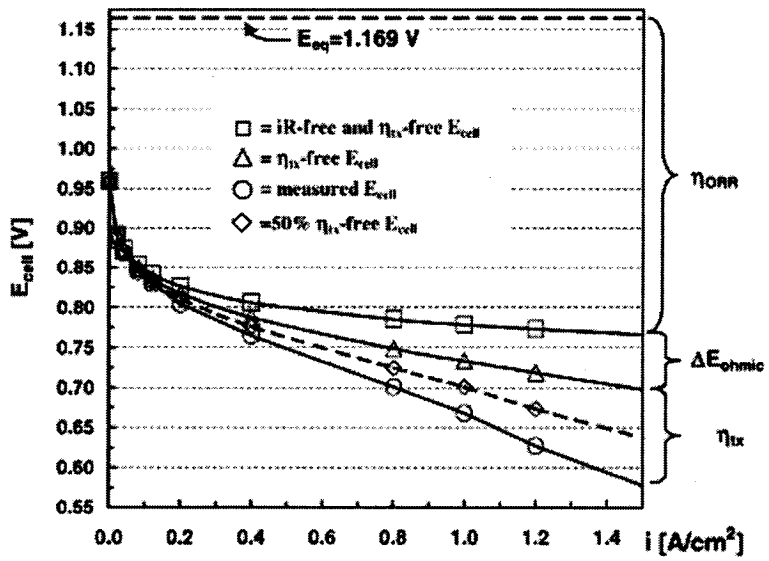

Figure 1.13 *Polarization data for a state-of-the-art hydrogen fuel cell from General Motors. (a) Circular symbols: 50 cm^2 single-cell H_2/air performance at T_{cell} = 80°C (80°C dew points, i.e., 100% RH) at a total pressure of 150 kPa_{abs} and stoichiometric flows of s = 2.0/2.0. Catalyst-coated membrane (CCM) based on a ca. 25-μm low-EW membrane (ca. 900 EW) coated with electrodes consisting of ca. 50 wt.% Pt/carbon (0.4/0.4 $mg_{Pt} \cdot cm^{-2}$ (anode/cathode)) and a low-EW ionomer (ca. 900 EW; ionomer/carbon ratio = 0.8/1). (b) Square symbols: E_{cell} versus i for the mass-transport-free and ohmically corrected (i.e., iR-free) E_{cell}/i-curve shown in (a). In situ measurements of the high-frequency resistance versus current density were obtained at 1 kHz (ranging from 45 to 55 $m\Omega \cdot cm^{-2}$) and used for the ohmic correction. (c) Triangular symbols: Addition of the ohmic losses, ΔE_{ohmic}, to the polarization curve shown in (b). (d) Diamond symbols: E_{cell}/i-curve shown in (a) corrected for 50% of the mass-transport losses. η_{tx} designates the mass transfer losses. (Taken from reference [87])*

The proceeding treatment is perhaps the simplest approach for quantifying and formulating PEMFC polarization curves. Larger systems such as fuel cell stacks are considerably more complicated and one needs to consider the effects of catalyst layers, mass transport (gas, water) and heat flow. Modeling the voltage profiles of the fuel cells (stacks) then quickly becomes very complicated [75-77, 88].

1.8 Current Problems Facing PEMFC

Successful commercialization of PEMFC relies on solving or mitigating many problems. Hydrogen production and storage is one area of intense research [89-92]. Current methods of producing and storing hydrogen are neither sufficient nor CO_2-free. For fuel cells, cost reduction of materials and improving their stability and performance are the most important areas of research. Recent cost analysis data of PEMFC materials is therefore provided for reference, followed by some discussion of the catalyst prospects.

1.8.1 Hydrogen Production and Storage

Besides the PEMFC and its related hardware, equally important and also very challenging is the question of producing hydrogen fuel and its storage. Where and how can hydrogen be obtained? Currently, about 40 million tons of hydrogen are produced annually world-wide. The main applications are in fertilizer production and the space program. The current economically feasible method of producing hydrogen is steam reformation of carbon-based fuels such natural gas. In this process natural gas and steam are mixed in a reactor which utilizes a catalyst such as Ni to decompose the natural gas. The products are H_2, unreacted natural gas, CO and CO_2. The important point here is that hydrogen from hydrocarbon fuels does produce CO_2, which is a greenhouse gas. For this reason, there is currently extensive research on producing H_2 by alternative routes, within, for example, the research programs of National Renewable Energy Laboratory (NREL) and the Department of Energy (DOE)-initiated centers of excellence in hydrogen production/storage are very active. The interested reader is referred to the web sites of NREL and DOE, whose research initiatives, reports and current research programs on hydrogen energy and PEMFC can easily be accessed [62, 63].

The Holy Grail of hydrogen production is the clean and efficient production of H_2 from water. The electrolysis of water is a well-known possibility; however, the overall process is not cheap and efficient. Today's electrolyzers can reach up to 80-85% efficiency; however, clean power is needed to drive them. Hydroelectric power is not abundant enough for this purpose. Other options are direct solar water-splitting, thermochemical and photo-biological methods. The idea of driving an electrolyzer from solar-power powered electricity is very appealing and has been suggested as an ultimate solution. Wind-derived power is also an alternative which was alluded to in the previous section. Wurster *et al.* discuss solar and wind energy coupled with electrolysis and fuel cells [93].

Several solar-hydrogen demonstration and testing centers have recently been established. Three examples include Clean Air Now (CAN)-Xerox project (early 1990s) in California, the Solar-Wasserstoff Bayren (SWB) project in Germany and the Hydrogen-Solar (HYSOLAR) project of Germany-Saudi Arabia. All these projects successfully demonstrated the practicality of solar powered H_2 and PEMFC cars; however, because of economics most of these programs were stopped at a demonstration stage [94]. Peter Hoffmann provides a very interesting summary of hydrogen as a fuel [94]. Bilgen studies the economics of an integrated solar-electrolysis system in the US, using current technologies for solar cells and electrolyzers and concludes that this approach would become economically feasible only if government subsidies are established. This approach would become competitive only if the photovoltaic-electrolyzer system price is several times lower than present and/or the price of fossil fuels becomes several times higher [95].

Another very important route in production of hydrogen under current consideration is the use of thermochemical cycles which can be coupled to nuclear power plants. Steam and heat produced in these reactors in conjunction with suitable chemical routes, for example the sulfur-iodine cycle, can produce hydrogen without the emission of green house gases [96].

It must be stressed that the current consensus among the experts and proponents of hydrogen fuel is that initial phase of a converting to hydrogen fuel would be based on hydrogen derived from carbon-fuels. CO_2-free hydrogen would be a longer term goal.

For hydrocarbon-derived hydrogen, there is also the option of CO_2 sequestration. Damen *et al.* study the production of electricity and hydrogen from coal and natural gas coupled with CO_2 sequestration [97, 98]. More on hydrogen as fuel can be found elsewhere [99-105].

Another important issue, which comes up in the case of hydrogen fuel is its storage, especially for automotive applications. An alternative to high pressure tanks and cost of liquification is the use of solids which currently hold up to 8% of their weight as hydrogen. There are very active research programs in this area, with carbon-based materials, such as multi-walled carbon nano-tubes (CNT) being promising materials [106].

1.8.2 Fuel Cell Catalysts

1.8.2.1 PEMFC Cost Analysis

A cost analysis of PEMFCs has been recently reported by Carlson *et al.* from NREL [107]. The authors report on the cost of materials, components, single and stacked FCs and integrated systems. Manufacturing costs, economic factors, fluctuations and other aspects are considered using inputs from various industrial sources. According to their estimates, about 90% of the PEMFC stack cost is materials related, i.e. MEA, bipolar plates, etc. Furthermore, they predict reductions in the costs of all materials (eg. Nafion membrane, GDL, seals, bipolar plates) over time, except for that of the Pt-based catalysts! The cost of Pt catalysts actually shows an increase which is partly due to increased Pt price (now $USD 900/troy ounce unlike the traditionally stable $USD 450/troy ounce between 1985 and 2000). Figure 1.14 shows an estimated break down of the PEMFC stack baseline cost as of 2005. The stack baseline cost is somewhere about $70/kW.

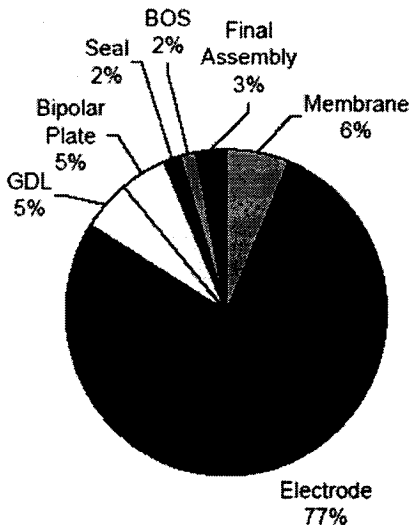

Figure 1.14 *Hydrogen fuel cell stack baseline cost breakdown. (Taken from reference [107])*

Figure 1.15 shows a complete Ballard PEMFC-BOP (Balance of Plant) system for light-duty vehicle application. It weighs about 100 kg, occupies 0.076 m^3 (2.7 ft^3) and delivers 85 kW of power (300 A at 284 V) [107].

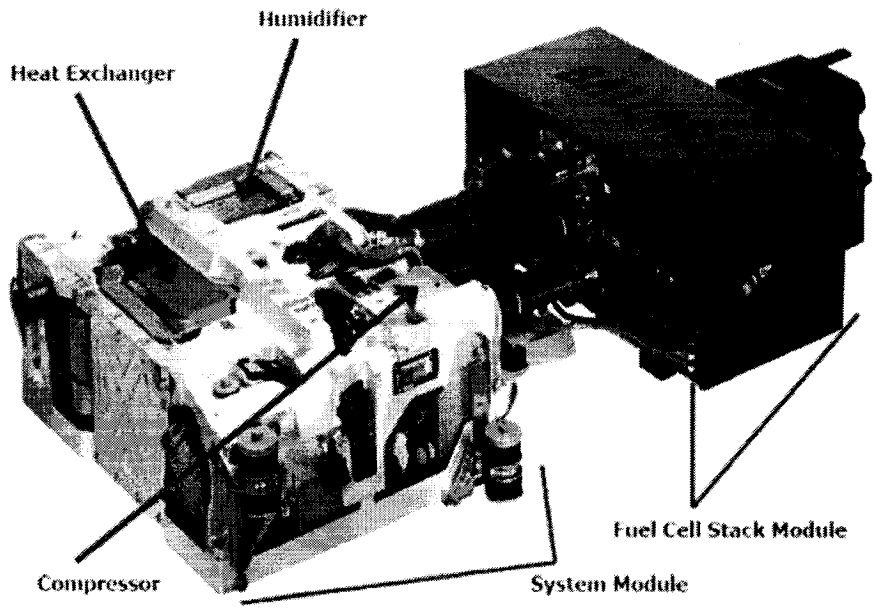

Figure 1.15 *Hydrogen fuel cell stack and balance of plant. (Taken from reference [107])*

A typical BOP system consists of air management unit (filtration and compressor), water management, thermal management and fuel management. The overall cost of the BOP-PEMFC system is about $110/kW and its cost breakdown is shown in Figure 1.16.

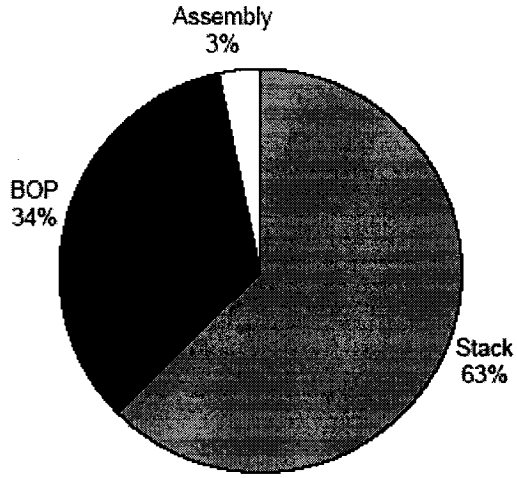

Figure 1.16 *Stack and BOP contributions to a PEMFC stack system cost. (Taken from reference [107])*

1.8.2.2 PEMFC Catalysts: Requirements and Expectations

Desirable catalysts and MEA materials should provide: high catalyst mass activity, high catalyst utilization at all current densities, low mass transport losses, high tolerance to multiple surface area loss mechanisms, tolerance to a wide humidity and temperature operating window, thousands of hours of operation, cold start and freeze tolerance and the ability to be fabricated by robust high volume-compatible and low cost processes. The stability of membranes against $OH^{\cdot}$ radical attack and the stability of gas diffusion layers against carbon oxidation or decomposition that can cause impedance increases and loss of hydrophobicity are also very important.

Besides ORR activity, a cathode electrocatalyst must show stringent durability in the working environment of the PEMFC. The catalyst is exposed to a low pH medium, a temperature of 80°C or more and to an electrochemical potential, with occasional excursions to high potentials (1.2-1.5 V). Pt dissolution and agglomeration during exposure to high potentials, which leads to a loss in the active surface area and hence a reduction in the performance, has been reported by several research groups [108-111]. Corrosion of the carbon support, due to the presence of Pt catalyst and dissolution of transition metals in the Pt-alloys because of the acidic medium have also been reported [108, 112-114].

To increase the catalyst activity, or alternatively to lower the Pt loading, numerous ideas have been explored. Some of these ideas include: a) alloying of Pt with other

transition meals like Co or Ni [115-117], b) designing of core-shell type electrocatalysts with surface monolayers of Pt [118], c) metal oxide supports (strong metal-support interaction) [119], d) polyoxometalate additives [120], e) metal oxide overlayers [121], f) severely strained lattice structures [122], g) metal hexaboride supports [123] and h) nano-structured thin film support (NSTF) structures [124]. The NSTF technology will be described in more detail in later chapters. In addition to Pt electrocatalysts, there are non-Pt based catalysts, both noble metal based like Ru-Se and non-noble metal based such as Fe-C-N systems, chalcogenides, or even oxides, which are also being considered for electrocatalysis of the ORR [125-130]. However, at the present time, non-noble metal catalysts can not compete with Pt-based catalysts in terms of performance and normally produce a larger amount of H_2O_2, which lead to membrane degradation [127, 131, 132].

The most intensely studied approach to enhance the electrocatalytic activity of Pt is alloying of Pt with some transition metals. This approach was first explored and now is in use, for the oxygen reducing cathodes of phosphoric acid fuel cells [133-135]. Although it has been shown that alloys like Pt-Co provide about 2 to 2.5 times the kinetic activity gain of Pt, the long term stability of alloys under the working conditions of PEMFCs is not very well known. More on the activity and stability of Pt-alloys will be presented in the later chapters.

1.9 Conclusions

The current problems with fossil fuels, namely their limited resources and their contribution to the global warming, were discussed. Methods to produce clean energy such as wind and solar generated power were reviewed. Fuel cells and in particular PEMFC were described in some detail.

The challenges in PEMFC research are: a) production, storage and handling of clean fuel, for example CO_2-free H_2 and b) fuel cell related issues. The most important problems facing fuel cells themselves are: cost, performance and stability of materials used, in particular the PEM and the catalysts. Engineering aspects of fuel cells such as stack design, water management, heat management, freezing-temperature start and overall endurance are all very important; however, they were not discussed here. For all

these topics, both engineering and materials related, the four volume *Handbook of Fuel Cells* and references therein remain excellent sources of information.

1.10 Structure of Thesis

This thesis discusses research which was performed on both the activity and the stability of Pt-based and non-Pt based catalysts for the oxygen reduction reaction. Chapter 2 presents a basic theoretical background to the field of electrocatalysis, emphasizing some of the most recent research and breakthroughs in fundamental understandings of electrocatalytic properties of oxygen reducing materials. Chapter 3 explains the experimental techniques that were used. Chapter 4 presents the corrosion experiments that were performed on the combinatorial libraries of Pt-alloys. Chapters 5, 6 and 7 present the RRDE measurements of Pt and Pt-Ta films deposited on glassy carbon disks, Pt-Co films deposited on glassy carbon disks and Pt/NSTF samples, respectively. Chapter 8 discusses the impact of catalyst (both Pt-based and non-Pt based) loading in the RRDE experiments.

Chapter 2

Theory of Catalysis and Electrocatalysis

Both electrodes of a PEMFC use Pt as a catalyst. A simple but haunting question is: Why is Pt such a good catalyst? More generally speaking, what determines the surface reactivity of metals? In general these are not easy questions to answer and despite decades of both experimental and theoretical research, there still remain a lot of unanswered questions. Some of the basic and key aspects of catalysis and in particular electrocatalysis are discussed in this chapter. The focus will be on some recent experimental and theoretical work done on Pt alloys.

2.0 Heterogeneous Catalysis

Catalysis is, broadly speaking, grouped into homogeneous and heterogeneous categories. Homogeneous catalysis refers to a situation where the catalyst and the reactants are in the same phase. One good example of this case is the breakdown of O_3 molecules by Cl, where both O_3 and Cl are gaseous [136].

In heterogeneous catalysis, the catalyst and the reactants are in different phases. Catalytic reactions involving liquid and gas molecules by metals are very common examples. The following are well known examples of heterogeneous catalysis and their discoverers [136]:

$2NH_3 + 2.5O_2 \rightarrow 2NO + 3H_2O$ catalyst: Pt (Ostwald, 1901)

$C_2H_4 + H_2 \rightarrow C_2H_6$ catalyst: Pt (Sabatier, 1902)

$N_2 + 3H_2 \rightarrow 2NH_3$ catalyst: Fe (Haber, 1914, Nobel Prize 1918) (2.1)

Oxidation of hydrogen and reduction of oxygen in the PEMFC are also examples of heterogeneous catalysis, where the terminology of electrocatalysis and electrocatalyst are more appropriate. The elementary steps in the dissociation of a molecule on a surface are complicated and include many processes like adsorption, diffusion, bond breaking and desorption. There are adsorbate-adsorbate interactions too, which complicate the matter even more. Heterogeneous catalysis is part of the vast field of surface science which

involves studies of the chemistry and physics of surfaces as well as surface reactions. The field has gone through explosive growth since the 1960s when ultra high vacuum technologies became available. Some good introductions are those of Kolasinski, Zangwill and Somorjai [137-139]. For heterogenous catalysis, *Concepts of Modern Catalysis and Kinetics*, is an 'up-to-date' textbook by Chorkendorff and Niemantsverdiet [140].

2.1 Adsorption and Desorption of Gas Molecules on Surfaces

A solid surface, for example a metal surface, in the presence of a gas forms a dynamic equilibrium with the gas molecules. Gas molecules adsorb on and desorb from the surface, however at equilibrium there is no change in the number of adsorbed molecules on the surface. The coverage, θ, refers to the average number of adsorbed molecules divided by the total number of sites available on the solid surface. Therefore $\theta = 1$ refers to a full monolayer of adsorbed molecules.

Energetically speaking, adsorption is divided into physisorption, where gas-metal bonding is weak (< 0.35 eV) and chemisorption where electron transfer occurs and strong chemical bonds (> 0.35 eV) form. The later is important in catalysis, because bond formation and scission have to occur in order for molecular dissociation or formation to happen. What governs the kinetics of adsorption is the presence of activation energy barriers. Laidler discusses chemical kinetics and surface kinetics in detail [141].

It is useful to consider Figure 2.1 where chemisorption and physisorption of O_2 on a surface are schematically and qualitatively described. Figure 2.1 shows two energy curves; (i) adsorption of atomic oxygen and (ii) adsorption of an oxygen molecule. Curve (ii) is the case where physisorption occurs and the molecule lowers its energy by falling into the physisorption well. No strong bonds are formed with the surface. The chemisorption curve, however, shows a very deep well, i.e. oxygen atoms are strongly bonded to the surface, but note that it is not energetically favorable for the oxygen molecule to dissociate in the gas phase and follow the chemisorption path to form bonds with the surface. This is because the gas phase dissociative energy of O_2 (E_{diss}) as shown in the Figure) is very high. An alternative path is for the molecule to physisorb first and cross the energy barrier (E^a) before falling into the chemisorption well. The barrier, or

the activation energy, is significantly lower than the gas phase dissociative energy. When the activation barrier (E^a in Figure 2.1) is above zero energy the process is said to be activated, otherwise it is referred to as a non-activated reaction. The rate of reaction is related to the activation energy. For the simple case of a unimolecular (e.g. O_2) reaction and a Langmuir isotherm, the reaction rate, is given by

$$\upsilon = k\theta, \qquad (2.2)$$

where θ is the coverage k is called the rate constant and is related to the activation energy by the Arrhenius (Nobel Prize 1903) equation:

$$k = A \exp(-E^a/k_B T), \qquad (2.3)$$

where A, E^a, k_B and T are the frequency factor, activation energy, Boltzman constant and temperature, respectively.

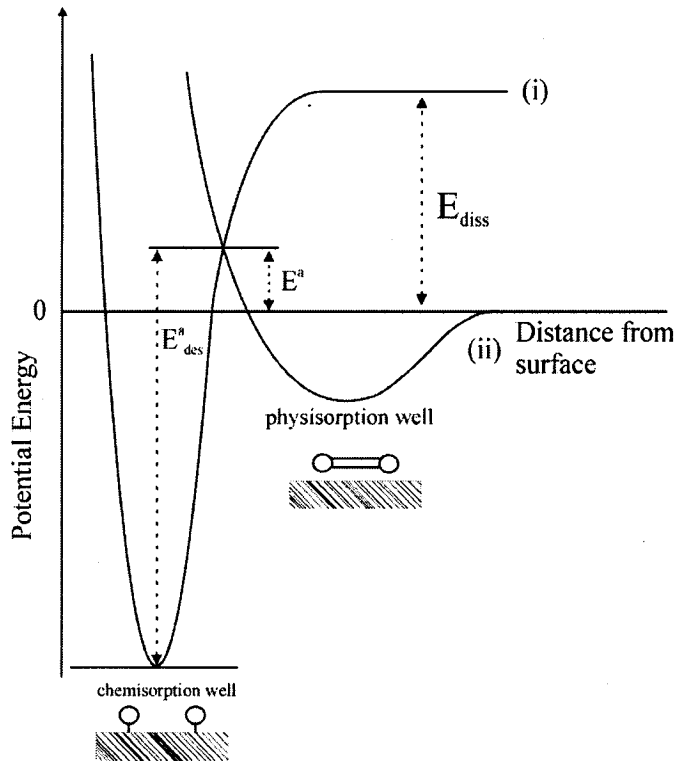

Figure 2.1 *One-dimensional potential energy diagram for dissociative adsorption. (Adapted from reference [142])*

2.2 Chemisorption and Catalysis on Metal Surfaces

A central question in surface science concerns the reactivity of surfaces. How does the activation energy of a surface reaction relate to the fundamental parameters of the surface and/or adsorbate? In the past decade or so, Norskov and Hammer have developed what is

essentially a two-level interaction model for reactions of simple molecules on transition metals [143]. It turns out that the d electrons, which occupy the valance band of transition metals and have a very different band structure from the s (or sp) electrons, are instrumental in many catalytic reactions. The chemisorprtion energies and activation energies, to very good approximations, can be related to the d-band center or the mean energy of the d electrons. In other words the location of the d-band with respect of the Fermi level of the metal becomes a very good reactivity indicator [143].

An atomic species forms bonding and anti-bonding levels with the metal surface, similar to what happens in a diatomic molecule. Here the energy states involved in the formation of bonding and anti-bonding states are the discrete energy state of the atom and the d-band electrons of the solid. One can take the d-band center, ε_d, as a measure of the d electron's energy. Figure 2.2 shows a qualitative picture of an atomic chemisorption to the surface. The interaction with the broad sp band causes a broadening in the adsorbate level. The interaction with the narrow d band causes the adsorbate level to split. Here the d band can be considered as a broad orbital itself. The result of these interactions is formation of a pair of bonding and antibonding chemisorption orbitals.

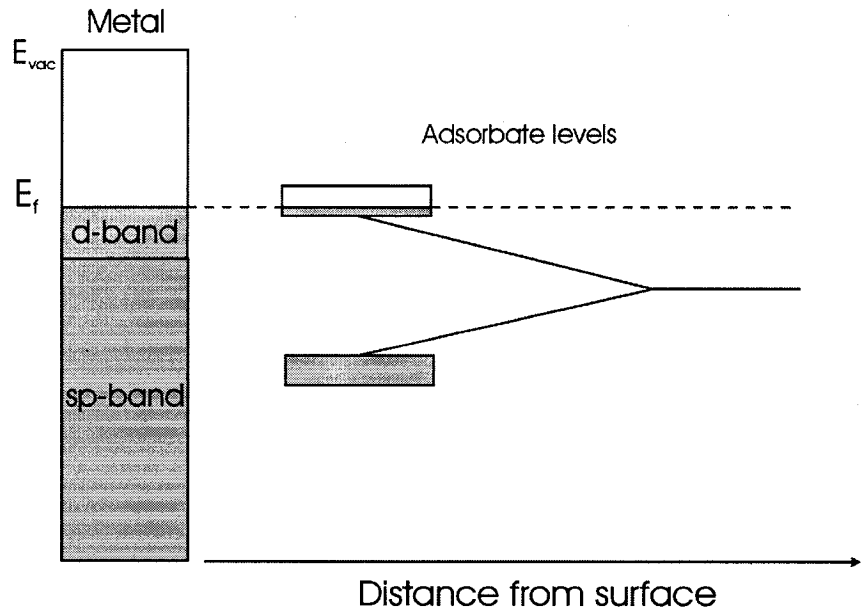

Figure 2.2 *Interaction between an atomic adsorbate with one valence level and a transition metal, which possesses a broad sp band and a narrow d band located at the Fermi level. The strong interaction with the d band causes splitting of the adsorbate level into a bonding and antibonding level. The part of the adsorbate levels below the Fermi level is occupied by electron density. (Adapted from reference [140])*

The filling of the substrate-adsorbate anti-bonding states dictates the bond strength and this in turn depends on ε_d. When ε_d is far below the Fermi level, E_f, the solid-adsorbate anti-bonding states will be occupied and no bonding will occur.

In the case of molecular adsorption, similar things happen. Now the molecular bonding and anti-bonding levels interact with the d-band and form four types of levels. The molecule needs to adsorb (i.e. make bonds) on the surface and then its anti-bonding levels must fill in order for dissociation to occur. Filling the molecular anti-bonding states destabilizes the molecule and leads to its dissociation. Figure 2.3 shows a qualitative picture of molecular chemisorption.

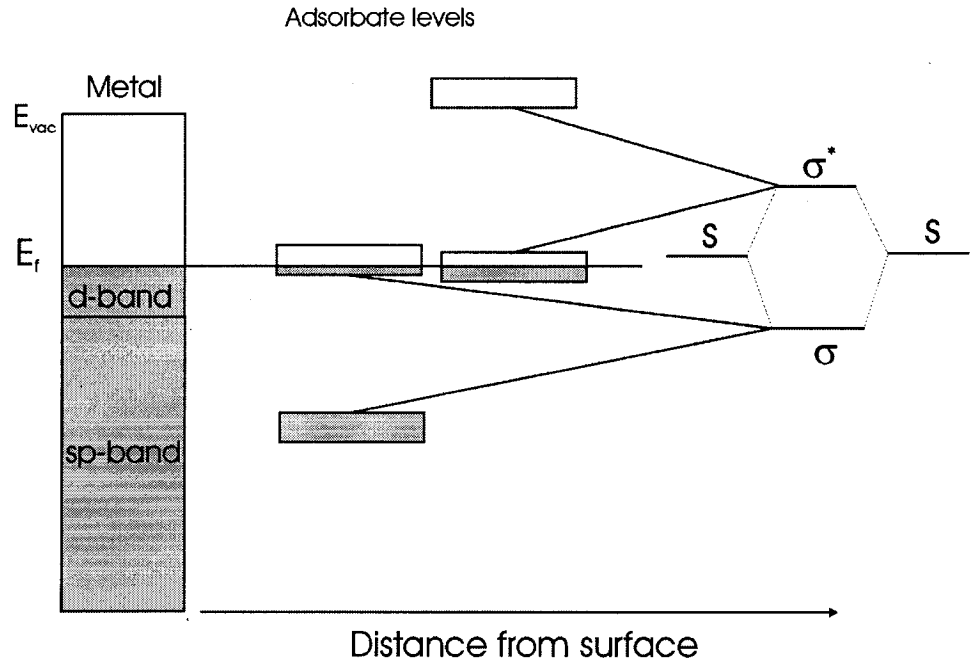

Figure 2.3 *A molecule with a bonding σ and antibonding σ* orbitals interacts with both the sp band and the narrow d band of the transition metal. The former leads to the lowering and broadening of the energy levels, while the latter results in splitting into bonding and antibonding orbitals. Note that if electrons fill the antibonding orbital of the molecule then the internal bonding in the molecule becomes weaker, which may lead to dissociation of the molecule. (Adapted from reference [140])*

Gold has the lowest d-band center, ε_d, of all the transition metals and consequently does not chemisorb other species very strongly. This is basically why Au has a very noble surface [144]. One can then explain trends across the transition metal rows based on the ε_d parameter. Moving left across a row of transition metal elements, ε_d moves higher (closer to E_f) which leads to lowered activation energies; however this makes the

chemisorption also stronger. A compromise needs to be made between these two factors and usually the catalytic activity, which requires optimum chemisorption, shows a so-called "volcano-curve" moving through the elements of a transition metal series. This is called the Sabatier principle in heterogeneous catalysis: for the best catalytic activity the molecules and/or reaction intermediates need to chemisorb neither too weakly nor too strongly. Volcano behavior is seen in many examples of heterogeneous catalysis, for example, NH_3 synthesis and H_2 evolution [140, 145].

There are many other factors that can complicate the picture of reactivity. Different facets of crystals generally show different reactivities. Low coordination sites, such as steps, are higher in energy and could lead to stronger metal-adsorbate bonds [146]. Strain in the lattice, which can be induced in overlayer or sub-layer metal structures, can affect the electronic properties and shift ε_d [146]. Particle size also plays a very important role [146].

Theoretical and fundamental experiments almost always deal with model catalysts which are extended, such as single crystal surfaces. Practical catalysts, however, are almost always nanoparticles and generally show significant differences in their catalytic activity compared to model catalysts. Au nanoparticles are a very good example. Although bulk Au is inert, nanoparticles of Au (smaller than 5 nm) are surprisingly good catalysts for many reactions. Meyer *et al.* provide a very good review of this subject [147]. Raimondi *et al.* provide a very good review of nanoparticle catalysts and their applications in electrochemistry and heterogeneous catalysis [146].

Fine-tuning or tailoring the properties of materials in order to design superior catalysts has been one of the driving forces in surface science. The design of catalysts purely from theoretical considerations, although very appealing, has been seldom reported. One excellent example of a theoretically tailored catalyst is that of the Au surface-doped Ni catalyst for the decomposition of methane. In a Ni-Au alloy, Au does not dissolve in the bulk but remains segregated on the surface. Ni is used as a catalyst in methane decomposition and one problem associated with the reaction is formation and adsorption of carbon on the surface which poisons the surface by blocking the reaction sites. First-principle calculations showed that the presence of Au atoms in the surface layer would act as an inhibitor for the formation of carbon and would thus make Ni-Au a

better catalyst for this reaction. Subsequent experiments confirmed the calculations and showed that Au doped Ni could be used as a catalyst in this industry [148].

2.3 Catalysis versus Electrocatalysis

The term electrocatalysis was first used in the 1960's when fuel cells were a hot research topic [149]. It is a more appropriate terminology than catalysis, when electrochemical reactions, involving electrolyte and an electric potential, are present. The presence of solvent, electric potential and the often complicated reaction pathways all make the field of electrocatalysis theoretically and experimentally much more challenging than heterogeneous catalysis.

Bockris and Khan discuss the concept of potential in great detail [150]. The overall effect is that the chemical potential, which now includes a zeV (z = number of charges, e = elementary charge, V = electric potential) term, is called the electrochemical potential. For neutral particles, chemical and electrochemical potentials are identical. In the case of electrocatalysis, the electrochemical potential, hence adsorption/desorption, is controlled electrically rather than by changing the gas pressure.

For detailed analysis and derivations, besides Bockris and Khan's *Surface Electrochemistry*, the first five chapters of the *Kinetics and Mechanisms of Electrode Processes* (*Comprehensive Treatise of Electrochemistry* vol. 7) are very useful references [151-155]. These few chapters discuss electrochemical kinetics both fundamentally and phenomenologically. Other more fundamental approaches are Goodisman's *Electrochemistry: Theoretical Foundations* and Bockris & Khan's *Quantum Electrochemistry* [86, 149].

At equilibrium, oxidation and reduction of a species occur at equal rates. These reactions can be written as:

$$O^+ + e^- \rightarrow R \qquad \text{(cathodic reaction)}$$
$$R \rightarrow O^+ + e^- \qquad \text{(anodic reaction),} \qquad (2.4)$$

where O and R are the oxidized and reduced forms. The general current density-potential (Butler-Volmer) equation for this very simple one electron transfer electrochemical reaction is:

$$j = j_o\left\{\exp\left[\frac{-\alpha nF(E-E^o)}{RT}\right] - \exp\left[\frac{(1-\alpha)nF(E-E^o)}{RT}\right]\right\}, \qquad (2.5)$$

where j_o is the exchange current density, α is the charge transfer coefficient, n is the number of electrons, F is the Faraday constant, E is the applied potential, E^o is the equilibrium potential, R is the ideal gas constant and T is the temperature. The deviation from the equilibrium potential ($E-E^o$) is called the overpotential or η. At equilibrium (η = 0) both reactions occur simultaneously and the net current density (j) is zero. The rate at which these reactions occur is proportional to the exchange current density, j_o, which can not be experimentally observed. The first exponential term represents the cathodic current density and the second term corresponds to the anodic current density. When the equilibrium potential is lowered and the reaction is pushed in the cathodic direction, the anodic term becomes negligible and one obtains the Tafel relation presented in the first chapter:

$$j \cong j_o \exp\left(\frac{-\alpha nF\eta}{RT}\right). \qquad (2.6)$$

The derivation of (2.5), which is phenomenological in nature, can be found in Goodisman's book [86]. Equation 2.6 is usually written in its logarithmic form or

$$\eta = \frac{-RT}{\alpha nF}\ln(j) + \frac{RT}{\alpha nF}\ln(j_o), \qquad (2.7)$$

where RT/αnF is called the Tafel slope for the simple one electron transfer reactions of equation 2.5. For different reactions, e.g. adsorption or bond scission, the Tafel slope can be slightly different. In any electrochemical reaction (anodic or cathodic) the goal is to reduce the overpotential, η. According to 2.7, the two system parameters are j_o and α and increasing both these parameters increases the current for a given η. What is the origin of these two parameters?

For α, one needs to consider the free energies of the reactants and products of an adsorbate-solid system. The free energies include internal energy (adsorbate-surface interactions) and the entropy effects. Assuming that the entropy term is not affected by the potential, changes in the potential energy of the reactant are good measures of what is going on. Consider the potential curves of Figure 2.4 and consider the forward reaction only i.e. $O^+ + e^- \rightarrow R$. Figure 2.4 is an intersection of two parabolic potential curves.

The reaction coordinate represents the progress along the reaction path. In a simple 1-dimensional case, it could represent the bond lengths. The forward reaction is exothermic, but activated by: $\Delta G_r^{\ddagger} = G_c - G_o$. Reducing the activation energy then would effectively accelerate the rate of this forward reaction. This is exactly what the overpotential does: it effectively increases the energy level of the reactant O.

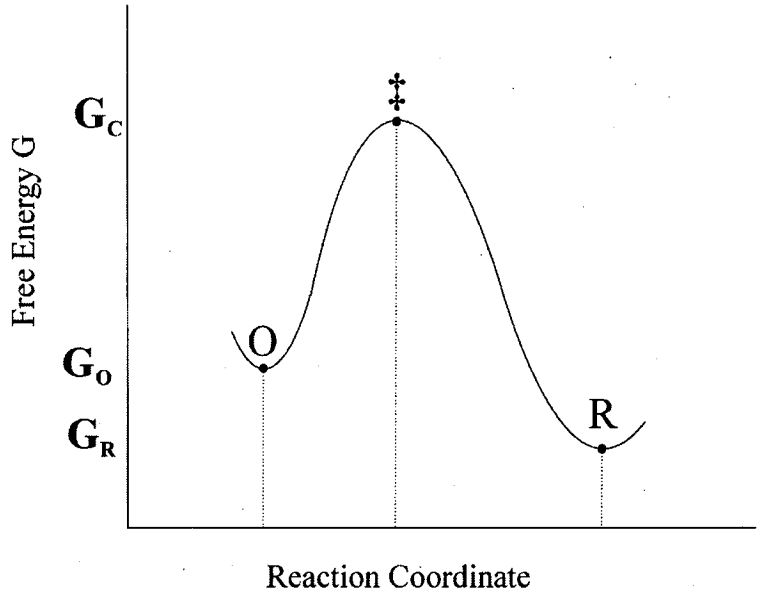

Figure 2.4 *Free energy diagram for a chemical reaction. O and R denote the reactant and the product for a forward reaction, respectively. Free energies of O, R and the activated complex (‡) are shown on the curve. (Adapted from reference [86])*

Figure 2.5 illustrates this point for a simple metal oxidation ($M \rightarrow M^+ + ze^-$) reaction. The important point of this figure is the change in the reaction coordinate of the activated complex. Although the overpotential raises the energy of the reactant by $e\eta$, the energy of the activated complex also increases, therefore only a fraction of overpotential helps to reduce the activation energy. This fraction is referred to as the *charge transfer coefficient* or α and it is the amount of electrical energy that is used to lower the activation barrier. α is also sometimes referred to as the "symmetry factor" because its value is determined by the ratio of the slopes of the energy curves at the intersection point.

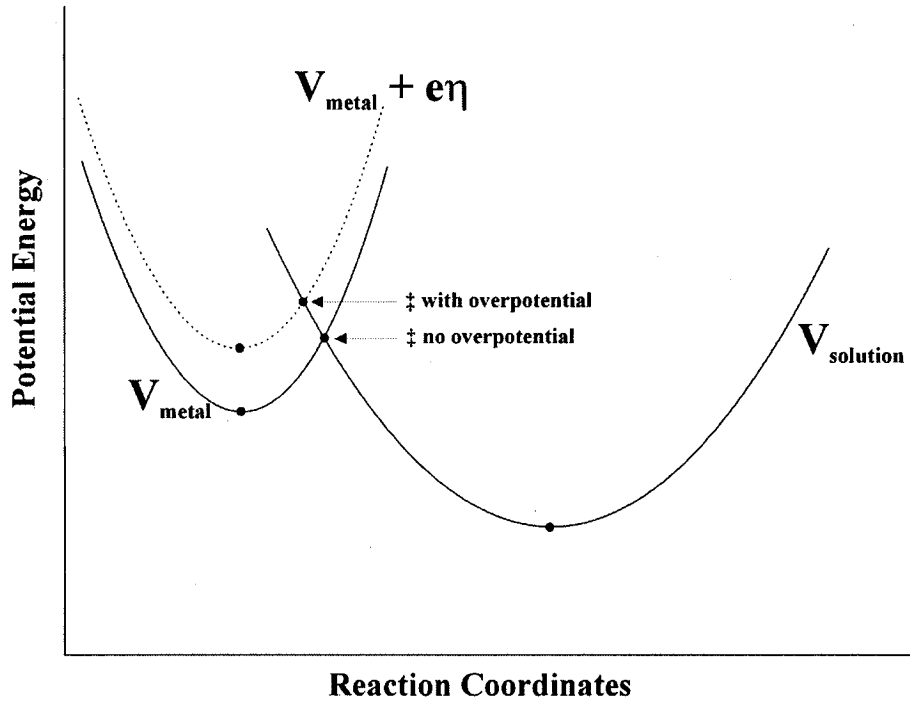

Figure 2.5 *Potential energy diagram of a metal oxidation (going left to right). The impact of a metal-solution potential is shown on the energy curve of the reactant (metal). Minimum energy points (on the energy curves) and the points of intersections (activated complexes) are shown by black circles. (Adapted from reference [86])*

The value of α is usually somewhere about ½ and although extreme values (0 and 1) have also been observed in some experiments, these situations are very rare and difficult to observe. Trasatti and Bard discuss α in some detail for single and multi-electron reactions [156, 157]. It suffices to say that, α and hence the Tafel slope, do not depend on the molecular nature of the reactions. The Tafel slope depends on the reaction mechanism and the nature of rate determining steps (in a multi-step reaction). Pletcher *et al.* show how different mechanisms in the hydrogen evolution reaction, for instance, lead to different Tafel slopes [158]. Common values of Tafel slopes are usually 60 and 120 mV/decade, but 30 and 40 mV/decade have also been observed. Decade here means a factor of 10 in current.

The potential dependence of α has been a subject of much debate in the electrochemical community over the years. Simple Bulter-Volmer type kinetics assumes α is constant. However Marcus' electron transfer theory (Nobel Prize 1992) predicts that α varies as a function of potential. In practice, it is by increasing the exchange current that improvements in an electrocatalyst are made, not by changes in the Tafel slope.

The exchange current density is influenced by the binding strength of adsorbates and poisoning effects and it depends on the nature of the electrocatalyst. If the binding energy of the reactants is weak, or if the intermediates in the reaction (or other poisons) bind strongly, the reaction rate will be low. The exchange current density will be explained better for the specific case of the oxygen reduction reaction in the next few sections.

2.4 Oxygen Reduction Reaction

Even before the recent frenzy in PEMFC research, the ORR was a subject of interest for both fundamental studies and applications such as oxygen sensors and electrolyzers. Kinoshita's *Electrochemical Oxygen Technology* is a good exposition on oxygen electrochemistry [159]. An older but comprehensive book is a monograph by Hoare entitled *The Electrochemistry of Oxygen* [160]. With regard to applications of ORR in PEMFC and recent developments, various researchers have summarized their work in different chapters of the *Handbook of Fuel Cells* [129, 130, 161-164]. Only some of the highlights of ORR on Pt-based electrocatalysts are presented here.

The oxygen reduction reaction is a complicated reaction and is still not completely understood. Oxygen can reduce to form water, hydroxide or peroxide depending on the solution pH and the nature of the electrode where the reduction reaction occurs. Generally speaking, the reduction of oxygen falls into two categories: a) direct 4-electron pathway and b) 2-electron peroxide pathway. Examples of these two types of pathways for acidic solutions are:

Direct 4-electron pathway: $O_2 + 4H^+ + 4e^- \rightarrow H_2O$ (2.8)

Peroxide pathway: $O_2 + 2H^+ + 2e^- \rightarrow H_2O_2$ (2.9)

Followed either by the reduction of peroxide

$$H_2O_2 + 2H^+ + 2e^- \rightarrow 2H_2O \quad (2.10)$$

Or the decomposition of peroxide

$$2H_2O_2 \rightarrow 2H_2O + O_2 \quad (2.11)$$

In alkaline solutions the reactions are different:

Direct 4-electron pathway: $O_2 + 2H_2O + 4e^- \rightarrow 4OH^-$ (2.12)

Peroxide pathway: $O_2 + H_2O + 2e^- \rightarrow HO_2^- + OH^-$ (2.13)

Followed either by the reduction of peroxide

$$HO_2^- + H_2O + 2e^- \rightarrow 3OH^- \qquad (2.14)$$

or decomposition of peroxide

$$2HO_2^- \rightarrow 2OH^- + O_2 \qquad (2.15)$$

The 4 electron pathway is more prevalent on noble-metal electrocatalysts and some transition-metal macrocycles. The peroxide pathway is predominant on graphite, Au, Hg, oxide-covered metals like Ni and some other transition-metal macrocycles. Each pathway takes a series of stepwise reactions where intermediate species form. In the case of noble metal electrodes like Pt or Au, Kinoshita quotes 16 different reaction pathways for oxygen reduction that have been proposed over the years [159]. Adzic also provides a very good review of oxygen electrocatalysis [165]. A generalized ORR scheme, which would account for every possible elementary step, is very complicated and could contain more than 20 rate constants [159]. Thus, very simple pathways, such as the one shown in Figure 2.6, are usually mentioned in the literature. In Figure 2.6, each reaction step is characterized by a unique rate constant [164]. According to this model there are two ways to reduce oxygen to water: the direct path (k_1) and the peroxide path (k_2, k_3).

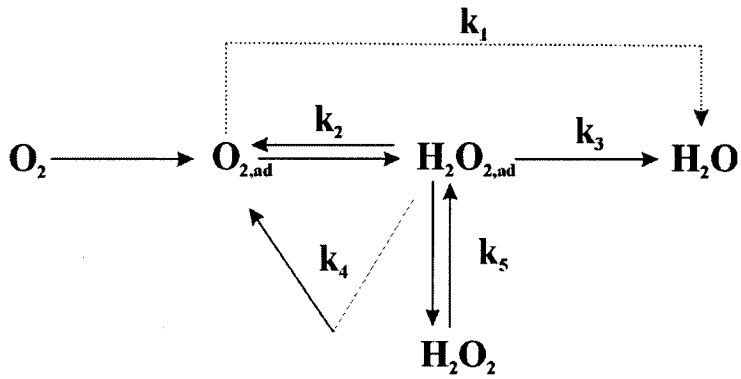

Figure 2.6 *A proposed model for oxygen reduction in acidic electrolytes. (Adapted from reference [166])*

The role of surface facets on the rate of ORR on single crystal surfaces in different pH media have been studied in detail by the research group of Markovic [166]. There is significant variation of activity depending on the facets of the Pt particle which arises from the presence of anions. In H_2SO_4 solution the order of ORR activity for Pt facets goes as Pt(111) < Pt(100) < Pt(110) planes [165]. The Pt(111) facet has the lowest activity because of strong bisulfate adsorption. In $HClO_4$, where anions are weakly

adsorbed, the order of activity is Pt(100) < Pt(111) < Pt(110) [165]. Particle size effects have been studied by Kinoshita. The activity of Pt particles reaches an optimum level for 2 nm sized particles. Kinoshita discusses these based on a cuboctahedral model of particles [159].

Another very important factor is the adsorption or poisoning effect of intermediates such as OH on the surface of the Pt electrode. This has been discussed by many researchers in the literature and is generally considered as the most important factor in hindering the kinetics of ORR on Pt electrocatalysts. The binding of OH to Pt is somewhat too strong, thus making the OH essentially act as a poison.

The adsorption effects of OH and O on Pt and Pt-alloys have been discussed by other researchers more recently. Generally speaking, when Pt is alloyed with one of the transition metals like Fe, Ni or Co about 20-40 mV is gained in the activation overpotential [115]. This gain comes directly as an increase in j_o and not the Tafel slope. The Tafel slopes remain unchanged for the alloys, indicating the charge transfer coefficient and the reaction mechanism are unchanged [117, 167]. The enhancement of ORR in the Pt-alloys comes about, accordingly, through a smaller adsorption of OH on the surface. The proposed kinetic equation for the rate of ORR on Pt and Pt-alloy surfaces is:

$$j = nFKc_{O2}(1-\Theta_{ad})^x \exp(\gamma\Delta G)\exp(-\alpha nFE/RT), \qquad (2.16)$$

where n is the number of electrons, K is the chemical rate constant, c_{O2} is the concentration of O_2 in the solution and Θ is the total surface coverage by all adsorbed species, x is either 1 or 2 depending on the site requirements of the adsorbates, j is the observed current, E is the applied potential, α and γ are the symmetry factors (assumed to be ½) and ΔG is the change in the adsorbate free energy, which would in general depend on the coverage [168]. Accordingly then, the parameters that change from Pt to Pt-alloys are the pre-exponential term (1- θ_{ad}), where θ here is θ_{OH} and the free energy ΔG. [117, 169]. Using this model, Markovic and co-workers have also demonstrated the devastating effect of impurity anions (eg. Cl^-, Br^- at ppm levels!) or metal ions (Cu^{2+}) on the current density [170, 171]. These impurities act like poisons in blocking the reactive sites on the Pt and lower the pre-exponential term $(1- \theta_{OH})^x$ [169, 171, 172]. Other researchers have also noted the inhibition of adsorbed OH in the Pt-alloys. In 1995

Mukerjee *et al.* using X-ray absorption spectroscopy on working fuel cells, observed that OH adsorption is inhibited on Pt-Cr surfaces [173]. The OH adsorption is potential dependent. Alloying Pt with other transition metals increases the adsorption potential of OH, hence lowering the OH coverage of the metal surface in the kinetic region of ORR.

In recent years, Norskov and co-workers have applied their d-band center theory of heterogeneous catalysis to ORR electrocatalysts with some success. The method basically relies on calculating the adsorption energies of two adsorbed species: O and OH on the Pt(111) surface in the presence of adsorbed water and an electric field. Their work is very interesting because it can apparently be generalized for the activation overpotentials of any electrochemical reactions and it is ab-initio. Their approach avoids complicated pathways and finding transition states. Instead a simple O_2 dissociation and two protonation steps are used:

$$\tfrac{1}{2}\, O_2 + * \rightarrow O^* \qquad (2.17)$$

$$O^* + H^+ + e^- \rightarrow OH^* \qquad (2.18)$$

$$OH^* + H^+ + e^- \rightarrow H_2O + *, \qquad (2.19)$$

where * designates a surface site. Using the binding energies of O and OH species, the authors recover the 400 mV or so activation loss observed for ORR in Pt electrocatalysts. Furthermore, the calculations for Pt-alloys show changes in the O and OH binding energies which yield volcano-type relations for the ORR activity. Figure 2.8 shows theoretical and experimental volcano behavior of oxygen reduction activity of several Pt-alloys. The volcano-behavior is really an interplay between the $(1-\theta_{ad})$ and ΔG terms: on the right side (Pt-side) the $(1-\theta_{ad})$ term is rate determining and on the left side ΔG is rate determining. Note that activities in Figure 2.8 are defined as $k_B\, T\, \ln(j)$, where k_B, T and j are the Boltzman constant, temperature and rate of the reaction, respectively.

Although the d-band center model has been applied very successfully here and elsewhere for ORR [174, 175], there still remain important unanswered questions. Recently Stamenkovic *et al.* [176] showed single crystals of Pt_3Ni with an ORR improvement of 10× over Pt. These alloy single crystals also show structural sensitivity like Pt single crystals. The activity of Pt_3Ni (111) is, for instance, about 9 times or so better than Pt_3Ni (100); however the d-band centers of both facets are very similar [176].

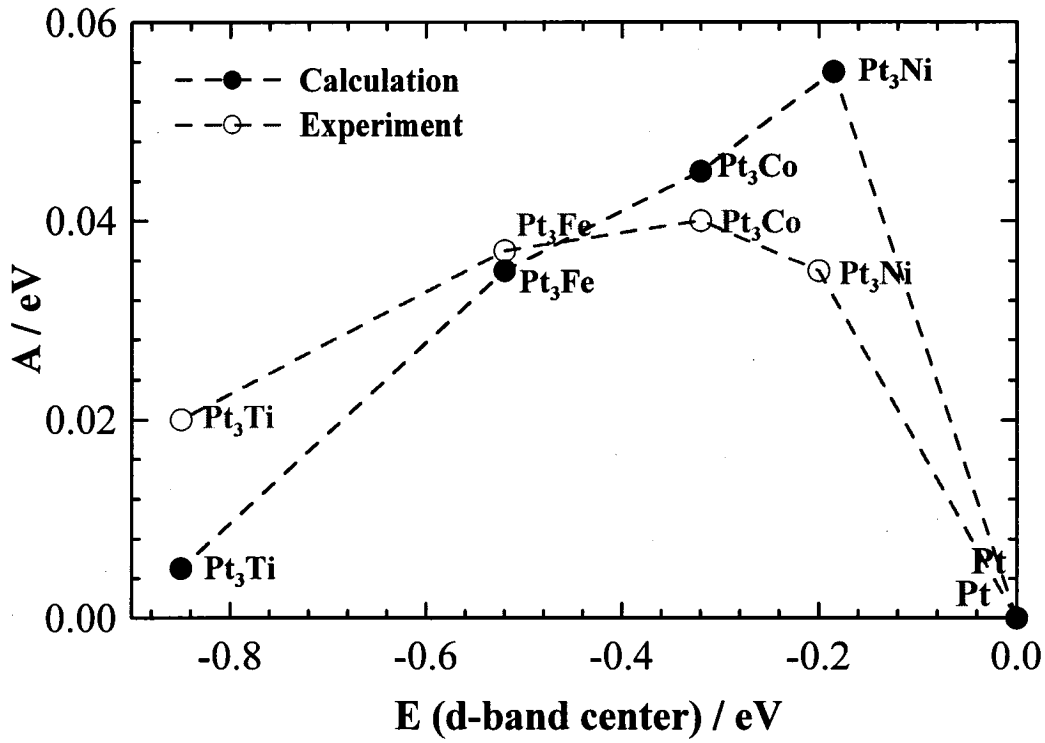

Figure 2.8 *Activity versus the experimentally measured d-band center relative to platinum. The activity predicted from DFT simulations is shown by filled circles and the measured activity is shown by open circles. (Adapted from reference [177])*

Perhaps the most puzzling is the reactivity of Au. Au (100) has shown exceptionally good (better than Pt) ORR activity in alkaline solutions [164]. The reason(s) for this are not known and d-band center theory alone does not explain this observation.

Many other metals, even when they have the right electronic/geometric properties, can not be good ORR catalysts because they are not stable in the low pH environments of operating fuel cells. Metals in general are unstable and thermodynamically speaking, they prefer to form compounds. Au and Pt are two well-known exceptions. Many transition metals like Fe, Ni, Co etc. will dissolve at the pH level of PEMFC and form hydroxide/oxides which will render them unsuitable for catalysis. Pt is a notable exception: it is immune to dissolution (corrosion) and has the right electronic properties. Au is also stable against corrosion, but it is catalytically inactive towards ORR in acidic media.

Chapter 3

Experimental Techniques

3.0 Introduction

The experimental techniques that were used in the studies presented in this thesis are briefly explained in this chapter. More attention is paid to the rotating ring-disk electrode (RRDE) technique because it was used for the first time in our lab.

3.1 Combinatorial Materials Science (CMS)

3.1.1 A Short Historical Background

Combinatorial and high throughput materials science involves synthesis and characterization of numerous compositions in parallel, thus greatly reducing the time in discovery of materials of interest. One of the early pioneers of high-throughput methods was J. J. Hanak, who back in the 1960's, developed the multiple-sample concept when he was a research scientist at the Radio Corporation of America. His approach was based on sputtering multi-component targets to produce composition spread films [178]. Hanak searched for high temperature superconductors in the 1970's using his methods. However, interest in combinatorial synthesis faded, mostly because of the lack of efficient screening techniques and funding.

In the 1980's the pharmaceutical industry invested heavily in parallel synthesis and screening of organics compounds for drug discovery. These methods, which usually involve solution-based samples, are referred to as *combinatorial chemistry*. In the early 1990's, Xiang and co-workers at LBNL developed methods for combinatorial production and characterization of solid state materials for a variety of applications. Armed with computers and powerful characterization tools, the field of combinatorial materials science was re-born and soon similar methodologies were adopted by many research groups. CMS has been applied to various fields like dielectrics/ferroelectrics, display phosphors, catalysts and superconductors [179-186]. Symyx Technologies and

Intematix Inc. are two companies which develop combinatorial related technologies and perform combinatorial materials discovery.

Xiang and Tackeuchi have edited an excellent book on CMS [187]. Other books on CMS are those of Potyrailo & Amis and Ptyrailo & Maier [188, 189]. *High-Throughput Screening in Chemical Catalysis* by Hagemer *et al.* describes CMS for heterogeneous catalysts and electrocatalysts [190]. The authors describe the development of CMS for catalyst discovery and provide examples of catalysts discovered by CMS. Strasser *et al.* describe combinatorial Pt-alloy libraries prepared by thin film deposition and their characterization for ORR and CO-tolerant HOR in solution-based cells [191]. Reddington, Jiang and Jayaraman have used a CMS approach in the discovery of methanol oxidation catalysts [192-194]. Smotkin *et al.* describe combinatorial DMFCs for screening methanol oxidation catalysts [195, 196].

3.1.2 Combinatorial Materials Science at Dalhousie

Development of CMS at Dalhousie dates to the summer of 2000, when a magnetron sputter deposition system was purchased with the goal of producing combinatorial samples. CMS methods, established at Dalhousie, enable one to continuously map the composition space of desired binary, ternary and quaternary systems [197, 198]. Fleischauer *et al.* provide a good review of the CMS work done at Dalhousie on negative electrode materials for Li-ion batteries [199]. For more detailed information on production of combinatorial libraries (binary, ternary and quaternary systems) the reader is referred to the thesis works of Hatchard, Fleischauer and Chevrier [200-202].

These CMS methods have also been applied to FC electrocatalysts. Pt-alloys, for ORR and hydrogen oxidation reaction (HOR) and non-noble metal catalysts for ORR, have been routinely produced. A 64-electrode fuel cell has also been developed and successfully used in search for CO-tolerant anode electrocatalysts. Stevens *et al.* describe the application of this 64-electrode fuel cell to binary and ternary Pt-containing alloys [203, 204].

3.2 Magnetron Sputtering and CMS at Dalhousie

Good references on physical vapor deposition and thin film science are those of Mattox, Smith, Vossen and Mahan [205-208]. Magnetron sputtering, in particular, is covered by Wasa in [209, 210]. Magnetron sputtering is a very versatile physical vapor deposition technique and is widely used in producing thin films in industry and academia. The sputtering targets and the substrates, where the film is deposited, are all contained in a vacuum chamber which typically reaches 1×10^{-7} Torr or less. A process gas, like Ar, is used to form plasma. The targets are negatively charged with respect to the rest of the chamber and this accelerates the Ar^{+} ions into the targets causing target atoms to scatter off and deposit on the substrates as a film. The process is highly inelastic and produces a lot of heat. For this reason the sputtering targets and substrate table are water-cooled. The addition of magnets, placed behind the targets, allows for the trapping of the plasma and increases the efficiency of the process. Figure 3.1 shows a typical magnetron sputtering chamber. Conductors, like metals, can be sputtered using either DC or RF power sources. For insulating targets, RF sources are used.

To produce a binary library, i.e. to map an entire composition range of two given elements A and B, a circular table (dia. 40 cm) is rotated over two stationary targets of A and B. The sputtering targets are behind specially-designed masks which lead to either constant or linearly varying deposition profiles on the substrate table. Figure 3.2 shows the layout of a sputtering table and two targets, Pt and Co, which are projected into the plane of the sputtering table, but in reality they are about 6 cm away from it. Note how the targets are covered by masks. These masks produce a constant deposition of Pt and a linearly varying amount of Co on the substrates over a range of about 7.5 cm. The thickness of film deposited during each pass can be adjusted using the sputtering powers and the rotation speed of the table. In most cases, the powers and table rotation speed are chosen to produce intimately mixed alloys. Detailed information about the mask design and deposition profiles are given by Dahn *et al.* [197].

All the films were produced by a Corona Vacuum Coaters V3T magnetron sputtering machine. The sputtering chamber reaches a typical base pressure of about 1×10^{-7} Torr and is equipped with four 2" diameter target magnetrons, one plasma cleaning electrode, two Advanced Energy (AE) RF generators and three AE DC MDX-1K power sources.

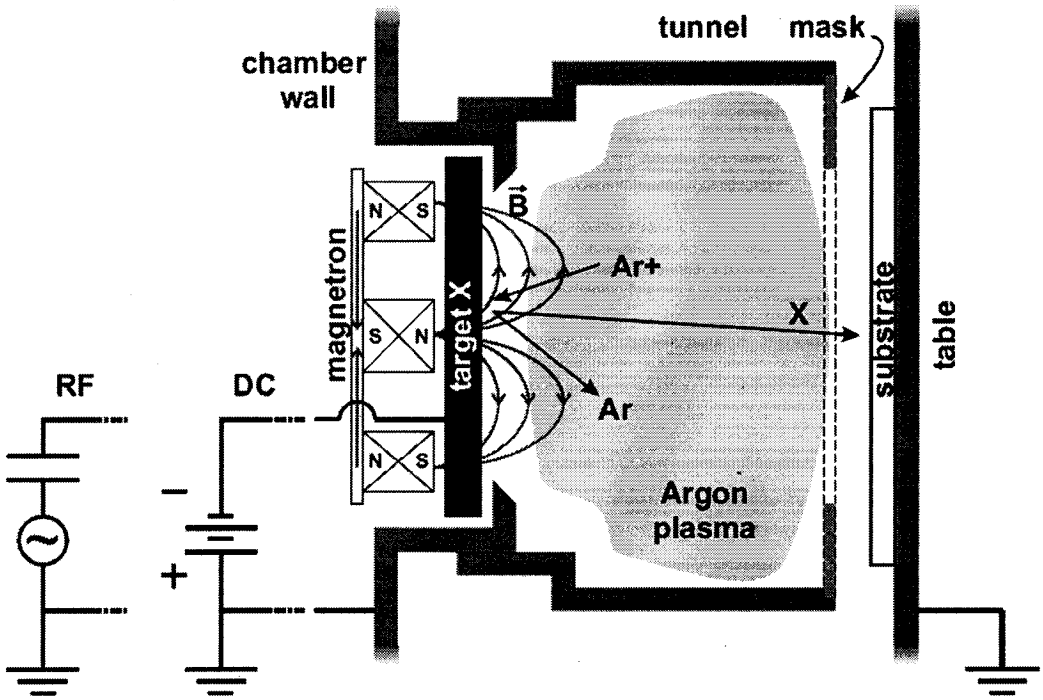

Figure 3.1 *A schematic diagram of a magnetron sputtering chamber. The sputtering target is biased negatively (using DC or RF source) and this will attract the positive Ar^+ ions. Collision of Ar^+ ions with the target material will cause ejection of target material atoms onto the substrates, positioned in front of the target. (Taken from reference [202])*

Home-made additions, such as substrate tables, ternary substrate tables and masks allow CMS to be performed. A detailed explanation of this system, including hardware and software, is given by the author in an earlier thesis [211].

Targets used consisted of two-inch diameter targets of pure (99.9%) metals such as Pt, Ni, Co etc. and grade 1008 low carbon steel (less than 0.08% carbon by weight, balance Fe). All depositions were performed by DC power supplies. Typical powers, for the case of Pt-Co libraries, were 43W (370V, 0.11A) for Pt and 55W (275V, 0.19A) for Co. Typical Ar pressure during sputtering was about 3.0 mTorr. All depositions were done at room temperature. The substrates that were generally used consisted of silicon (110 oriented) wafers, aluminum foil and 3M NSTF supports.

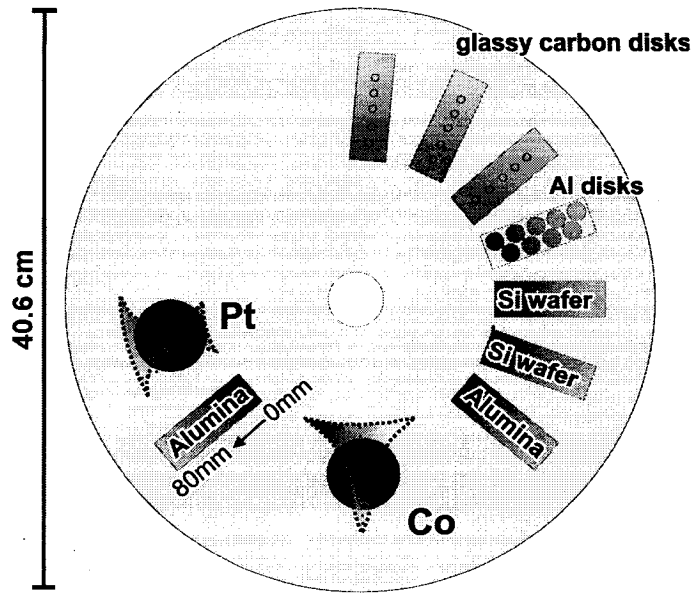

Figure 3.2 *A schematic drawing of a typical sputtering table layout, used in many experiments described in this thesis. Pt and Co targets are behind specially shaped masks which produce constant and linearly-varying depositions of Pt and Co on the mounted substrates, respectively. In this drawing, the Pt and Co targets are projected into the plane of sputtering of sputtering table; however in reality they reside about 6 cm away from the table.*

3.3 X-ray Diffraction

X-rays, discovered by Wilhelm Röntgen in 1895 (Nobel Prize 1901), soon proved to be ideal for probing the crystal structure of materials. This is because X-rays with wavelengths comparable to the inter-atomic distances of crystalline materials will diffract. This led to Bragg's diffraction law, named after the physicists W. H. Bragg and his son W. L. Bragg (Noble Prize 1915) [212]. A similar diffraction phenomenon occurs when neutrons or electrons are used as the incident radiation. These diffraction techniques are the most powerful tools for determining the crystal structure of materials.

3.3.1 Principles of X-ray Diffraction

Figure 3.3 shows the Bragg condition for the diffraction of two incident X-ray waves from two atomic planes. The condition where constructive interference of X-rays scattered from a periodic lattice structure is satisfied, is given by the Bragg law

$$n_{integer}\lambda = 2d\sin(\theta), \qquad (3.1)$$

where d, θ, λ and n are the atomic plane spacing, the angle between incident ray and the scattering planes, the X-ray wavelength and an integer, respectively.

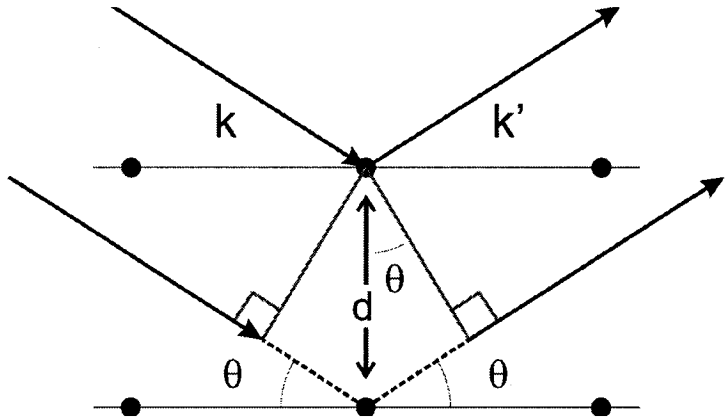

Figure 3.3 *A simple schematic showing the diffraction geometry. Outgoing reflected rays are exactly in phase and will coherently diffract from this set of atomic planes. (Taken from reference [202])*

A typical XRD measurement consists of counting the scattered X-rays as a function of the scattering angle, 2θ. The compilation of data then results in a series of diffraction peaks, referred to as the Bragg peaks, versus the scattering angle. The peaks are identified by their Miller indices (hkl), which denote atomic planes orthogonal to the (hkl) direction in the basis of the reciprocal lattice vectors. The positions of the peaks ($2\theta_{hkl}$) depend on the plane spacing and are used to obtain the lattice constants of the crystal's unit cell. This is achieved from relationships between d and the lattice constant a, which for the simple case of a cubic lattice is given by

$$\frac{1}{d^2} = \frac{h^2 + k^2 + l^2}{a^2}. \qquad (3.2)$$

The magnitude of the peaks depends on several factors: beam intensity, atomic scattering factor, structure factor, multiplicity of the planes and possible preferential orientation of the crystal planes. The broadening of the diffraction peaks depends on the crystallite size, strain and the resolution of the detector. However, the crystallite size (or grain size) is the dominant factor and thus, after correcting for the instrumental resolution, the full width at half maximum (FWHM) of the peaks is often used to obtain a measure of the grain size, using Scherrer's equation:

$$D_{grain-size} = \frac{0.9\lambda}{FWHM \cdot \cos(\theta)}. \qquad (3.3)$$

Detailed information about crystal structures, the physics of X-ray scattering, XRD instrumentation and interpretation of data can be found in Cullity's *Elements of X-ray Diffraction*, which is a very good introduction to the subject and covers nearly all aspects of X-ray diffraction. Other good references on this subject are those of Jenkins *et al.* and Warren [213, 214]. Crystal structures are covered in the International Tables of X-ray Crystallography [215].

3.3.2 X-ray Diffractometer

For rapid structural analysis of the entire composition range deposited on a glass slide, an Inel curved position sensitive detector (CPS 120) and a PW-1720 Phillips X-ray generator using Cu Kα radiation were used. The system is equipped with an automated x-y motion stage, which makes it an ideal tool for analyzing combinatorial samples. The size of the x-ray beam spot on the specimen is about 1 mm by 1 mm. In this configuration the sample and incident X-ray beam are stationary. The curved detector then simulates a rotating detector. As a result, the scattering wave vector is not always perpendicular to the substrate as shown in Figure 3.4. The X-ray beam is incident at about 6° with respect to the flat sample. Atomic planes that would satisfy the Bragg condition at $2\theta = 12°$, are parallel to the substrate. For this configuration, the direction of the normal to the planes which diffract at a given Bragg angle (θ), make an angle $(87+\theta/2)°$ with respect to the sample surface.

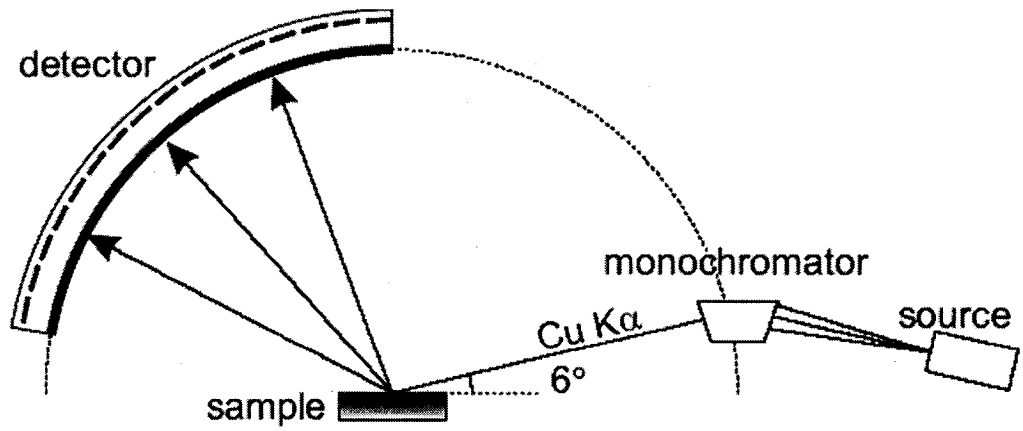

Figure 3.4 *A schematic of the Inel diffraction geometry. The sample and the incident beam are stationary and the curved detector resembles a scanning detector. (Taken from reference [202])*

The scattered X-rays are detected by measuring the current produced when X-rays ionize the Ar gas in the detector. There are 4096 cathodes which detect the ionization current and each corresponds to a certain 2θ value.

3.4 Composition Determination

3.4.1 Principles of Electron Microprobe

Electron microprobe (EM) is an analytical tool for determination of the composition of solid materials. The intensity of X-rays produced from an element in a compound, when it is struck by an electron beam, is proportional to the amount of that element. Elements from boron to uranium can be detected on a micrometer length scale. The system requires a source of focused, high energy electrons (2-20 keV) and a good vacuum chamber. For all these reasons EM, is nearly always coupled with a scanning electron microscope, which is widely available in many materials science labs. SEM and EM are described by Goldstein *et al.* [216].

Atomic transitions occur whenever an incident electron excites a core level electron of a solid material. An X-ray photon is emitted when a higher energy electron falls into the lower level hole created by the incident electron. Figure 3.5 (a) shows the possible K transitions, i.e. electronic transitions from the L and M shells into the K shell. Figure 3.5 (b) also shows a photon emission, when an incident electron strikes an atom. The energy of the emitted photons, also known as characteristic X-rays, depends on the energy of the transition states. Thus a spectrum of characteristic X-rays produced, when an electron beam irradiates a sample, forms a 'fingerprint' of the elements in the samples. Elemental identification of a sample can be performed from the energies of the detected X-rays. To quantify the composition of a sample, peak intensities are used. A simple explanation of the quantification procedure is given below.

Two ways of detecting X-rays are used and they are referred to as energy dispersive spectroscopy (EDS) and wavelength dispersive spectroscopy (WDS). In EDS, Li-Si semiconductor-based detectors are used to detect X-rays of different energies. An absorbed X-ray causes a photoelectron to be ejected from the Si atom. The ejected photoelectron loses energy and gives rise to electron-hole pairs. These electron-hole

pairs are then turned into a detectable signal by applying a bias voltage. More on X-ray detection can be found elsewhere [216].

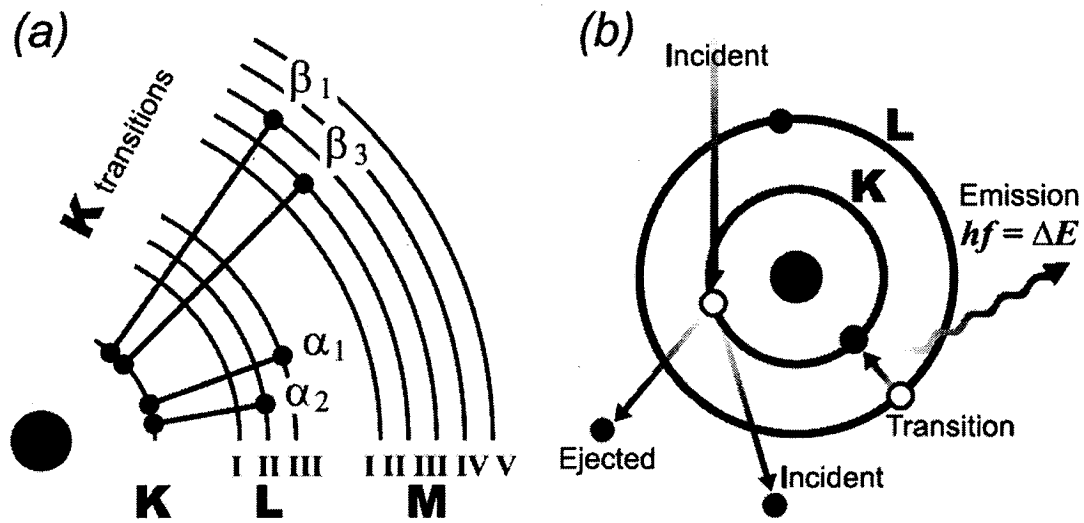

Figure 3.5 *(a) A description of some atomic transitions. (b) Ejection of an electron by an incident electron causes a vacancy in a K shell. A subsequent transition from an L shell leads to an emission of a photon with a characteristic energy given by the energy difference between levels. (Taken from reference [202])*

WDS uses diffraction of X-rays from crystals with known plane spacings. In essence WDS is the opposite of X-ray diffractometry. Here crystals with known atomic plane spacings are used to diffract X-rays of particular wavelengths which then will be detected by proportional gas counters. WDS is very sensitive and allows for trace elements to be detected. Lighter elements, like oxygen, are analyzed with WDS.

The relative intensities of the peaks can be used to determine the elemental concentration in a sample. The X-ray intensity ratio of an element in the sample to that of a standard (a sample with known composition) is equal to the mass concentration ratio of the element in the sample by:

$$\frac{C^i_{SAMPLE}}{C^i_{STANDARD}} = [ZAF]^i \frac{I^i_{SAMPLE}}{I^i_{STANDARD}} = [ZAF]^i k^i, \qquad (3.4)$$

where C^i and I^i are mass concentration and X-ray intensity and k^i is the $I^i_{SAMPLE}/I^i_{STANDARD}$ ratio, respectively. ZAF is the collective correction that accounts for the contributions of atomic number (Z), absorption (A) and fluorescence effects (F). These arise from the differences in the interactions of X-rays with the sample and standard. The actual calculations can be found elsewhere [216]. The atomic number

correction deals with the differences of electron beam penetration and backscattering in the sample and the standard. The absorption factor arises due to the difference in the degree of X-ray absorption between the sample and standard. The characteristic X-rays from one element i can sometimes generate X-rays from another element j and this is the fluorescence effect (F).

The calculations of Z, A and F factors for an element i in the sample require knowledge of the concentration of the other elements in the sample. So equation 3.4 is in fact applied iteratively, using ZAF = 1 as an initial assumption. The iteration follows by normalizing the k^i values and using 3.4 to calculate new estimates of the C^i values. The process is continued until no further changes are seen in the C^i estimates. The calculations involve a lot of numerical processing and are performed by a computer.

3.4.2 Electron Microprobe Instrument

The bulk structure and composition of the samples, prior to and after acid treatment, were studied by X-ray diffraction (XRD) and electron microprobe. The composition of the films was determined quantitatively by a JEOL JXA-8200 Superprobe equipped with one energy dispersive (EDS) spectrometer and five wavelength dispersive (WDS) spectrometers. The metal content (Pt, Ni, Fe, Mn, Co and Si substrate), was measured by EDS and the oxygen content was analyzed by WDS. The real count time was about one minute for each measurement. The optical autofocus feature of the microprobe was used for the films deposited on the Si wafer. For the rougher NSTF substrate films, selected points were manually focused and the beam was operated in scanning mode (covering an area of 150 μm × 110 μm) to obtain accurate results. Measurements on libraries deposited on smooth Si wafers and on the NSTF substrates showed the same stoichiometry variation with position in the library.

Typical conditions of the probe for measurements of Pt-Co films on Si-wafer and GC disks, are mentioned here. The standards used were Pt_3Fe for Pt, CoMn for Co and $PbCrO_4$ for oxygen, respectively. The beam voltage and current were 15 kV and 2×10^{-8} A. The beam size was 10-40 μm. The characteristic peaks used for quantifications were K_α for O, K_α for Co and L_α for Pt.

3.5 X-ray Photoelectron Spectroscopy (XPS)

XPS is a very powerful tool for probing the surface properties of solids and is used very widely in materials science. The basic principle behind XPS is Einstein's photoelectric effect for which he got the Nobel Prize in 1921. Kai Siegbahn and his group made significant contributions to XPS and with the help of Hewlett–Packard developed the first commercial instrument in 1969. Siegbahn received the Nobel Prize in 1981 for his contributions in the development of XPS. Interestingly, Kai's father, Manne Siegbahn also received the Nobel Prize for his work in X-ray spectroscopy in 1924. XPS is sometimes called photoemission electron spectroscopy (instead of photoelectron), by which it refers to the incident photon beam. It is also sometimes referred to as Electron Spectroscopy for Chemical Analysis (ESCA).

XPS can give a quantitative determination of the surface composition, the oxidation state of the elements and in certain cases the film thickness. XPS can also be coupled to depth-profiling systems, which use an impinging Ar^+ beam to remove surface layers. Because XPS is a surface analysis tool, performing XPS is significantly harder than EM. There are numerous good references which detail the theory and experimental techniques behind XPS [217-219]. Extensive online databases of XPS spectra for various materials can be found on the NIST website [220].

3.5.1 Principles of X-ray Photoelectron Spectroscopy

When a solid is radiated by an incoming photon source, electrons are excited and emitted. The energy of the emitted electrons is related to the binding energy (BE) of the solid, the work function of the spectrometer and the energy of the incident photons by

$$E_{kin} = \hbar\omega - |E_B| - \phi, \qquad (3.5)$$

where E_{kin}, E_B and Φ are the kinetic energy of the photoelectron, binding energy of the electron and the spectrometer's work function, respectively. $\hbar\omega$ is the energy of the incident X-ray photon. Figure 3.6 shows an energy diagram of this process. The electrons in the solid are grouped into the core levels, with discrete energy levels and into a continuous energy band depicting the valence electrons. Levels below E_f, the Fermi level, are filled and the gap between E_f and E_{vac} is designated by ϕ or the solid's work function. E_{vac} is the vacuum level where electrons are considered free. The binding

energy of electrons, E_B, is measured with respect to the Fermi energy, E_f. The broadening of the photoelectron peaks is due to different contributions such as the natural energy width of the X-ray source, the pass energy of the analyzer and the life-time of the core-holes.

Usually two X-ray sources, Mg and Al, are used which together can cover excitations from all the elements. The X-ray generation in the gun is similar to XRD guns: a high energy beam of electrons is impinged on the target anode, which is kept at high voltage. X-ray monochromators, if present, reduce the bandwidth of the photon beam, hence increasing the resolution. For insulating samples charging occurs, which shifts the peak energies. For insulators, conductive paths can be made by conductive tapes or by using an electron flood gun. A chamber pressure of 1×10^{-9} Torr or better is usually required. The electrons are detected at the detector, after they pass through a semi-spherical analyzer, shown in Figure 3.7. The energy of the electrons is retarded to E_o, or the pass energy, at the analyzer entrance aperture.

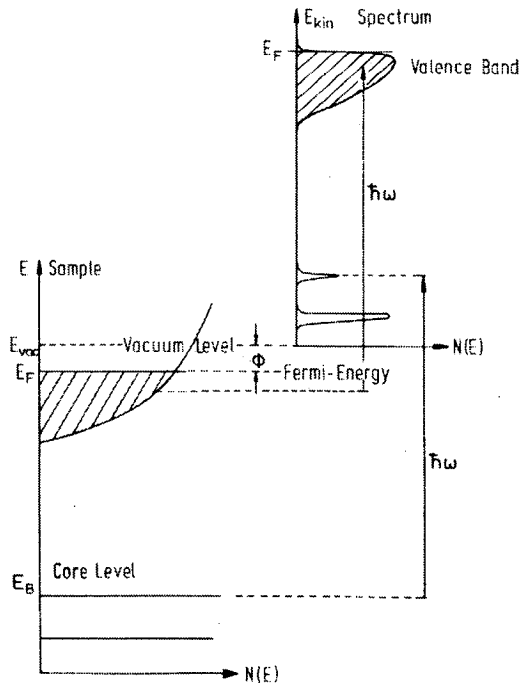

Figure 3.6 *Relation between the energy levels in a solid and the electron energy distribution produced by photons of energy ħω. The natural axis for the photoelectrons is the kinetic energy with its zero at the vacuum level of the sample. E_B is the binding energy of the electrons, which in solids is generally referred to the Fermi level and in free atoms or molecules to the vacuum level. (Taken from reference [217])*

To detect these electrons, a potential difference is applied between the inner and outer hemispheres. This potential difference is related to E_o by: $E_o = V/C$. C is a constant of the analyzer and is given by: $C = 1/((R_{out}/R_{in}) - (R_{in}/R_{out}))$. Thus by sweeping the retardation potential, electrons with different kinetic energies can be detected.

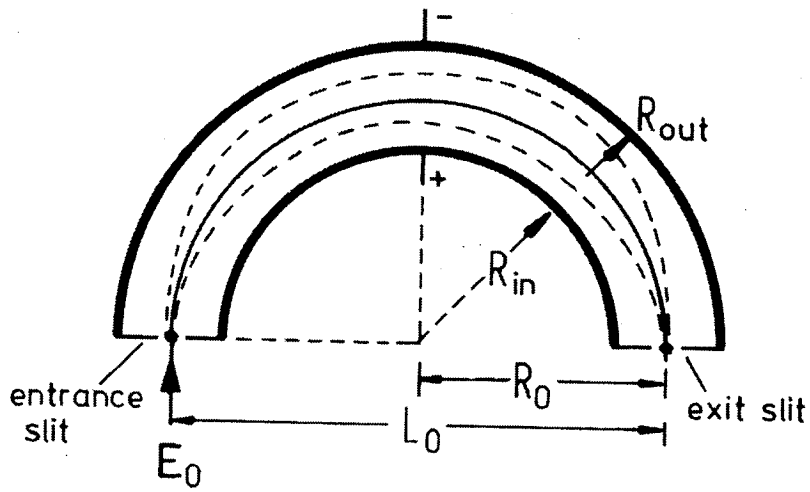

Figure 3.7 *Hemi-spherical electron analyzer used in XPS. (Taken from reference [217])*

3.5.2 XPS System Used and Experimental Procedures

The system used for the measurements was a VG Microtech Multilab XPS system (Thermo Electron Corporation) equipped with a CLAM-4 hemispherical analyzer and a Mg Kα, (15 kV, 20 mA) source with a 600 μm diameter analysis spot. No monochrometer was available, thus the limiting resolution was about 0.7 eV. Typical pass energies were in the range of 20-35 eV. Charging, if present, was corrected using the adventitious carbon C 1s peak present on the films as a reference. To do this, a carbon scan was performed before and one was taken after the desired scans (e.g. Pt and Co) were taken for a given spot. The deviations from 284.5 eV, the dominant peak of the adventitious carbon overlayer, were averaged and used to correct the spectra for that spot.

3.5.3 XPS Data Analysis and Quantification

The quantification of data to obtain the surface chemical composition of the sample is briefly discussed here. Detailed derivations can be found elsewhere [218, 219]. The intensity of an electron peak for an element A at a given energy depends on several

factors such as X-ray intensity, X-ray cross-section (σ), the transmission function of the analyzer (T), detector efficiency (D), number density of atom A in the sample (ρ_A) and the mean free path of the electrons (λ). A product of these parameters is called the sensitivity factor (SF) and can be written for the electrons of element A at kinetic energy E as:

$$SF = \sigma(\hbar\omega)\, T(E)\, D(E)\, \rho_A\, \lambda(E). \qquad (3.6)$$

The ratio of the atomic fraction of two elements is proportional to the ratio of the areal peak intensities of the respective peaks normalized by their SFs:

$$\frac{X_A}{X_B} = F_{AB}\frac{I_A/SF_A}{I_B/SF_B}. \qquad (3.7)$$

The proportionality constant, F_{AB} is matrix factor of the two elements given by

$$F_{AB} = \left(\frac{A_B\rho_A}{A_A\rho_B}\right)^{0.5}. \qquad (3.8)$$

For quantification one needs to know the values of the sensitivity factors and these are tabulated by Wagner in [219].

All the data analysis was performed by the Avantage software package provided by Thermo Electron. For metallic peaks, mixed Gaussian-Lorentzian shapes with asymmetric tail functions, was used. Similar profiles, but with no asymmetry factors, were used for the oxide peaks. The Wagner SFs assume a transmission function with a 1/E behavior; however, the transmission function of the instrument was obtained using a procedure suggested by Thermo Electron (see Appendix A). The SF values were corrected to account for this. More specific details about data analysis are provided when the results are discussed.

3.6 Rotating Ring Disk Electrode Measurements

The majority of electrochemical measurements presented in this thesis were made using the rotating ring-disk electrode (RRDE) technique. This method provides an alternative way of assessing the ORR activity of a catalyst other than FC testing.

RRDE is a fundamental approach to studies of ORR electrocatalysis and many of the measurements done using RRDE can not be made in fuel cells. Some of the unique aspects of RRDE measurements include: control of the working pH, a convenient way of

detecting hydrogen peroxide produced during the ORR and studying the impact of impurities. In addition, the RRDE technique has been used on single crystals of Pt and Pt-alloys with impressive success by Lawrence Berkeley National Lab (LBNL) scientists. These studies have, for instance, revealed surface structural dependencies of ORR for the first time. There is no other technique that can provide such information for ORR. If performed properly, RRDE can provide highly accurate and objective measurements of ORR activity. Complexities that exist in the electrode structure and mass transport effects in a PEMFC are not present in RRDE, thus RRDE results must, at least ideally, be highly reproducible. The mass transport equation in RRDE has been solved analytically.

A critical factor in RRDE measurements, which is especially true for Pt-based electrocatalysts, is the purity of the experimental setup. Presence of minute (ppm levels) amounts of impurities (anions, cations and hydrocarbons) can negatively impact the measurements. Leakage of fluid into the electrode tips can also cause problems. Patience is the key to successful measurements, otherwise poor results, irreversible damage to electrodes, frustration or a combination of these will be the outcome!

RRDE is covered in nearly every electrochemistry textbook [221]. Bard and Faulkner [157] cover RRDE in detail. Brett and Brett discuss RRDE and hydrodynamic electrochemistry in more mathematical detail [222]. As far as FC electrocatalysts are concerned, Schmidt and Gasteiger's chapter on RRDE in the *Handbook of Fuel Cells* is an indispensable reference for the interested researchers [223]. Pine Instruments also provides several good technical documents, some of which discuss characterizations of ORR electrocatalysts [224].

3.6.1 Hydrodynamic Electrochemistry

RRDE falls into a category of electrochemical techniques which are collectively referred to as hydrodynamic electrochemistry. These electrodes work in a regime of forced convection. Forced convection increases the transport rate of electroactive species to the electrode leading to higher current densities, greater sensitivity and better reproducibility. In addition, this allows rate-determining processes to be probed. Techniques include RRDE, wall-tube, wall-jet and stationary disk in rotating fluid. Solutions of transport equations (Fick's laws of diffusion with a convection term) with appropriate boundary

conditions, lead to a unique limiting current which is a unique function of the cell geometry and the flow characteristics. Brett and Brett provide good information on these hydrodynamic techniques [222].

3.6.2 Diffusion-Limited Current in RRDE

In solution cells, activation and Ohmic losses are similar to those in FCs. The mass-transport polarization, on the other hand, is a unique property of the experimental system and in certain cases can lead to an analytical expression for the mass-transport (or diffusion-limited) current. RRDE is one example, where an analytical expression for the diffusion-limited current has been derived. The convective-diffusive equations for the RDE geometry in the case of a laminar flow regime (3.9 and 3.10) were solved by Viniyamin Levich, after whom the solution is named. These are:

$$J = c\upsilon - D\nabla c \tag{3.9}$$

$$\frac{\partial c}{\partial t} = -\upsilon\nabla c + D\nabla^2 c, \tag{3.10}$$

where J, c, υ and D correspond to flux of species, concentration of species, fluid velocity and diffusion constant, respectively. The detailed solution is not reproduced here, but can be found elsewhere [222]. It suffices to say that several approximations are used: convective forces due to the walls are ignored, the disk is assumed to be a perfectly flat plane of an infinite extent, etc. The solution then involves solving for the flow velocity in terms of rotation speed and derivation of the diffusion length, δ, in terms of angular velocity ω. The solutions for δ and $j_{diffusion\text{-}limited}$ are then:

$$\delta = 1.61 D^{1/3} \nu^{1/6} \omega^{-1/2} \tag{3.11}$$

$$j_{diffusion\text{-}limited} = 0.62 n F D^{2/3} \nu^{-1/6} \omega^{1/2} c, \tag{3.12}$$

where ν is the fluid viscosity, ω is the angular speed of the disk and the other variables are defined as before. An approximation is that, within the diffusion layer, i.e. the layer that is stagnant next to the electrode surface, there is no convection and mass transport occurs solely by diffusion.

In the absence of any mass transfer effects, i.e. when the current is small, only kinetic contributions are significant. Since the diffusion-limited current can easily be observed,

it can be accounted for so that the kinetic current can be obtained using the Koutecky-Levich (KL) equation:

$$\frac{1}{j} = \frac{1}{j_k} + \frac{1}{j_{diffusion-limited}}, \qquad (3.13)$$

where j, j_k and $j_{diffusion\text{-}limited}$ are the measured, kinetic and diffusion-limited current densities, respectively. More detailed information on KL equation an be found elsewhere [157]. Applications of 3.13 for ORR are explained in later chapters.

3.6.3 Applications of RRDE

There are numerous ways by which RRDE can be used in electrochemistry. For example, it can form an electroanalytical technique whereby one can measure the concentration of an analyte using the Levich relation (3.12), given that other parameters like viscosity and diffusion constant are known. Use of a ring electrode allows for the products of the reaction(s) to be detected.

As far as ORR is concerned, the RRDE has been a long time favorite tool of electrochemists. In complicated, multi-electron reactions like ORR, however, disk and ring current measurements alone are not sufficient to elucidate the reaction pathway. Adzic notes that the number of parameters (rate constants) far exceeds that which the available data, i.e. disk and ring currents, can provide [165].

3.6.4 RRDE Instrumentation

All the measurements were carried out with a Pine Instruments system (Raleigh, NC, US). Pine Instruments has been manufacturing RRDE systems for several decades and is the leader in this field. The electrodes manufactured by Pine are extremely high quality and allow for glassy carbon (GC) disks to be inserted and removed. Two complete systems have been acquired and are currently in use. Figure 3.10 shows a typical two compartment electrochemical cell and a Pine rotator.

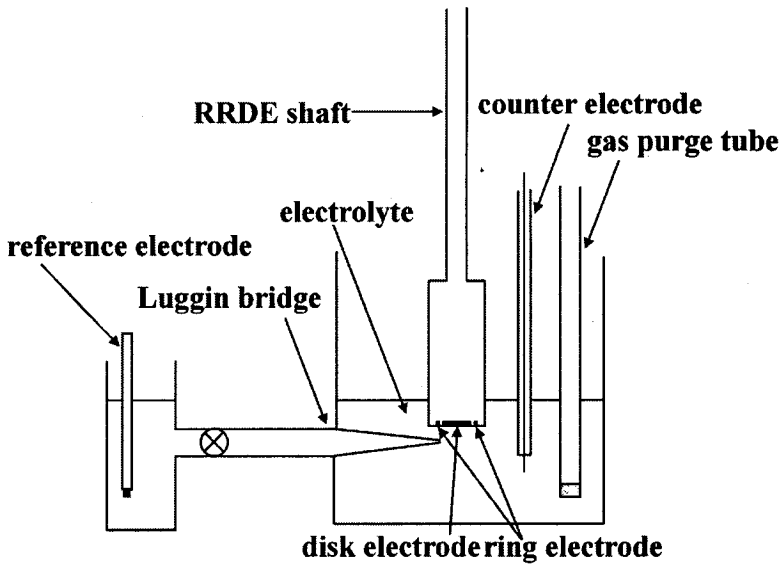

Figure 3.8 *Schematic of a two-compartment cell for ORR measurements. The working and Pt counter electrodes are inserted in the main body of the cell and the reference electrode is separated by a bridge.*

Figure 3.11 shows the two RRDE setups in use. Both systems are housed in a double glove box converted into a pseudo-fumehood.

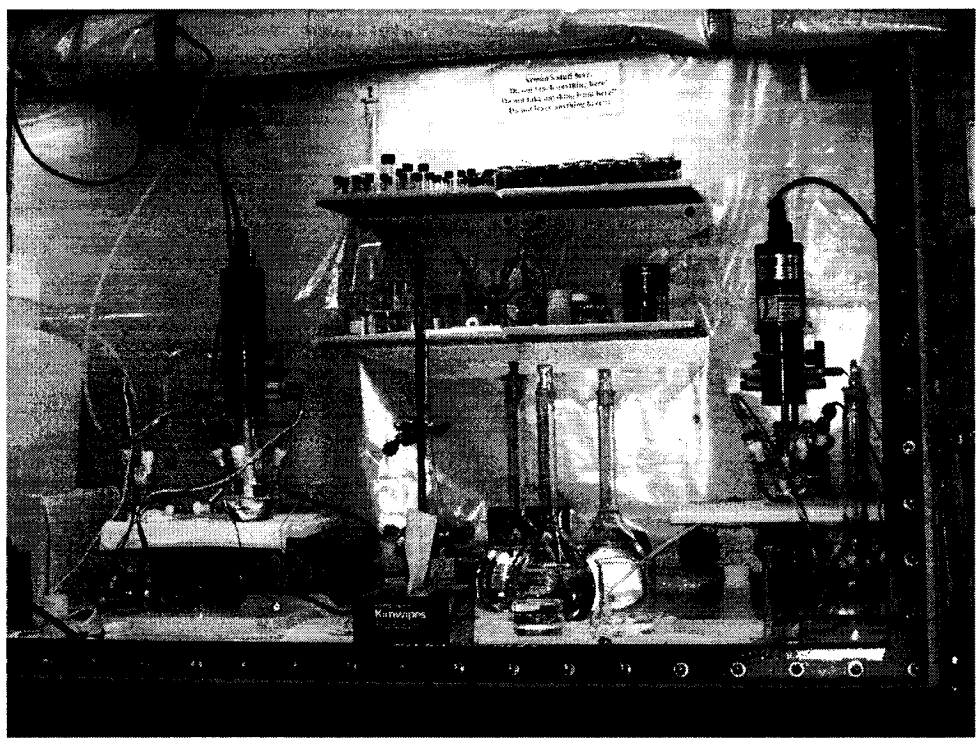

Figure 3.9 *Pine rotators and single-compartment cells in use.*

3.6.4.1 Pine FCBP1 Bipotentiostat

The bipotentiostat has a true analogue output, which is usually preferred and is controlled by software. The bipotentiostat allows for the potential/current of the disk and the ring to be controlled and measured independently, but it does not have an auto-ranging capability. The digital averaging capability of the software is almost always used to smooth the data.

3.6.4.2 RDE and RRDE

The RDE and RRDE electrodes are mounted in the AFMSRX rotator and contacts are made by clamping brushes. The rotator has a precision motor and is controlled manually. The controller can go up to 10,000 rpm; however, according to the manufacturer's instructions speeds higher than 3,000 rpm should never be used. The RDE electrodes contain only the disk and consist of either GC or Pt disks embedded into Teflon. The disks in these electrodes are permanent and can not be reinserted.

The RRDE is considerably more complicated as it contains insertable disks in an assembly that needs to be leak-tight. Figure 3.12 (a-c) shows the internal structure of a typical RRDE electrode. The disk electrode is electronically insulated from the ring by a teflon shroud commonly referred to as a 'U-cup'. Leakage around the U-cup is a very serious problem and must be avoided. Leakage of acid into the U-cup both damages the electrode parts and obscures the measurements. Large background currents in the ring data and slanted CVs are indications of leakage. Exposure to high temperature (higher than room temperature) and usage over time leads to leakage in the U-cups. Since Teflon is very difficult to machine and because precision U-cups are needed, spare parts from Pine are outrageously expensive (> $100 USD). Their high price led to the development of U-cups by Simon Trussler, the Dahn group's machinist. The U-cups are very difficult to manufacture; hence, they are made in batches of 100 which usually last several months.

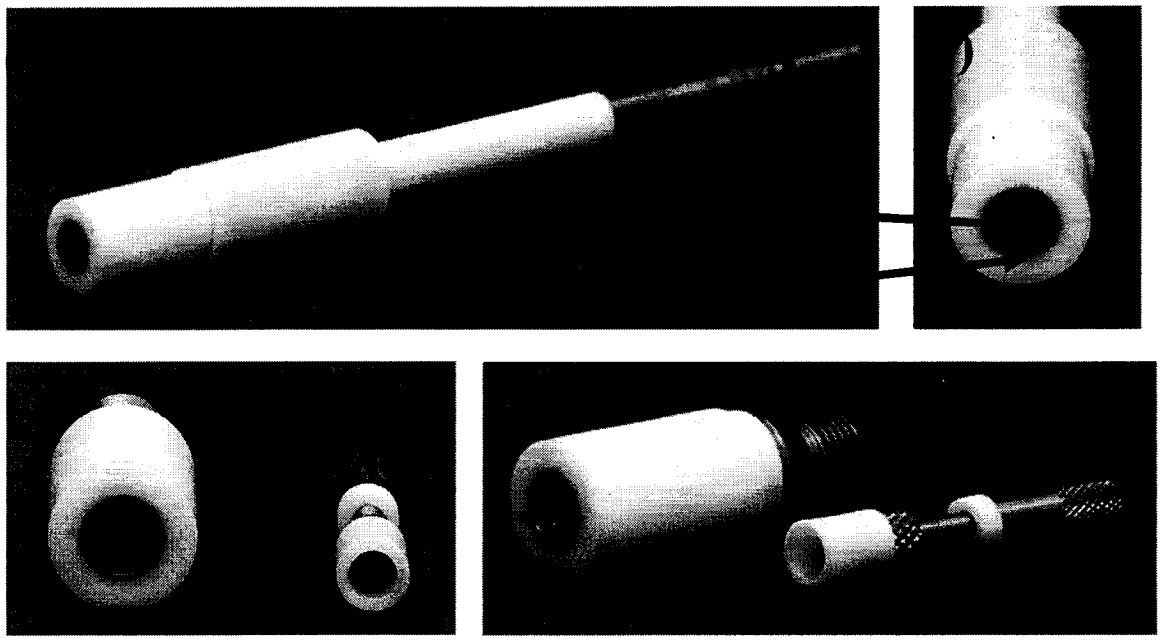

Figure 3.10 *A complete RRDE electrode (a). Disk and ring electrodes of an RRDE (b). Internal parts of RRDE showing front view (c) and side view (d). Disk electrode is 5 mm in dia.*

3.6.4.3 Cell Glassware

Two types of cells were used: one-compartment and two-compartment. To reduce the Ohmic resistance, it is usually desired to have the reference electrode (REF) tip very close (a few millimeters) to the working electrode (WE). This is usually achieved by a Luggin-capillary bridge. Another reason for using a Luggin capillary is to minimize the REF's ion impurities from contaminating the WE. Figure 3.10 shows a two-compartment cell where the REF is separated from the cell by a Luggin bridge. Figure 3.11 shows two single-compartment cells in use. In practice single-compartment cells were found to be equally as good as two-compartment cells and because they were simpler to setup, they were used for most of the measurements. Cleaning of the glassware and other cell parts is explained in appendix B.

3.6.4.4 Reference Electrodes (REF)

Generally two types of REF electrode were used: the MMS or mercury/mercurous sulfate, which is Cl^- free and the Ag/AgCl electrode. For Pt-based samples it is essential to minimize Cl^- impurities from the REF because Cl^- poisons the Pt surface. This can be

done by using a 2-compartment cell (and keeping the stopcock closed) or using a Cl^--free REF electrode. The REF electrodes are always rinsed with nano-pure water and stored in appropriate solutions (0.05M H_2SO_4 for MMS, 4M KCl for Ag/AgCl).

Whatever the choice of reference electrode, it was always calibrated versus the reversible hydrogen electrode (RHE) and all the measurements are reported versus RHE. The RHE scale for the MMS electrode was established by purging H_2 in the solution and measuring the open circuit voltage of the cell using both the disk electrode (if it is Pt-based) or the ring electrode as the WE. The OCV values of disk and ring, always within 5 mV or less, were averaged and used as the RHE scale for the given sputtered GC disk. This reference calibration was performed for each individual disk measurement. When the disk material was not Pt-based (i.e. in the case of NNMC), the calibration was done using only the Pt-ring electrode.

3.6.4.5 Counter Electrode (CE)

The CEs commonly used in electrochemical measurements were Pt wire, Pt foil or Pt mesh. For all the experiments reported here a Pt wire, sealed in a glass tube and soldered to an Al wire, was used. The tip of the electrode must be checked for leakage, as this could lead to contamination. These electrodes must be made with a special glass (Pt glass) for sealing and usually show very good resistance against cracks.

3.6.4.6 Glassy Carbon Disks

Glassy carbon is probably the most popular choice of electrode material in electrochemistry. It is very hard, can be polished to a mirror surface, has good conductivity, is very durable in extreme pH and temperatures ranges and exhibits very little surface chemistry. However, the manufacture of GC is a very time consuming process. Kinoshita has authored an excellent book on the physiochemical and electrochemical properties of carbon, which discusses glassy carbon [225]. GC is available in various forms (disk, rod or plate) and dimensions. Disks that were used in these experiments were about 5 mm in dia. and 4 mm in height. These were cut from 10 cm long rods purchased from Tokai Carbon.

All the disks were polished using a Leco autopolisher, where up to six disks were mounted in a specially-designed jig using one stage grinding (15 μm) and two stage (5 μm and 0.05 μm) polishing. Special GC holders were made for sputtering and XPS experiments.

3.6.5 RRDE Studies of ORR

Several types of samples were studied for their ORR properties: sputtered films of Pt-alloy and NNMC on GC, sputtered Pt-alloys on NSTF and NNMC powder samples synthesized by various reactions. Pt and Pt-alloys sputtered onto GC or NSTF are discussed in chapters 5, 6 and 7 respectively. Preparation of powder slurries for NNMC and their results are discussed in chapter 8 where loading effects are also discussed. In the next section we briefly explain a typical sequence of the measurements. More detailed step-by-step procedures are provided in appendix C.

3.6.5.1 RRDE Measurements

The electrolyte used was about 125 mL of 0.1M $HClO_4$ prepared from doubly-distilled GFS Chemicals $HClO_4$ and 18 MΩ Barnstead nanopure water. All the currents were normalized by either the geometric or the electrochemical active surface area (ECSA), as explained below.

Both sputtered glassy carbon disks and the Pt ring electrode were first electrochemically cleaned by sweeping their potential between -100 mV and open circuit voltage (OCV) at 500 $mV \cdot s^{-1}$ until steady state cyclic voltammograms (CV) were obtained. Slow rate CVs were then acquired in the range of 1050 to 65 mV (the onset of H_2 evolution) at 50 $mV \cdot s^{-1}$. The OCVs of the disk and ring, in O_2-saturated electrolyte, were generally about 1050 mV and were not exceeded in any of the measurements. Oxygen reduction scans were made in the same potential range (1050 to 65 mV) and at the same sweep rate (50 $mV \cdot s^{-1}$) for two full cycles, while purging O_2 at a rate of about 1 $L \cdot min^{-1}$ through a 2 μm fritted tube (Ace Glass). The ORR measurements were performed at 400, 900, 1600 and 2500 rpm. All measurements were performed at room temperature (21±1°C). Typically about two or three disks were measured in a given cell setup before the electrolyte was changed. In addition to sputtered films of Pt and Pt-Co

on GC disks, similar CV and ORR measurements were performed using a Pine Pt (polycrystalline) rotating disk electrode (RDE) with a 1 μm polish as an additional Pt standard.

To analyze the Tafel kinetics, the following corrections were made to the measured current. The electrochemical active surface area (ECSA) of each glassy carbon disk was estimated by averaging the integrated charge for the H^+_{ads}/H^+_{des} regions of the CVs taken in an Ar-purged cell and using the 210 $\mu C \cdot cm^{-2}$ conversion factor commonly used to calculate the ECSA [87].

$$ECSA = (H_{ads} + H_{des})_{from\ Ar\text{-}CVs} / (2 \times 210\ \mu C \cdot cm^{-2}) \quad (3.14)$$

These CVs (examples are shown in later chapters) were taken before and after the ORR measurements and the resulting ECSAs were averaged. The difference in the ECSA of disks, before and after ORR measurements, was always less than about 10%. The surface enhancement factor (SEF) was obtained from the ratio of the ECSA to the disk's geometric surface area ($SA_{geometric} = 0.195\ cm^2$):

$$SEF = ECSA / SA_{geometric} \quad (3.15)$$

The Faradaic current, i.e. the current due to the oxygen reduction alone, normalized by the geometric surface area, was found by:

$$j_{Faradaic,\ geometric} = -(j_{Disk\text{-}ORR} - j_{Disk\text{-}Ar\text{-}CV}) / (SA_{geometric}) \quad (3.16)$$

Next, the kinetic current density was obtained using the Koutecky-Levich relation:

$$j_{Faradaic,\ kinetic,\ geometric} = \frac{\left(j_{Faradaic,\ geometric} \times j_{diffusion-limited,\ Faradaic,\ geometric}\right)}{\left(j_{diffusion-limited,\ Faradaic,\ geometric} - j_{Faradaic,\ geometric}\right)} \quad (3.17)$$

The diffusion-limited current was read directly from the ORR ($j_{Faradaic,\ geometric}$ versus $V_{versus\ RHE}$) data for each corresponding rotation speed. The value of the current in the middle of the current plateau was chosen as the diffusion-limiting current. This value of the diffusion-limited current, in general, was very close to the diffusion current that was otherwise found by the Koutecky-Levich analysis [117, 167]. Finally, (3.15) was divided by the SEF factor to obtain the ESCA-normalized current density:

$$j_{Faradaic,\ kinetic,\ EC} = j_{Faradaic,\ kinetic,\ geometric} / SEF \quad (3.18)$$

Hence, for Tafel kinetic analysis, a current density normalized by the ESCA and corrected for the non-Faradaic contribution and the diffusion-limited current was used.

The Ohmic resistances in the electrode contacts and electrolyte solution were assumed to be the same for different disks and were not included in the corrections.

3.6.5.2 Ring Measurements

The ring electrode was used to detect the amount of H_2O_2 that was produced and released into the solution during the ORR. The ring current only detects a fraction of those H_2O_2 molecules that are released into the solution. This is known as the collection efficiency of the ring and can be determined by oxidation/reduction of ferrocynide ions as explained by Gasteiger *et al.* [223]. This is discussed in Appendix D.

During the ORR measurements, the ring electrode was held at 1.2 V versus RHE to oxidize H_2O_2. The ring background current, which was normally about 0.1 μA, was subtracted from the measured ring current. The percentage of hydrogen peroxide produced was calculated using:

$$\%H_2O_2 = 200 \times \frac{I_{Ring}/N}{I_{Disk} + I_{Ring}/N}, \qquad (3.19)$$

where N designates the collection efficiency.

3.7 Nano-Structured Thin Film (NSTF)

During the past ten years, 3M scientists have developed a new class of nanostructured thin film (NSTF) support for fuel cell electrocatalysts. These new support structures are oriented nanometer-sized crystalline organic whisker structures that are obtained by thermal sublimation and subsequent annealing of a red organic pigment, N,N-di(3,5-xylyl)perylene-3,4:9,10bis(dicarboximide) (called perylene red or PR) on polymer substrates like polyimide. The crystalline whisker structures have lengths of about 500 - 1000 nm, cross sectional diameter of about 50 nm and an areal number density of 3 - 5 billion cm^{-2}. Their chemical, thermal and electrochemical durability render them very suitable for supports in the corrosive environment of PEM fuel cells. Details of the growth and physical characterizations of these nano-sized whiskers can be found elsewhere [11,12]. Catalysts are deposited on these whiskers by chemical methods or by vacuum deposition processes like sputtering; however, the latter allows for better coating control. Both the high number density and nanometer size dimensions of the whiskers as

well as the roughness of the catalyst coating on these whiskers add to the overall surface area enhancement factor, which is crucial for better fuel cell performance. Further information on Pt-coated whisker supports, fabrication of membrane electrode assemblies and performance of the resulting fuel cells can be found in [124].

3.8 Fuel Cell Testing of Sputtered Films at 3M

The sputtered electrocatalysts were transferred to a Nafion (117, 127 μm thick) membrane using a hot press lamination process and were incorporated in a fuel cell using the methods described in [124]. Typical fuel cell testing procedures included cyclic voltammetry measurements from 0.02 to 0.65 V at 100 $mV \cdot s^{-1}$ and polarization measurements with H_2/O_2 (10/10 psig) from 0.9 to 0.6 V for about 1 hour. All electrochemical measurements were performed at 80°C. After these measurements, the fuel cell was disassembled and the catalyst layer on the Nafion membrane was studied using the electron microprobe.

Details of membrane electrode assembly (MEA) construction for NSTF catalysts are provided by Debe [124]. Using a decal process, the NSTF catalyst was transferred from the initial substrate web to a 3M-fabricated Nafion PEM to make a catalyst-coated membrane (CCM). Fuel cell performance measurements were carried out in 50-cm^2 Fuel Cell Technologies test cells with quad-serpentine flow fields. The CCMs were sandwiched, without lamination, between two gas diffusion layers (GDLs). The membrane electrode assemblies (MEAs) were tested on a Fuel Cell Technologies fuel cell test station. For the combinatorial libraries, two ½-CCM's with catalyst coated on only one side, were used. This allowed the anode and cathode components of the MEA to be easily separated for analysis after fuel cell testing. Electrochemical characterization tests (such as surface area measurements) as well as polarization curves under oxygen were performed at room temperature and 75°C under humidified gasses using a segmented MEA in an eight-segment segmented cell. Tests continued for several days until performance reached a steady level.

3.9 Slurry Preparations for RRDE

The Pt/NSTF slurries were made using catalysts sputtered onto NSTF substrate, carefully brushed off the coated NSTF roll with a solder brush, and NPW. Precautions were taken to avoid any contamination of the catalyst with impurities, mechanical or otherwise. No alcohol or Nafion was used. To make a deposition, 15 μL of slurry was dropped on a cleaned GC RRDE tip and was dried in a flowing Ar stream for about 20 minutes. The deposition was normally very uniform. No catalyst was lost during the measurements and this was confirmed by taking CVs and comparing the ECSA of the samples at the beginning and end of every measurement sequence.

The non-noble metal catalyst (NNMC) slurries consisted of 350 μL ethanol, 95 μL Nafion (5% by wt in ethanol) and catalyst (different amounts). The slurries were sonicated for 0.5 hour. About 7 μL was placed on the electrode tip and was dried in air.

3.10 Various other Measurements

Other measurement tools and techniques that were used are briefly explained in this section.

Acid treatments were made on electrocatalysts coated on the NSTF supports. The samples were soaked in 25 mL of 0.3M or 1M acid and were kept in sealed glass vials at different temperatures (25°C, 55°C or 80°C) for different periods of time. H_2SO_4 or $HClO_4$ (reagent, analytical grade) were the acids used for testing. After treatment, the samples were washed with de-ionized water and in air-dried before further study. Special care was always taken so as not to damage the nano-sized whiskers on the films during handling.

After the soaking period, the solutions were analyzed for their metal contents by a Perkin-Elmer atomic absorption spectrophotometer with detection limits of 0.01, 0.01 and 0.2 ppm for Fe, Ni and Pt respectively.

The amount of film deposition was determined gravimetrically, by weighing 1.3 cm diameter Al disks before and after deposition using a precision (0.1 μg) Cahn 29 electrobalance.

The thickness of the libraries sputtered onto a Si wafer was determined using a Dektak 8 advanced development profilometer (Veeco Instruments Inc.).

The morphology of sputtered films were studied with a Hitachi S-4700 field emission scanning electron microscope.

When required, post-deposition annealing of the films deposited on glassy carbon disks were done at 750°C and 950°C using a Modular Process Technology RTP-600S rapid thermal processor (RTP). Films were heated to the annealing temperature under Ar (flow rate of 2 $L \cdot min^{-1}$) and with a heating rate of $5°C \cdot s^{-1}$. The films were kept for 400 s at the annealing temperature. For heat treatment, separate sets of identical samples were used.

Chapter 4

Corrosion Studies of $Pt_{1-x}M_x$ (M = Fe, Ni, Mn; $0 \leq x \leq 1$) and $Pt_{1-x-y}M_xM_y$' (M, M' = Co, Ni, Mn, Fe) Combinatorial Libraries

4.0 Introduction

This chapter presents a vast amount of data collected from measurements that were performed on binary of Pt-M and pseudo-ternary Pt-M-M' libraries, where M and M' were chosen from Ni, Mn, Fe and Co [113, 114]. These libraries were produced and studied in close collaboration with researchers of the fuel cell program at 3M Company. Production and characterization of the libraries were all performed at Dalhousie University and fuel cell evaluations were performed at 3M. Here only the production and corrosion studies of these combinatorial libraries are discussed. Debe *et al.* discuss the FC performance of sputtered Pt-alloys [226]. First a brief introduction to corrosion of metals is provided.

4.1 A Background on Corrosion of Metals

The corrosion of metals refers to the dissolution of metals (or other materials) in aqueous environments. The oxidation reaction, where a metal becomes a cation, occurs in conjunction with a reduction reaction to conserve overall charge neutrality. In an acidic medium, it is normally the H^+ ions which are reduced. Dissolved O_2 molecules, can also be reduced to water. The following reactions show a very simplified corrosion scenario for Fe in an acidic solution:

$$Fe \rightarrow Fe^{2+} + 2e^- \quad \text{(oxidation of Fe, anodic reaction)} \quad (4.1)$$

$$2H^+ + 2e^- \rightarrow H_2 \quad \text{(reduction of } H^+\text{, cathodic reaction)} \quad (4.2)$$

or

$$\tfrac{1}{2}O_2 + 2H^+ + 2e^- \rightarrow H_2O \quad \text{(reduction of } O_2\text{, cathodic reaction)} \quad (4.3)$$

The anodic and cathodic reactions occur on the surface of the metal and the respective regions are referred to as anodic and cathodic regions. Figure 4.1 shows schematically what happens during a corrosion situation.

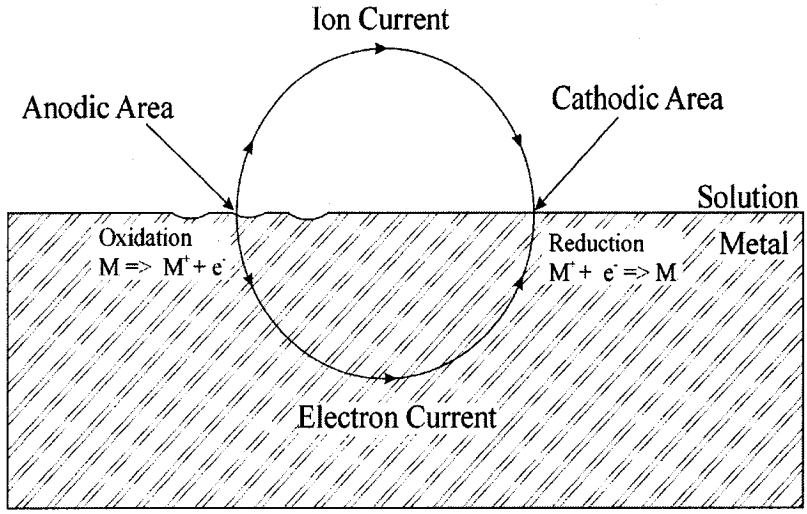

Figure 4.1 *Schematic of the Evans Diagram for a metal corroding in an acid. (Adapted from reference [227])*

Each of these reactions is called a half-cell reaction, whose equilibrium potential can be obtained by the Nernst equation. Most metals, with exception of the noble metals, are unstable in their metallic form and are always found as compounds in nature. The occurrence of corrosion is now considered from a thermodynamic point of view.

4.2 Thermodynamics of Corrosion and Pourbaix Diagrams

As in the case of the H_2/O_2 fuel cell, when the free energy change of a corrosion reaction is negative, corrosion is thermodynamically favorable. The following equation, which we encountered in the first chapter, expresses the free energy (molar) of a corrosion reaction of a metal in terms its redox potential:

$$\Delta g_f = -nFE \qquad (4.4)$$

where, again as before, n is the number of electrons transferred, F is the Farady's constant and E refers to the difference between the anodic and cathodic potentials. It turns out that corrosion of many metals in acidic media occurs spontaneously. Au and Pt are noble exceptions. Both the cathodic and anodic potentials show pH dependence, thus corrosion thermodynamics also exhibits significant pH dependence. In fact the thermodynamics of metals have been extensively studied as a function of potential and pH. These studies,

which were originally initiated by Marcel Pourbaix, have been summarized in the so-called Pourbaix (also E-pH) phase diagrams [228]. These phase diagrams show what Pourbaix originally classified as regions of corrosion, passivation and immunity. Passivation occurs when a layer of oxide (or hydroxide) forms a protective coating on the surface of the metal. Many alloys achieve their corrosion resistance by passivation. Immunity refers to a region when a metal is immune to dissolution. Very few metals (Pt, Au) are immune at the working pH and potentials of typical PEMFCs. However, even Pt can show dissolution! Corrosion of Pt will be discussed at the end of this chapter.

Figure 4.2 shows the Pourbaix diagram of water. The region between the two lines is called the water stability region. Above the first line (labeled O_2/H_2O) oxygen evolution occurs and below the lower line (labeled H_2/H_2O) hydrogen evolution. The H_2/H_2O line corresponds to hydrogen evolution by:

$$2H^+ + 2e^- \leftrightarrows H_2 \qquad \text{or} \qquad \text{(acidic)} \qquad (4.5)$$

$$2H_2O + 2e^- \leftrightarrows H_2 + 2OH^-. \qquad \text{(alkaline)} \qquad (4.6)$$

The potential for this reaction is pH dependent (Nernst equation) and is given by $E = -0.059 \cdot pH$. At more negative potentials, hydrogen evolution occurs spontaneously. More negative potentials favor the reduction reaction. Similarly the O_2/H_2O line corresponds to the reactions:

$$O_2 + 4H^+ + 4e^- \leftrightarrows 2H_2O \qquad \text{(acidic)} \qquad (4.7)$$

$$O_2 + 2H_2O + 4e^- \leftrightarrows 4OH^- \qquad \text{(alkaline)} \qquad (4.8)$$

For more noble potentials (above the O_2/H_2O line) oxygen evolution occurs.

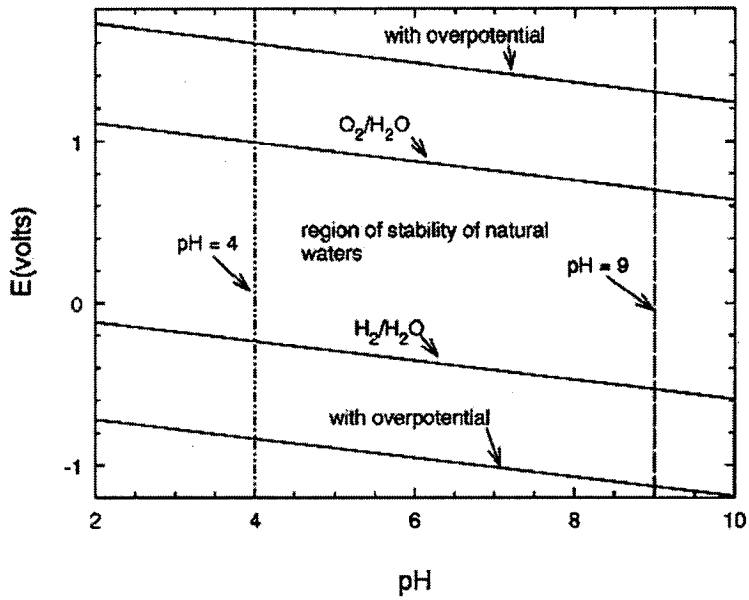

Figure 4.2 *Pourbaix diagram of water. (Taken from reference [229])*

Figure 4.3 shows the Pourbaix diagram for Fe. The diagram summarizes the nature of Fe as a function of potential and pH as passive (Fe_3O_4 or $Fe(OH)_2$), immune (Fe) or corrosive (Fe^{2+}, Fe^{3+}). It should be mentioned that these diagrams only present the thermodynamic states, i.e. they do not make any prediction for the kinetics of corrosion. What happens to the electrochemical potential of the surface when it is corroding and how fast does corrosion occur? The potential of the surface will be somewhere between the half cell potentials of the oxidation and reduction reactions.

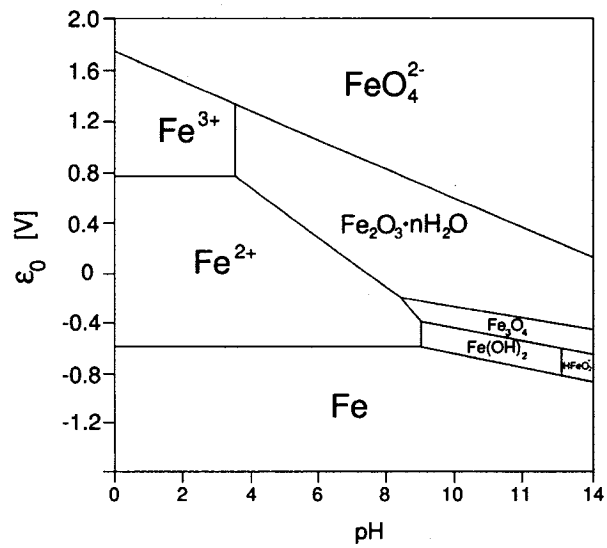

Figure 4.3 *A simplified version of the Fe Pourbaix diagram. (Taken from reference [230])*

4.3 $Pt_{1-x}M_x$ (M = Fe, Mn, Ni; 0 < x < 1) Libraries

In this section the corrosion results for binary Pt-M systems, where M = Fe, Mn, or Ni are presented. First, the materials science aspects of the as-deposited Pt-Fe and Pt-Ni combinatorial libraries including composition and crystal structures are described. Next, the composition changes after acid treatment are measured and compared to catalysts that have been exposed to the PEMFC environment. Figure 4.4 shows Pt-Fe libraries that were sputtered deposited onto 1 cm × 7.5 cm long NSTF supports. Each strip shown contains the entire binary range of $Pt_{1-x}Fe_x$ (0 < x < 1). Similar libraries were prepared for the Pt-Ni binary system.

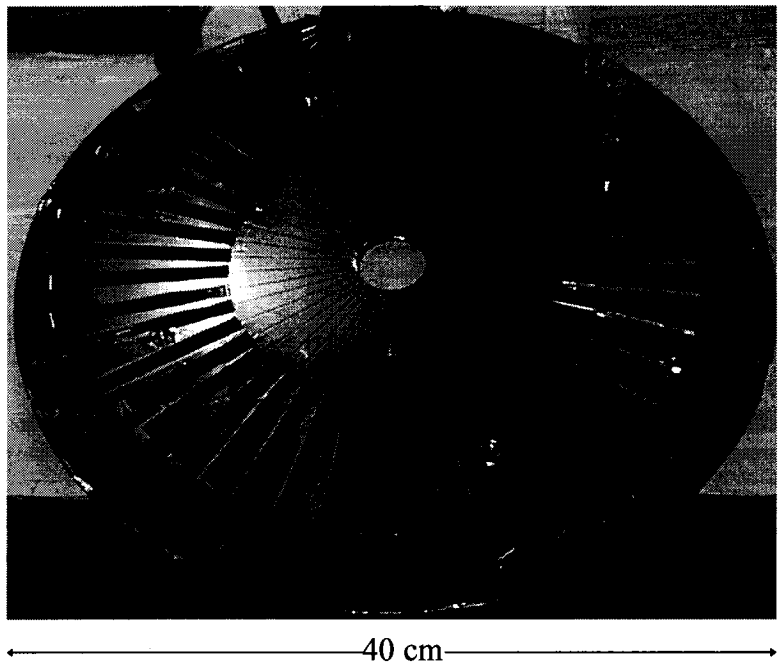

Figure 4.4 *The sputtering table used to support the 1 cm × 7.5 cm long NSTF substrates and Si wafers shown after a deposition experiment.*

4.3.1 Compositional Mapping of $Pt_{1-x}M_x$ (M = Fe, Ni, 0 < x < 1)

Figure 4.5 shows the composition versus position of the sputtered films on the Si wafer substrates. Figure 4.5 shows that the oxygen content of the libraries is low except at the transition metal rich end. The oxygen thought to originate after the deposition is mostly in form of $Ni(OH)_2$ as XPS measurements showed.

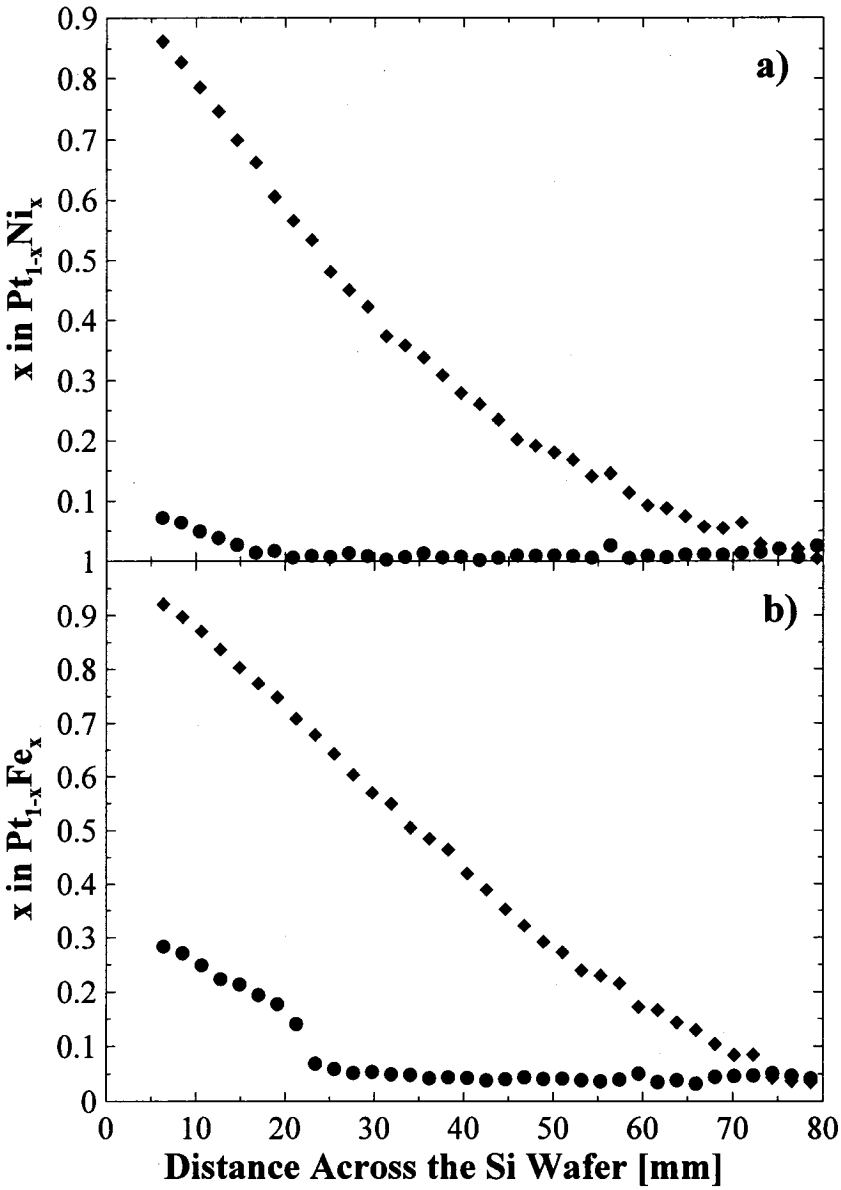

Figure 4.5 *The composition of $Pt_{1-x}Ni_x$ (top) and $Pt_{1-x}Fe_x$ (bottom) libraries across the Si wafer obtained by electron microprobe. The diamonds show x, the atomic fraction of M (M = Ni, Fe) in $Pt_{1-x}M_x$ and the circles show the oxygen fraction in $[Pt_{1-x}M_x]_{1-y}O_y$. The uncertainties in the measurements are about 2%.*

4.3.2 Crystallographic Structures of $Pt_{1-x}Fe_x$ ($0 < x < 1$) and $Pt_{1-x}Ni_x$ ($0 < x < 0.8$) Deposited on Si (111) Wafers

Figure 4.6 shows X-ray diffraction patterns of the $Pt_{1-x}Fe_x$ library over a wide range of scattering angles. A randomly ordered fcc phase for low Fe concentrations ($0 < x < 0.7$) and a randomly ordered bcc phase for the Fe rich ($0.71 < x < 0.95$) regions are observed.

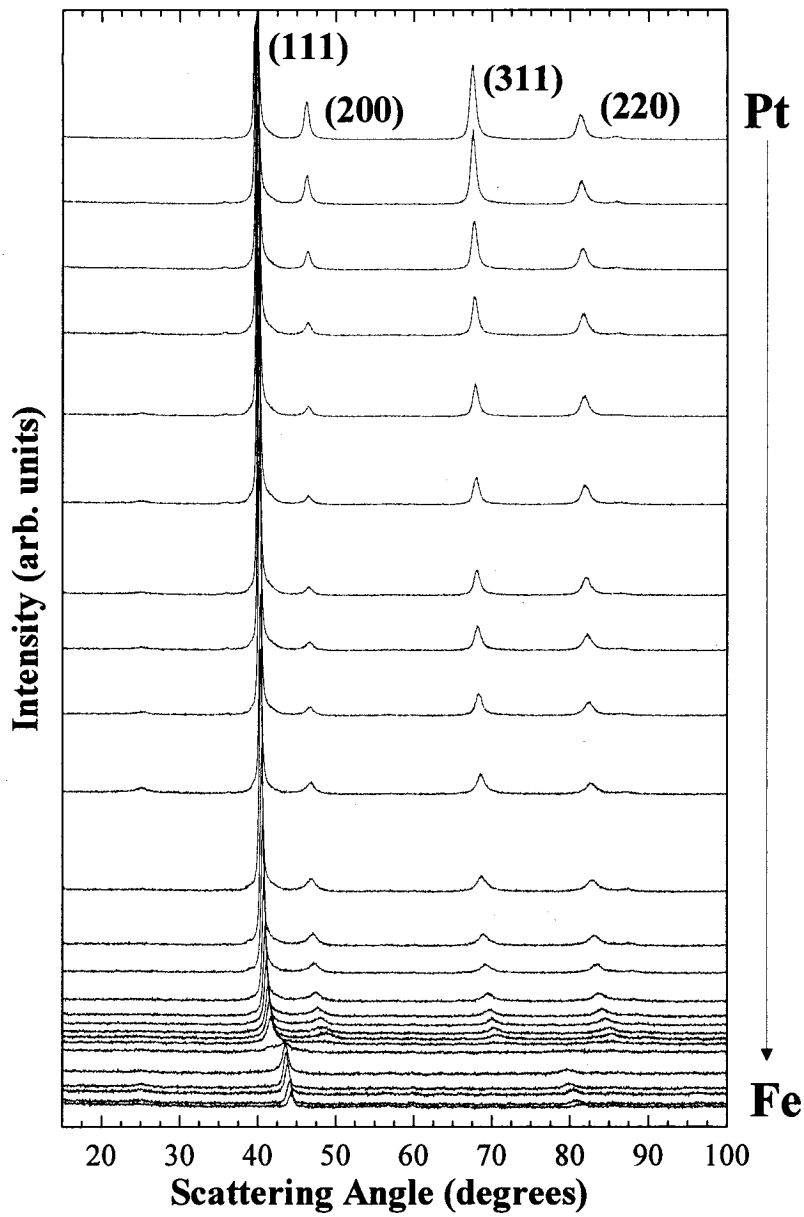

Figure 4.6 *X-ray diffraction profiles of the $Pt_{1-x}Fe_x$ film deposited on a Si wafer for the range of x shown in Figure 4.5. The top pattern corresponds to fcc Pt and bottom pattern is that of bcc Fe. Miller indices of the fcc and bcc phases are indicated.*

A detailed view of Figure 4.6 is shown in Figure 4.7. For $x < 0.7$, fcc solid solutions of $Pt_{1-x}Fe_x$ are formed. Fe atoms that have a smaller atomic radius than Pt tend to shrink the lattice as it is substituted in the fcc sites and this results in a shift of the Bragg peaks to higher angles.

At higher Fe concentrations the bcc structure forms and inclusion of Pt atoms tends to expand the bcc lattice. A co-existence of fcc and bcc phases is observed near $x \approx 0.70$.

Note that the Bragg peaks also broaden as the Fe concentration increases, indicating that the grains are getting smaller.

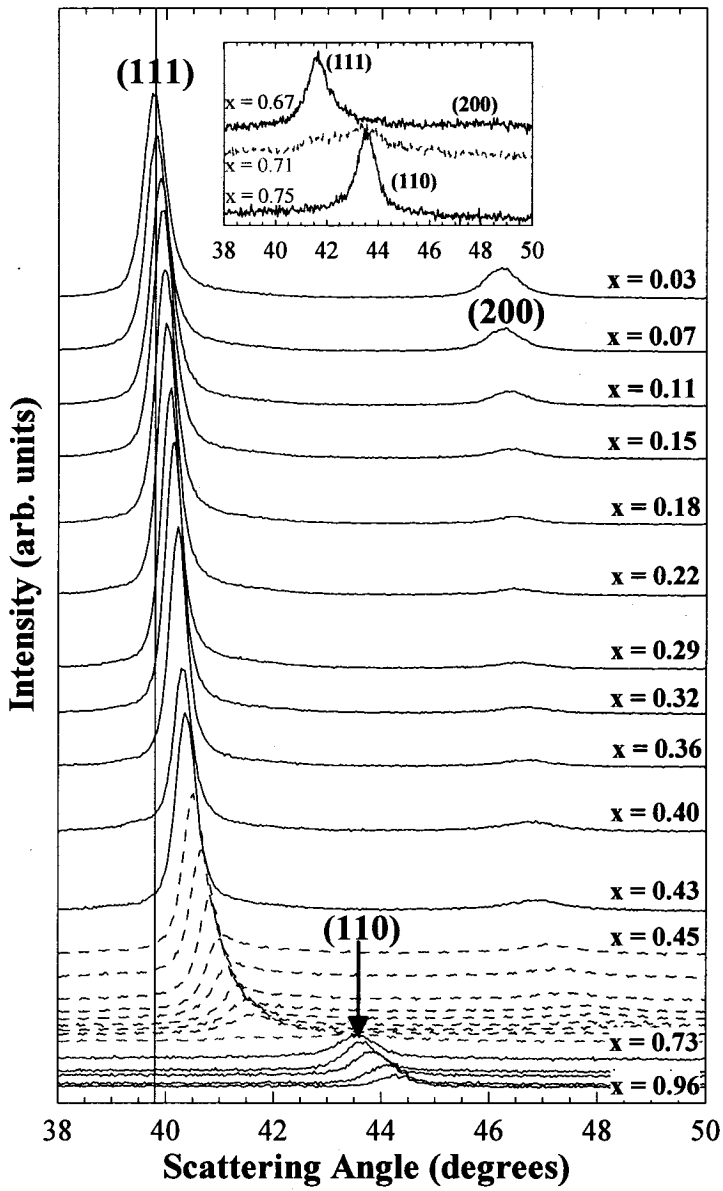

Figure 4.7 *A magnified view of the XRD patterns for the Pt-Fe binary deposited on a Si wafer shown for 38° < 2θ < 50°. x in $Pt_{1-x}Fe_x$ for each diffractogram is indicated (± 2%). A clear shift of the (111) and (200) peaks indicates that the fcc lattice shrinks as the iron content is increased. The vertical line around 2θ = 39.9° indicates the position of the platinum (111) peak. The dashed patterns show a rather faster change of lattice constant with x in $Pt_{1-x}Fe_x$. The inset shows a zoomed view of the fcc (111) and bcc (110) peaks where the fcc-bcc phase transition occurs. Two phase co-existence is observed for $x \approx 0.70$.*

The lack of any long range ordering as found in Pt_3Fe, PtFe and $PtFe_3$ phases in these films is attributed to the non-equilibrium conditions of the sputtering process.

To obtain a quantitative measure of the lattice constant versus x, the XRD peaks were fit with Lorentzian-shaped peaks and the lattice constants were calculated by averaging values obtained from several different peaks. Figure 4.8 shows the lattice constants versus x in $Pt_{1-x}Fe_x$. The variation of the fcc lattice constants versus x in $Pt_{1-x}Fe_x$ shows two different Vegard-like linear trends. The change in the lattice parameter with composition almost doubles when $x > 0.4$ i.e. a steeper slope is observed.

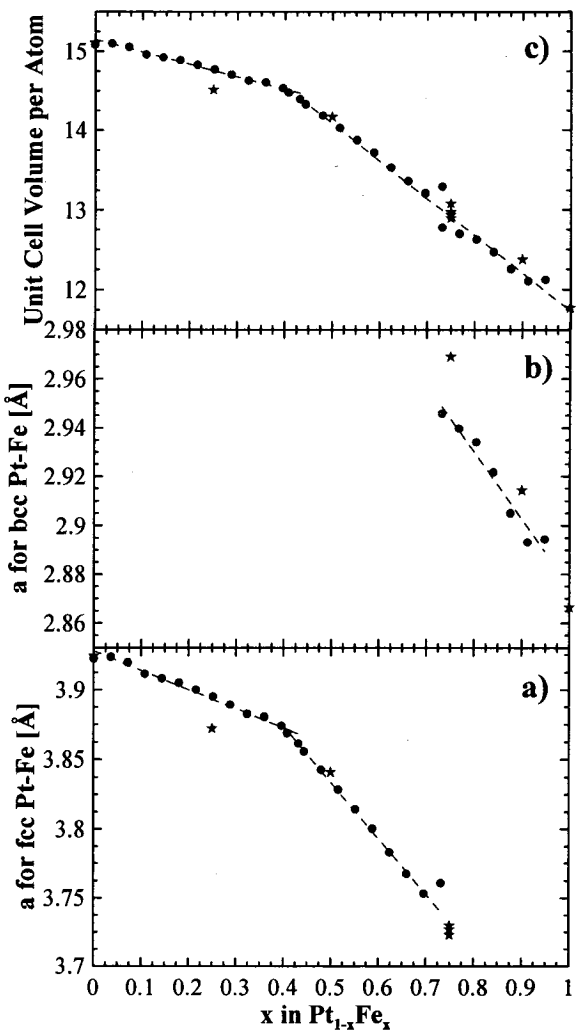

Figure 4.8 *(a) The fcc lattice constant versus x in $Pt_{1-x}Fe_x$ ($0 < x < 0.70$) deposited on a Si wafer. (b) The bcc lattice constant versus x in $Pt_{1-x}Fe_x$ for $0.72 < x < 1.0$. (c) Unit cell volume ($Å^3$) per atom for fcc and bcc cells versus x in $Pt_{1-x}Fe_x$ for $0 < x < 1.0$. In all three panels, the dashed lines are drawn as guides to eye. The stars indicate the lattice constants (a,b) and unit cell volumes (c) based on the values reported in the literature [231-233].*

The lattice parameters reported here are in good agreement with those of bulk thermodynamic $Pt_{1-x}Fe_x$ phases [231-234]. However, Toda *et al.*, who prepared PtFe

electrocatalysts by sputtering Pt and Fe on glassy substrates reported higher values of lattice constants and observed only a single linear trend for $0 < x < 0.8$ [235]. They reported values of 3.92 - 3.90 Å for $0 < x < 0.8$, whereas we observe lattice variations of 3.92 - 3.75 Å for $0 < x < 0.75$ [235]. In their case, it is possible that good intermixing (or alloying) has not occurred. Figure 4.8b also shows the bcc lattice constant *versus* x in $Pt_{1-x}Fe_x$ as well as the reported values for the equilibrium phases [236, 237]. Figure 4.8c shows that the atomic volume versus x in $Pt_{1-x}Fe_x$ varies smoothly, although there is a small discontinuity near the fcc – bcc transition.

For the $Pt_{1-x}Ni_x$ library, only single phase fcc solid solution crystallites are formed (Figure 4.9).

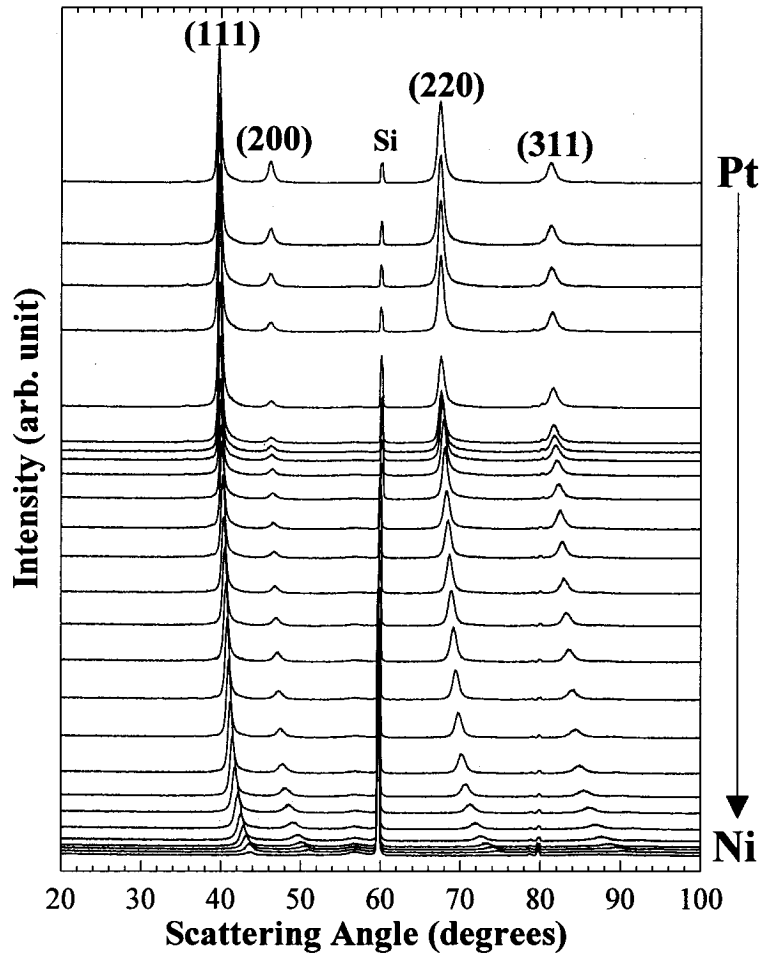

Figure 4.9 *X-ray diffraction profiles of the $Pt_{1-x}Ni_x$ film deposited on a Si wafer for the range of x shown in Figure 4.5a. The Miller indices of the Bragg peaks from the fcc phase are indicated.*

Figure 4.10 shows the movement of the (111) and (200) Bragg peaks. As for the $Pt_{1-x}Fe_x$ alloys, the Bragg peaks broaden when the Ni content increases.

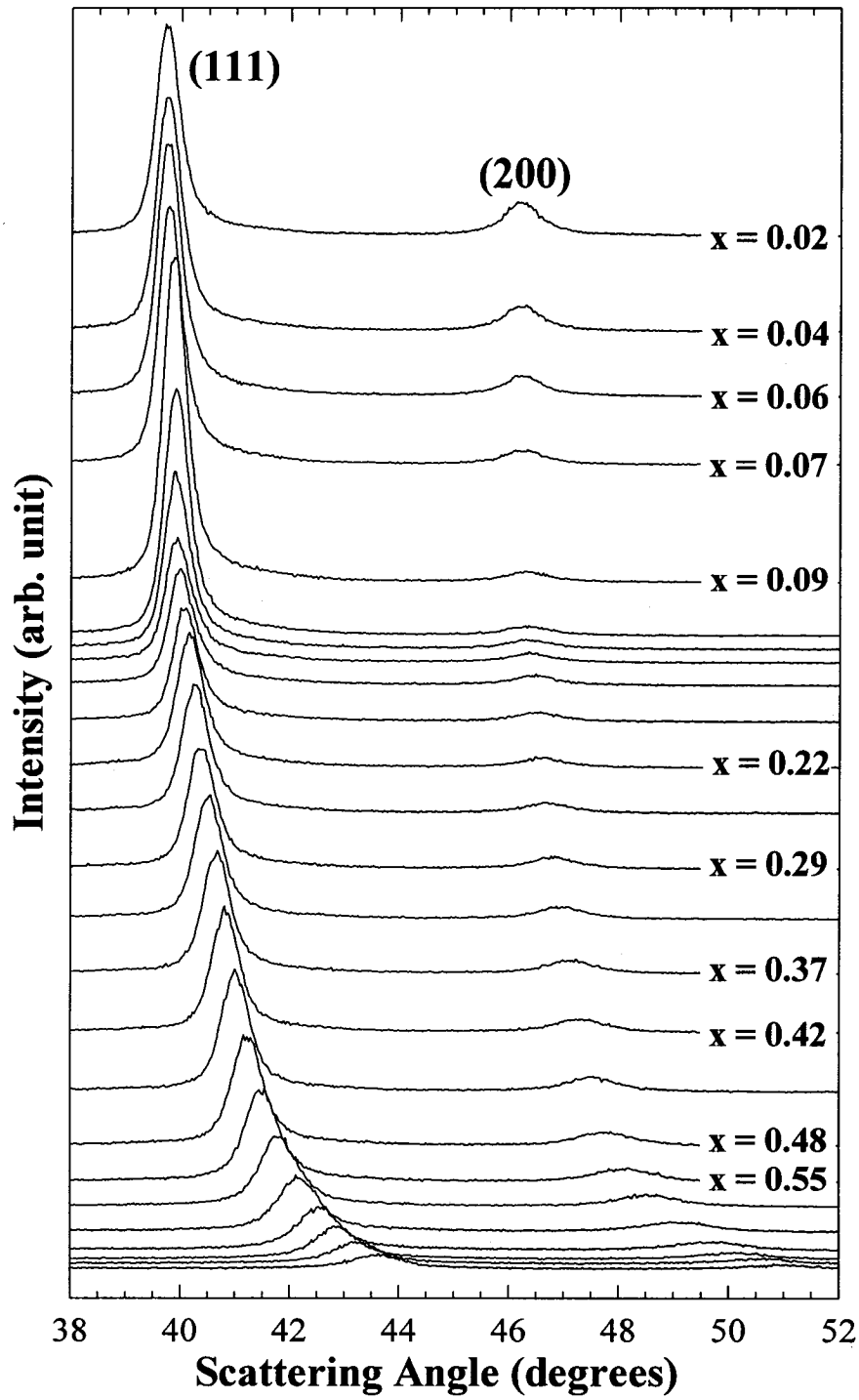

Figure 4.10 *A magnified view of the diffraction patterns of Pt-Ni binary deposited on a Si wafer for 38° < 2θ < 50°. The nickel content, or x in $Pt_{1-x}Ni_x$, is shown for selected patterns.*

Figure 4.11 shows the variation of the fcc lattice parameters for $Pt_{1-x}Ni_x$ samples studied here and the bulk sample values taken from the literature [234, 238, 239].

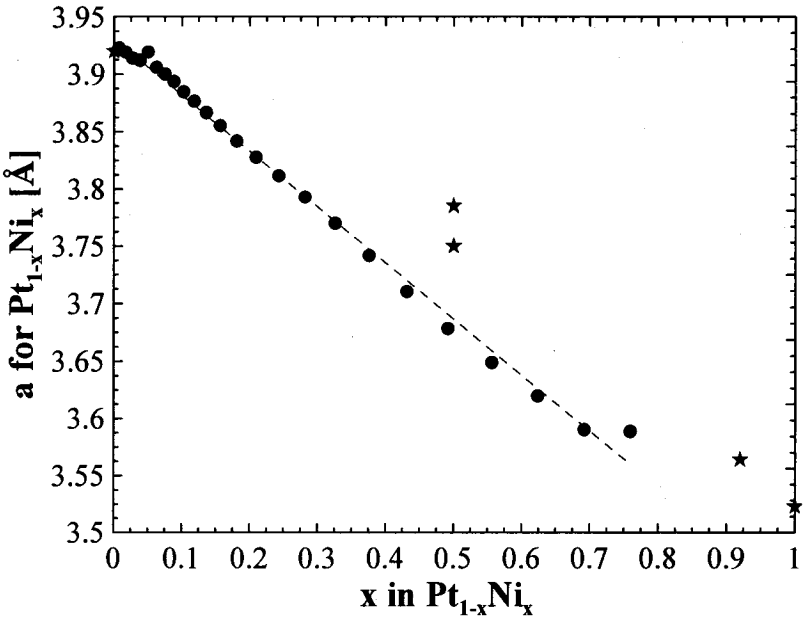

Figure 4.11 *A magnified view of the diffraction patterns of Pt-Ni binary deposited on a Si wafer for 38° < 2θ < 50°. The nickel content, or x in $Pt_{1-x}Ni_x$, is shown for selected patterns. The stars represent literature data [234, 238, 239].*

4.3.3 Morphology of $Pt_{1-x}M_x$ Electrocatalyts Sputtered on NSTF

Figure 4.12 shows an SEM image showing the typical morphology of sputtered electrocatalysts on the NSTF support. The image shown in Figure 4.12 corresponds to a composition of $Pt_{0.7}Ni_{0.3}$. Catalyst crystallites of about 10 to 15 nm size are attached to the surface of the whiskers.

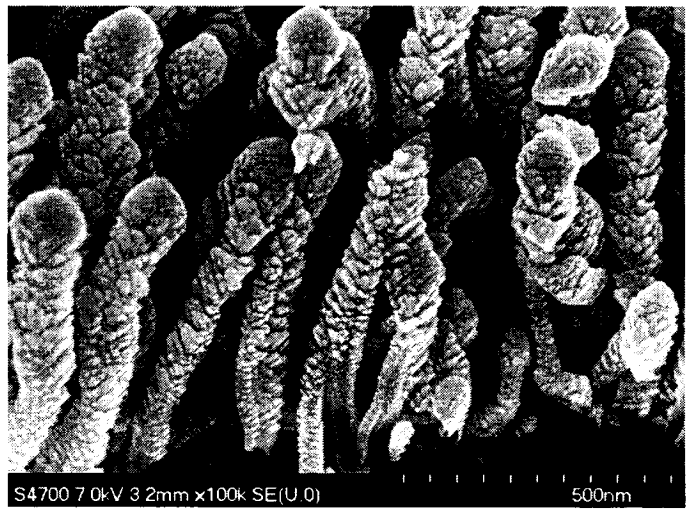

Figure 4.12 *Morphology of $Pt_{1-x}Ni_x$ library at a composition of x = 0.3.*

4.3.4 Time Dependence of Transition Metal Dissolution

The composition of the $Pt_{1-x}Fe_x$ and $Pt_{1-x}Ni_x$ electrocatalysts after exposure to different 0.3M acids at room temperature for different periods of time is shown in Figures 4.13 and 4.14, respectively. The composition was measured by electron microprobe and this represents the average of surface and bulk compositions. The results show increasing amounts of transition metal dissolution as time progresses. More transition metal is removed when x is initially larger. Composition changes at the large x end of the libraries are still occurring after 150 hours when the tests were stopped.

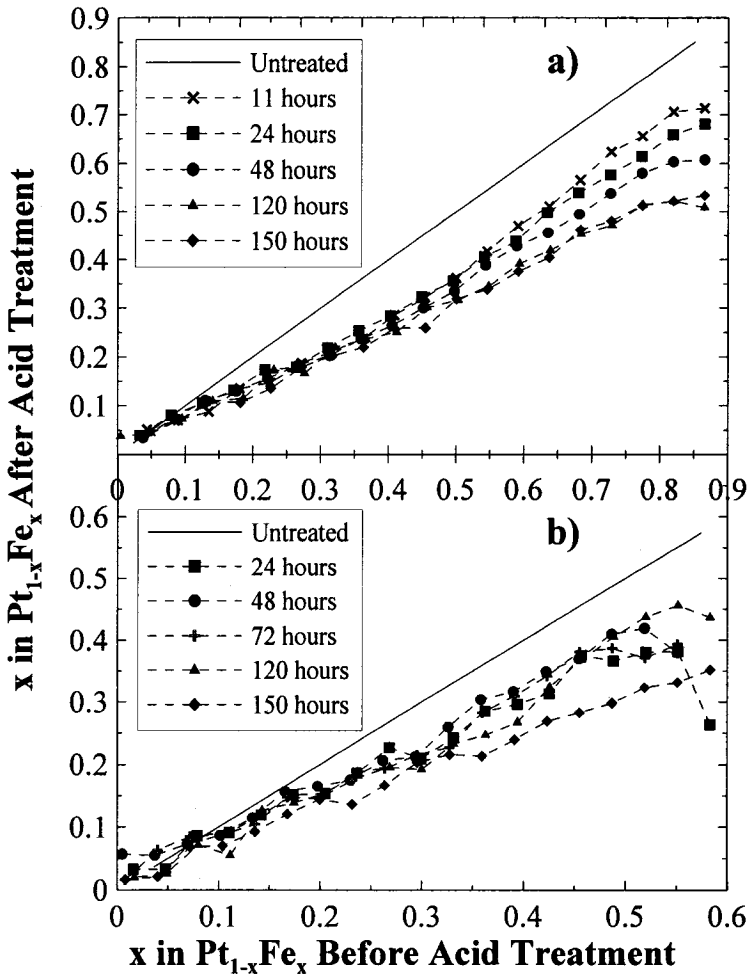

Figure 4.13 *Electron microprobe measurements of x_{after} in $Pt_{1-x}Fe_x$ for the $Pt_{1-x}Fe_x$ library deposited on NSTF substrate after soaking in acid plotted versus x_{before} in $Pt_{1-x}Fe_x$. Libraries were soaked in a) 1M H_2SO_4 and b) 0.3M H_2SO_4 for various time periods at room temperature. The straight lines in both panels depict the iron content of the untreated sample.*

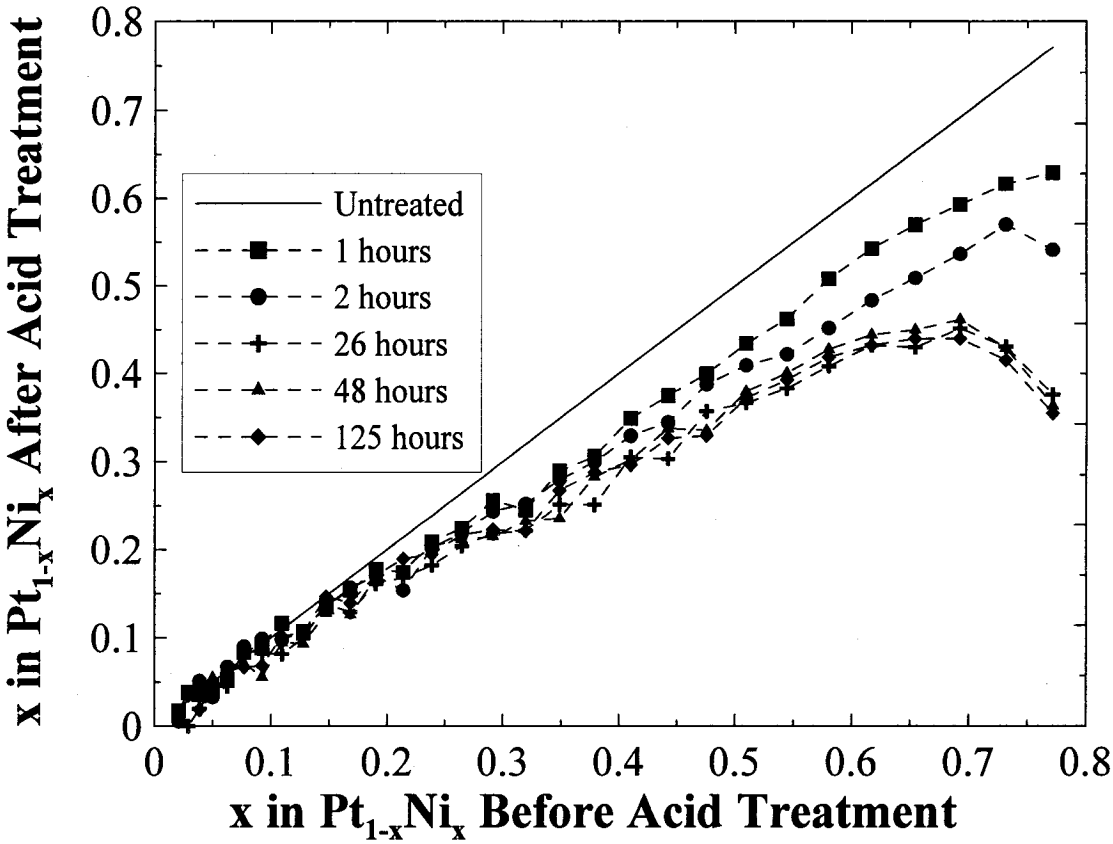

Figure 4.14 *Electron microprobe measurements of x_{after} in $Pt_{1-x}Ni_x$ for the $Pt_{1-x}Ni_x$ library deposited on NSTF substrate after soaking in acid plotted versus x_{before} in $Pt_{1-x}Ni_x$. Libraries were soaked in 0.3M $HClO_4$ for various time periods at room temperature. The straight line shows the nickel content of the untreated sample.*

The acid solution containing the above $Pt_{1-x}Fe_x$ electrocatalyst libraries were analyzed for Fe and Pt content by atomic absorption spectroscopy as a function of time. No Pt was observed in solution in any of the measurements to within our detection limit. Figure 4.15 shows the Fe concentration in the acid plotted versus time.

The dissolution rate of Fe from the alloy is initially rapid and slows at later time. It should be noted that the dissolved Fe in the solution comes from the entire $Pt_{1-x}Fe_x$ library and Figures 4.13 and 4.14 show that the dissolution rate depends on x. Nevertheless, Figure 4.15 gives an indication of the 'average' time scale of the dissolution process at room temperature. All the subsequent acid treatments were performed for a period of 10 days, where final compositions are near a steady state value.

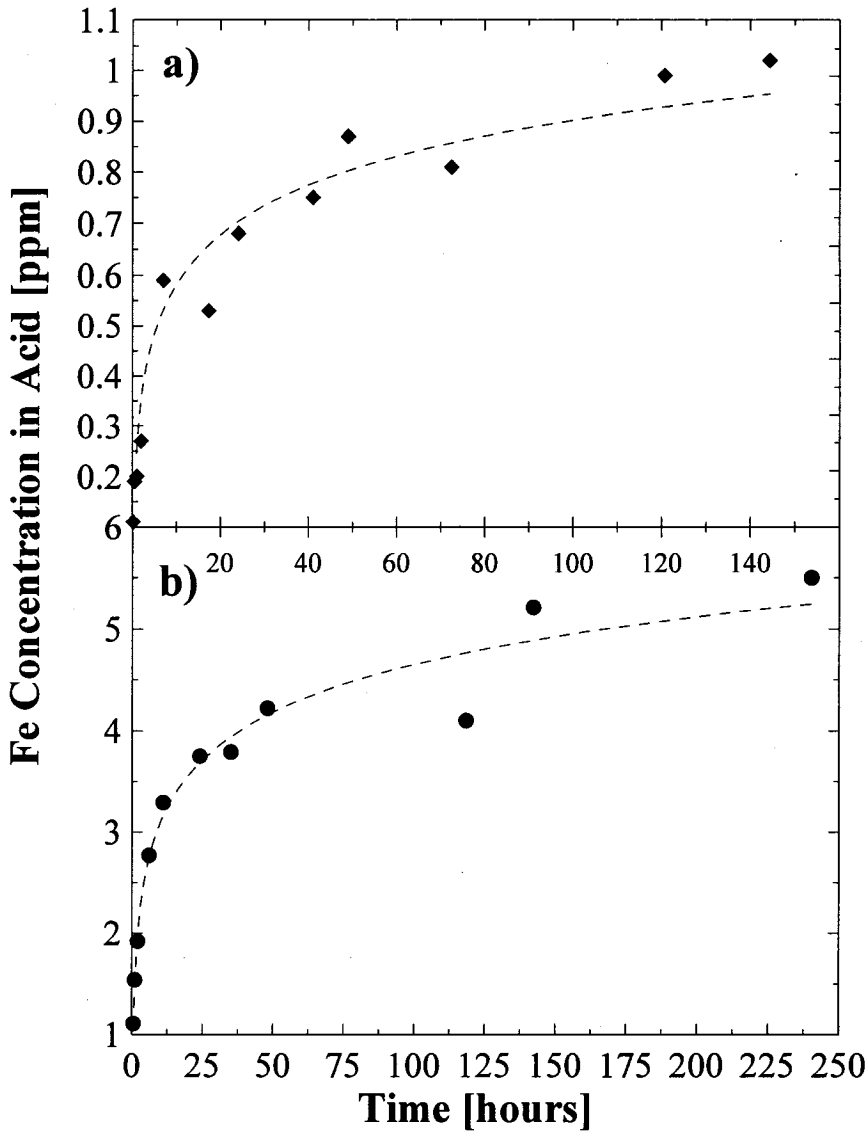

Figure 4.15 *Dissolution of iron from a $Pt_{1-x}Fe_x$ library (deposited on NSTF substrate) as a function of time for: a) 0.3M $HClO_4$ and b) 0.3M H_2SO_4 acids at room temperature obtained by atomic absorption spectrophotometry. The dashed lines are guides to the eye.*

4.3.5 Bulk Properties of As-Sputtered and Acid Treated $Pt_{1-x}Fe_x$ and $Pt_{1-x}Ni_x$ Electrocatalysts

Figure 4.16 shows the composition, x_{after}, of $Pt_{1-x}Fe_x$ catalysts after acid treatment plotted *versus* the composition, x_{before}, before acid treatment for various different conditions. The increase in temperature accelerates the rate of Fe dissolution and has a more pronounced effect than the acid concentration.

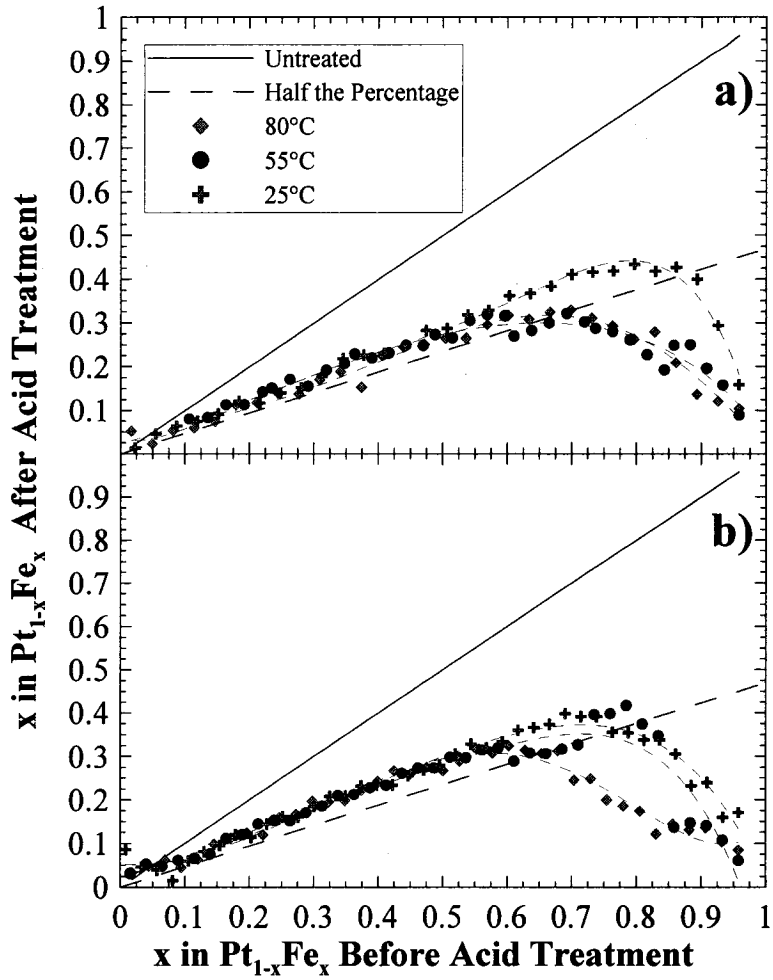

Figure 4.16 *x_{after} in $Pt_{1-x}Fe_x$ of the $Pt_{1-x}Fe_x$ library (deposited on NSTF substrate) plotted versus x_{before} in $Pt_{1-x}Fe_x$ after a 10 day soaking in: (a) 0.3M and (b) 1M H_2SO_4 acid. The soakings were made at 25, 55 and 80°C as indicated. The straight lines indicate the composition of an untreated sample and the dashed lines show a 50% reduction in x and are drawn to guide the eye. The measurements were performed by electron microprobe.*

In all cases, the post-acid Fe atomic fraction for $x_{before} < 0.6$, is slightly higher than one half of the original Fe atomic fraction. The effect of temperature on the dissolution of Fe for $x_{before} < 0.6$ seems to be weak. The maximum amount of Fe in the films after acid treatment at 80°C occurs at $x_{before} = 0.6$ and is about $x_{max} = 0.3$. For $x_{before} > 0.6$, x_{after} does not remain at about 0.3, but decreases strongly.

Figure 4.17 shows the composition, x_{after}, of $Pt_{1-x}Fe_x$ catalysts after treatment in 0.3M and 1M $HClO_4$ solutions plotted versus the initial composition, x_{before}. Again, as in the sulfuric acid treatments at 80°C, the maximum amount of Fe in the samples after treatment at 80°C is about $x_{max} = 0.3$ and occurs at $x_{before} = 0.6$. The data for 55°C and

80°C are quite similar to those made at the same temperatures in H_2SO_4, however the room temperature data show only a small amount of Fe dissolution at large x_{before}.

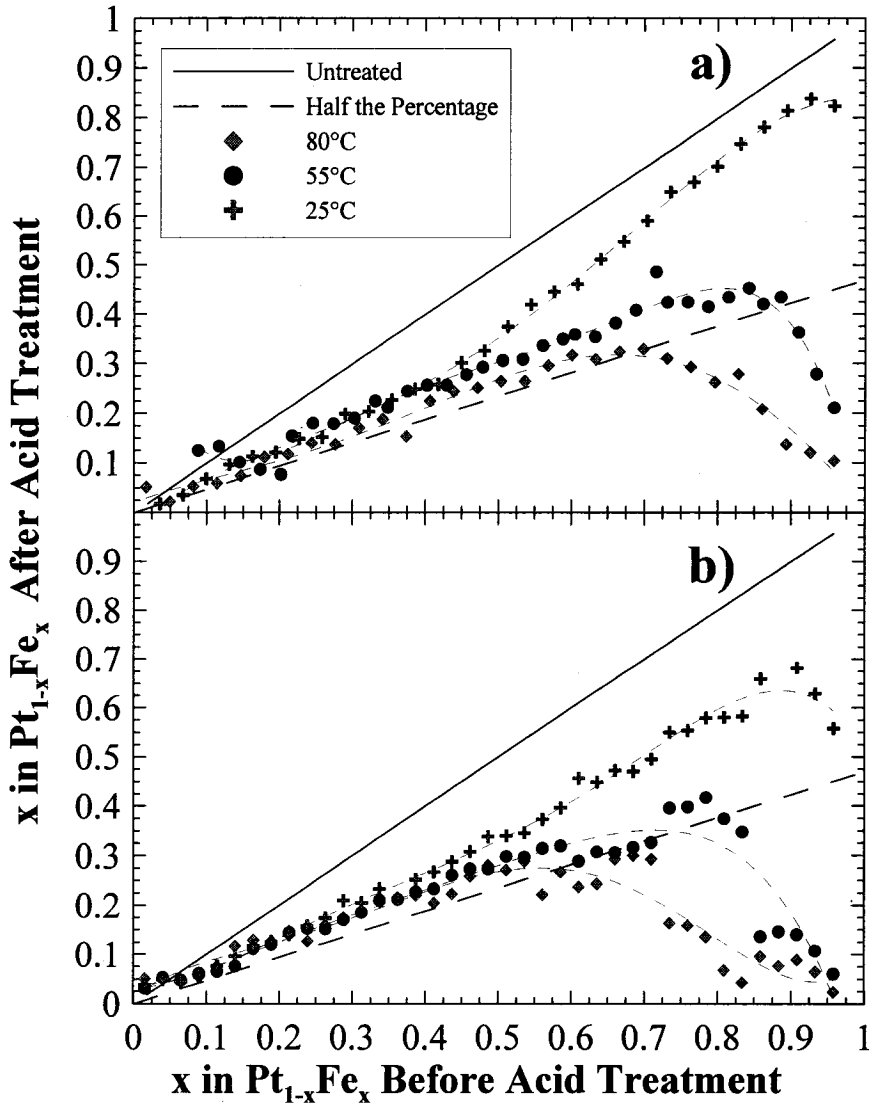

Figure 4.17 *x_{after} in $Pt_{1-x}Fe_x$ of the $Pt_{1-x}Fe_x$ library (deposited on NSTF substrate) plotted versus x_{before} in $Pt_{1-x}Fe_x$ after a 10 day soaking in: (a) 0.3M and (b) 1M $HClO_4$ acid. The soakings were made at 25, 55 and 80°C as indicated. The straight lines indicate the composition of an untreated sample and the dashed lines show a 50% reduction in x and are drawn to guide to the eye. The measurements were performed by electron microprobe.*

This suggests that removal of Fe from the bulk of $Pt_{1-x}Fe_x$ alloys proceeds very slowly, if at all, in $HClO_4$ at room temperature.

Figure 4.18 shows XRD patterns taken on the $Pt_{1-x}Fe_x$ library deposited on the PR whiskers on the polyimide film before acid treatment. The polyimide support was

mounted on a flat aluminum block with two-sided tape for measurement. The polyimide and the tape are transparent enough to X-rays to allow the Al (111) Bragg peak of the

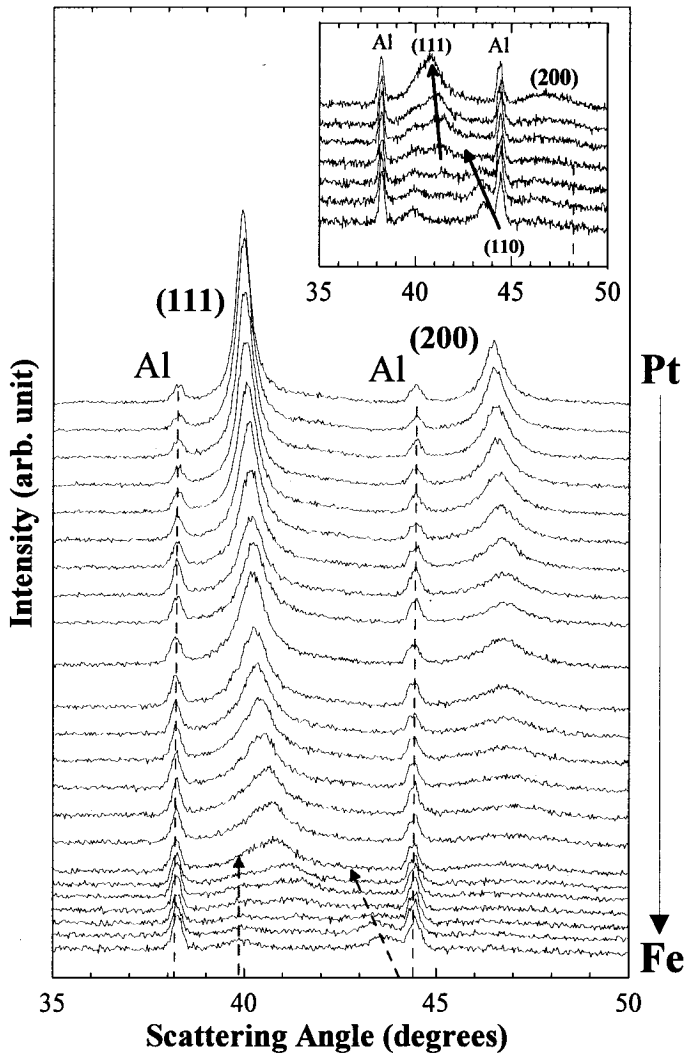

Figure 4.18 *X-ray diffractograms of an untreated $Pt_{1-x}Fe_x$ library deposited on the nano-structured PR whiskers are shown for $38° < 2\theta < 50°$. The top pattern corresponds to platinum and the iron content of the films gradually increases towards the bottom. The aluminum peaks are due to the sample holder. The right and left arrows indicate the Pt reference layer in the substrate and the bcc phase of Pt-Fe alloy, respectively. The inset shows details (bcc→fcc transition) of the lower six diffraction patterns.*

block to be observed. This Al peak serves as a reference peak. The patterns in Figure 4.18 reveal the same structures and phases that we saw earlier for the same library deposited on Si wafer substrates (see Figure 4.6). The fcc structure is present for $x < 0.7$ and a bcc phase is present for $x > 0.7$. A small weak peak near 39.8^{o} (indicated with a vertical arrow) originates from a thin Pt reference layer.

Figure 4.19 shows the XRD patterns taken on the same $Pt_{1-x}Fe_x$ library after treatment in 1M H_2SO_4 at 80°C for 10 days. Comparing Figures 4.18 and 4.19 we observe that the (110) peaks of the bcc phase have disappeared and the (111) fcc peak shifts to lower scattering angles for compositions with $x_{before} > 0.6$. The shift to lower scattering angle indicates that the lattice constant is increasing for $x_{before} > 0.6$, which is explained by Fe being removed from the bulk of the alloy (for $x_{before} > 0.60$).

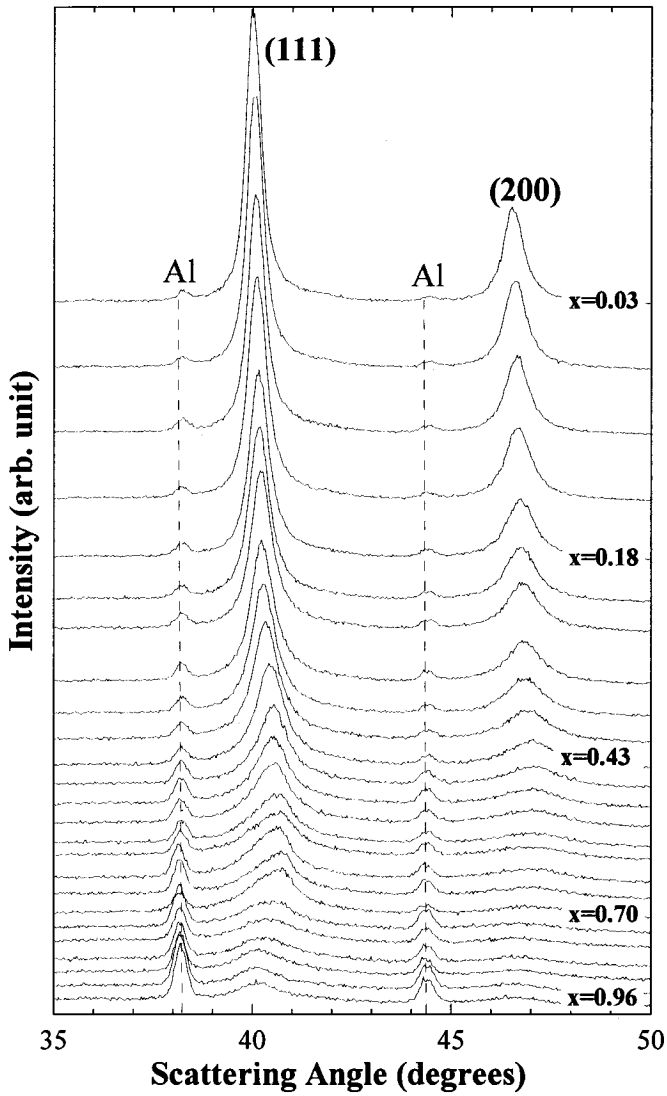

Figure 4.19 *X-ray diffractograms of an acid treated (1M H_2SO_4 at 80°C) $Pt_{1-x}Fe_x$ library deposited on nano-structured PR whiskers are shown for $38° < 2\theta < 50°$. The fcc (111) peak for $x_{before} > 0.6$ has shifted to lower angles compared to the patterns shown in Figure 4.18* and *the bcc $Pt_{1-x}Fe_x$ phase is absent. The values of x_{before} for representative scans are shown in the figure.*

Figure 4.20 shows the XRD patterns taken on the same $Pt_{1-x}Fe_x$ library after treatment in 1M $HClO_4$ at room temperature for 10 days. The bcc Fe-Pt phase can still be easily

seen and the shift of the (111) peaks of the fcc phase are much smaller than observed in Figure 16. This suggests that very little Fe is removed from the bulk of $Pt_{1-x}Fe_x$ alloys by treatment in $HClO_4$ at 25°C.

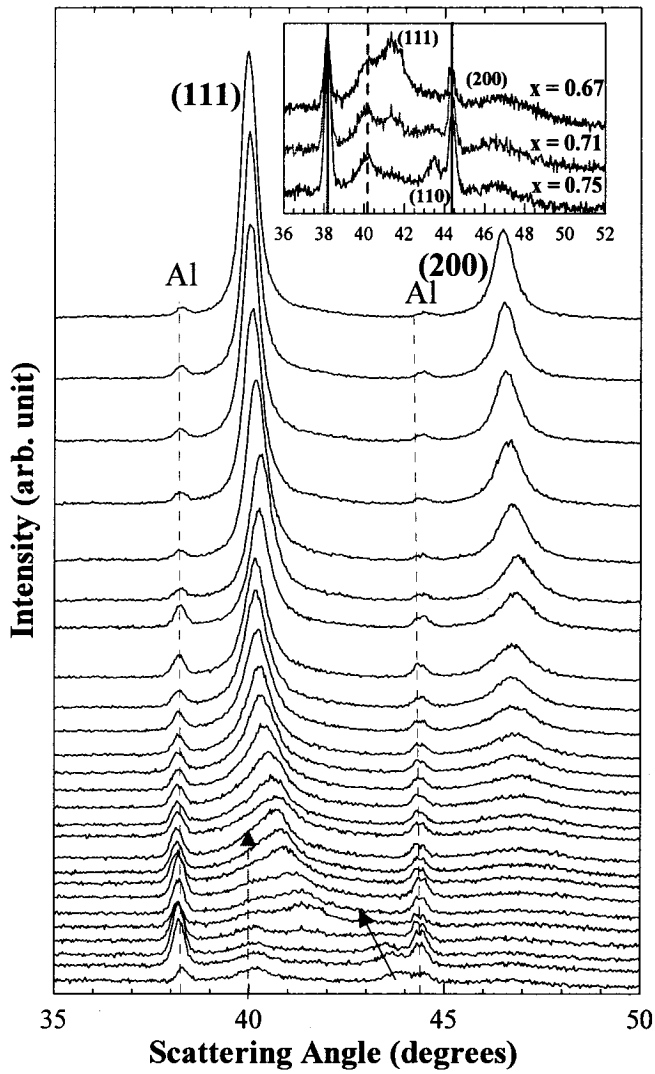

Figure 4.20 *X-ray diffractograms of an acid treated (1M $HClO_4$ at 25°C) $Pt_{1-x}Fe_x$ library deposited on the nano-structured PR whiskers are shown for 38° < 2θ < 50°. The top pattern corresponds to platinum and iron content of the films gradually increases towards the bottom. The values of x_{before} for representative scans are shown in the figure. The right and left arrows indicate the Pt reference layer in the substrate and the bcc phase of Pt-Fe alloy, respectively. The inset shows the fcc-bcc transition region.*

Figure 4.21 shows the lattice constants of the $Pt_{1-x}Fe_x$ electrocatalysts as a function of position in the library before and after acid treatment for a number of conditions. The data shown in Figure 4.21 can be broadly grouped into two regions. For $x_{before} < 0.6$, the difference between the lattice constant of treated and untreated samples is rather

negligible, whereas for $x_{before} > 0.6$, there is a much larger change in the lattice constant caused by the acid treatment. For $x_{before} < 0.6$ or so, Fe dissolves primarily from the surface, so the lattice constants do not change, however at higher Fe concentrations a larger change in the lattice constant indicates that more Fe is dissolving from the bulk of grains.

The value of $x > 0.6$, where the lattice constants of samples treated in acid at high temperature begin to differ from their untreated values, is also the composition that corresponds to the peak Fe content observed in microprobe results for samples treated in acid at 80°C presented in Figures 4.16 and 4.17. This suggests that the downturn of the data in Figures 4.16 and 4.17 for $x > 0.6$ is caused by the removal of Fe from the bulk of the electrocatalyst particles.

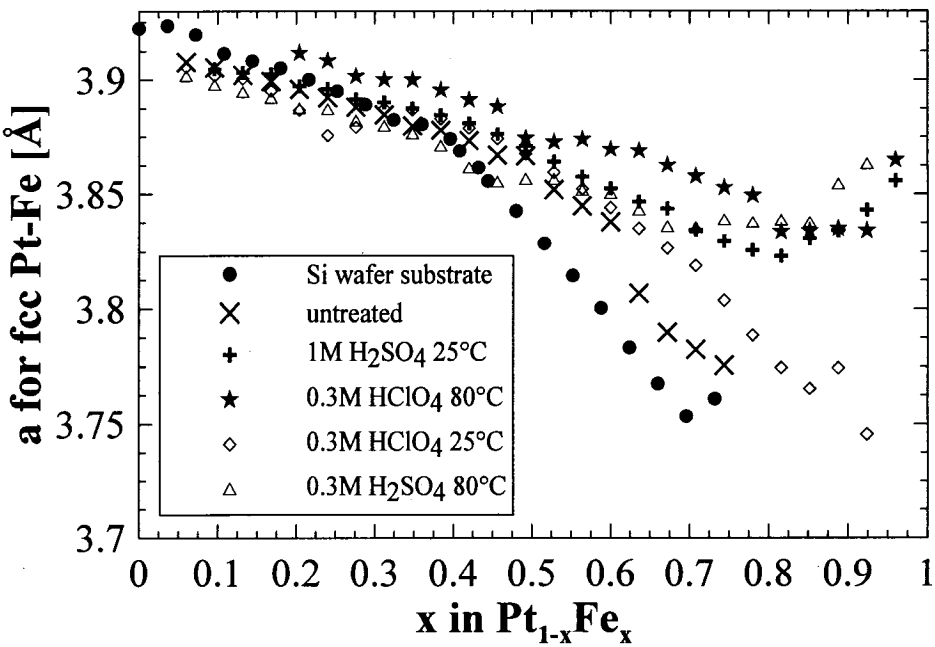

Figure 4.21 *Variation of lattice constants versus x_{before} in $Pt_{1-x}Fe_x$ (deposited on Si or NSTF) for acid treated $Pt_{1-x}Fe_x$ libraries. Note that the lattice constants of the acid treated samples differ from the untreated sample for $x_{before} > 0.5$ in $Pt_{1-x}Fe_x$.*

Similar trends, that is bulk and surface dissolution for $x > 0.6$ and mostly surface dissolution for $x < 0.6$ were observed in dissolution of Ni in the Pt-Ni libraries. These data are reported elsewhere [113].

4.3.6 Surface Composition of $Pt_{1-x}Ni_x$ Films after Acid Treatment

Figure 4.22 shows three selected XPS spectra of $Pt_{1-x}Ni_x$ (x = 0.01, 0.4 and 0.8) films deposited on NSTF substrates. Before acid treatment Ni 2p peaks can easily be observed, whereas after acid treatment no Ni can be detected. Figure 4.23 shows the surface composition, x in $Pt_{1-x}Ni_x$, as measured by XPS, versus position in the untreated library prepared on the PR whiskers. For comparison, the bulk composition, x in $Pt_{1-x}Ni_x$, versus position for the same library as measured by electron microprobe is also given in the Figure.

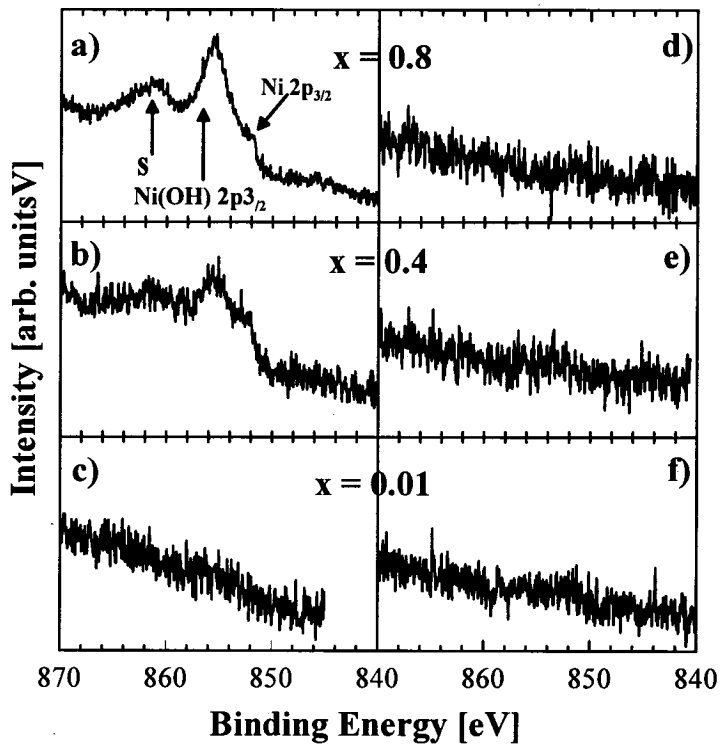

Figure 4.22 *Selected XPS spectra of $Pt_{1-x}Ni_x$ films deposited on NSTF substrate. x corresponds to the bulk composition of the as-deposited (a-c) and acid (H_2SO_4 at 80°C for 10 days) treated (d-f) films. All the peaks are labeled. The shakeup peak is labeled S.*

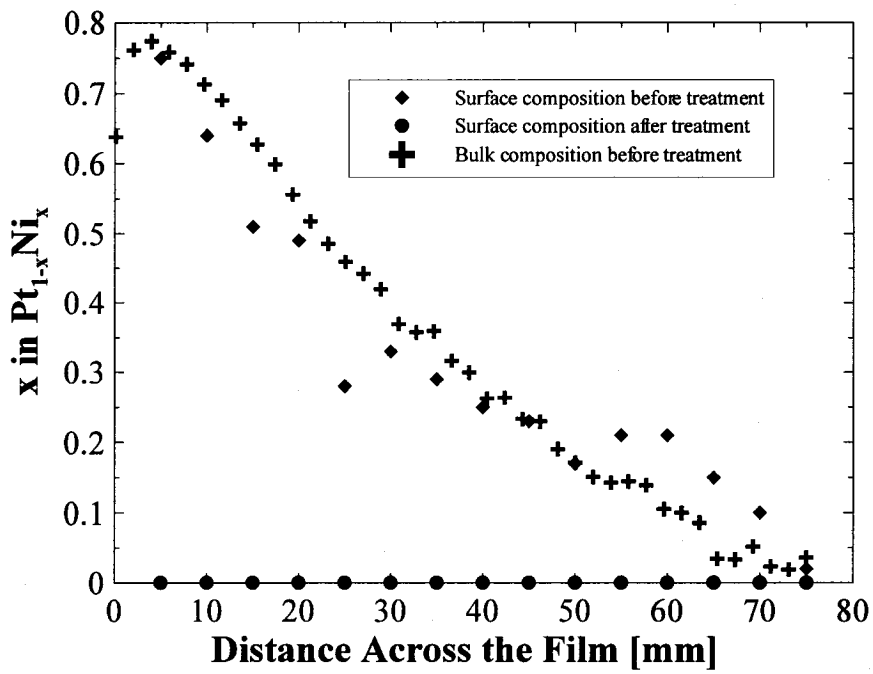

Figure 4.23 *Surface composition (XPS) and bulk composition (electron microprobe) of the $Pt_{1-x}Ni_x$ library prepared on NSTF substrate versus position on the library. The data points after acid treatment (H_2SO_4 at 80°C for 10 days) show no evidence for the presence of surface Ni atoms at any point in the library.*

The sampling depth for Ni atoms is estimated to be about 3 nm. The surface composition of the film is similar to that of the bulk. However, after the H_2SO_4 treatment at 80°C for 10 days, Figure 4.22 shows that XPS failed to detect any signal from Ni for all starting bulk compositions, x_{before} in $Pt_{1-x}Ni_x$. These results show that Ni atoms are removed from the first 3 nm of the surface layers. According to the width of the (111) Bragg peaks of the $Pt_{1-x}Ni_x$ library, the grain size of the electrocatalyst is about 12 nm. Removal of Ni to a depth of at least 3 nm represents removal of all surface Ni atoms.

4.4 $Pt_{1-x-y}M_xM_y$' (M, M' = Co, Ni, Mn, Fe) Libraries

The libraries that are discussed in this section are of two types: *Type I*: $Pt_{1-x}M_x$ or $Pt_{1-x}[M_yM'_{1-y}]_x$ where a constant thickness Pt layer alternates with a wedge shaped layer of transition metal M or metals $M_yM'_{1-y}$ with y constant throughout the library (Libraries 1 - 6) and *Type II*: $Pt_{1-x}[M_yM'_{1-y}]_x$ where constant thickness layers of Pt were modulated by mixed compositionally graded layers of $M_yM'_{1-y}$. In Type II libraries, x was kept approximately constant and y varied between 0 and 1 (Libraries 7 - 12). A schematic diagram of these two types of libraries, showing only the first two bilayers, is shown in

Figure 4.24. To fabricate a Type I library (Figure 4.24a) the sputtering table rotated slowly (1 rpm) and the target powers were adjusted so as to deposit the desired thickness of Pt and M or $M_yM'_{1-y}$ during each pass of the library under the sputtering targets. To grow the Type II libraries, where M and M' were homogeneously mixed (Figure 4.24b), a rapid table rotation (10 rpm or higher) was needed.

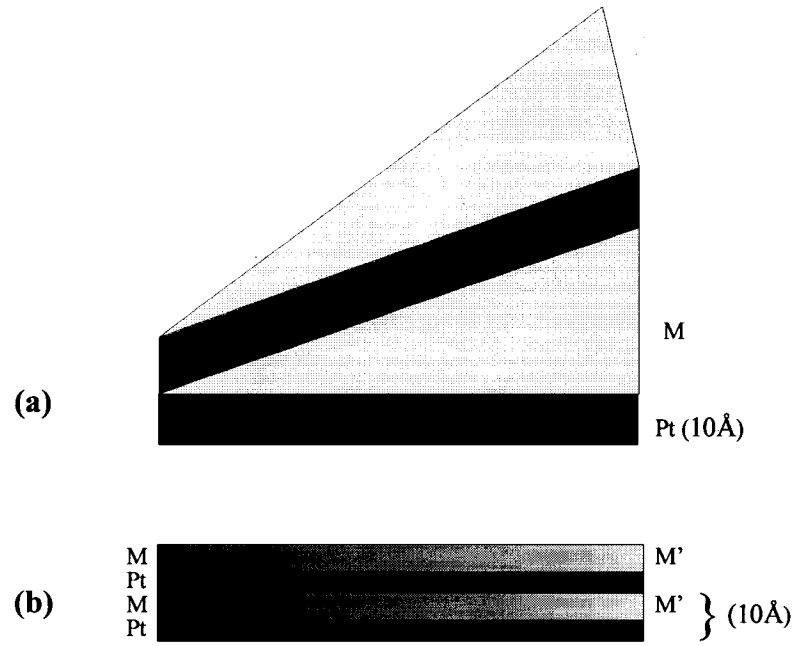

Figure 4.24 *Fabrication of the Type I: $Pt_{1-x}M_x$ or $Pt_{1-x}[M_yM'_{1-y}]_x$ and Type II: $Pt_{1-x}[M_yM'_{1-y}]_x$ libraries. a) In the Type I libraries, constant thickness layers of Pt are separated by layers of transition metal M, or $M_yM'_{1-y}$ (with y constant), which vary linearly in thickness. b) In the Type II libraries constant thickness Pt layers alternate with constant thickness $M_yM'_{1-y}$ ($0 \leq y \leq 1$) layers, where M and M' vary linearly in thickness in opposite directions. The shading in the figure is an indication of the variations in the composition. For the Type II libraries, the bilayer thickness was kept at about 10 Å, however, the ratio of Pt to transition metals (Pt : M + M') was varied in different libraries (see Table 4.1).*

The machine software was altered to allow for turning the plasma power sources ON or OFF as desired during the growth. The films prepared and studied here are summarized in Table 4.1.

The total thickness of Pt was 500 Å in all libraries. The total number of bilayers was chosen to obtain the desired film compositions in each library. For example in the Type II libraries, the number of bilayers were about 60, 80 and 120 for x = 0.3, 0.5 and 0.7, respectively. Thus the total film thickness, on flat Si wafer substrates, were

approximately about 600, 800 and 1200 Å, assuming bulk densities for all the deposited metals.

Table 4.1 *Summary of the films deposited.*

Library	*Sample ID*	*Type*	*Composition*	*Figures*
1	SPI4	I	$PtMn_x$ $(0 \le x \le 3)$	**4.24, 4.28, 4.34, 4.36**
2	SPI84	I	$Pt_{1-x}Ni_x$ $(0 \le x \le 1)$	**4.36**
3	SPI44	I	$Pt_{1-x}Fe_x$ $(0 \le x \le 1)$	**4.36**
4	SPI24	I	$Pt_{1-x}[Mn_{0.375}Fe_{0.625}]_x$, $(0 \le x \le 0.75)$	**4.29, 4.33, 4.34, 4.37**
5	SPI40	I	$Pt_{1-x}[Mn_{0.167}Fe_{0.833}]_x$, $(0 \le x \le 0.75)$	**4.38**
6	SPI42	I	$Pt_{1-x}[Mn_{0.5}Ni_{0.5}]_x$, $(0 \le x \le 0.75)$	**4.39**
7	SPI139	II	$Pt_{0.7}[Co_{1-y}Ni_y]_{0.3}$ $(0 \le y \le 1)$	**4.31, 4.34, 4.35, 4.40**
8	SPI134	II	$Pt_{0.5}[Co_{1-y}Ni_y]_{0.5}$ $(0 \le y \le 1)$	**4.31, 4.34, 4.35**
9	SPI133	II	$Pt_{0.3}[Co_{1-y}Ni_y]_{0.7}$ $(0 \le y \le 1)$	**4.31, 4.24, 4.27, 4.28, 4.30, 4.35, 4.41**
10	SPI140	II	$Pt_{0.7}[Co_{1-y}Mn_y]_{0.3}$ $(0 \le y \le 1)$	**4.32, 4.34, 4.35, 4.40**
11	SPI141	II	$Pt_{0.5}[Co_{1-y}Mn_y]_{0.5}$ $(0 \le y \le 1)$	**4.32, 4.34, 4.35, 4.40**
12	SPI143	II	$Pt_{0.3}[Co_{1-y}Mn_y]_{0.7}$ $(0 \le y \le 1)$	**4.25, 4.32, 4.34, 4.35, 4.41**

The stoichiometries are ideal. The actual film compositions, in some case, were slightly different. The actual compositions obtained by electron microprobe data are shown in the figures.

Superlattice structures (i.e. layered structures) were produced in the libraries deposited on the Si wafer substrates, but random alloys were the result of the depositions on the NSTF substrates. This is because the NSTF films have a surface area about 15 times the geometric surface area so a 1 nm layer deposited on a smooth planar surface is less than a monolayer thick on the NSTF support. Therefore, alternating 1 nm layers of Pt and M give a superlattice structure when deposited on smooth Si, but a random alloy when deposited on the NSTF substrates as the XRD patterns will show.

4.4.1 Composition and Structure of the Libraries

Figure 4.25 shows the composition variation versus position for examples of Type I and Type II libraries.

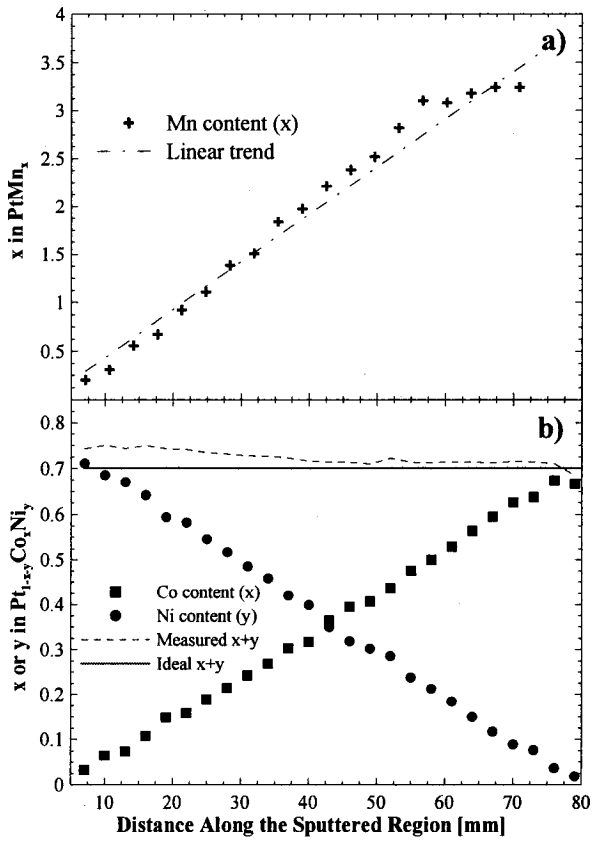

Figure 4.25 *Composition of films described in Figure 1 along the sputtered region as obtained by electron microprobe. a) Type I library: the intended composition variation was achieved for $PtMn_x$ ($0 \leq x \leq 4$) Library 1. b) Type II library: the composition of $Pt_{1-x-y}Co_xNi_y$ Library 9 along the sputtered region. The measured transition metal content, $x + y$, is close to the desired value everywhere in the library. Both libraries shown here were prepared on Si wafers.*

Figure 4.25a shows the linear variation of Mn content in $PtMn_x$ along the film and Figure 4.25b shows the opposing linear changes in Co and Ni content in $Pt_{1-x-y}Co_xNi_y$ for libraries deposited in Si wafer substrates.

The variation in the composition of the films with position on the NSTF and Si wafer substrate libraries is similar. Figure 4.26 shows the composition of $Pt_{1-x}[Co_{1-y}Mn_y]_x$ ($x = 0.7, 0.5$; $0 \leq y \leq 1$) Libraries 11, 12 and $Pt_{1-x}[Mn_{0.375}Fe_{0.675}]_x$ ($0 \leq x \leq 0.75$) Library 4 deposited on the NSTF support and on the Si wafer. The agreement between the compositions of the libraries deposited on the two different substrates is very good.

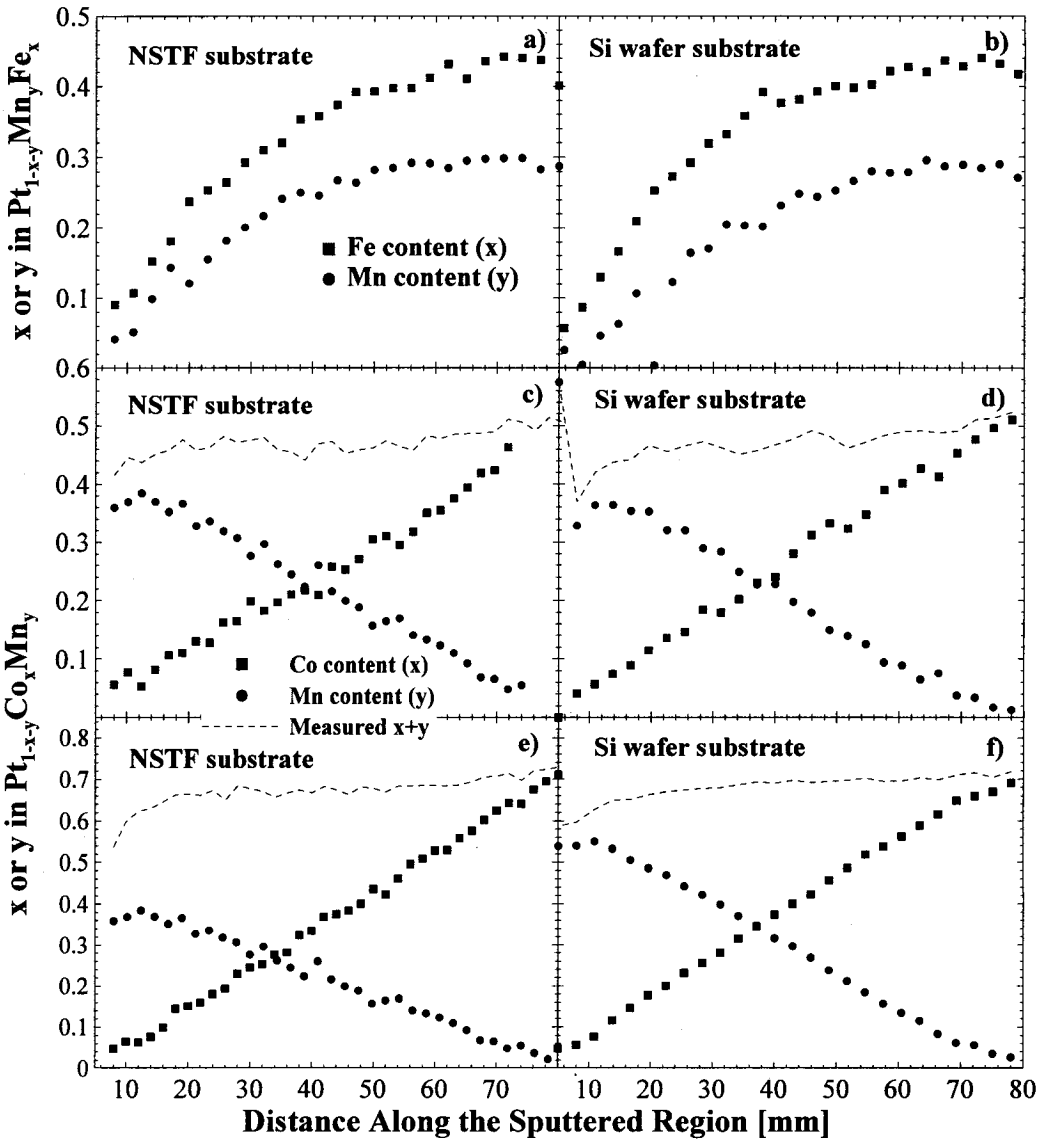

Figure 4.26 *Composition of several libraries as measured on NSTF (a, c, e) and Si wafer (b, d, f) substrates. The compositions of the films deposited on the two different substrates are in good agreement.*

The crystal structure of these combinatorial films depends on the choice of substrate used to grow the films and can be determined by small angle and wide angle X-ray diffraction. Figures 4.26 and 4.27 show the measured low-angle superlattice peaks observed for $PtMn_x$ ($0 \leq x \leq 3$) Library 1 and $Pt_{0.3}[Co_{1-y}Ni_y]_{0.7}$ ($0 \leq x \leq 1$) Library 9 deposited on a Si wafer substrate, respectively. In Figure 4.27, the movement of the diffraction peaks to lower scattering angles indicates that the thickness of the bilayers is

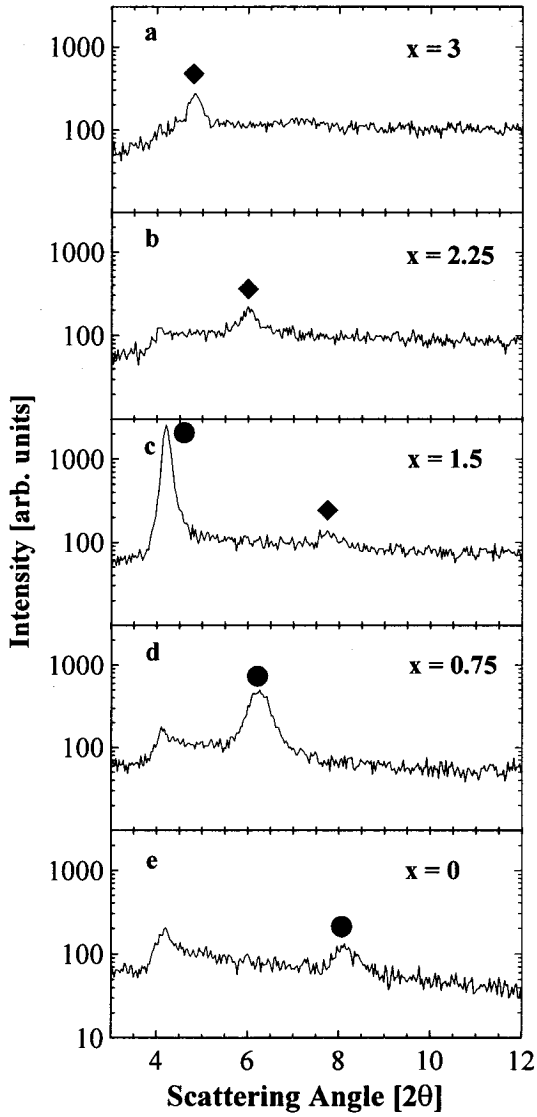

Figure 4.27 *Small angle X-ray diffraction pattern of selected positions of $PtMn_x$ Library 1 deposited on Si wafer. Movement of the superlattice peaks to lower scattering angles indicates that the bilayer thickness is increasing. The diffraction patterns were taken at equal intervals along the library. The corresponding composition for each pattern (x in $PtMn_x$) is indicated on the plot. Filled circles and diamonds denote the first and second reflection orders, respectively.*

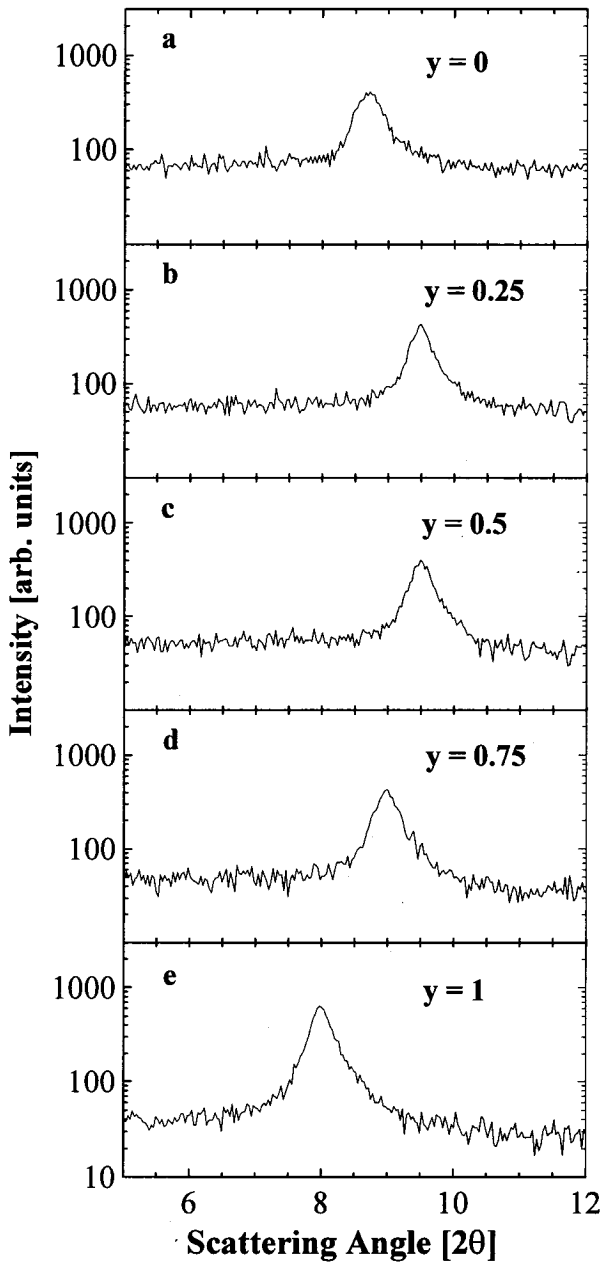

Figure 4.28 *Small angle X-ray diffraction pattern of selected positions of* $Pt_{0.3}[Co_{1-y}Ni_y]_{0.7}$ *Library 9 deposited on a Si wafer, with y values indicated on the plot. The superlattice peak is nearly stationary across the library.*

increasing as the Mn content increases, as expected based on Figure 4.24a. Figure 4.28 shows that the superlattice peaks measured for $Pt_{0.3}[Co_{1-y}Ni_y]_{0.7}$ ($0 \leq y \leq 1$) Library 9 are almost stationary, i.e. the bilayers have constant thickness across the sample, as expected based on Figure 4.24b. Using the Bragg law, the superlattice periodicities versus position

for these two libraries were determined and are shown in Figure 4.29. Similar superlattice peaks were observed in all other libraries deposited on Si wafers.

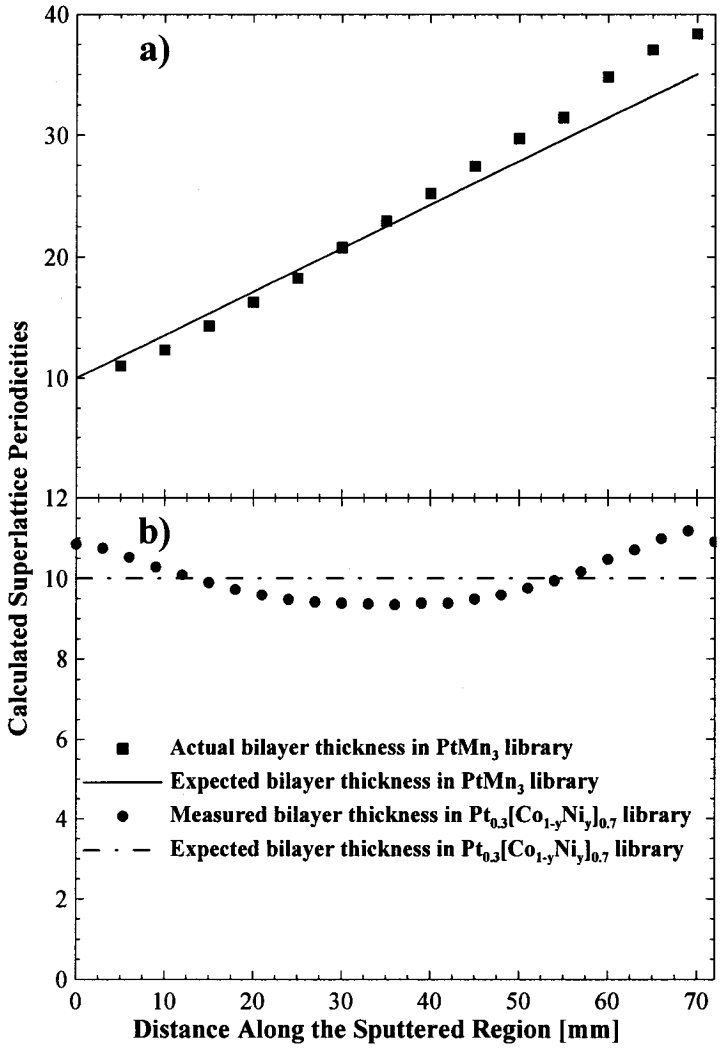

Figure 4.29 *Bilayer (Pt - metal) thickness of Type I $PtMn_x$ Library 1 and Type II $Pt_{1-x-y}Mn_xCo_y$ Library 9 obtained from small angle scattering (SAX). Both libraries shown here were prepared on Si wafer substrates. The linear increase of the bilayer thickness of the $PtMn_x$ film is shown in (a)* and *the nearly constant bilayer thickness of $Pt_{1-x-y}Mn_xCo_y$ is shown in (b). The agreement between the expected and actual bilayer thickness is good.*

When a flat substrate like Si wafer is used, multi-layered, superlattice structures are formed. On the NSTF substrates, however, which have an approximate 15-fold increase in surface area, well-mixed, random fcc alloys, (not multilayer superlattice structures), form. An exception to the fcc alloy structure-type, is $Pt_{1-x}Fe_x$ with $x \geq 0.73$, which is a random bcc alloy.

Figure 4.30 shows the small-angle X-ray (SAX) data for a number of libraries deposited on NSTF substrate. Panels a-e in the left column of Figure 4.30 show the absence of superlattice peaks for a few different values of x in $PtMn_x$ ($0 \leq x \leq 3$) Library 1 and $Pt_{1-x}[Mn_{0.375}Fe_{0.625}]_x$ ($0 \leq x \leq 0.75$) Library 4. The next two columns in Figure 4.30, panels f-j and k-o, show the SAX scattering region of Type II Libraries 7, 8, 9 and 10, 11, 12 for a number of different compositions. Note that unlike the libraries deposited on Si wafers, no low angle superlattice peaks are observed for any libraries deposited on NSTF.

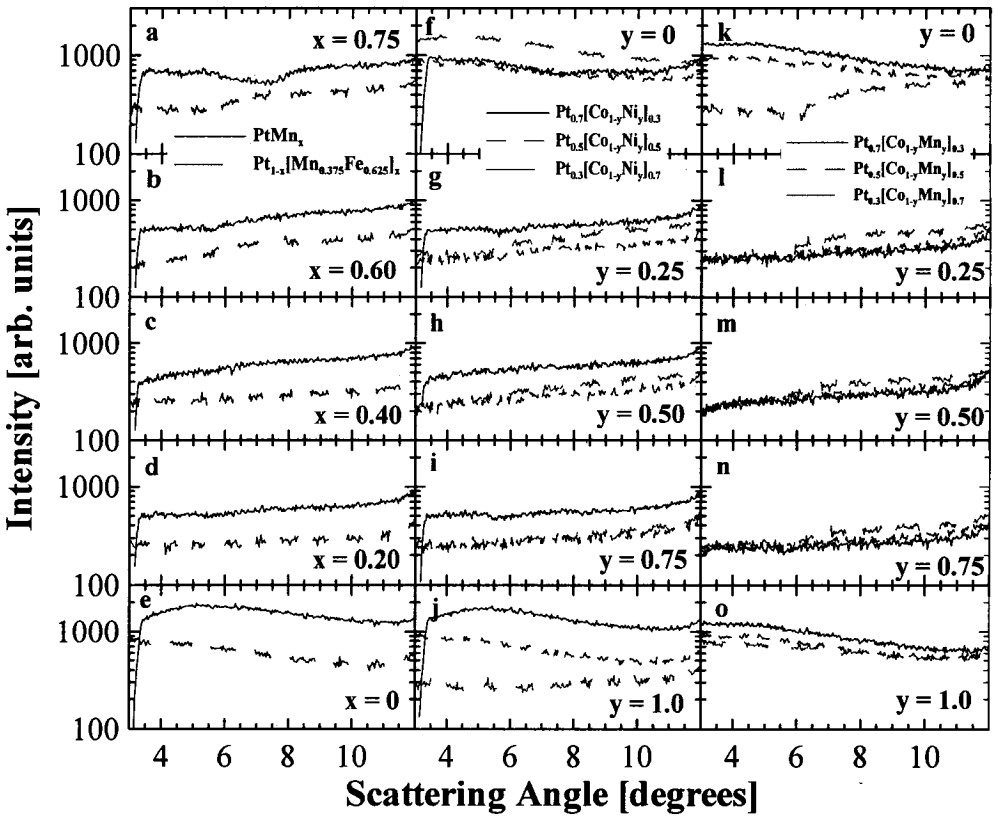

Figure 4.30 *Small angle X-ray diffraction patterns of selected positions of Type I* $Pt_{1-x}Mn_x$ *and* $Pt_{1-x}[Mn_{0.375}Fe_{0.625}]_x$ *($0 \leq x \leq 0.75$) Libraries 1 and 4 (a-e) and Type II* $Pt_{1-x}[Co_{1-y}M_y]_x$ *(M = Ni, Mn; x = 0.3, 0.5, 0.7; $0 \leq y \leq 1$) Libraries 7, 8, 9, 10, 11* and *12 (f-o). The values of x and y are indicated in the Figure. No superlattice peaks are observed in any library. Al samples shown here were prepared on NSTF substrates.*

Further insight into the crystallographic structure of the libraries deposited on NSTF can be obtained by examining the fcc Bragg peaks. Figure 4.31 shows the XRD patterns collected across $Pt_{0.3}[Co_{1-y}Ni_y]_{0.7}$ ($0 \leq y \leq 1$) Library 9. Broad diffraction peaks of nano-

sized, fcc-structured crystallites are observed for all compositions. Similar fcc patterns were seen on all the libraries deposited on NSTF substrates.

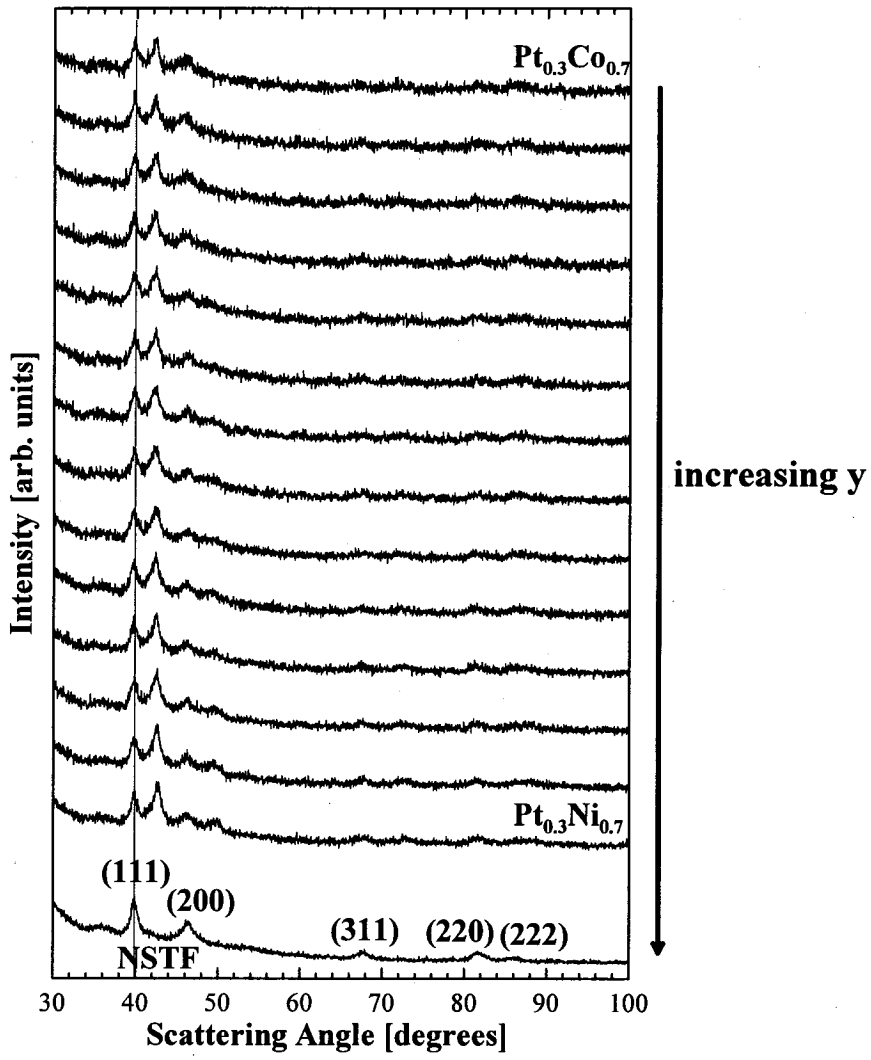

Figure 4.31 *Wide angle X-ray diffraction patterns of Type II $Pt_{0.3}[Co_{1-y}Ni_y]_{0.7}$ ($0 \leq y \leq 1$) Library 9. The bottom pattern is that of a bare NSTF support, showing the diffraction of X-rays from the Pt sublayer beneath the organic whisker structures. No other crystalline phases are observed.*

The (111) and (220) Bragg peaks for $Pt_{1-x}[Co_{1-y}Ni_y]_x$ ($x = 0.3, 0.5, 0.7$; $0 \leq y \leq 1$) Libraries 7, 8 and 9 are shown in Figures 4.32a, b and c, respectively. The bottom XRD pattern in Figures 4.32a, b and c corresponds to the bare NSTF substrate with the 300 Å thick Pt reference layer. Each diffraction pattern corresponds to a change in composition of about $\Delta y \approx 0.06$. In Figure 4.32a, all the fcc (111) peaks are shifted to higher angles compared to the Pt 111 position of the base NSTF support. This shift is more

pronounced in Figures 4.32b and c, where the transition metal content is higher (x = 0.5, 0.7). When x = 0.5 or x = 0.7, a doublet of fcc (111) peaks can easily be observed. The higher angle (111) peak corresponds to the Pt-M-M' alloy and the lower angle (111) peak is that of the Pt sublayer. When the transition metal content is low (x = 0.3), the two fcc (111) peaks overlap and are not resolved in our measurements. Note that the shift of the (111) Bragg peak for a given value of x is constant for all the y values, which suggests that Ni and Co contract the fcc lattice to an equal extent.

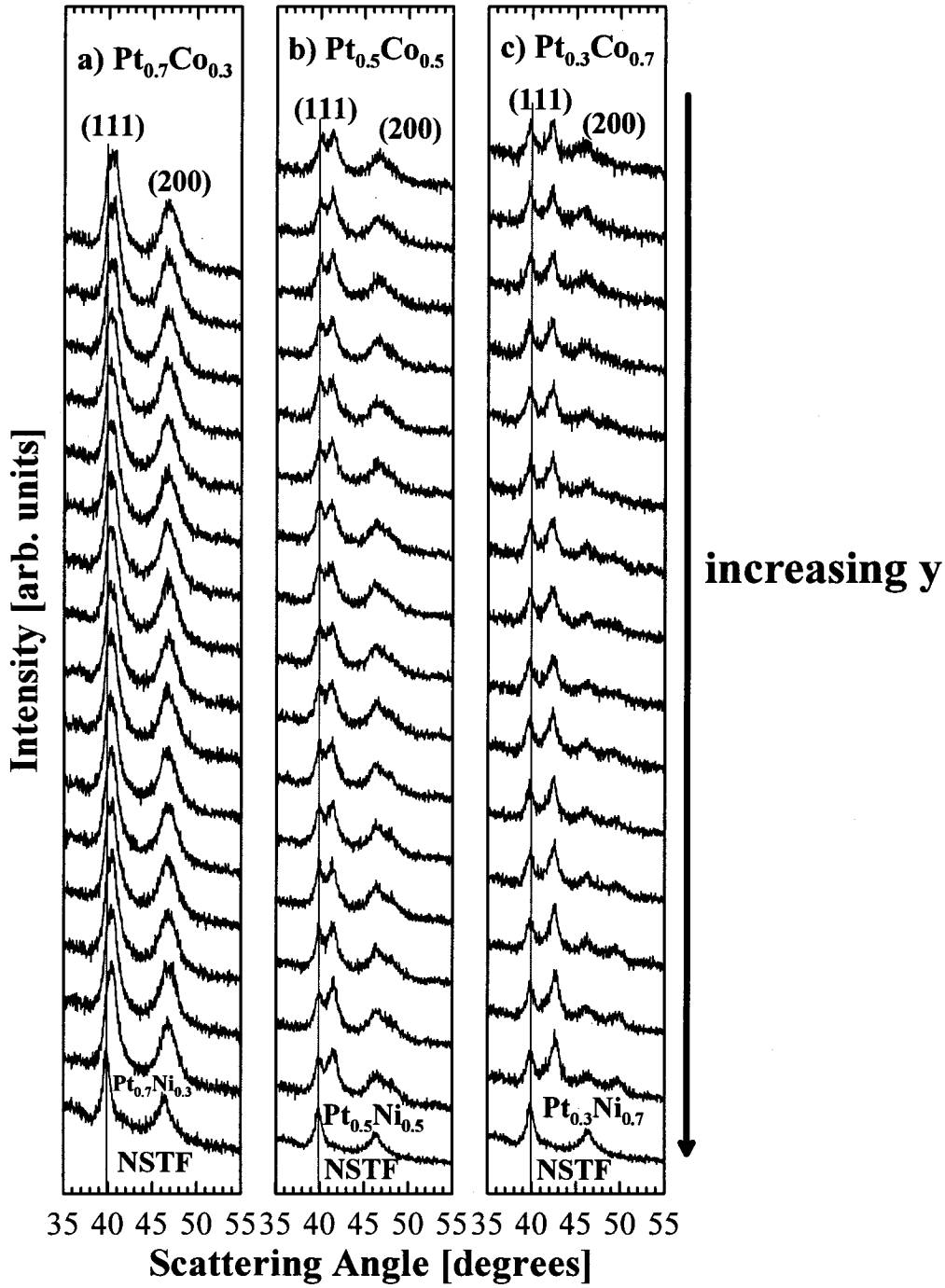

Figure 4.32 *Diffraction patterns of $Pt_{1-x}[Co_{1-y}Ni_y]_x$ (a) x = 0.3, b) 0.5 and c) 0.7; $0 \leq y \leq 1$) Libraries 7, 8 and 9 prepared on NSTF substrate showing a clear movement of the alloy fcc peaks to higher angles. The shift of the (111) peaks is greater for larger values of x.*

Figures 4.33a, b and c show XRD patterns for $Pt_{1-x}[Co_{1-y}Mn_y]_x$ ($x = 0.3, 0.5, 0.7$; $0 \leq y \leq 1$) Libraries 10, 11 and 12 deposited on NSTF. Each diffraction pattern corresponds

to a change in composition of about $\Delta y \approx 0.06$. The shift of the diffraction peaks to higher angles becomes more noticeable as y increases, i.e. as the Mn content decreases in the library. When $y \approx 0$, i.e. at $Pt_{1-x}Co_x$ ($x = 0.5, 0.7$), a similar shift of the (111) peak as in Figure 4.32 is observed. The fcc lattice size for $Pt_{1-x}[Co_{1-y}Mn_y]_x$ ($x = 0.3, 0.5, 0.7$; $0 \leq y \leq 1$) Libraries 10, 11 and 12 depends on the values of both x and y.

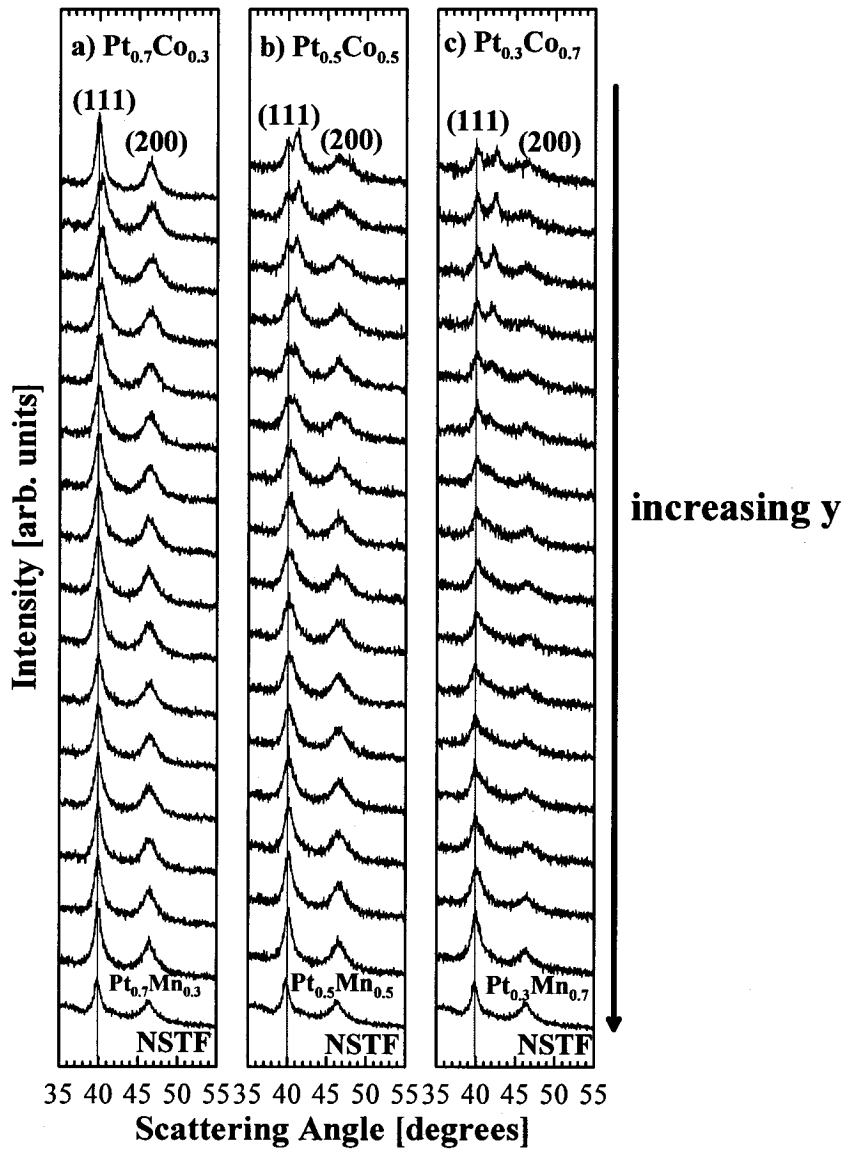

Figure 4.33 *Diffraction patterns of $Pt_{1-x}[Co_{1-y}Mn_y]_x$ (a) $x = 0.3$, b) 0.5 and c) 0.7; $0 \leq y \leq 1$) Libraries 10, 11 and 12 prepared on NSTF substrate showing a clear movement of the alloy fcc peaks to higher angles. The shift of the (111) peaks is greater for larger values of x and smaller values of y (i.e. Pt-Co end) in the library.*

Figures 4.34a and b show the (111) peak in $Pt_{1-x}Mn_x$ and $Pt_{1-x}[Mn_{0.375}Fe_{0.625}]_x$ ($0 \leq x \leq 0.75$) Libraries 1 and 4 deposited on NSTF support. Each diffraction pattern corresponds to a composition change of $\Delta x \approx 0.05$. The shift of the (111) peaks in $Pt_{1-x}Mn_x$ ($0 \leq x \leq 0.75$) Library 1 to higher angles is difficult to see because of peak overlap with the Pt sublayer. Furthermore, as mentioned before the change in the lattice constant of the Pt-Mn phases is not substantial. This shift is more noticeable in $Pt_{1-x}[Mn_{0.375}Fe_{0.625}]_x$ ($0 \leq x \leq 0.75$) Library 4, because Fe impacts the lattice size more than Mn. The separation between the (111) peaks of the Pt sublayer and the $Pt_{1-x}[Mn_{0.375}Fe_{0.625}]_x$ alloy increases as x approaches 0.75.

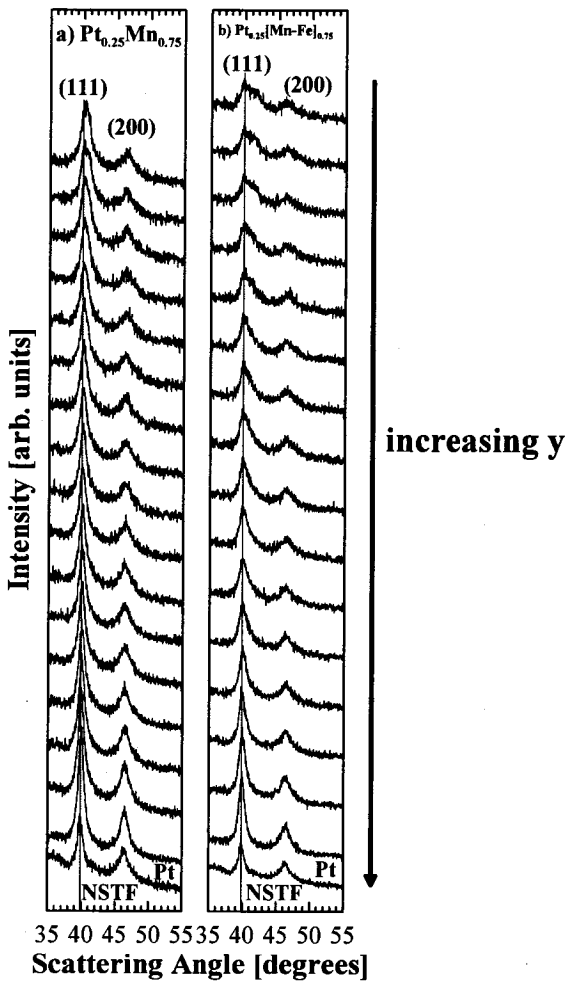

Figure 4.34 *Diffraction patterns of $Pt_{1-x}Mn_x$ and $Pt_{1-x}[Mn_{0.375}Fe_{0.625}]_x$ ($0 \leq x \leq 0.75$) Libraries 1 and 4 prepared on NSTF susbatrte. The Pt-Mn peaks are slightly shifted to higher angles. Here the Bragg peaks from the Pt sublayer on the NSTF support and the alloyed Pt-Mn peaks overlap. The (111) peaks of $Pt_{1-x}[Mn_{0.375}Fe_{0.625}]_x$ Library 4 show a more noticeable shift to higher angles as x increases.*

For a quantitative analysis of the XRD patterns, the (111) and (200) peaks in all the data shown before in Figures 4.32 , 4.33 and 4.34 were fitted and lattice constants were extracted for different compositions in each library. The peaks were fitted with a linear mixing of Lorenzian-Gaussian peak shapes (pseudo-Voigt shape) to obtain the lattice constants. When the fcc (111) peaks of the NSTF substrate and the sputtered alloys were easily resolved, for example in $Pt_{0.3}[Co_{1-y}Ni_y]_{0.7}$ ($0 \leq y \leq 1$) Library 9, both (111) peaks were fitted for each diffractogram. When the (111) peaks were unresolved, for example in the case of $Pt_{0.7}[Co_{1-y}Mn_y]_{0.3}$ ($0 \leq y \leq 1$) Library 10, peak deconvolution was performed by first fitting the Pt sublayer (shown as the bottom diffractogram in Figures 4.32 , 4.33 and 4.34) and including the results in fitting of the diffraction patterns of the libraries. The position, width and shape of the Pt sublayer peaks were kept fixed in fitting the patterns, wherever the Pt sublayer and the alloy peaks were unresolved. Although the deconvolution was generally not straightforward and the obtained parameters had higher uncertainties, reliable estimates were nevertheless achieved. An estimate of the grain size for the different alloy compositions was obtained using the Scherrer equation.

Figures 4.35a, b and c show the variation of the fcc lattice constant with composition in all the libraries discussed above. Figure 4.35a shows the lattice constants versus y in $Pt_{1-x}[Co_{1-y}Ni_y]_x$ Libraries 7, 8, 9 for x = 0.3, 0.5, 0.7. The contraction of the cubic lattice increases as x increases, i.e. as the total content of transition metals increases; however, it remains approximately constant for the entire range of $0 \leq y \leq 1$, because Ni and Co have similar atomic radii. Figure 4.35a also shows the lattice constant of several equilibrium intermetallic phases of Pt-Co and Pt-Ni. Pt-Co shows a number of ordered ($AuCu_3$-like) and randomly ordered (Cu-like) fcc structures [234, 239-243]. These phases are generally prepared at about 1000°C under an inert atmosphere. The three literature data points shown in Figure 4.35a for $Pt_{1-x}Co_x$ correspond to x = 0.25, 0.5 and 0.75. The $Pt_{0.5}Co_{0.5}$ data point is an average of several values reported in the literature [234, 239-241, 243]. The literature value reported for $Pt_{0.5}Ni_{0.5}$ is also an average of reported literature values for equilibrium phases [238, 239].

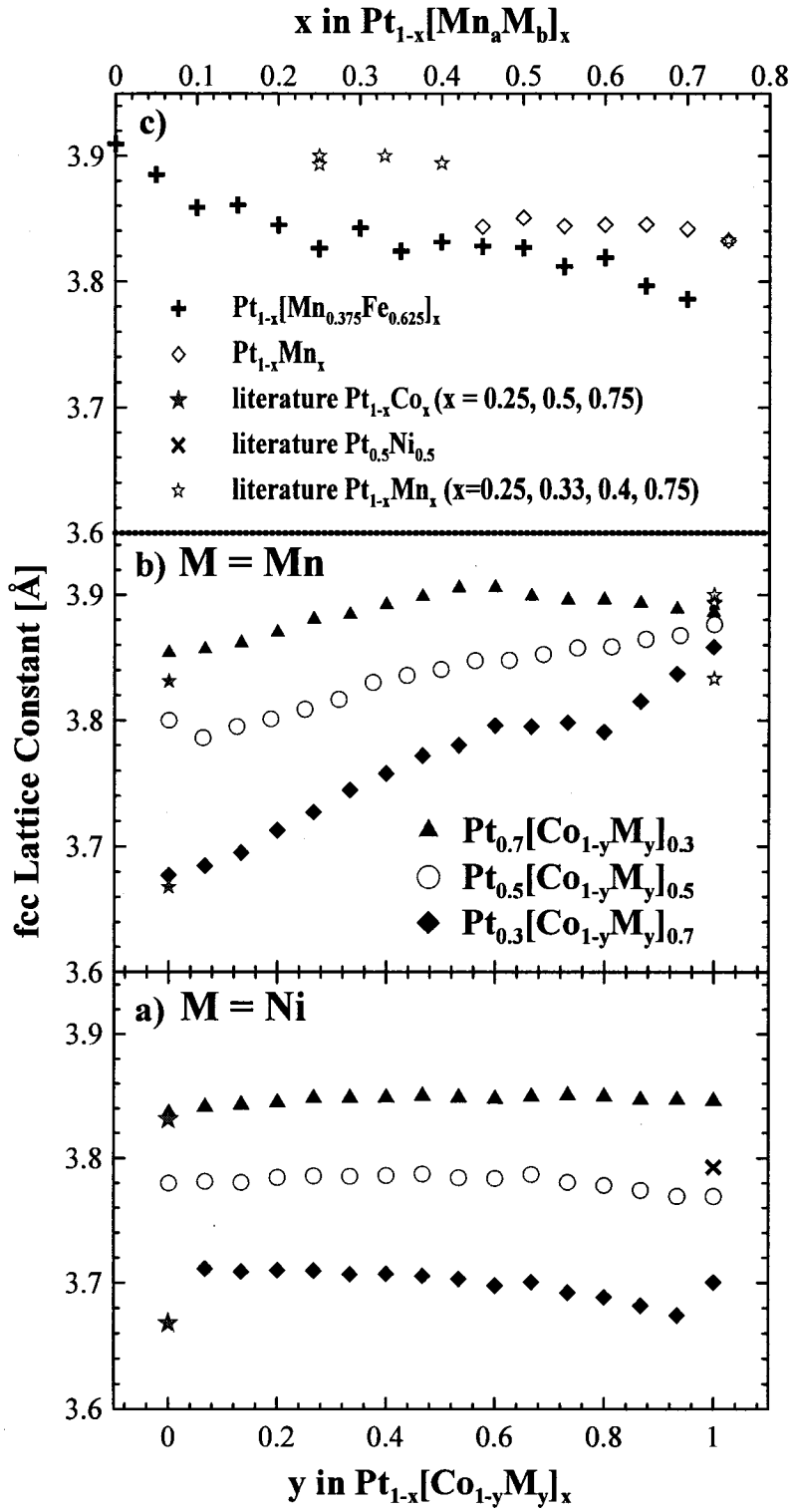

Figure 4.35 *Lattice constants derived from the diffraction patterns shown in Figures 4.31 , 4.32 and 4.33 versus y in $Pt_{1-x}[Co_{1-y}M_y]_x$ (M = Ni, Mn; x = 0.3, 0.5, 0.7; $0 \leq y \leq 1$) Libraries 7, 8, 9, 10, 11 and 12 (a, b) and versus x in $Pt_{1-x}Mn_x$ and $Pt_{1-x}[Mn_{0.375}Fe_{0.625}]_x$ ($0 \leq x \leq 0.75$) Libraries 1 and 4 (c). All libraries shown here were prepared on NSTF substrate.*

Figure 4.35b shows similar information as Figure 4.35a, but for $Pt_{1-x}[Co_{1-y}Mn_y]_x$ (x = 0.3, 0.5, 0.7; $0 \leq y \leq 1$) Libraries 10, 11 and 12. Note that the data for the Co-end of the libraries (or y = 0 in $Pt_{1-x}[Co_{1-y}Mn_y]_x$) is in good agreement with the Co-end of $Pt_{1-x}[Co_{1-y}Ni_y]_x$ (x = 0.3, 0.5, 0.7) Libraries 7, 8 and 9 shown in Figure 4.35a. Unlike Pt-Co-Ni libraries, the lattice dimension does not remain constant for $0 \leq y \leq 1$ in $Pt_{1-x}[Co_{1-y}Mn_y]_x$ for a given value of x. The change in the Pt lattice constant is much smaller at the Mn-end of the libraries than it is at the Co-end or Ni-end of the libraries. The equilibrium intermetallic phases of Pt-Mn also do not show a pronounced change in lattice constant compared to pure Pt. In general, two types of crystal structures are observed for the equilibrium Pt-Mn phases: tetragonal (AuCu-like) and fcc (Cu or $AuCu_3$-like). The literature values of the lattice constant for fcc $Pt_{1-x}Mn_x$ (x = 0.25, 0.33, 0.4, 0.75) are shown in Figure 4.35b for comparison [234, 244-246]. Figure 4.35c shows the lattice constant versus composition of $Pt_{1-x}Mn_x$ and $Pt_{1-x}[Mn_{0.375}Fe_{0.625}]_x$ Libraries 1 and 4. Only values for $x \geq 0.5$ in $Pt_{1-x}Mn_x$ are shown, because the peak positions for smaller values of x could not be unambiguously determined.

Figure 4.36 shows the grain size of the Pt-M-M' alloys sputtered on the NSTF libraries determined from the FWHM of the (111) peaks. For $Pt_{1-x}[Co_{1-y}Ni_y]_x$ (x = 0.3, 0.5, 0.7; $0 \leq y \leq 1$) Libraries 7, 8 and 9, the grain size is about 15 nm and quite constant for all x and y values. For the Mn-based libraries, (panels b and c), the scatter in the grain size data is much larger. This is largely due to the difficulty of deconvoluting the (111) peaks of the Pt sublayer and the Pt-alloy; however, on average the grain sizes are about 12 nm.

Given the evidence in Figures 4.31-4.36, it is clear that randomly ordered, nanocrystalline, substitutional fcc alloys of Pt with Co, Ni, Fe and Mn are formed on these NSTF supports in the libraries prepared. The observed changes in the lattice constants are in good agreement with those of previously reported equilibrium phases in the literature.

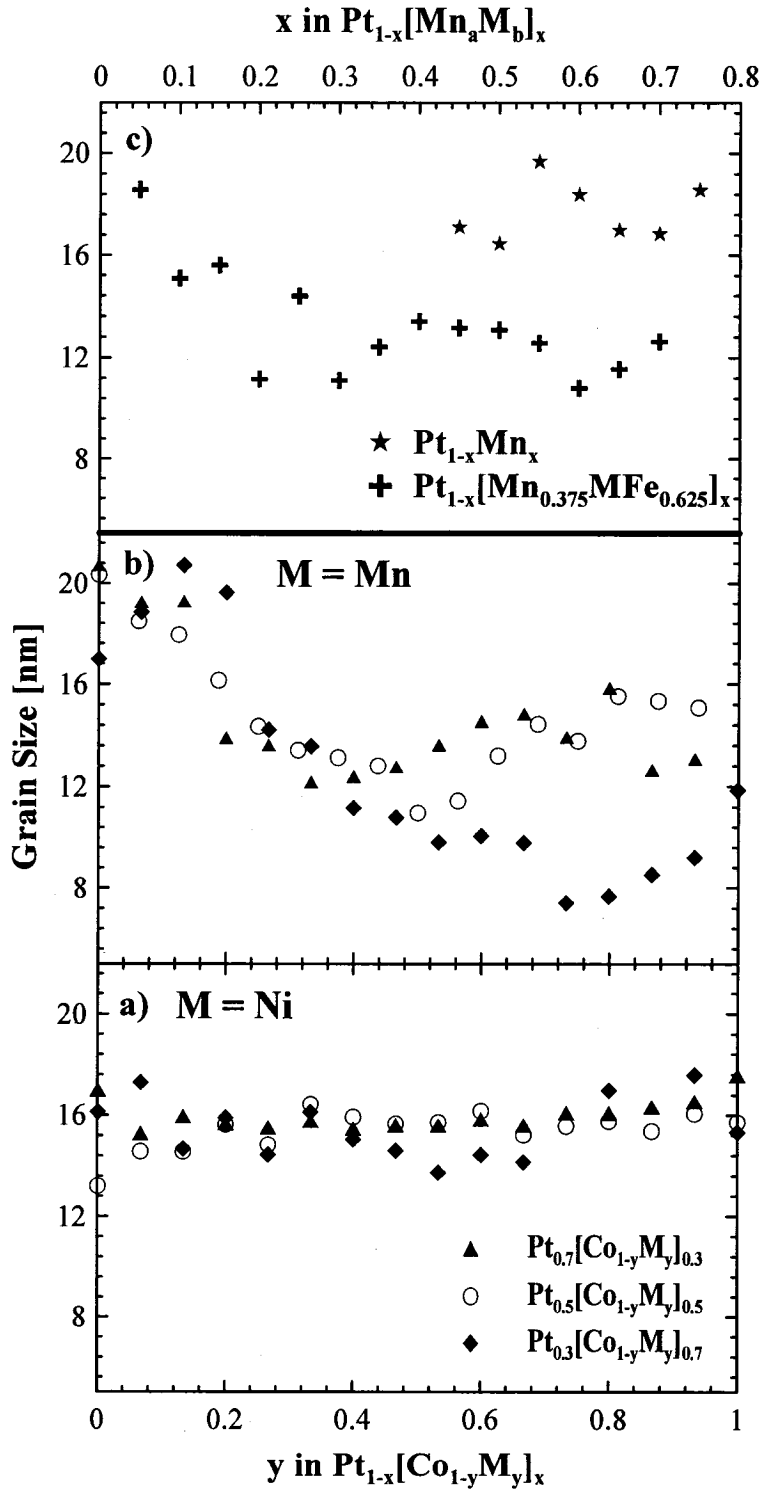

Figure 4.36 *Grain sizes obtained from the diffraction patterns shown in Figures 4.31, 4.32 and 4.33 versus y in $Pt_{1-x}[Co_{1-y}M_y]_x$ (M = Ni, Mn; x = 0.3, 0.5, 0.7; $0 \leq y \leq 1$) Libraries 7, 8, 9, 10, 11 and 12 (a, b) and versus x in $Pt_{1-x}Mn_x$ and $Pt_{1-x}[Mn_{0.375}Fe_{0.625}]_x$ ($0 \leq x \leq 0.75$) Libraries 1 and 4 (c). All libraries shown here were prepared on NSTF substrate.*

4.4.2 Composition of Acid Treated Electrocatalyst Libraries versus Post-FC Test Libraries: Results for $Pt_{1-x}Ni_x$, $Pt_{1-x}Fe_x$ and $Pt_{1-x}Mn_x$ Libraries

The composition, x, in type I Libraries 1, 2, 3, 4, 5 and 6 at the same set of positions in the libraries were measured before and after fuel cell testing and before and after acid treatment. For Type I libraries a convenient way to display the compositional changes that take place in the libraries due to corrosion is to plot the composition after treatment, x_{after}, versus the composition before treatment, x_{before}, for the same position in the library. Figure 4.37 shows such results for $Pt_{1-x}M_x$ (M = Mn, Ni) Libraries 1, 2 and 3 before and after treatment. The composition of the electrocatalysts after acid treatment ($x = x_{after}$ in $Pt_{1-x}M_x$) versus the M content of the as-deposited films ($x = x_{before}$ in $Pt_{1-x}M_x$) show the same trends that we reported previously in the case of $Pt_{1-x}M_x$ (M = Fe, Ni, $0 \leq x \leq 1$) libraries in section 4.3.5 [113, 247]. For low initial M content ($x_{before} \leq 0.6$) x_{after} is reduced to about half of x_{before}; however, the dissolution of M intensifies for higher initial values of x ($x_{before} \geq 0.6$). This increased leaching was attributed to the bulk dissolution of M because the fcc lattice constant after treatment increased over its value before treatment for $x_{before} \geq 0.6$ [113, 247]. A similar dissolution mechanism is likely to happen here. For $x_{before} \leq 0.6$, transition metals are dissolved primarily from the surface layers, whereas for $x_{before} \geq 0.6$ or so, bulk dissolution occurs also. The value of x_{before} in $Pt_{1-x}Fe_x$ Library 2 tested in the fuel cell and shown in Figure 4.37 spanned the range $0 \leq x_{before} \leq 0.5$. Notice the remarkable agreement between the post-fuel cell and post-acid treated compositions for $Pt_{1-x}M_x$ (M = Mn, Ni and Fe) Libraries 1, 2 and 3. These results show that the leaching of Mn, Ni and Fe, which occur in a PEMFC, can be rather accurately mimicked by a 10 day soaking in 1M H_2SO_4 solution at 80°C.

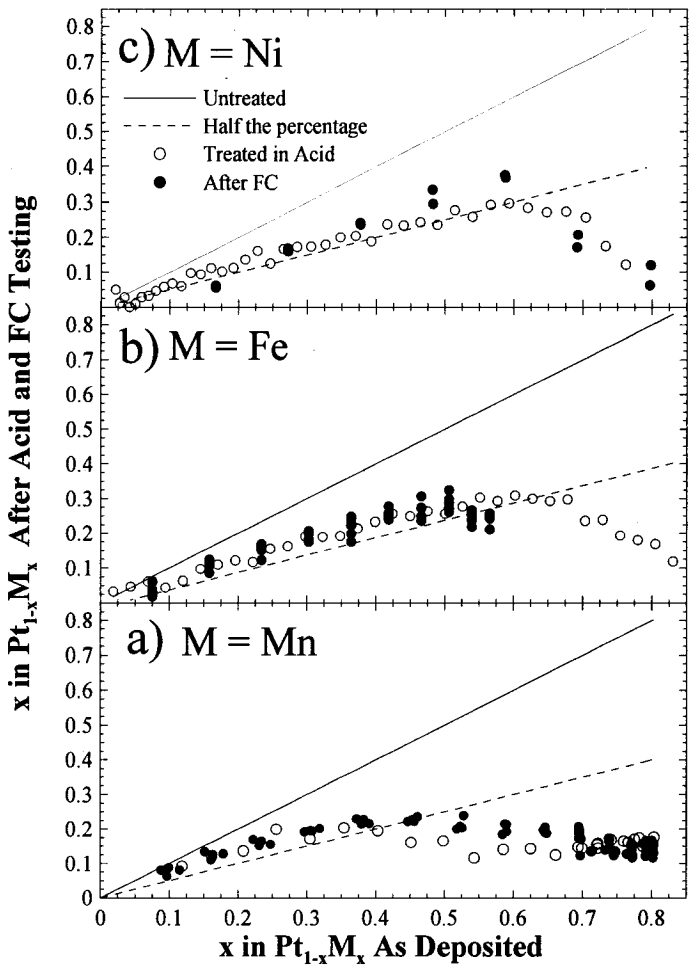

Figure 4.37 *Composition of Type I $Pt_{1-x}M_x$ (M = Mn, Ni, Fe) Libraries 1, 2 and 3 after FC testing and acid treatment (10 days in 1M H_2SO_4 at 80°C) versus the composition of the as-deposited films. All libraries shown here were prepared on NSTF substrate.*

4.4.3 Results for Type I Pt-MnFe and Pt-MnNi Libraries

Three other libraries of *Type I* electrocatalysts were prepared and their compositions before and after FC testing and acid treatment (10 days in 1M H_2SO_4 at 80°C) were studied by electron microprobe. The initial libraries were designed to be $Pt_{1-x}[Mn_{0.375}Fe_{0.625}]_x$, $Pt_{1-x}[Mn_{0.167}Fe_{0.833}]_x$ and $Pt_{1-x}[Mn_{0.5}Ni_{0.5}]_x$ with ($0 \leq x \leq 0.75$). These are Libraries 4, 5 and 6. The Mn : Fe and Mn : Ni ratios in these libraries did not remain constant during treatment; therefore, it is better to display the compositions in these libraries as x and y in $Pt_{1-x-y}Mn_yFe_x$ and $Pt_{1-x-y}Mn_yNi_x$. Before treatment, the ratio y : x is designed to be constant throughout the libraries and is nominally 0.6, 0.2 and 1.0, respectively for the three libraries. Figure 4.38 shows the results of the composition changes after fuel cell testing and after acid treatment for $Pt_{1-x}[Mn_{0.375}Fe_{0.625}]_x$ Library 4.

Figure 4.38a shows the Mn and Fe contents, y_{before} and x_{before}, before fuel cell testing and the Mn and Fe contents, y_{after} and x_{after}, after fuel cell testing, plotted versus the total transition metal content, $x_{before} + y_{before}$, before fuel cell testing. Figure 4.38a clearly shows that both Fe and Mn contents are reduced at all points of the library and that the change in the Mn content is larger than the change in the Fe content. Figure 4.38c shows the total transition metal content after fuel cell testing, $x_{after} + y_{after}$, plotted versus the total transition metal content, $x_{before} + y_{before}$, before fuel cell testing. After fuel cell testing, the total transition metal content is no more than $x_{after} + y_{after} = 0.25$ for any position in the library. Figure 4.38e shows the measured ratio of Mn to Fe content before fuel cell testing $y_{before} : x_{before}$ and after fuel cell testing $y_{after} : x_{after}$ plotted versus the total transition metal content, $x_{before} + y_{before}$, before fuel cell testing. Figure 4.38e shows that the Mn content is reduced by about a factor of three relative to Fe for all positions in the library during fuel cell testing. The panels on the right hand side of Figure 4.38 show analogous information for an identical library treated in acid. Note the similarities in the compositions of the acid treated libraries versus the libraries after FC testing.

Figure 4.39 shows analogous results to Figure 4.38 collected on $Pt_{1-x-y}Mn_yFe_x$ Library 5 with an initial ratio, $y : x = 0.2$. The ratio y : x after acid treatment and fuel cell testing was reduced to below 0.1. The acid-treated and post-fuel cell compositions again compare well. Figure 4.40 shows results on $Pt_{1-x-y}Mn_yNi_x$ with an initial ratio $y : x = 1$ presented in the same way as in Figure 4.38. The ratio y : x reduces to about 0.3, a 3-fold decrease. After both fuel cell testing and acid treatment, the maximum transition metal content, $x_{after} + y_{after}$, is about 0.25, regardless of the initial transition metal content for both libraries studied in Figures 4.39 and 4.40.

The results in Figures 4.38, 4.39 and 4.40 can be summarized as follows: 1) Acid treatment and fuel cell testing lead to almost the same compositional changes, point by point, in these electrocatalyst libraries; 2) Mn is selectively leached compared to either Fe or Ni; and 3) Provided the initial transition metal content, $x_{before} + y_{before} \geq 0.25$, after fuel cell testing or acid treatment the maximum transition metal content is reduced to about $x_{after} + y_{after} = 0.25$.

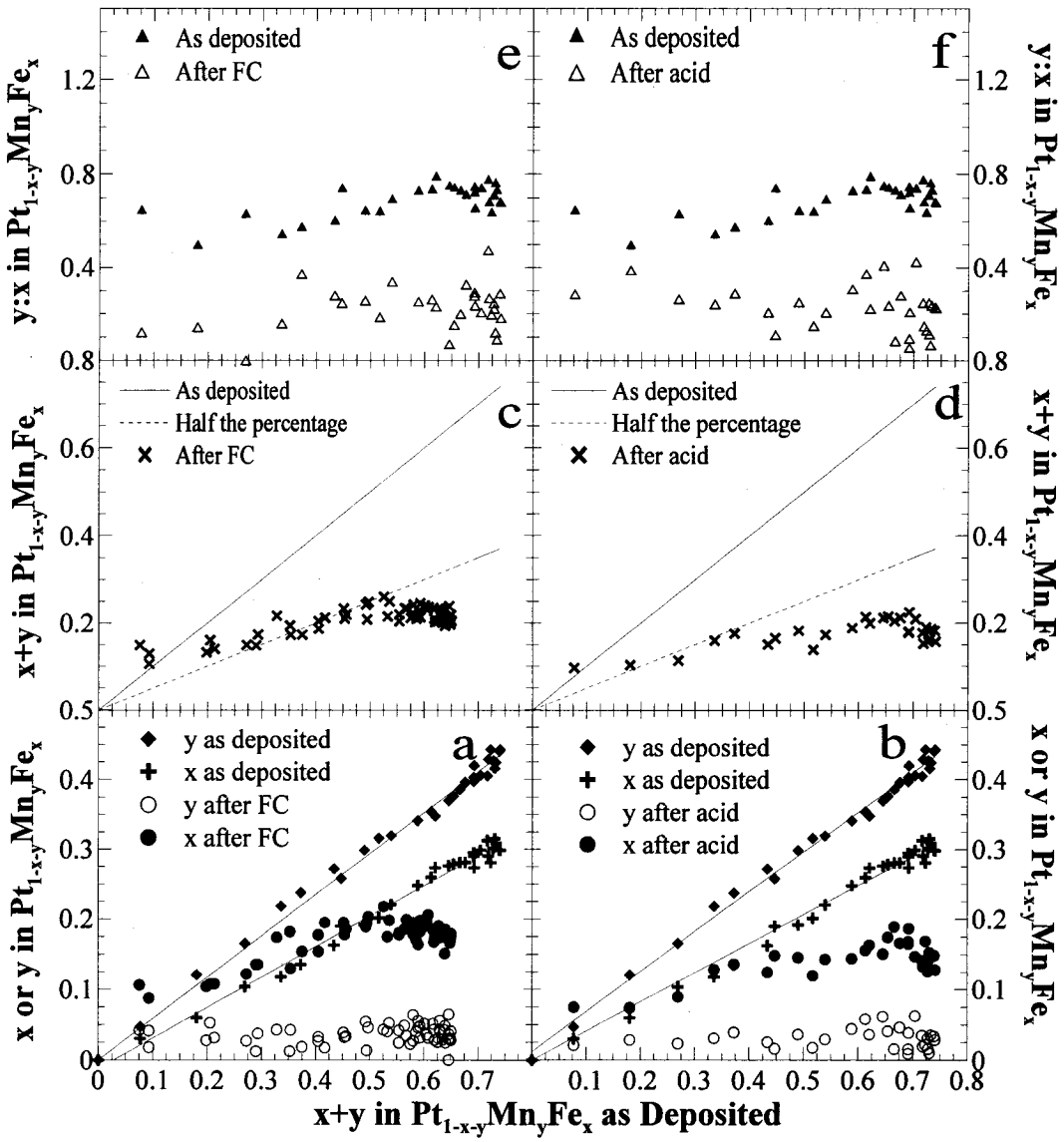

Figure 4.38 *Composition of the Type I $Pt_{1-x-y}Mn_yFe_x$ Library 4 with an initial Mn : Fe ratio = 0.65 after FC testing (a, c, e) and acid treatment (10 days in 1M H_2SO_4 at 80°C) (b, d, f) versus the composition of the as-deposited film. Panels a and b show the individual metal contents (x and y), panels c and d, show the total transition metal content (x + y)* and *panels e and f show the ratio of Mn to Fe (y : x). All libraries shown here were prepared on NSTF substrate.*

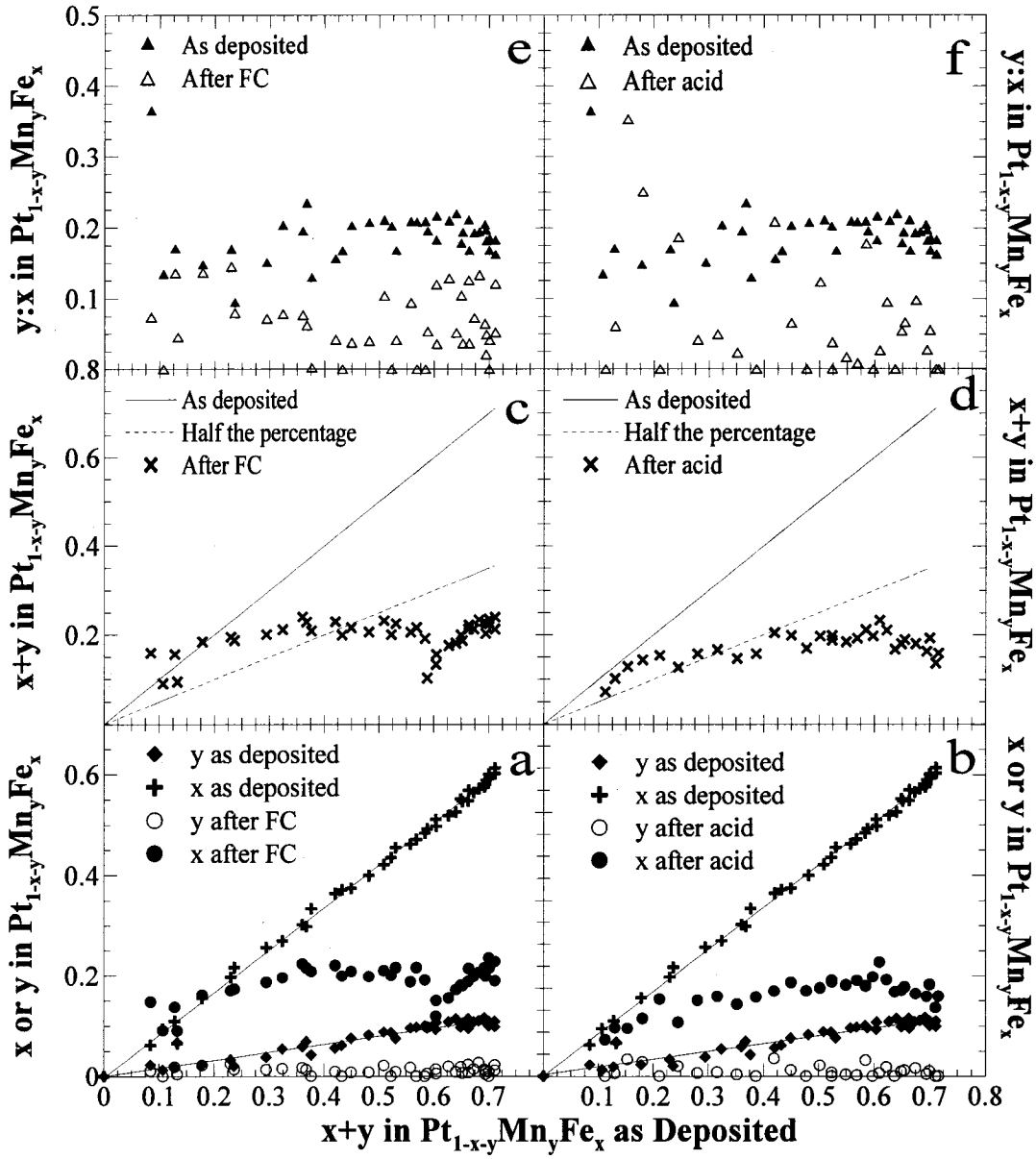

Figure 4.39 *Composition of Type I $Pt_{1-x-y}Mn_yFe_x$ Library 5 with an initial Mn : Fe ratio = 0.2 after FC testing (a, c, e) and acid treatment (10 days in 1M H_2SO_4 at 80°C) (b, d, f) versus the composition of the as-deposited film. Panels a and b show the individual metal contents (x and y), panels c and, show the total transition metal content (x + y)* and *panels e and f, show the ratio of Mn to Fe (y : x). All libraries shown here were prepared on NSTF substrate.*

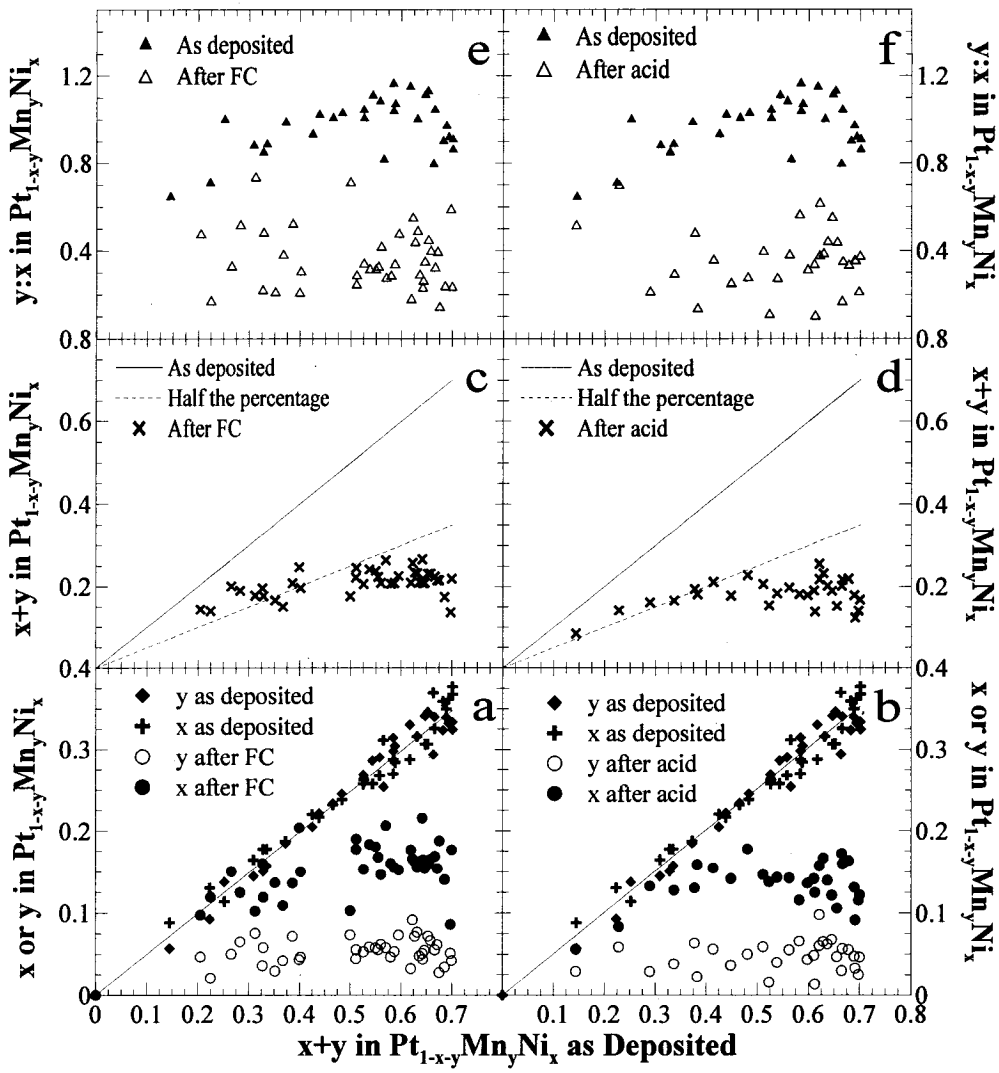

Figure 4.40 *Composition of Type I $Pt_{1-x-y}Mn_yNi_x$ Library 6 with an initial Mn : Ni ratio = 1.0 after FC testing (a, c, e) and acid treatment (10 days in 1M H_2SO_4 at 80°C) (b, d, f) versus the composition of the as-deposited film. Panels a and b show the individual metal contents (x and y), panels c and d, show the total transition metal content (x + y) and panels e and f, show the ratio of Mn to Ni (y : x). All libraries shown here were prepared on NSTF substrate.*

4.4.4 Results for Type II $Pt_{1-x}[M_yM'_{1-y}]_x$, M, M' = Co, Ni, Mn Libraries 7, 8, 9, 10, 11, 12

Figure 4.41 shows electron microprobe results for Libraries 7, 10 and 11 having nominal compositions, $Pt_{0.7}[Co_{1-y}Ni_y]_{0.3}$, $Pt_{0.7}[Co_{1-y}Mn_y]_{0.3}$ and $Pt_{0.5}[Co_{1-y}Mn_y]_{0.5}$ with $0 \leq y \leq 1$. The composition of the catalysts, designated as x and y in $Pt_{1-x-y}M_yM'_x$ before and after FC testing are shown in the left hand panels (Figures 4.41a, c and e). The overall transition metal content, x + y, before and after fuel cell testing is given in the right hand

panels (Figures 4.41b, d and f). For the three libraries described by Figure 4.41, the content of both transition metals is reduced during fuel cell testing and the overall transition metal content is reduced by about 50%. In no case is the final transition metal content greater than $x_{after} + y_{after} = 0.25$.

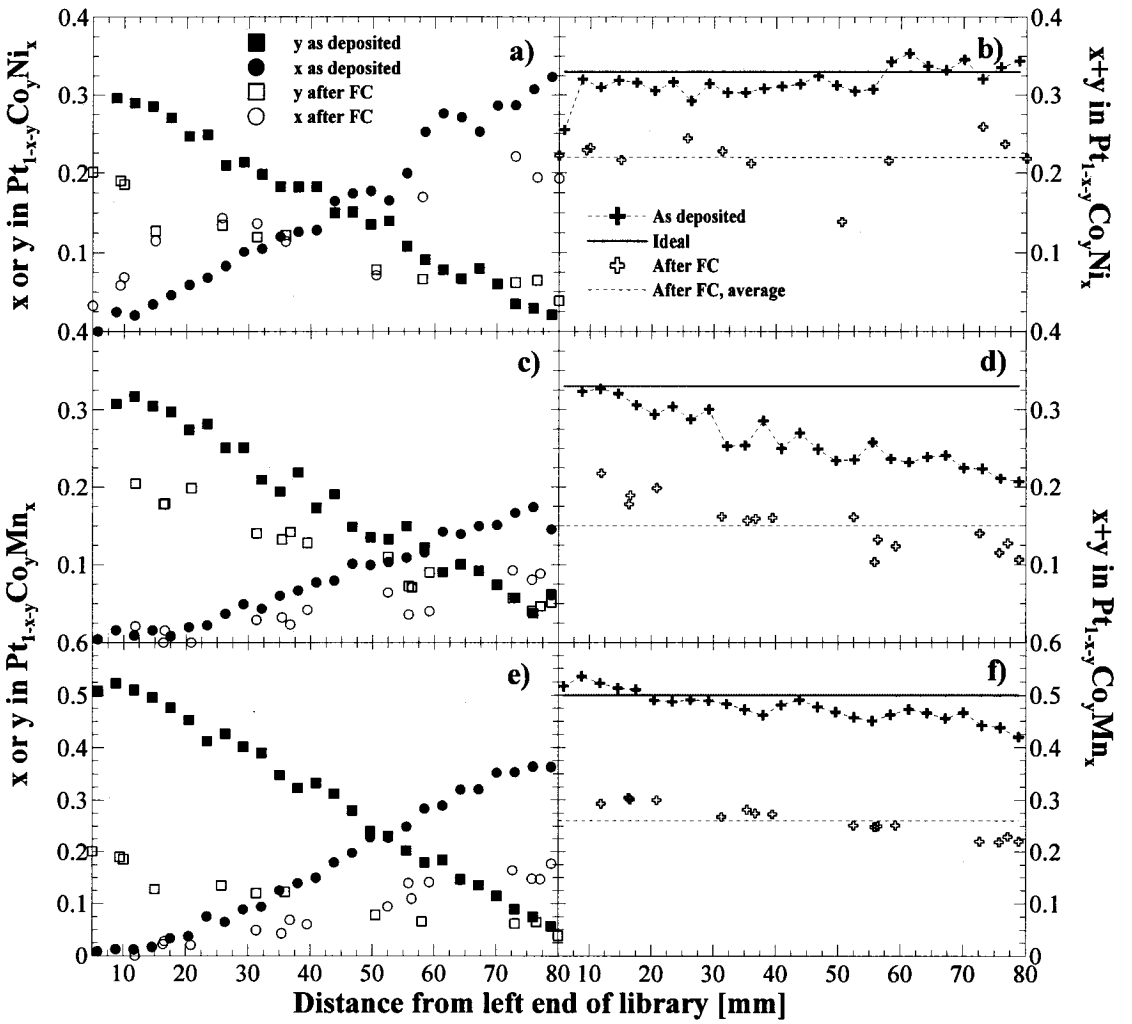

Figure 4.41 *Electron microprobe Results for three Type II libraries $Pt_{0.7}[Co_{1-y}Ni_y]_{0.3}$, $Pt_{0.7}[Co_{1-y}Mn_y]_{0.3}$ and $Pt_{0.5}[Co_{1-y}Mn_y]_{0.5}$ ($0 \leq y \leq 1$). These are Libraries 7, 10 and 11, respectively. The composition of the catalysts, designated as x and y in $Pt_{1-x-y}M_yM'_x$ before and after FC testing are shown in the left hand panels (a, c and e). The overall transition metal content, x + y, before and after fuel cell testing is given in the right hand panels (b, d and f). All libraries shown here were prepared on NSTF substrate.*

Figure 4.42 shows the composition changes of two further Type II libraries that initially have higher transition metal contents than the libraries described by Figure 4.41 and which have been subjected to both acid and fuel cell testing. Figure 4.42a-d shows

results for $Pt_{0.3}[Co_{1-y}Ni_y]_{0.7}$ Library 9 and Figure 4.42e-h shows results for $Pt_{0.3}[Co_{1-y}Mn_y]_{0.7}$ Library 12. The left hand panels of Figure 4.42 show the compositions x and y as well as the sum, x + y, in $Pt_{1-x-y}Co_yMn_x$ and in $Pt_{1-x-y}Co_yNi_x$ before and after fuel cell testing. The right hand panels show analogous information after acid treatment. The compositions that are attained at all points of the libraries after fuel cell testing and after acid treatment show the same trends, although the acid treatment removed somewhat more transition metals than did the fuel cell testing. For the fuel cell tested libraries, the transition metal atomic fraction is reduced from 0.7 to about 0.3 and for the acid-treated libraries, the transition metal content is reduced to about 0.2. Mn is removed preferentially from the Mn-containing alloy compared to Co, as seen in Figures 4.41a and 4.41b. Both Ni and Co are removed to about the same extent from the $Pt_{1-x-y}Co_yNi_x$ library in both fuel cell and acid testing.

The Pourbaix diagrams for the transition metals studied here (Fe, Ni, Co, Mn) show that these pure elements dissolve under the typical potential/pH conditions encountered in working PEM fuel cells [228]. When the initial transition metal atomic fraction is less than about 0.6, dissolution is primarily from the surface of the alloy and when the initial transition metal fraction is greater than 0.6, both bulk and surface dissolution occurs. The surface depletion of transition metals in Pt alloys has been discussed in the literature [235].

Selective leaching or dealloying of the transition metals from the $Pt_{1-x-y}M_xM'_y$ libraries studied here is probably similar to the widely known dezincification process of brass and the graphitic corrosion of cast iron [248]. In brass, for example, Zn which is more active (lower redox potential) is preferentially leached out when the alloy is exposed to corrosive environments, leaving behind a porous structure. During this corrosion Cu is also thought to dissolve, but later redeposits on the grains. In case of Pt-Co catalysts in hot phosphoric acid, Watanabe proposed a corrosion mechanism where Co and Pt dissolve and Pt redeposits onto grains with lower surface energy, leading to formation of a Pt skin layer [135]. In all the samples studied here, more active transition metals corrode more extensively. In the case of Pt-MnFe and Pt-MnNi, we observed a stronger dissolution of Mn over either Fe or Ni. This may be explained by the lower

reduction potential of Mn (-1.18V versus SHE) than Fe (-0.44 versus SHE) or Ni (-0.26V versus SHE), which would make Mn thermodynamically more active for corrosion.

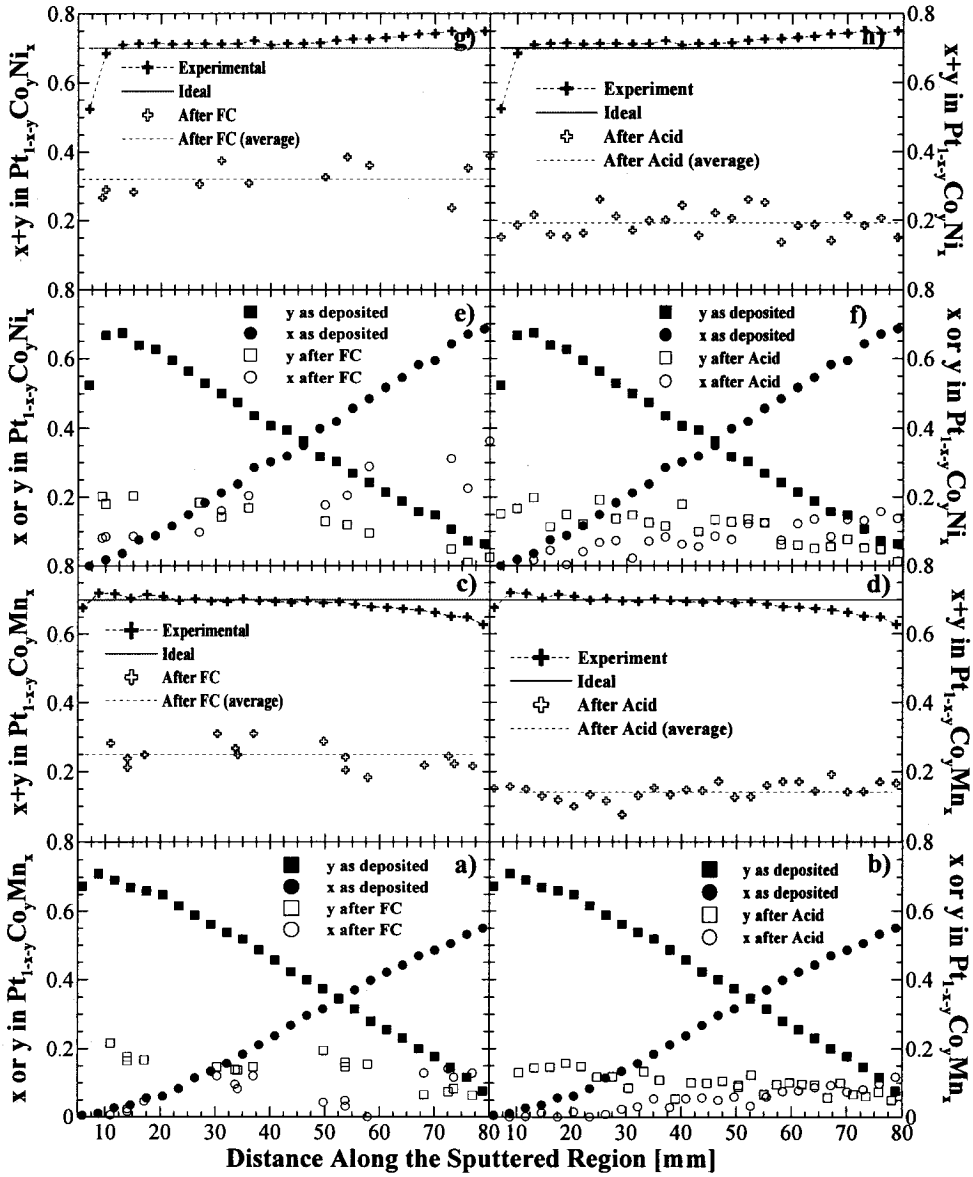

Figure 4.42 *Electron microprobe Results for two Type II libraries* $Pt_{0.3}[Co_{1-y}Ni_y]_{0.7}$ and $Pt_{0.3}[Co_{1-y}Mn_y]_{0.7}$ *(0 ≤ y ≤ 1). These are Libraries 9 and 12. The composition of the catalysts, designated as x and y in* $Pt_{1-x-y}M_yM'_x$ *before and after FC or acid testing (10 days in 1M* H_2SO_4 *at 80°C) are shown in the panels a, b, e and f. The overall transition metal content, x + y, before and after fuel cell or acid testing is given in panels c, d, g and h. All libraries shown here were prepared on NSTF substrate.*

The average particle size of the catalysts studied here is about 10-12 nm, which is larger than the typical 2-4 nm particles found in carbon-supported Pt catalysts. The NSTF-supported Pt catalysts are different from carbon-supported catalysts in that they

exhibit a larger specific activity (similar to bulk Pt crystals) and a much better Pt dissolution stability [124, 249-251]. The Pt grains in these NSTF-based catalysts are already "coarsened" and hence surface area degradation occurs more slowly. Corrosion stability of transition metals in the NSTF-supported Pt-alloys would thus be closer to bulk–like alloys, whereas smaller grain-size alloys are likely to lose larger fractions of transition metals.

4.5 2 Dimensional Libraries of Pt-Ni

Using the 2-axis sputtering table, binary 'cross-wedge' shaped libraries can be produced For more details of the 2-axis table see reference [197]. Two elements can be deposited in ramp shaped profiles in orthogonal directions. Figure 4.43 shows the mass per unit area of a Pt-Ni cross-wedge in a 3-dimensional map. This library contains all the compositions ($Pt_{1-x}Ni_x$, $0 < x < 1$) and a wide range of film thicknesses. Figure 4.44a shows the contour lines of constant composition across the library. The thickness varies almost linearly along each constant composition line. This sort of mapping is useful for simultaneous studies of the impact of film thickness and composition on corrosion and/or electrocatalytic activity.

Figures 4.43b, c and d show the corrosion results for a cross-wedge Pt-Ni library. Figures 4.43b and c show the composition of the libraries after acid treatment and post-FC testing, respectively. Both libraries were deposited on NSTF. Note the similarity between the two. In the top left hand corner, where the film thickness is largest, the least corrosion has occurred and compositions are similar to those shown earlier for the linear Pt-Fe library (Figure 4.16). Figure 4.44d shows the corrosion result for the same library deposited on a flat surface (graphoil carbon paper). Now the maximum Ni content retained (at the thickest end) is higher and is close to $x \sim 0.6$. Such an examination clearly shows the influence of surface area and film thickness on corrosion and stresses the point that low surface area Pt-alloys do not always simulate the corrosion of high surface area Pt-alloy electrocatalysts (be they NSTF or the usual carbon-supported). Figure 4.45 shows x_{after} in $Pt_{1-x}Ni_x$ versus x_{before} for all the points in the libraries considered in Figure 4.44b, c and d. Note that the after acid and after FC composition data of NSTF supported electrocatalysts overlap and show a pattern which is very similar

to that observed earlier, whereas the electrocatalyst library deposited on graphoil shows a wide range of x_{after} corresponding to the various thicknesses of the library.

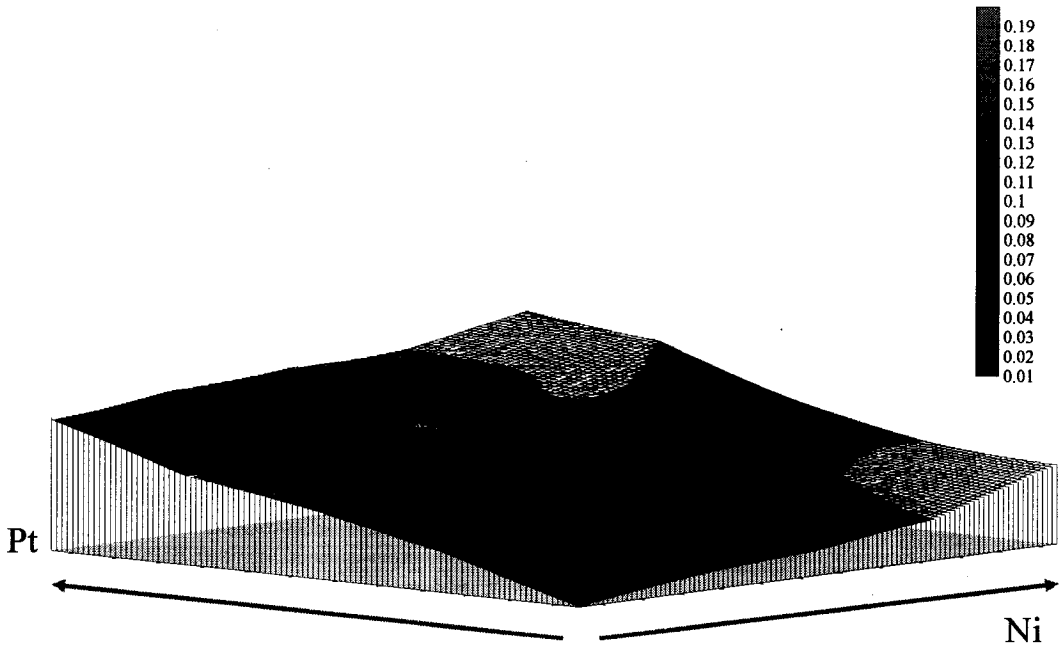

Figure 4.43 *Mass per unit area topography of a "cross-wedged" library of Pt-Ni. Pt and Ni mass increase as shown by the arrows in the diagram. The scale bar indicates the variation of mass per area in* $mg \cdot cm^{-2}$.

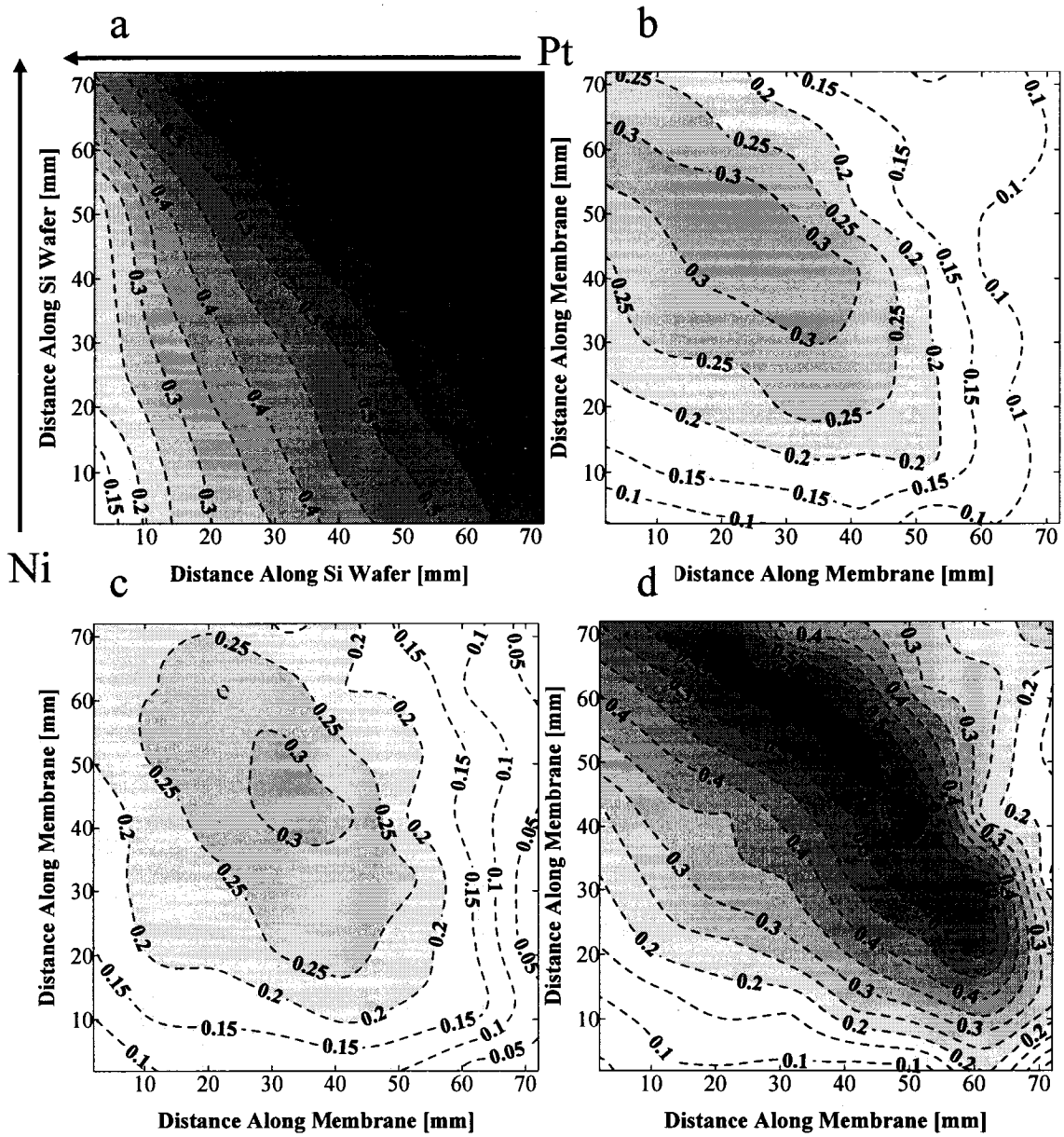

Figure 4.44 *Contour representations of x in $Pt_{1-x}Ni_x$ for Pt-Ni libraries whose mass topology was shown in Figure 4.43. top-left) as-deposited, top-right) after acid, bottom-left) after fuel cell, bottom-right) after acid on graphoil paper (flat surface).*

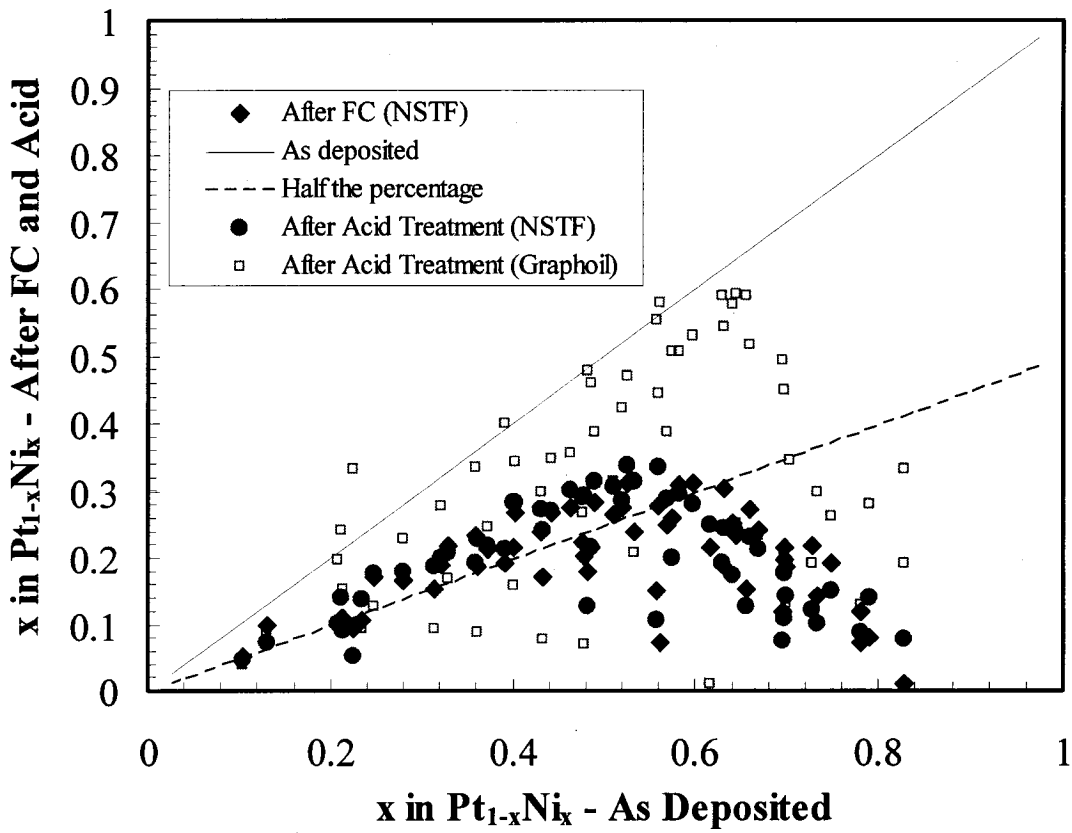

Figure 4.45 *Atomic fraction of Ni in Pt-Ni plotted versus the Ni content before acid treatment (10 days in 1M H_2SO_4 at 80°C) and fuel cell testing. Data are shown for as-deposited, after acid treatment (NSTF), after acid treatment (on a flat graphoil surface) and after fuel cell testing (NSTF).*

4.6 Discussion of Pt Corrosion

What about corrosion of Pt itself? In all the samples we studied here, Pt dissolution was negligible compared to that of the TMs. This was verified by AA measurements: no Pt was detected within the sensitivity limit. Does this mean that no Pt dissolves in PEMFC electrocatalysts? No, on the contrary Pt does dissolve and its dissolution has been reported [108, 110, 252-254]. However, dissolution of Pt occurs at much longer time scales and it highly depends on the morphology, grain size and the electrochemical potential. Dissolution of Pt from Pt/C electrocatalysts is serious problem for PEMFC. Two mechanisms of Oswald ripening and coarsening have been generally proposed. Nanometer-sized Pt particles dissolve and either agglomerate to form larger Pt grains, which leads to loss of surface area, or diffuse through the membrane and deposit in the

membrane or diffuse to the anode side. Several research groups have clearly reported this phenomenon. High potential excursions at the cathode accelerate the rate of Pt dissolution [255]. In particular, it would be very interesting to perform ex-situ studies of Pt nano-particle electrocatalysts under various acidic conditions. Ota *et al.* have performed such measurements on Pt/C and Pt wires under different H_2SO_4 concentrations, temperatures and oxygen partial pressures. The latter amounts to an effective control of potential, because the potential experienced by the catalyst is simply be related to $[O_2]$ through the Nernst equation. In case of bulk Pt, such as a Pt wire, Ota did not observe any detectable Pt as were measured by induction coupled plasma; however, with nano-sized Pt particles, detectable Pt^{2+} and Pt^{4+} ions were observed. Ota discusses the role of $[O_2]$, electrochemical potential and temperature on the dissolution of Pt [253].

4.7 Summary of the Corrosion Experiments

We have studied the corrosion of transition metals in numerous binary $Pt_{1-x}M_x$ and ternary $Pt_{1-x-y}M_xM'_y$ alloys (M = Ni, Co, Mn, Fe) deposited on NSTF support. Corrosion of the transition metal elements occurs when the electrocatalysts are subjected to 1M H_2SO_4 at 80°C and also when they are utilized under the typical working conditions of a PEMFC. The composition changes that occur during the acid treatment mimic those that occur during fuel cell testing very closely. Regardless of the initial overall transition metal atomic fraction, the average transition metal atomic fraction is reduced to at most a value of about 0.3. This suggests that it is difficult for the transition metal atoms to diffuse from the cores of the grains when the atomic fraction is less than 0.3. In all cases, for all the libraries studied, it is very likely that there is a significant loss of transition metals at the alloy surface. This explains why the average transition metal content is reduced even for alloys where the initial transition metal atomic fraction is less than 0.3.

Chapter 5

Stability and ORR Activity of $Pt_{1-x}Ta_x$ ($0 \leq x \leq 1$)

5.0 Introduction

This chapter presents the data that were published in [256]. First materials science, that is synthesis, physical characterization and corrosion studies of Pt-Ta films, is discussed. These results continue the theme of the previous chapter. Later, electrochemical results or the ORR activities of Pt-Ta films, are presented. Emphasis is placed on the characterization of pure Pt, which forms a baseline against which the activities of all other electrocatalysts are compared.

5.1 $Pt_{1-x}Ta_x$ ($0 \leq x \leq 1$) Libraries

The previous chapter studied the corrosion instability of the 3d transition metals when alloyed with Pt and used as electrocatalysts in FC or exposed to acid. A logical question would then be the impact of Pourbaix-stable elements such as Ta or Nb. These metals form a passivating layer in low pH media. Can one minimize transition metal leaching in Pt-alloys by including metals that are Pourbaix-stable, like Ta or Nb? In the recent years Hashimoto *et al.* have produced sputtered films of Ta and Nb-based alloys like Mn-Ta-Cr with excellent stability in acidic media [257, 258]. Before complex systems like Pt-Ta-Ni or Pt-Nb-Ni are investigated, it seemed wise to study the stability and activity of $Pt_{1-x}Ta_x$ and to determine the tolerance of Pt to the presence of a passivating metal like Ta, which would presumably reduce the ORR activity.

5.2 Materials Science and Acid Stability Tests

Two different types of Pt-Ta libraries were prepared. First, full binary libraries of $Pt_{1-x}Ta_x$ ($0 \leq x \leq 1$), where x varied linearly with position were made. These libraries were used in materials science studies. Figure 5.1 shows the composition versus position of such a library. The bulk oxygen content of the film is negligible.

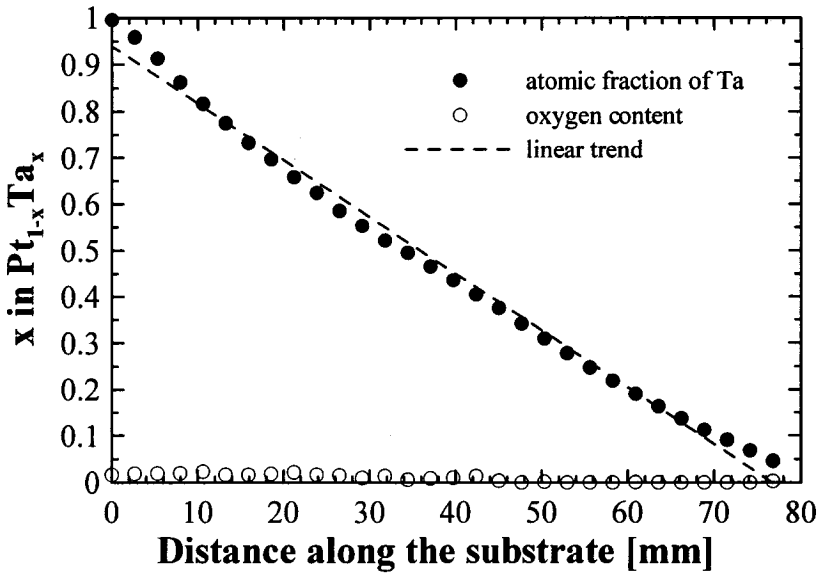

Figure 5.1 *The composition variation of the $Pt_{1-x}Ta_x$ ($0 \leq x \leq 1$) library deposited on a Si wafer determined by electron microprobe.*

A survey of the literature shows that a number of intermetallic phases have been observed in the Pt-Ta system using equilibrium preparation methods [259]. Several low symmetry phases like body-centered tetragonal Pt_4Ta, monoclinic Pt_3Ta, orthorhombic Pt_2Ta and their co-existence regions have been reported in the literature, plus a tetragonal σ and a superconducting A15 phase [260-262]. Figure 5.2 shows the XRD patterns of the sputtered $Pt_{1-x}Ta_x$ ($0 \leq x \leq 1$) library deposited on alumina. The composition change, between each adjacent diffractogram in Figure 5.2 is about $\Delta x = 0.05$. For $x < 0.5$, a single, face centered cubic (fcc) phase is observed. Ta, with a similar atomic radius to that of Pt (~ 1.5 Å), does not seem to strongly affect the fcc lattice size of Pt and random solid solutions are apparently formed over the range of $0 < x < 0.5$, which is not seen in the equilibrium Pt-Ta binary phase diagram. Only for $x \sim 0.45$ is the fcc (111) peak is shifted to lower scattering angles, indicating a slight increase of the lattice size. For $x > 0.5$, Figure 5.2 indicates a sudden transition to an overall nano-crystalline phase. Presumably increasing the Ta concentration beyond 50% or so disrupts the long range ordering of the fcc lattice and an amorphous-like film of $Pt_{1-x}Ta_x$ is formed. The glassy behavior of $Pt_{1-x}Ta_x$ for $x > 0.5$ observed here is not surprising, given the non-equilibrium nature of the sputtering process [199, 263]. The crystalline, intermetallic phases mentioned before in the literature, were reportedly formed after annealing at temperatures in the range of 1000 – 1600°C [260].

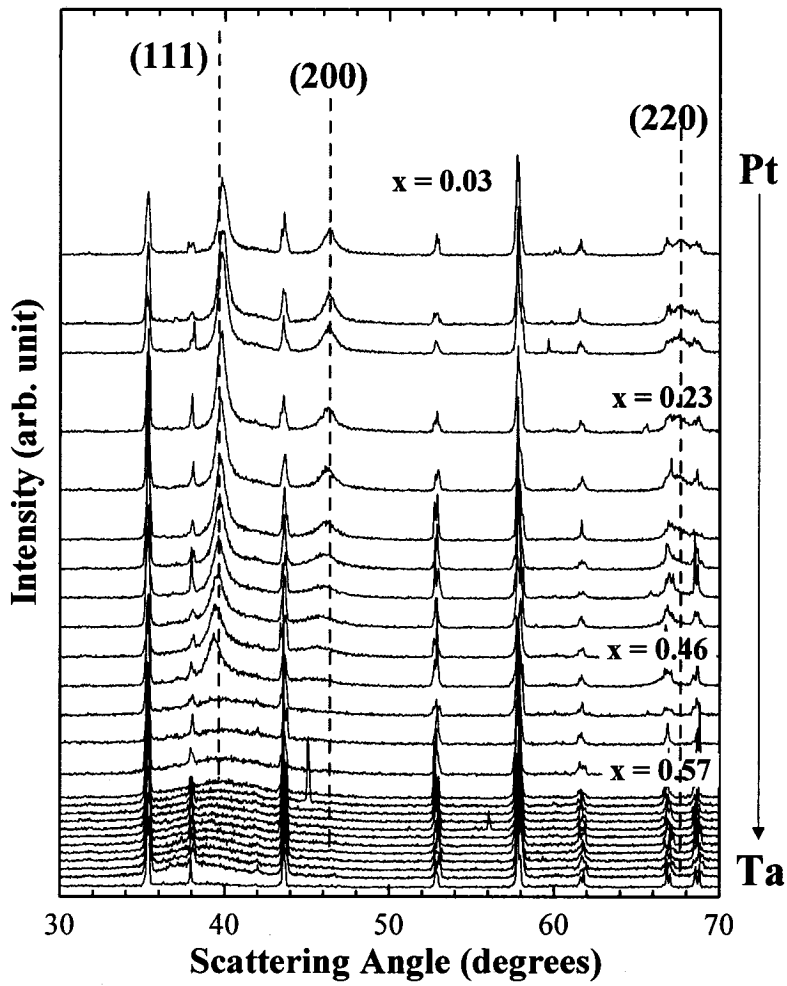

Figure 5.2 *X-ray diffractograms of the $Pt_{1-x}Ta_x$ ($0 \leq x \leq 1$) library shown for different values of x. The Miller indices of the fcc phase are indicated. Unlabeled peaks correspond to the alumina substrate.*

Microprobe measurements of bulk compositions were performed on acid treated libraries made on alumina and NSTF substrates. All the libraries contained the entire binary composition range. Figures 5.3a and 5.3b show the Ta content after acid treatment (x_{after} in $Pt_{1-x}Ta_x$) versus the Ta content before treatment (x_{before} in $Pt_{1-x}Ta_x$) on alumina (Figure 5.3a) and on NSTF (Figure 5.3b) substrates. The dashed line corresponds to the composition of an untreated sample. No dissolution of Ta is observed for any of the treated samples under the tested conditions. The testing conditions were similar to those of described in the previous chapter: 25°C or 80°C, in H_2SO_4 or $HClO_4$ on either alumina or NSTF substrates. These results are in marked contrast to binary and ternary alloys studied in the previous chapter, where significant leaching of 3d metals was observed.

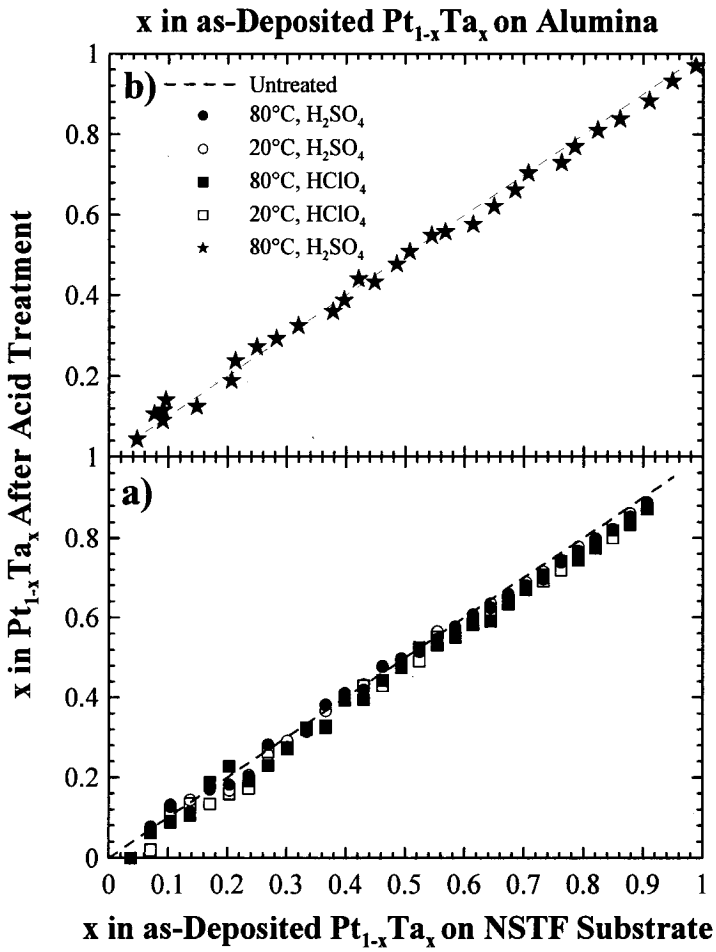

Figure 5.3 *The composition of the films determined by electron microprobe after acid treatment versus the composition of the films before acid treatment. No loss of Ta is seen on either alumina (flat surface) or NSTF (high surface area) substrates.*

The stability of Ta is not surprising because it passivates in acidic media. This was confirmed by XPS measurements.

Figure 5.4 shows the XPS spectra of the Ta core level $4f_{7/2}$ and $4f_{5/2}$ doublet peaks. The measurements were made for the as-made and acid treated libraries. Only a selected number of spectra are shown. The corresponding bulk composition, or x in $Pt_{1-x}Ta_x$ ($0 \leq x \leq 1$), is also indicated in the Figure. In the as-deposited library and for $x < 0.5$, two sets of 4f doublet peaks, a metallic and an oxide can be observed. The position of the Ta oxide 4f peaks roughly corresponds to those of the Ta^{5+} oxidation state [219]. For $x > 0.5$, however, a sub-oxide phase appears, which will be referred to here as Ta^{z+}. There are indications of sub-oxide phase(s) in the literature [257, 264]. Spectra taken on the

acid-treated library are shown in the right column of Figure 5.4. It is clear that for x > 0.5 all Ta is oxidized to form Ta_2O_5.

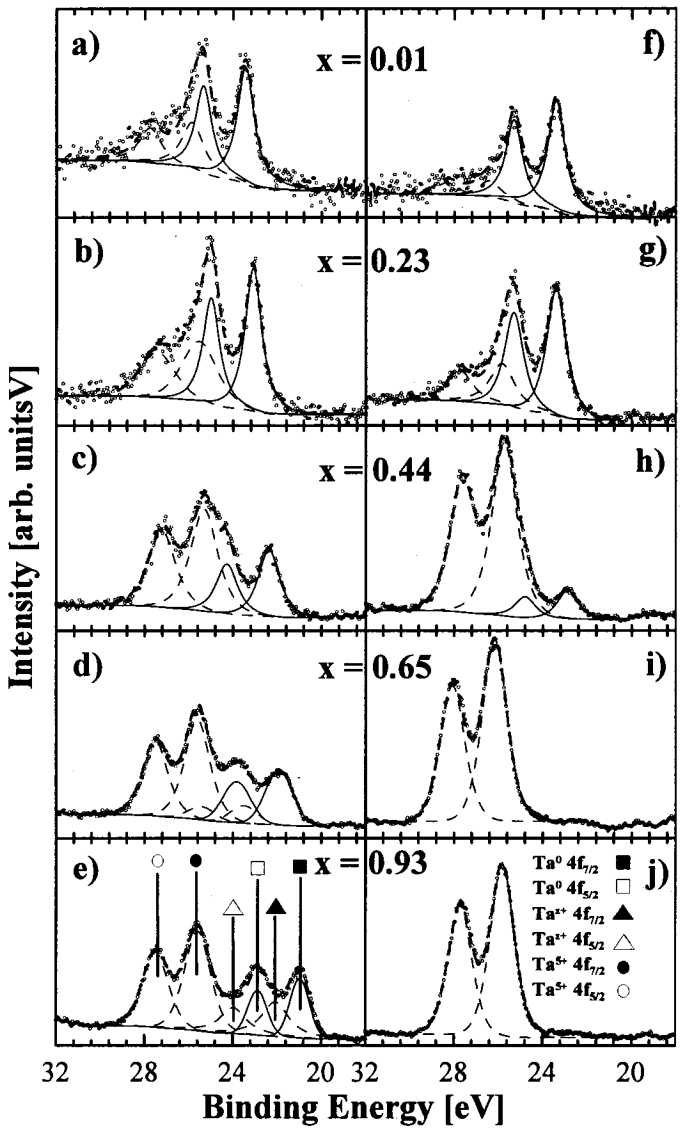

Figure 5.4 *XPS spectra of Ta 4f electrons for $Pt_{1-x}Ta_x$ ($0 \leq x \leq 1$) before acid (left) and after acid (10 days in 1M H_2SO_4 at 80°C) (right) shown for selected x values in the $Pt_{1-x}Ta_x$ ($0 \leq x \leq 1$) library. Dashed and solid lines are the fitted results for the Ta oxide and metallic Ta, respectively. The overall fitted envelope is shown as a dashed line through the experimental data points.*

Figure 5.5 shows the 4f doublet peaks of Pt before and after acid treatment, where except for some variations in the intensity, no other noticeable changes are observed.

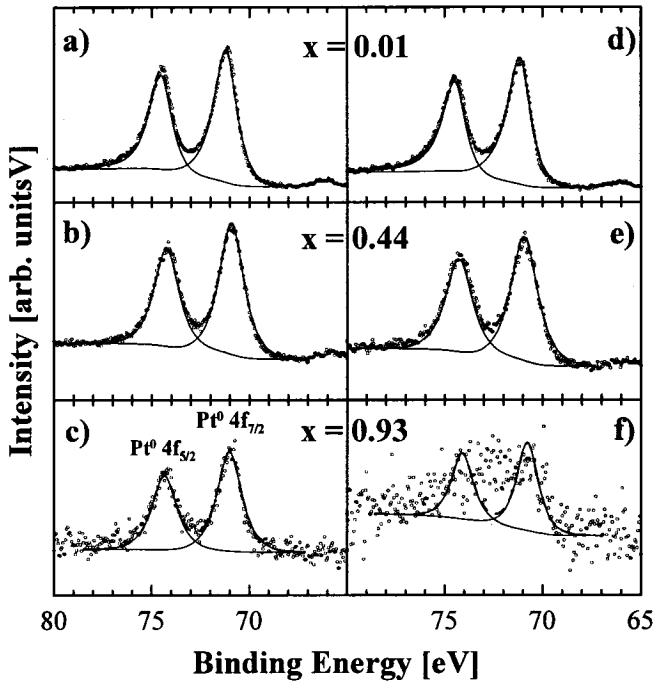

Figure 5.5 *XPS spectra of Pt 4f electrons for $Pt_{1-x}Ta_x$ ($0 \leq x \leq 1$) before acid (left) and after acid (10 days in 1M H_2SO_4 at 80°C) (right) shown for some values of x in $Pt_{1-x}Ta_x$ ($0 \leq x \leq 1$).*

Figure 5.6a shows the surface content of Ta in the film before and after acid treatment. Note that the pre-acid measurements are in a good agreement with the bulk composition obtained by electron microprobe. The penetration depth, where 95 % of the photoelectrons originate, can be estimated by 3 IMFP·cos(α), where IMFP is the inelastic mean free path and α is the emission angle of the electrons relative to the surface normal (0° in our case). Using IMFP values reported in Briggs [219] we can obtain an approximate value of 4-6 nm for the penetration depth. Thus probing to a depth of 4-6 nm the surface composition of the $Pt_{1-x}Ta$ ($0 \leq x \leq 1$) is bulk-like and no segregation is seen over this length. After acid treatment, however, an increase in the surface Ta content is seen for $x > 0.5$. It may be possible that oxidation of Ta at the surface induces a solid-state diffusion of Ta atoms to the surface and thus increases the overall surface Ta content.

Figure 5.6b shows the fraction of surface Ta that is in an oxidized form. As the Ta content increases across the library, the Ta oxide fraction also increases. For the acid-treated library, for $x_{before} < 0.5$, there seems to be a decrease in the surface Ta oxide

content. However, for x > 0.5, all surface Ta is in oxide form. The nano-crystalline nature of the film (for x > 0.5) may have promoted the passivation of Ta. Amorphous films are known to show good corrosion resistance by formation of passivating layers [265-267].

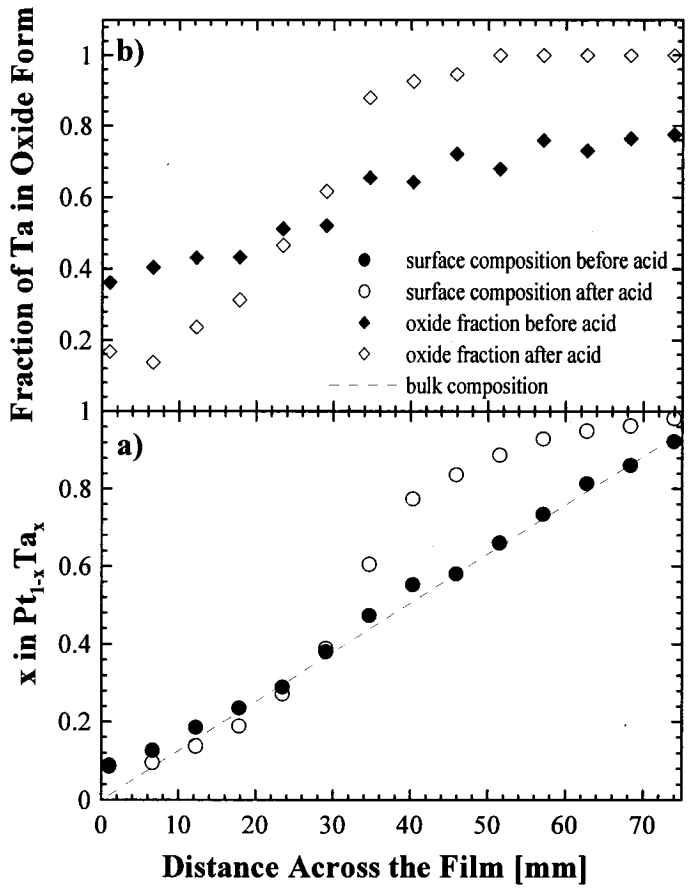

Figure 5.6 *a) Surface composition of $Pt_{1-x}Ta_x$ before acid (filled circles) and after acid treatment (10 days in 1M H_2SO_4 at 80°C) (open circles) plotted versus position in the library. b) Fraction of Ta in oxide form before acid (filled circles) and after acid treatment (open circles) plotted versus position in the library.*

The binding energies of Ta and Pt $4f_{7/2}$ core electrons are plotted versus x in $Pt_{1-x}Ta_x$ and are shown in Figure 5.7. Figure 5.7a shows the binding energy of metallic Ta versus x in $Pt_{1-x}Ta_x$ ($0 \leq x \leq 1$) before and after acid-treatment. As the Pt content increases in the library, the binding energy of the Ta $4f_{7/2}$ core level increases by about 2 eV. Some changes in the binding energy of Ta^{z+} can also be seen in Figure 5.7b. No changes in the binding energies of Ta^{5+} 4 $f_{7/2}$ (26 eV) and Pt^0 4 $f_{7/2}$ (71 eV) are observed in Figures 5.7c and d. The reason for the shift in the binding energy of Ta^0 is not clear, as this is unlikely a charge transfer to Pt. Bonding in Pt-Ta, where the electronegativity differences are

small (10%), is likely to be covalent and charge transfer probably could not account for this observed increase [268]. Ruckman *et al.* reported the appearance of a second metallic Ta 4f doublet for a monolayer of Pt on Ta (110).

Although $Pt_{1-x}Ta_x$ has been shown to be basically stable under the acid-exposure conditions tested here, the passivation effect could hinder the electrocatalytic properties of $Pt_{1-x}Ta_x$. One is therefore interested to know the maximum amount of a passivating metal like Ta that can be added to Pt without adversely affecting its catalytic behavior.

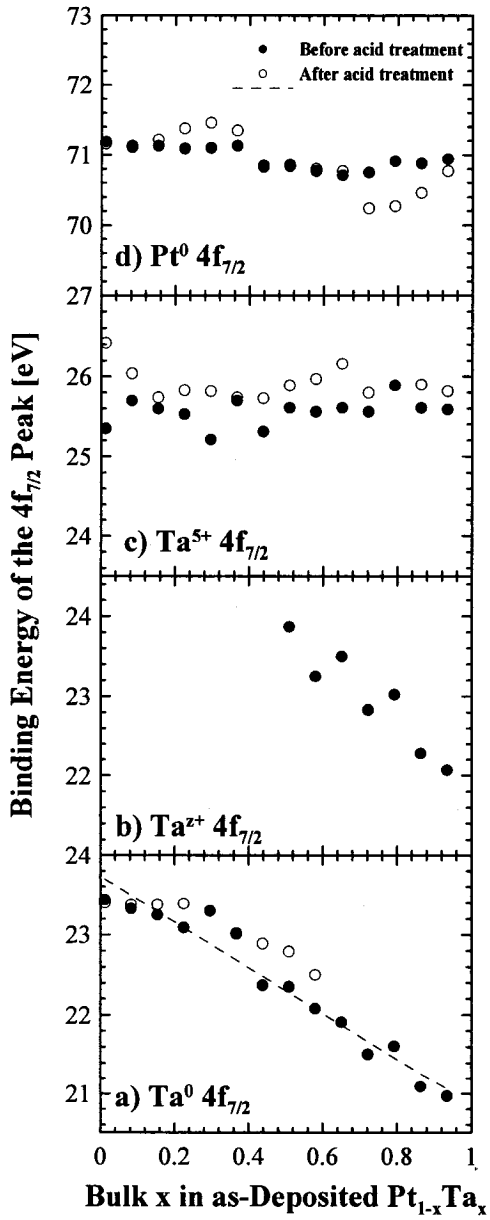

Figure 5.7 *Binding energies of the Ta 4f electrons in different oxidation states and for Pt in the $Pt_{1-x}Ta_x$ ($0 \leq x \leq 1$) combinatorial library.*

5.3 Electrochemical Characterizations

An extensive set of data on sputtered Pt as a baseline is presented first. In order to characterize and assess the electrocatalytic activity of materials, it is of utmost importance to establish state-of-the-art baseline measurements and compare the activities of different electrocatalysts as carefully and as objectively as possible. Gasteiger *et al.* illustrate this point by comparing the literature results of Pt baseline electrocatalysts from numerous sources [87]. Overall, the activity of pure Pt electrocatalysts, reported in FCs, vary by about one order of magnitude. The authors propose a set of guidelines for evaluating the activity of electrocatalysts using FCs and solution-based RRDE cells. Failure to establish state-of-the-art of Pt baseline measurements results in questionable conclusions. This point is discussed in some detail in the next chapter.

5.3.1 Physical Characterizations of Pt Baseline

X-ray diffraction patterns of as-sputtered and annealed Pt films of various thickness are shown in Figures 5.8a and b. Figure 5.8 shows the (111) and (200) Bragg reflections of fcc-structured Pt and the amorphous-like scattering of the GC substrate, which decreases with the increasing Pt thickness. From the peak widths and the Scherrer relation, we find an approximately four-fold, 20 ± 4 to 80 ± 10 nm, increase in the grain size of the Pt film crystallites after annealing the samples at 750°C under Ar.

SEM images of the films, before and after annealing, also indicate grain growth. Figures 5.9a-b show the SEM images of as-deposited and annealed Pt films (250 and 315 nm). Before annealing, irregular, small Pt grains are observed. After annealing, the fusion and formation of larger and more well-defined grains is seen. Grain sizes observed in the SEM pictures are approximately the same as those calculated by XRD peak broadening.

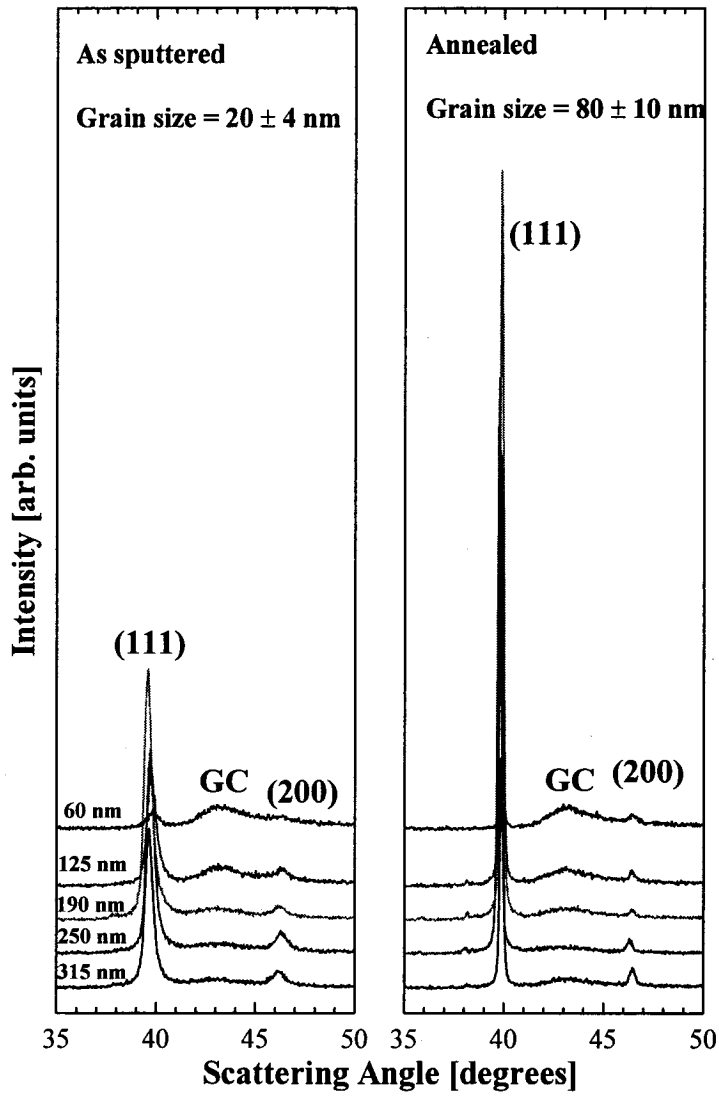

Figure 5.8 *X-ray diffraction patterns of Pt sputtered on GC disks a) as sputtered and b) after annealing.*

Figure 5.9 *SEM micrographs of Pt films (60 nm) deposited on GC disks before (left) and after annealing (right).*

5.3.2 Electrochemical Characterizations of the Sputtered Pt Baseline Samples

Different regions of the CV, i.e. adsorption/desorption of H and OH, are shown in Figure 5.10. This CV is a signature of a clean polycrystalline Pt in high purity $HClO_4$ solution. The adsorption/desorption peaks of H and OH are fully developed and no other peaks are present. After an electrode is inserted into the cell, it usually takes about 50-100 CVs for peaks to become fully developed and reach a steady state, as shown in Figure 5.10. The procedures were described in chapter 3 and are also outlined in Appendix C. Obtaining clean CVs, as shown in Figure 5.10, is a critical step in obtaining acceptable ORR data.

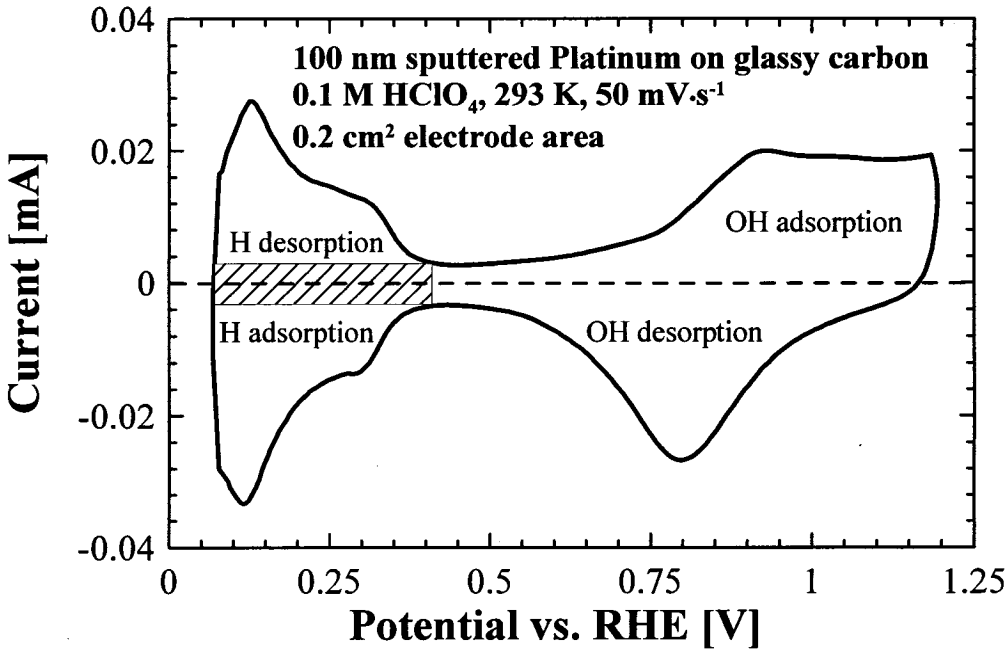

Figure 5.10 *Cyclic voltammogram of sputtered Pt on a GC disk in 0.1M $HClO_4$ with 50 $mV{\cdot}s^{-1}$ sweep rate. The double layer capacitance, subtracted during the electrochemical surface area calculation, is shown as a shaded rectangle.*

CVs of the as-deposited and annealed films, with different thickness, are shown in Figure 5.11. As-deposited Pt films show much larger $H^{+}_{ads/des}$ peaks, indicating their larger surface area. The surface enhancement factor for the as-deposited films is about 3 and is primarily due to presence of film roughness, grain boundaries and possible cracks in the film. For better adhesion of sputtered Pt, 15 μm finish glassy carbon (GC) disks were used. A CV of the Pine Pt RDE (polycrystalline, identical geometric surface is also shown for comparison. The as-deposited films show a range of ECSA with the thicker films (250 and 315 nm) having the highest surface areas. After sintering, there is a

significant reduction in the ECSA of all the films as shown in Figure 5.11b leading to an SEF value of about 1 for almost all the disks.

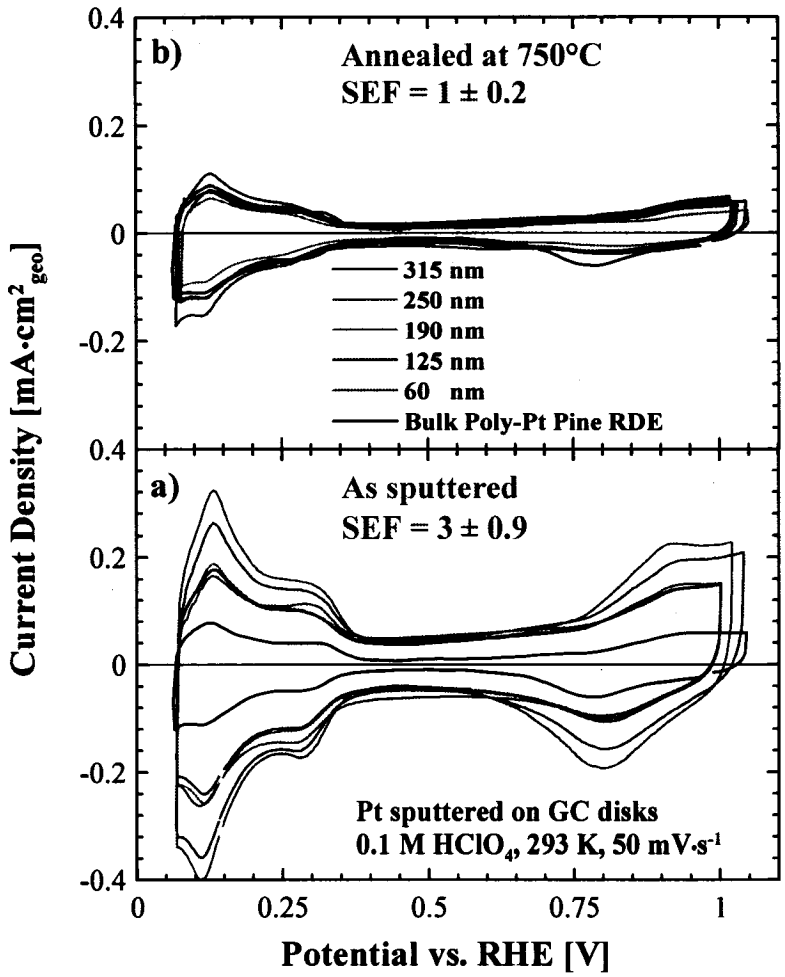

Figure 5.11 *Cyclic voltammograms of sputtered Pt films a) before and b) after annealing. The same scale was chosen in both panels to emphasize the reduction of ECSA after annealing.*

The oxygen reduction activity of the sputtered Pt film, whose CV was shown in Figure 5.10 is presented in Figure 5.12. All the currents were normalized by the geometric surface area. At all measured rotation speeds, the disk currents reached diffusion-limited current. The limiting-currents, in all cases, reached the theoretical values, which can be calculated by the Levich equation,

$$j_{diffusion} = 0.62nFAD^{2/3}\omega^{1/2}\upsilon^{-1/6}C, \qquad (5.1)$$

using literature reported values of $D = 1.93\times10^{-5}$ $cm^2\cdot s^{-1}$, $C = 1.26\times10^{-3}$ $mol\cdot L^{-1}$ and $\upsilon = 1.009\times10^{-2}$ $cm^2\cdot s^{-1}$, for oxygen diffusion, oxygen concentration and water kinematic

viscosity at room temperature [167]. The limiting-current can also be written in a more compact form as $j_{diffusion} = B \cdot \omega^{1/2}$ mA·cm$^{-2}_{geometric}$, where the 'B' parameter corresponds to the above constants and has a numerical value of about 0.15 rpm$^{-1/2}$·mA·cm^{-2}. H_2O_2, detected by the ring, is also shown in Figure 5.12 for all the rotation speeds. As is the case with polycrystalline Pt, H_2O_2 is only observed for potentials below 0.6 V or so. The yield rises to about 10-20% in the $H_{ads/des}$ region, where site blocking occurs.

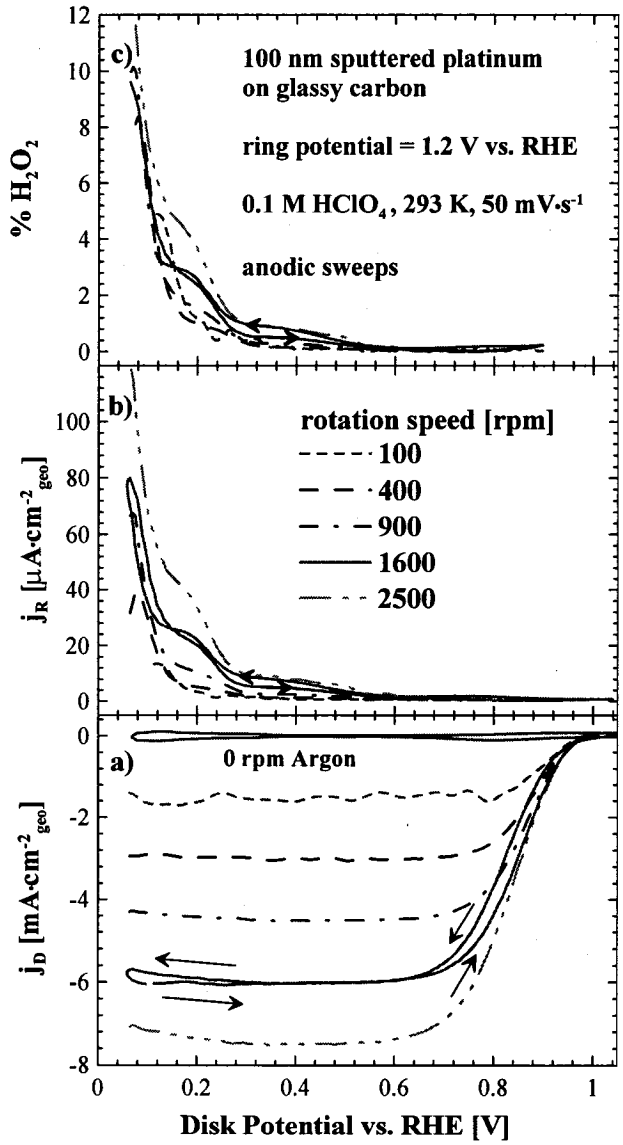

Figure 5.12 *a) Disk current densities for ORR of the sputtered Pt on GC disk in 0.1M $HClO_4$ are shown for different rotation rates. b) The ring current densities and c) percentage H_2O_2 produced are shown for different rotation speeds.*

Diffusion-limited currents can be read directly from the ORR data shown in Figure 5.12, or using Levich-Koutecky plots, where one plots $j_{diffusion}^{-1}$ versus $\omega^{-0.5}$. In these plots, the

slope of the lines is the 'B' parameter mentioned earlier and the intercepts are the reciprocal of kinetic currents at that particular potential. Identical slopes, as observed in Figure 5.13, indicate that diffusion-limiting currents are reached at all rotation speeds; that is, the turnover frequency and/or the number of active sites are not limiting the oxygen reduction currents. Using LK plots and equation 5.1 one can obtain a value of n, or number of electrons transferred in the reaction. This is an alternative way of obtaining the H_2O_2 yield.

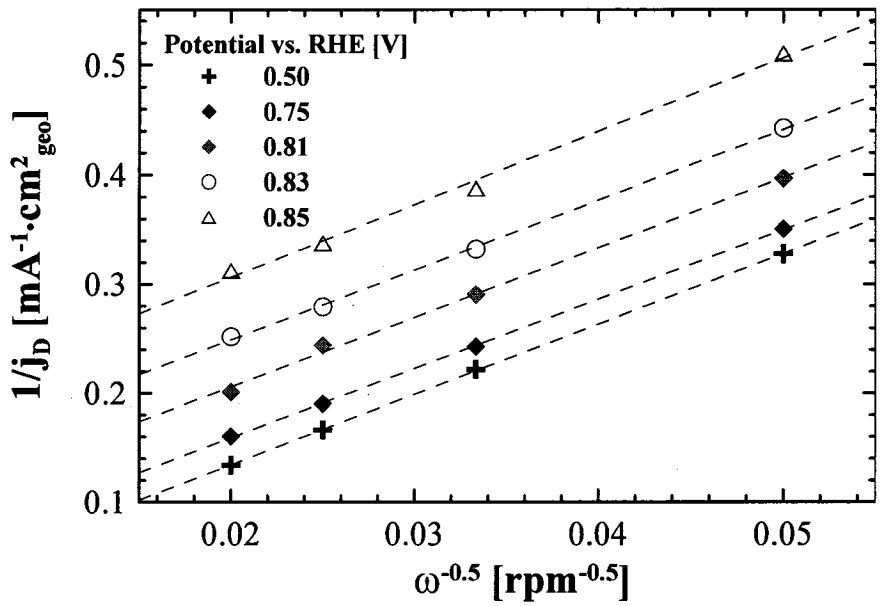

Figure 5.13 *Levich-Koutecky plots of the ORR results for the Pt sputtered GC disk are shown for various potentials.*

Figure 5.14 shows the ORR data of the sputtered Pt films with different thickness at 900 rpm. Note that essentially all the measurements, both disk and ring, are equivalent. All the disk measurements shown reach the theoretical diffusion-limited current, which is about 4.5 $mA \cdot cm^{-2}_{geometric}$. Ring currents and calculated H_2O_2 released into the solution are consistent with Pt measurements reported in the literature; that is, almost no peroxide detected above 0.6 V or so, with an increasing levels coinciding with the H adsorption/desorption region. Note that the annealed samples show more identical H_2O_2, which could be indicative of their surface uniformity.

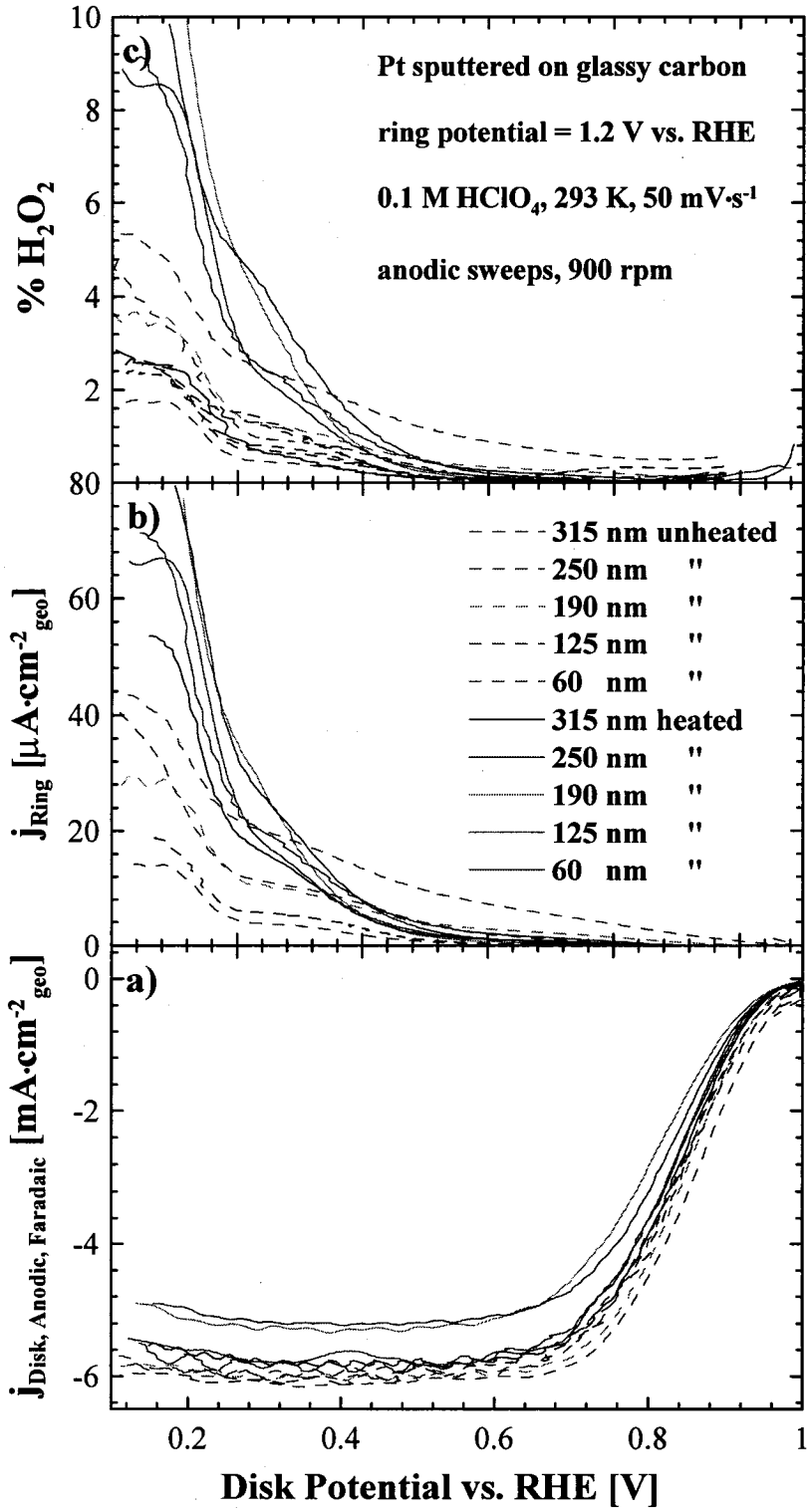

Figure 5.14 *RRDE results of sputtered Pt films for as-deposited (dashed) and annealed films (solid). a) Oxygen reduction (disk) currents, b) H_2O_2 oxidation current (ring) and c) H_2O_2 percentage released into solution during the ORR.*

The kinetic-diffusion region of these ORR measurements and the Tafel fits are shown in Figure 5.15. The currents shown, as was explained in the experimental section, are corrected for the non-Faradaic and mass-transfer contributions and are normalized by the ECSAs. Subtraction of the Ar-CVs (the non-Faradaic currents) from the ORR data makes the Tafel lines more straight at potentials higher than about 0.9 V. Although not very significant here, the non-Faradaic currents become important in the measurements of high surface area catalysts and/or measurements taken at high sweep rates.

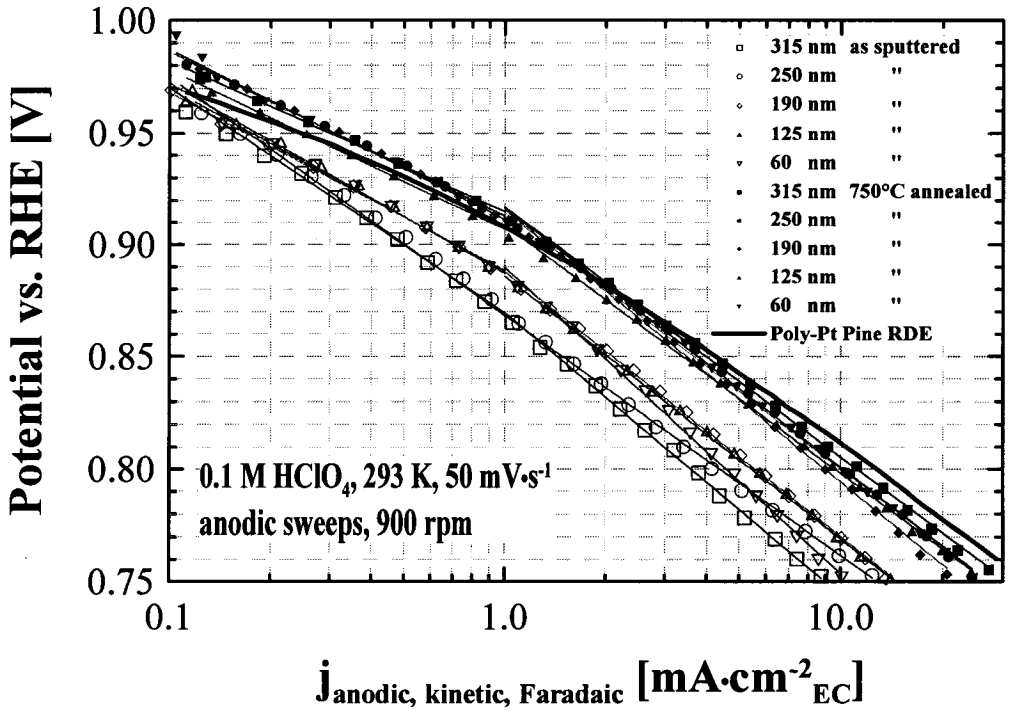

Figure 5.15 *Tafel kinetics region of Pt films for a) as-deposited (not dashed) and b) annealed (dashed). Tafel fits to data are also shown.*

Note that as-deposited measurements fall into two groups. The reason for the differences observed in the as-deposited film is not known; however, we notice that the thick Pt films (250, 315 nm) which show lower activity have the highest ECSA (Figure 5.11). We could speculate that there is either a significant surface morphology/impurity difference between these two samples and the rest in the group or that normalization by ECSA doe not always lead to a one to one correspondence between ECSA and measured current. For the 250 nm thick Pt film, the data can be fit by one Tafel slope of about – 110 ± 5 mV·decade^{-1}. The other four as-deposited Pt films show a two-slope region with

values of –82 ± 3 and –124 ± 1 mV·decade^{-1} for the data above and below 0.9 V, respectively.

The data for the annealed samples show higher activity and show more consistency. Note that overall there is a significant difference in the overpotential of the lowest (as-deposited, 250 nm) and the highest (annealed, 250 nm) Tafel lines: 40 mV difference at 1 mA·cm$^{-2}_{EC}$. This variation is almost as large as the largest overpotential gains reported for best carbon-supported Pt-alloys over Pt/C [162]. What is the cause of these deviations? Part of the difference might be attributed to presence of different Pt crystal facets. Activity of Pt towards ORR shows both structural and electrolyte dependencies. In $HClO_4$, the activity of different crystallographic planes decreases in the order of Pt(110) > Pt(111) > Pt(100) [165]. Annealing presumably leads to more thermodynamicaly stable facets and helps in formation of more homogenized surfaces. In addition, the impact of Pt nanoparticle size on ORR activity has been reported in the literature. According to Mayerhofer *et al.* [249] in larger grain size Pt nanoparticles, higher activity, coupled with a shift of the OH adsorption to higher potentials, is observed when the grain size changes from 2-3 to15 nm or so [249]. However, for the as-sputtered and annealed samples studied here, where the grain size changes from 20 to 80 nm or so, no significant changes in the OH adsorption region were observed.

The Tafel lines of these annealed Pt films with different thicknesses are consistent with one another and are in agreement with that of the Pine polycrystalline Pt electrode, used as a control. The Tafel slopes of the annealed Pt films are –72 ± 3 and –115 ± 4 mV·decade^{-1} for the data above and below 0.9 V, respectively. The Pine Pt electrode shows Tafel slopes of –65 and –103 mV·decade^{-1} for the data above and below 0.9 V, respectively. These values are in close agreement with the values often reported for the Tafel slope of ORR observed on Pt surfaces in $HClO_4$ [165, 269]. In $HClO_4$ solution, with weak anion adsorption, two slopes (60 and 120 mV·decade^{-1}) have been observed on all three different Pt surfaces [269]. In H_2SO_4 both slopes have been observed for (100) and (110), where anion adsorption is weak and only 120 mV·decade^{-1} has been seen for the (111) facet with strong anion adsorption [166]. The 60 mV·decade^{-1} slope has been in the past attributed to a Temkin-type adsorption of oxide species [161]. More recently, Wang *et al.* proposed a model, which by consideration of site blocking and energetic

effects of OH and anions, could quantitatively account for the differences in the Tafel slopes observed for Pt (111) in H_2SO_4 and $HClO_4$, where bisulfate and OH adsorption are the inhibiting factors, respectively [270]. In $HClO_4$ the changes in the Tafel slope coincide with the changing coverage of OH in the mixed kinetic-diffusion region [161, 270]. The Pt measurements reported here are consistent with the state-of-the-art measurements reported in the literature [167, 172, 176]. Thus it is believed that they form a fair and valid set of Pt baselines for comparing alloys, like Pt-Ta discussed below and Pt-Co discussed in the next chapter.

5.3.3 RRDE Electrochemical Characterizations of $Pt_{1-x}Ta_x$ ($0 \leq x \leq 0.3$)

To measure the ORR activity of Pt-Ta films, a $Pt_{1-x}Ta_x$ library, with $0 \leq x \leq 0.3$, was prepared. This library consisted of a constant Pt deposition and a linearly varying Ta content in $PtTa_y$ ($0 \leq y \leq 0.4$). Figure 5.16 shows that the Ta content, y in $PtTa_y$, varies linearly versus the position on the library. The $PtTa_y$ ($0 \leq y \leq 0.4$) notation is equivalent to $Pt_{1-x}Ta_x$ ($0 \leq x \leq 0.3$); thus the corresponding x values are also indicated in Figure 5.16. For the remaining measurements and discussions here, the $Pt_{1-x}Ta_x$ ($0 \leq x \leq 0.3$) notation is used. The location of the glassy carbon disks are indicated in Figure 5.16. Disk 1 corresponds to a composition of pure Pt. The glassy carbon disks have a diameter of 5 mm and hence have some variation in composition over the disk which can be estimated from the slope of the data in Figure 5.16. The composition reported for each disk is the average composition and typically the local composition varies by 5 atomic % or less over each disk.

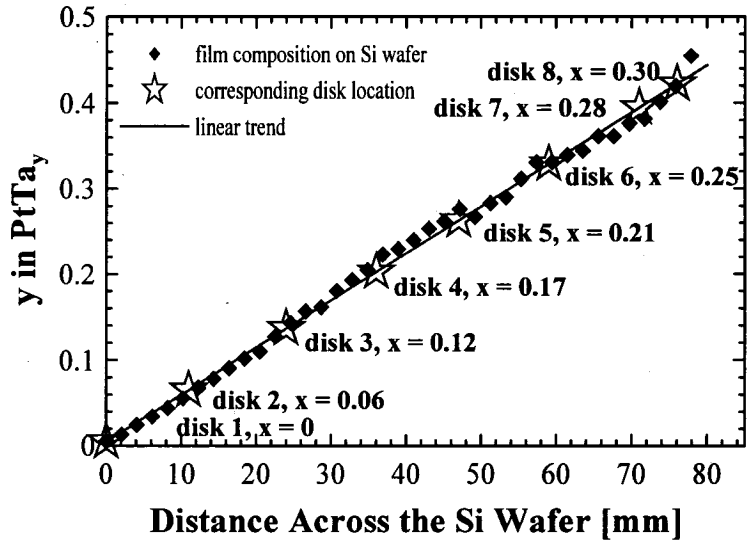

Figure 5.16 *Composition of the $PtTa_y$ library ($0 \leq y \leq 0.4$) deposited on a Si wafer as determined by electron microprobe. The corresponding positions of the glassy carbon (GC) disks are clearly indicated. For the GC disks, the corresponding values of x in $Pt_{1-x}Ta_x$ ($0 \leq x \leq 0.3$) are also shown.*

Similar measurements, CV under Ar and disk/ring measurements in oxygen-saturated solution at different rotation speeds, were performed for the other disks. Figure 5.17a shows the CV of several $Pt_{1-x}Ta_x$ compositions. The variation in the CV areas in Figure 5.17a is primarily due to the nature of the film surfaces, not the composition of the films, because when the current is normalized by the electrochemical surface area, as in Figure 5.17b, the CVs overlap for all the Ta-containing films.

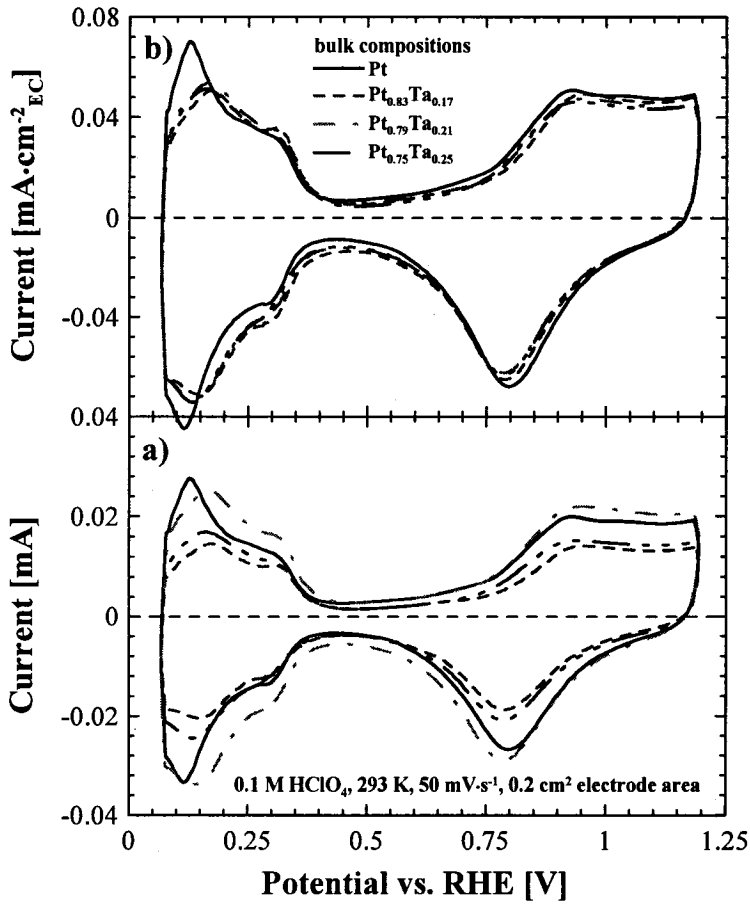

Figure 5.17 *a) Cyclic voltammograms of $Pt_{1-x}Ta_x$ ($0 \leq x \leq 0.3$) for selected values of x. b) The same CVs shown in (a) except the current has been normalized by the electrochemical surface area.*

Some disks showed a rougher morphology than others. Figure 5.18 shows SEM images of disks 3 and 4 (with x = 0.12 and x = 0.17) after RRDE measurements. Note the roughness induced by film wrinkles in Figures 5.18a and b. Disk 4, on the other hand, shows a very smooth morphology. The changes in the morphology are most likely due to differences in the surface of the glassy carbon disks. The variations in the surface morphology lead to surface enhancement factors (SEF) between 1.3 and 2.4 for the disks studied here.

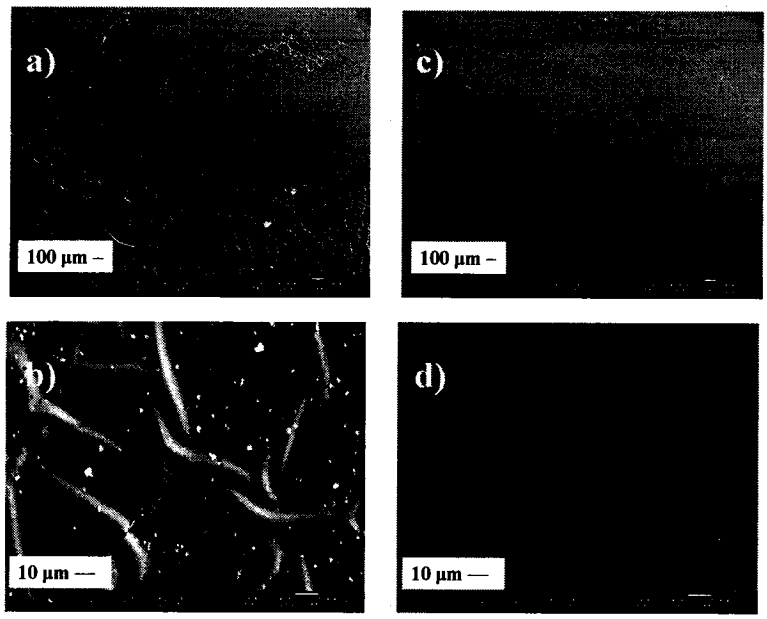

Figure 5.18 *SEM micrographs of $Pt_{0.88}Ta_{0.12}$ (a, b) and $Pt_{0.83}Ta_{0.17}$ (c, d) after RRDE measurements.*

Figure 5.19 shows the 1600 rpm disk and ring measurements of the $Pt_{1-x}Ta_x$ ($0 \leq x \leq 0.3$) disks. The ORR curves in Figure 5.19a can be divided into two groups: (I) where $x \leq 0.12$ and little apparent changes in the ORR curves are seen and (II) where $x > 0.2$ and significant loss of ORR activity is observed. The composition, $Pt_{0.83}Ta_{0.17}$, is apparently near the point where this transition occurs. A similar division can be applied to the detected H_2O_2 as is shown in Figure 5.19c. Poor activity in the ORR is coupled to an increased fraction of H_2O_2 production. This observation will be discussed somewhat more in chapter 8.

Detailed data for $Pt_{0.83}Ta_{0.17}$ and $Pt_{0.75}Ta_{0.25}$ are shown in Figure 5.20. In Figure 5.20a ORR measurements of Pt are shown for comparison. Note that activity drops, the diffusion limited current is not reached and the onset of H_2O_2 production has shifted from 0.6 V (Figure 11c) to about 0.8 V. Figures 5.20d, e and f show similar measurements for $Pt_{0.75}Ta_{0.25}$. The inset in Figure 5.20d shows a full cycle of ORR at 1600 rpm. The ORR activity is reduced and the background current due to adsorption/desorption of H/OH becomes significant.

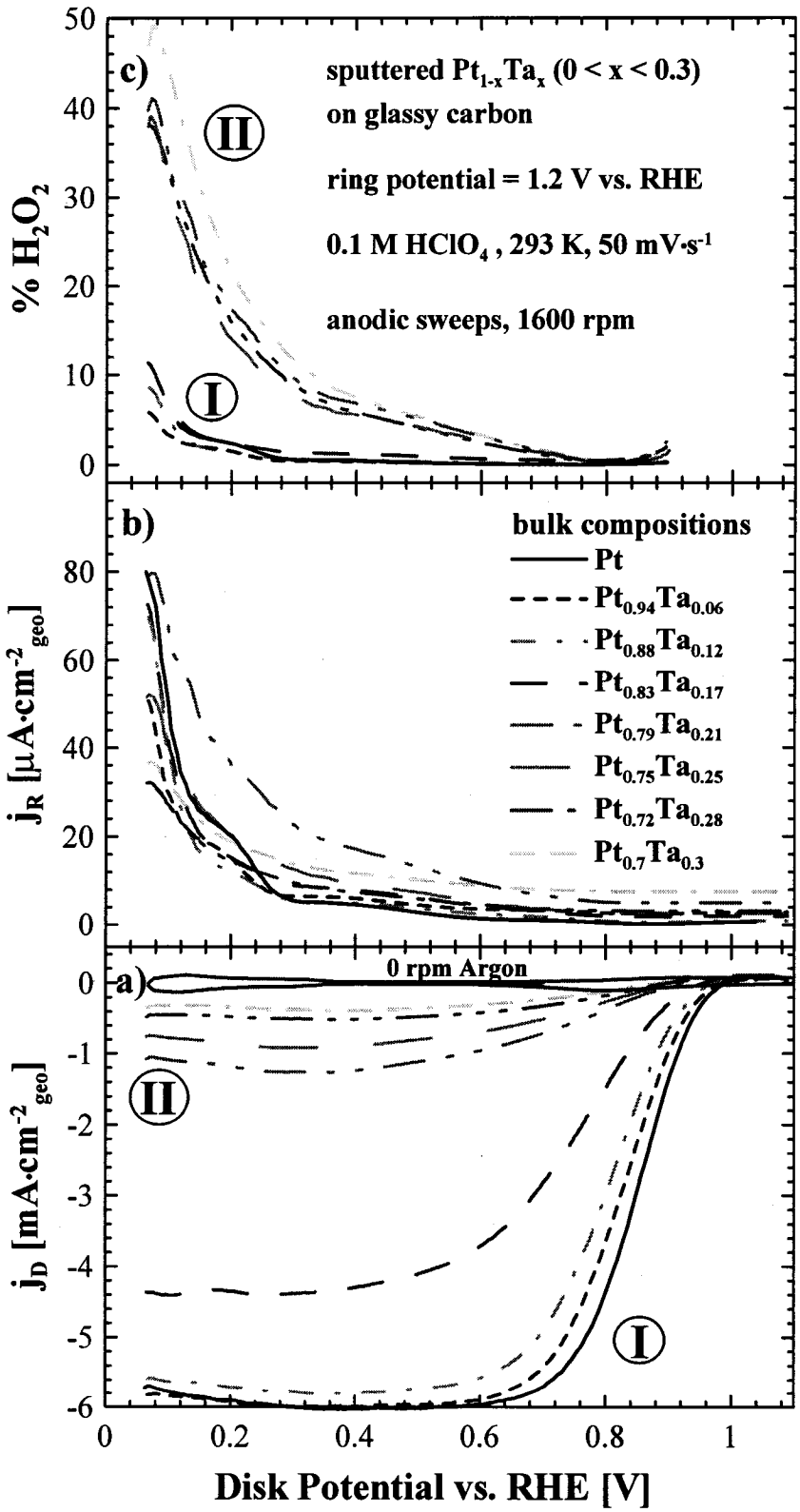

Figure 5.19 *a) The oxygen reduction behavior of several $Pt_{1-x}Ta_x$ ($0 \leq x \leq 0.3$) compositions shown at 1600 rpm and room temperature in 0.1M $HClO_4$. Panels b) and c) show the corresponding ring current and percentage of H_2O_2 produced, respectively.*

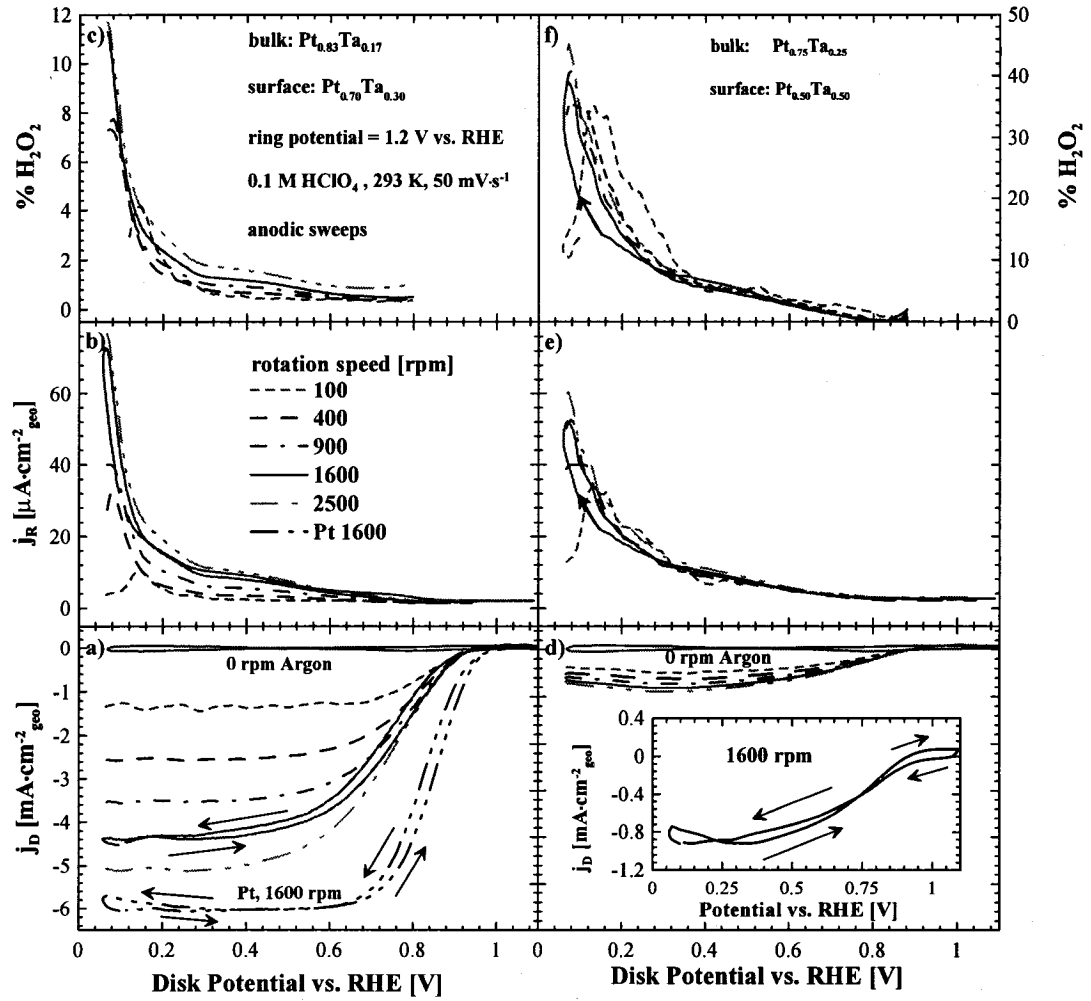

Figure 5.20 *Oxygen reduction current, ring currents and $\%H_2O_2$ shown for $Pt_{0.93}Ta_{0.07}$ (a, b, c) and for $Pt_{0.75}Ta_{0.25}$ (d, e, f). Panel (a) shows ORR of Pt for comparison. All the sweeps are anodic unless otherwise noted. If a cathodic/anodic cycle is shown, the sweep directions are indicated by an arrow. The inset in panel (d) shows a full cycle of the ORR measurement at 1600 rpm.*

Figure 5.21 shows the Tafel region of the ORR curves from Figure 5.19a for the different Ta concentrations. The XPS results in Figures 5.4, 5.5 and 5.6 suggest that there should still be significant Pt at the surface for $x < 0.3$, so it is somewhat difficult to understand the reason for the dramatic reduction in activity with Ta content. However, XPS probes to a depth of about 4-6 nm, so it is possible that the content of Ta, presumably in oxide form, is higher in the first few surface layers.

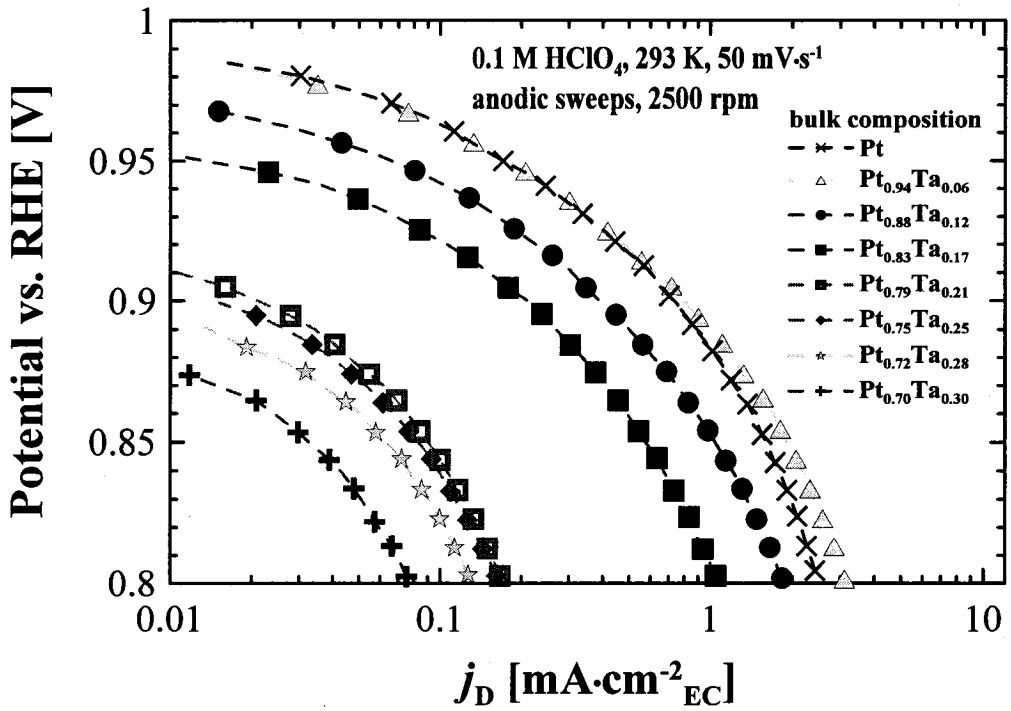

Figure 5.21 *Tafel region of the ORR of $Pt_{1-x}Ta_x$ ($0 \leq x \leq 0.3$) shown for the anodic sweeps.*

Figure 5.22 shows the XPS measurements of the $PtTa_y$ ($0 \leq y \leq 0.4$) (= $Pt_{1-x}Ta_x$ ($0 \leq x \leq 0.3$)) library used for the electrochemical studies. A similar analysis was performed as in the case of the $Pt_{1-x}Ta_x$ ($0 \leq x \leq 1$) library described by Figures 5.4, 5.5 and 5.6, except that in this case, measurements were made before and after the RRDE experiments. Figure 5.22 shows that for $x > 0.15$, the surface composition of the as-deposited film on a Si wafer shows a larger concentration of Ta compared to the bulk composition measured by electron microprobe.

XPS measurements made on the glassy carbon disks, after the RRDE measurements, show surface compositions relatively close to those of the as-deposited films. For this library, the surface Ta is about 60 % in oxide form before the RRDE measurements and after RDE measurement the oxide fraction increases to about 80% for the Ta-rich end of the library. This increase in oxide content could help explain the poor ORR kinetics of the group II samples in Figure 5.19.

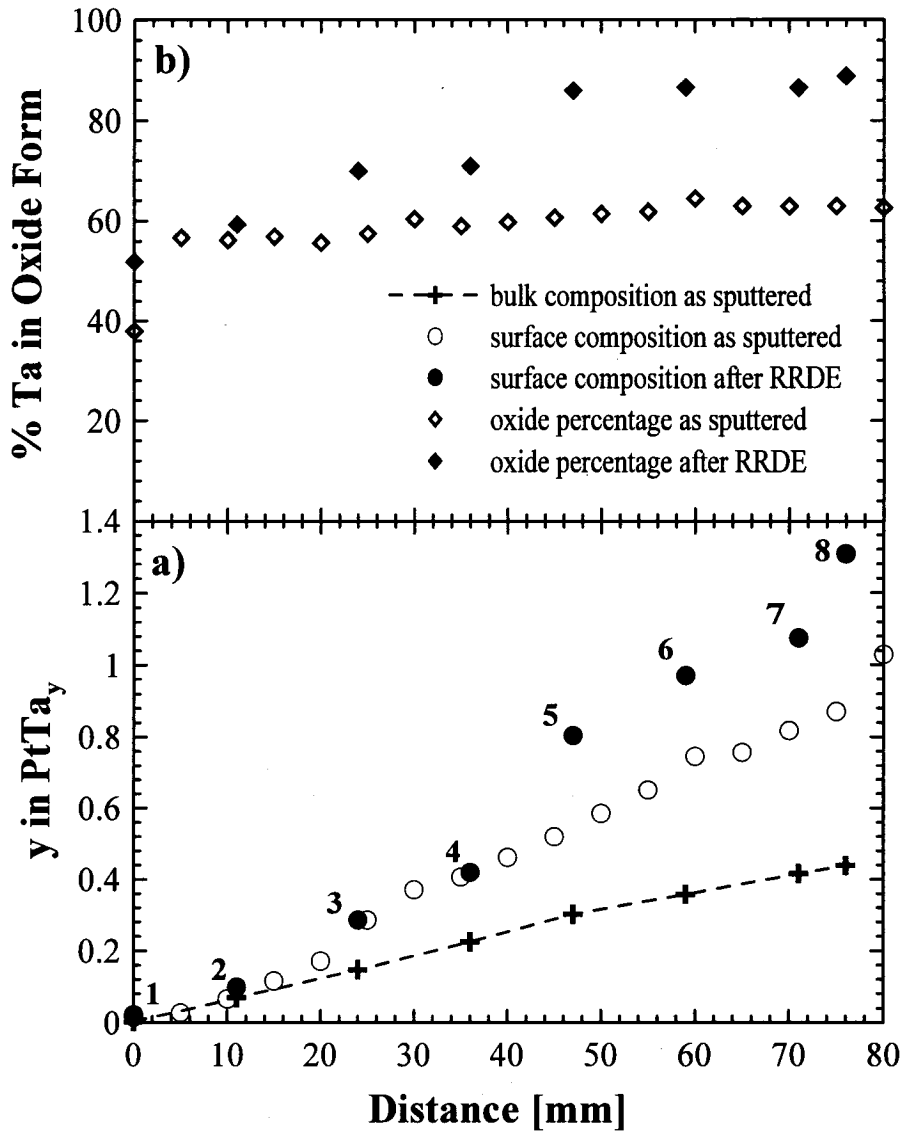

Figure 5.22 *a) Bulk and surface composition of $Pt_{1-x}Ta_x$ ($0 \leq x \leq 0.3$) films determined by electron microprobe and XPS respectively. b) Fraction of Ta in oxide form on the as-deposited library and after RRDE measurements.*

This work shows the impact of a passivating metal like Ta when it is included with Pt. Increasing amounts of Ta lead to lower ORR activity, a higher fraction of H_2O_2 production with a higher onset potential and increased oxidation of surface Ta after electrochemical measurements. It is worth noting that the activity loss is small for $x \leq 0.12$ in $Pt_{1-x}Ta_x$ and thus Pt may be tolerant to the presence of Ta in a film of Pt-Ta-Ni, for example, when the Ta content is 10% or less.

5.4 Conclusions

This chapter provided a set of CV and ORR data for as-sputtered and annealed Pt films using RRDE cells which match the state-of-the-art measurements reported in the literature.

Corrosion stability and oxygen reduction activity of combinatorially sputtered $Pt_{1-x}Ta_x$ alloys were also presented. Treatment in 1M sulfuric acid at 80°C apparently lead to a passivation which stabilized the Ta against dissolution in both low and high surface area films. Addition of Ta leads to a dramatic decrease in the ORR activity when the Ta atomic percentage is more than about 10% or so. This implies that addition of passivating metals such as Ta and Nb, as corrosion stabilizing agents in alloys such as Pt-Ni, needs to be done carefully. The compositions and structures need to be optimized so that the passivation effect does not disturb the ORR activity of the electrocatalyst.

Chapter 6

Materials Science and Oxygen Reduction Activity of Sputtered Pt-Co on GC Disks

6.0 Introduction

Clear volcano-type relations between ORR activity and x in sputtered films of $Pt_{1-x}M_x$ (M = Co, Ni, Fe; $0 < x < 1$) have been reported by Toda *et al.* [235]. However, the reported measurements are not reliable because the reported kinetic activity of baseline Pt is very low; subsequently the observed activity gains (up to 25 ×) are questionable and unrealistic. Figure 6.1 shows the reported data. The kinetic current density of pure Pt is only 0.2 $mA \cdot cm^{-2}$ at 0.76 V! By comparison it was shown in the previous chapter that that the kinetic current density is 1 $mA \cdot cm_{Pt}^{-2}$ at 0.9 V in 0.1M $HClO_4$. It is not clear if the data in [235] are normalized by the geometric surface area or the ECSA. The large variations in the observed activities are probably partly due to the variations in ECSA.

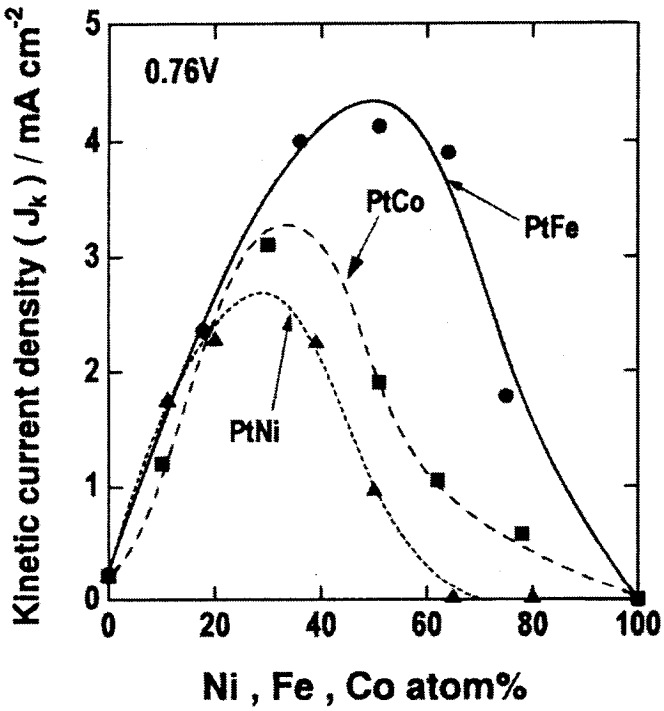

Figure 6.1 *Kinetically controlled current densities for the ORR at 0.76 V in room temperature 0.1M $HClO_4$ as a function of the bulk composition of alloy electrodes. (Taken from reference [235])*

He *et al.* have recently reported a combinatorial investigation of Pt alloys for ORR using RDE [271]. Their reported Pt baseline is also low: only 1 $mA \cdot cm^{-2}$ at 0.8 V or 100 mV higher overpotential than the Pt measurements reported in the previous chapter! Note that Figure 6.2 shows an order of magnitude improvement in the ORR current measurements. In addition to Cu, the authors report on similar activity gains for several different Pt alloys [271].

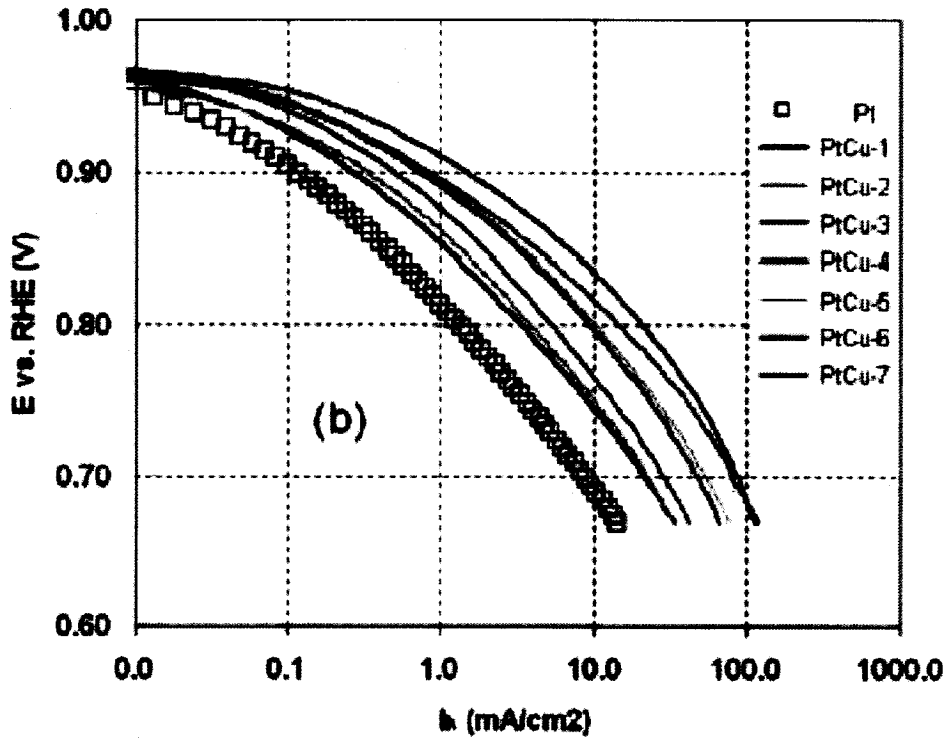

***Figure 6.2** Kinetic current densities of several Pt-Cu alloys. (Taken from reference [271])*

The objective of studies presented here was to synthesize $Pt_{1-x}Co_x$ ($0 < x < 0.5$) libraries combinatorially and to measure their ORR activity as objectively as possible. Could any volcano-type behavior be observed at Dalhousie?

6.1 $Pt_{1-x}Co_x$ ($0 \leq x \leq 0.5$) Films: Material Characterization and Acid Treatment

A composition map of a typical Pt-Co library, determined by electron microprobe, is shown in Figure 6.3. The composition, or x in $Pt_{1-x}Co_x$, varies continuously across the sputtered region. The composition of the corresponding GC disks is also shown.

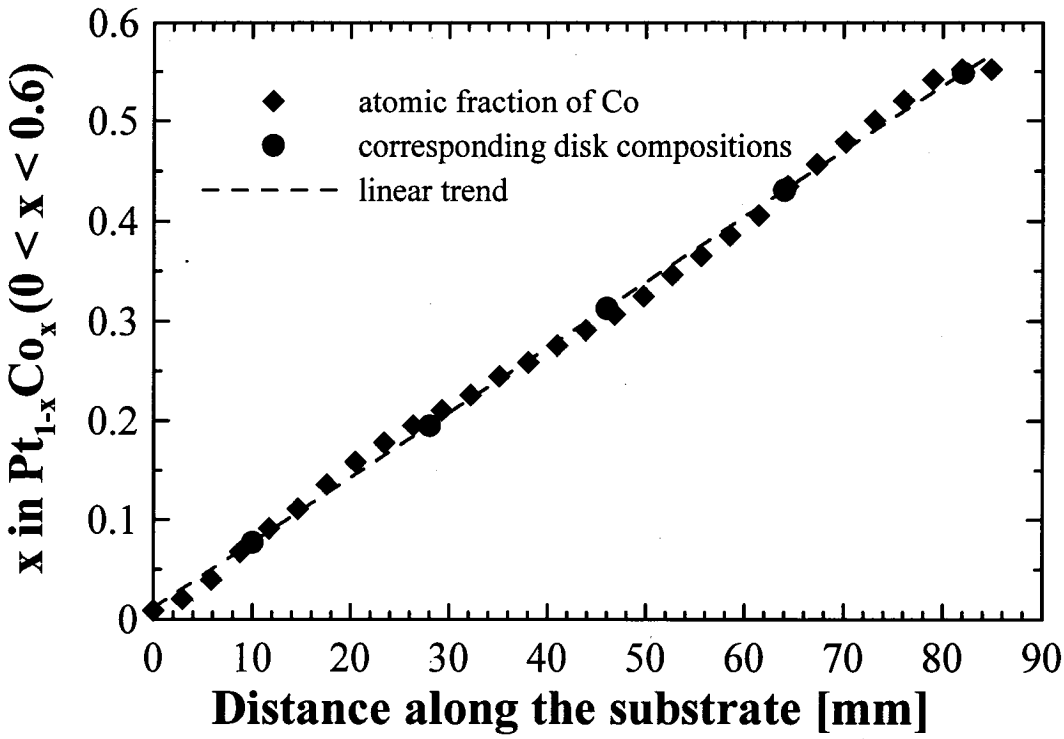

Figure 6.3 *The composition variation of the $Pt_{1-x}Co_x$ ($0 \leq x \leq 0.5$) library deposited on a Si wafer and the corresponding GC disks.*

X-ray diffraction patterns of a typical as-deposited and annealed (750°C) Pt-Co library are shown in Figures 6.4a and b, respectively. The shift of Bragg peaks to higher angles indicates that lattice contraction occurs and alloys are formed. Annealing at 750°C causes Pt grains to grow. The diffractograms were further analyzed to obtain an estimate of the lattice constants and grain sizes. These are shown in Figures 6.5a and b for as-deposited and annealed libraries. The lattice constants of the sputtered films are in close agreement with those reported for bulk alloys prepared by typical metallurgical methods [260]. After annealing, there is a 4× growth of the grains as shown in Figure 6.5b.

Figures 6.6a-c show the morphology of typical Pt-Co films deposited on GC disks for as-deposited, 750°C and 950°C annealed samples. Sintering and grain growth in the films is observed.

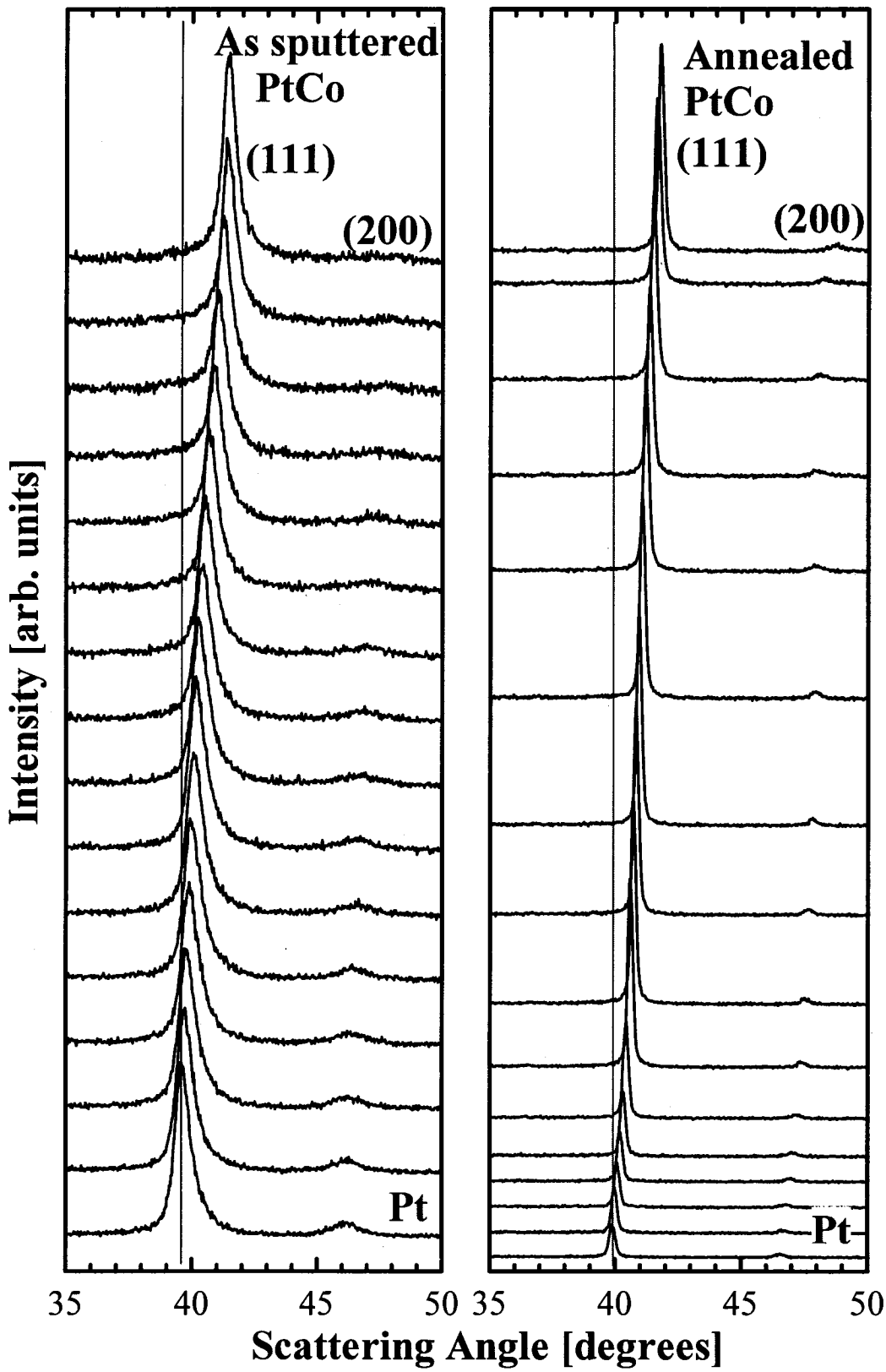

Figure 6.4 *X-ray diffraction patterns of the $Pt_{1-x}Co_x$ ($0 \leq x \leq 0.5$) library sputtered on Si wafer for a) as-deposited and b) heat treated 750℃. The Miller indices of the fcc phase are indicated.*

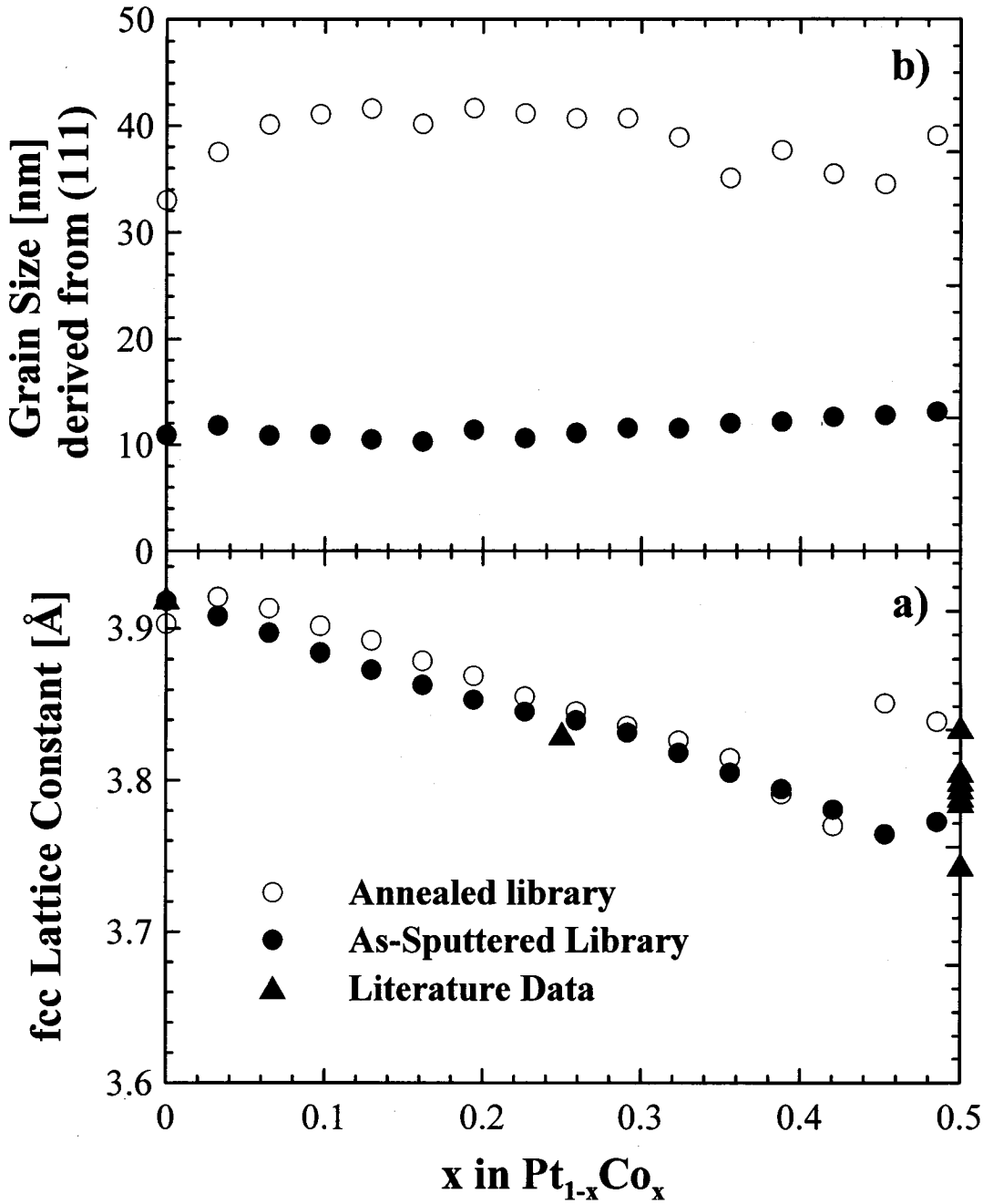

Figure 6.5 *a) Lattice constants and b) grain sizes of $Pt_{1-x}Co_x$ ($0 \leq x \leq 0.5$) films deposited on a Si wafer substrate shown for as-sputtered annealed libraries.*

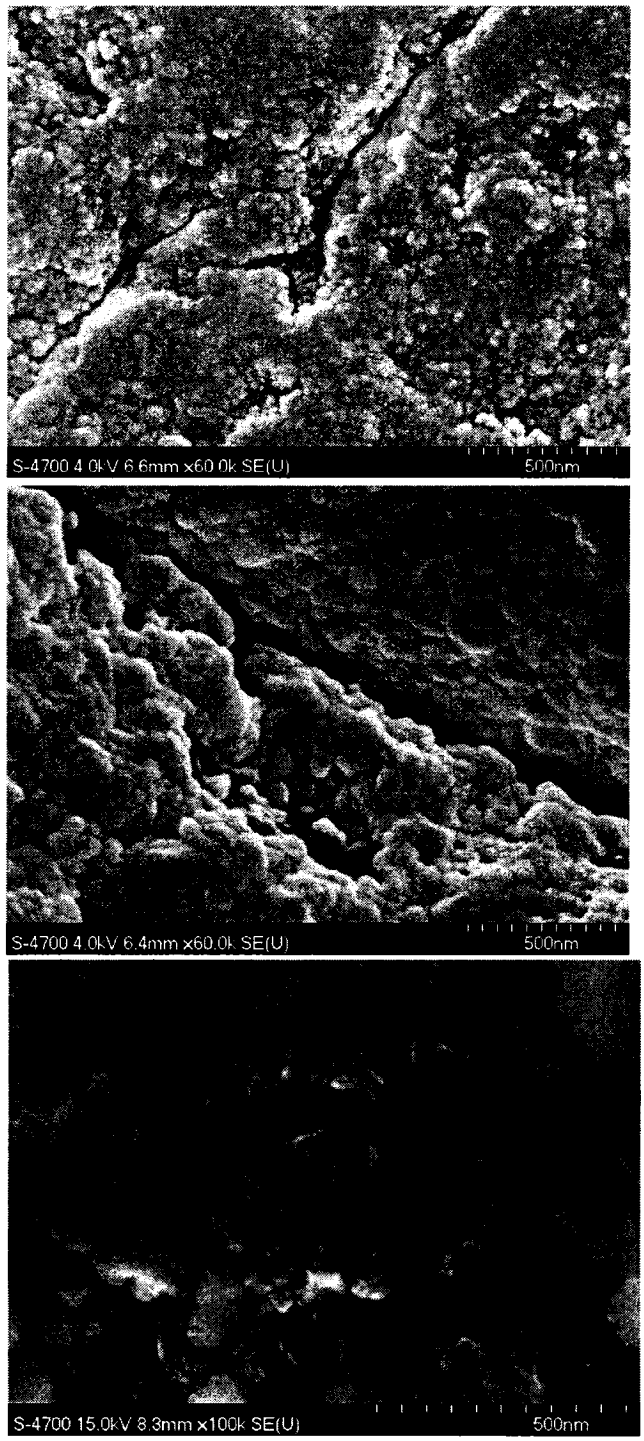

Figure 6.6 *SEM micrographs of PtCo films deposited on GC disks before annealing (top), after 750°C annealing (middle) and after 950°C annealing (bottom).*

Acid treatment experiments, similar to those presented in chapter 5, were performed in order to test the stability of Co in the Pt-Co alloys. The composition of the $Pt_{1-x}Co_x$ library after acid treatment is plotted in Figure 6.7 versus the composition of the

untreated library. The straight line shown in the figure corresponds to a situation where no Co dissolution occurs. For all values of $x_{untreated}$, the value of $x_{treated}$ is reduced. For $x_{untreated} \geq 0.6$ or so, the loss of Co occurs at a faster rate, indicating more Co loss from the core of the grains. The maximum bulk content of Co seen anywhere in the library, after the acid treatment, is no more than 30% or so. These results are similar to those of other alloys (binary, ternary) presented in chapter 4.

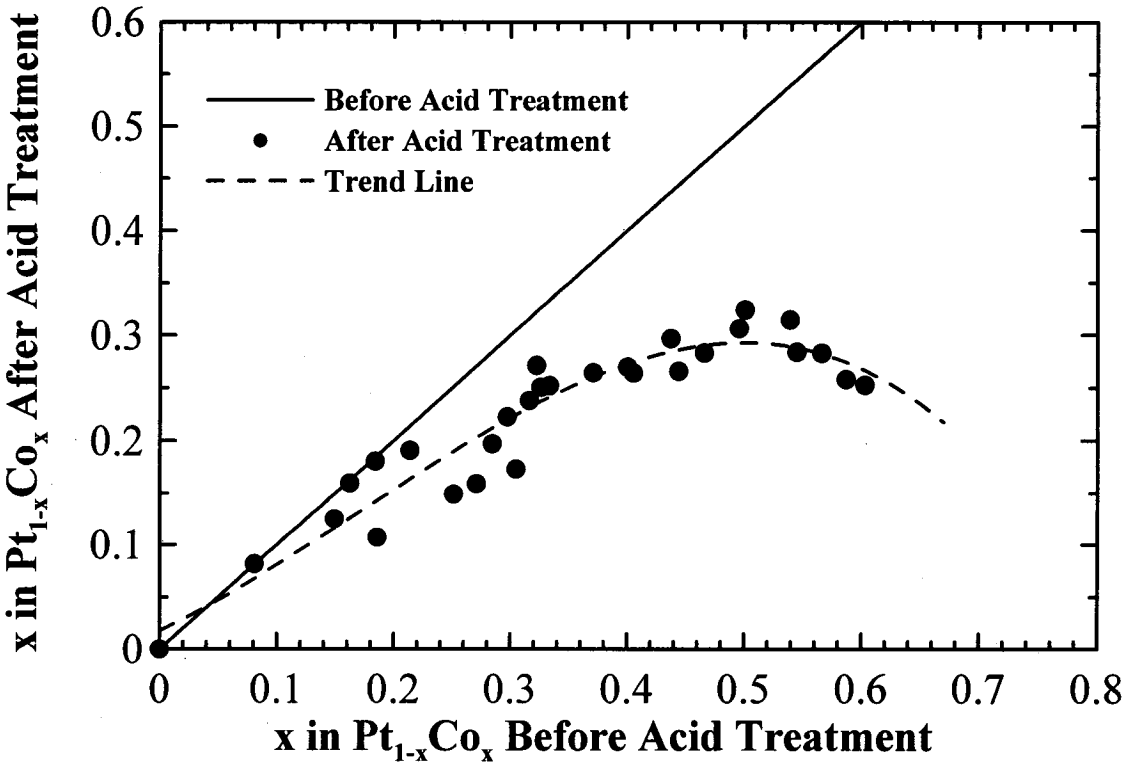

Figure 6.7 *Bulk Co content of $Pt_{1-x}Co_x$ films deposited on NSTF after acid treatment (1M H_2SO_4 for 10 days).*

Figure 6.8 shows the X-ray diffraction patterns of as-deposited and acid treated $Pt_{1-x}Co_x$ ($0 < x < 0.5$) libraries for selected compositions. As the Co concentration increases along the library, the Pt-Co (111) peaks shift to higher angles and separate from the Pt (111) sublayer for the as-deposited library. At the highest Co contents, the Pt-Co (111) peak shifts to lower angles as evidently more Co is lost from the bulk during acid treatment. As discussed in chapter 5, $x \sim 0.5$ marks the onset of bulk transition metal dissolution in the composition range.

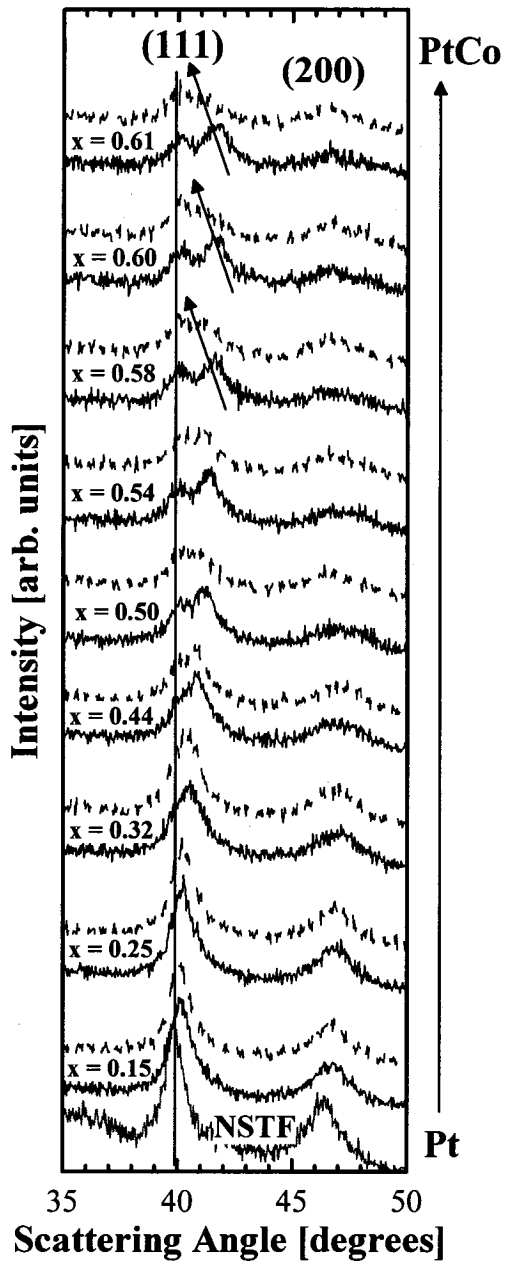

Figure 6.8 *XRD patterns of $Pt_{1-x}Co_x$ shown for selected compositions of as-sputtered (solid) and acid-treated (dashed) libraries. For $x > 0.5$, the movement of the Pt-Co (111) peak to lower angles is an indication of more bulk Co dissolution. The (111) Bragg peak marked by a line corresponds to the Pt sublayer in the NSTF support used as an X-ray standard. The XRD pattern of the NSTF support is shown at the bottom.*

The surface composition of Pt-Co films was determined by XPS, where penetration depths probed are about 3 nm. XPS data were collected on several Pt-Co libraries sputtered on GC before and after electrochemical measurements. Figure 6.9 shows the

Co $2p_{3/2}$ peaks for several bulk compositions of $Pt_{1-x}Co_x$, before and after electrochemical measurements.

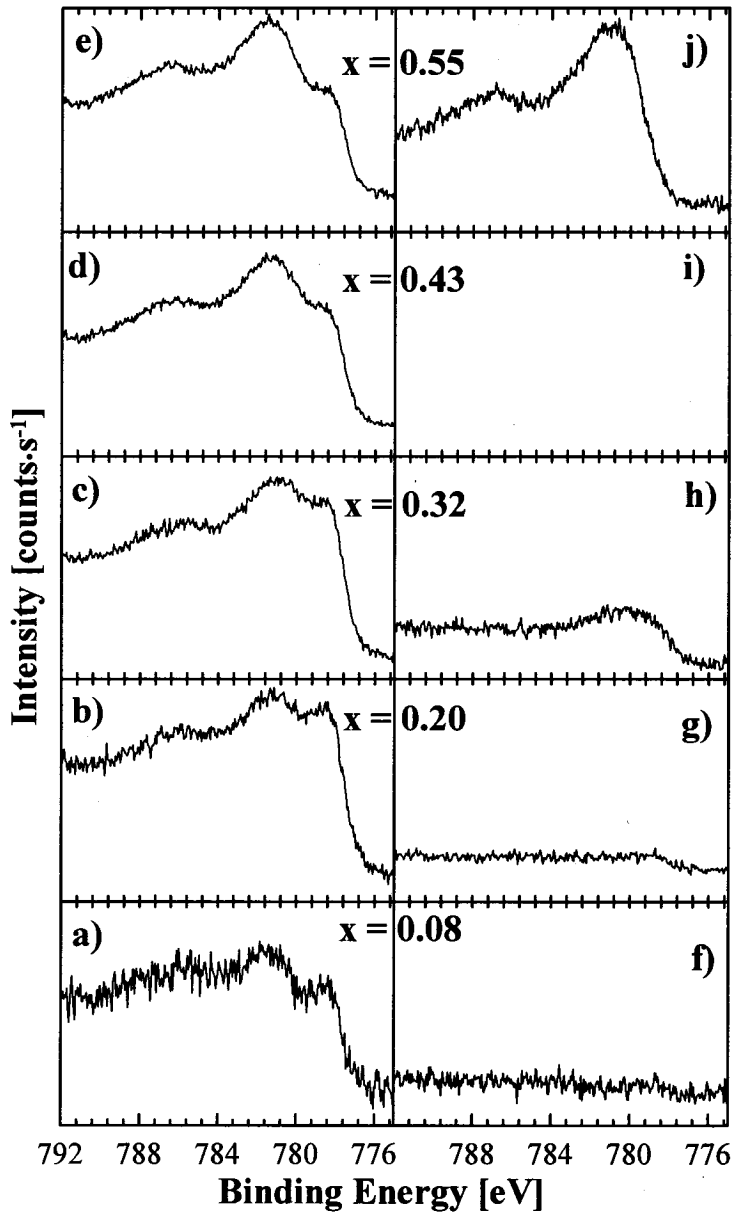

Figure 6.9 *X-ray photoelectron spectra of Co $2p_{3/2}$ electrons in $Pt_{1-x}Co_x$ shown for as-deposited (a-e) and after RRDE measurements (f-j). The value of x before RRDE is shown on the graphs.*

After exposure to acid and potential cycling, there is a significant loss of Co. Figure 6.10 shows how the Co peaks were analyzed.

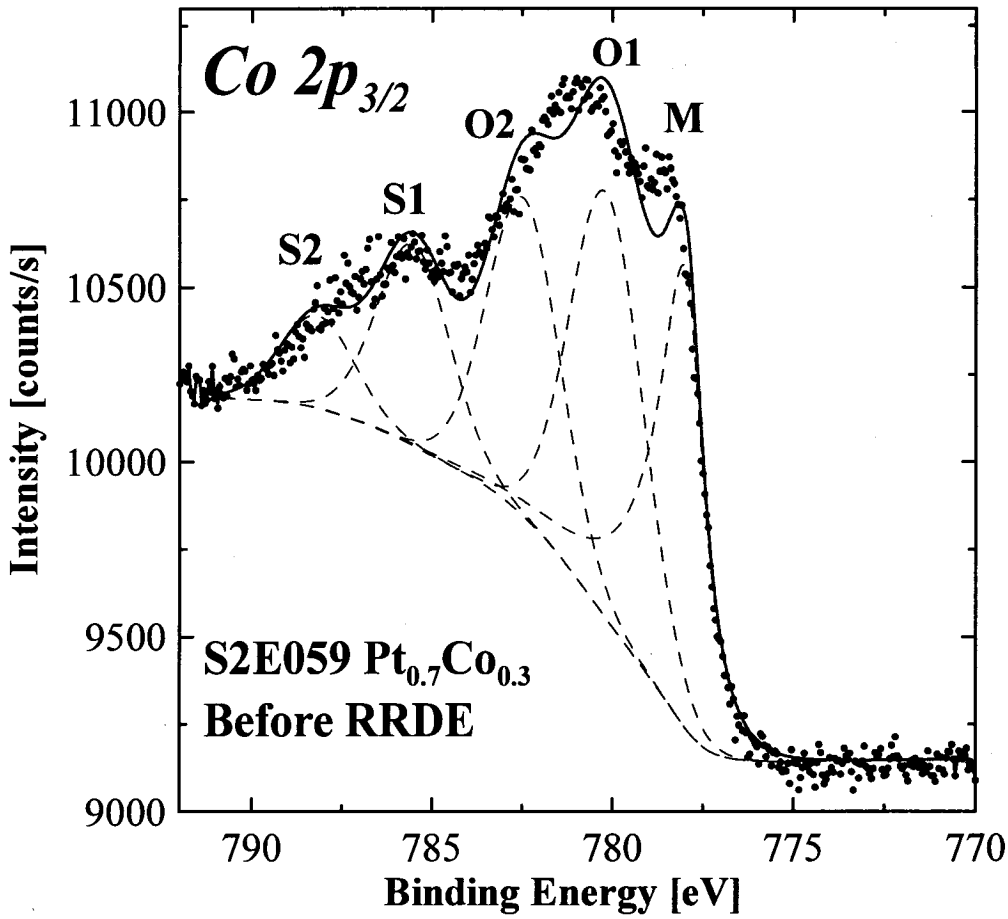

Figure 6.10 *Co $2p_{3/2}$ peaks and the fit showing one metal (M), two oxides (O1, O2) and two shake-up (S1, S2) peaks.*

All the Co data were fitted to one metallic component (778 eV) and two oxide phases. Two shake-up components were also included. The XPS of Co-oxide phases have been thoroughly investigated by Hagelin-Weaver *et al.* [272]. The presence of different oxides/hydroxide phases with overlapping binding energies makes the analysis difficult. However, for the purpose of determining a total concentration of Co and obtaining the metallic/oxide fraction, the data can be reasonably well analyzed. The fitting and quantification procedures were described earlier in chapter 3. Figure 6.11 shows the bulk and surface compositions of the Pt-Co films before and after electrochemical measurements. Note that the bulk Co content, measured by electron microprobe, is almost unchanged before and after RRDE measurements. However, the surface Co content, which initially is identical to the bulk, decreases after RRDE measurements so that after RRDE $x_{surface}$ is no more than 0.1 in all samples. It is most likely that the first

one or two surface layers are completely free of Co and a Pt skin is present. In two samples, where $x_{initial} = 0.55$, only cobalt oxide is observed.

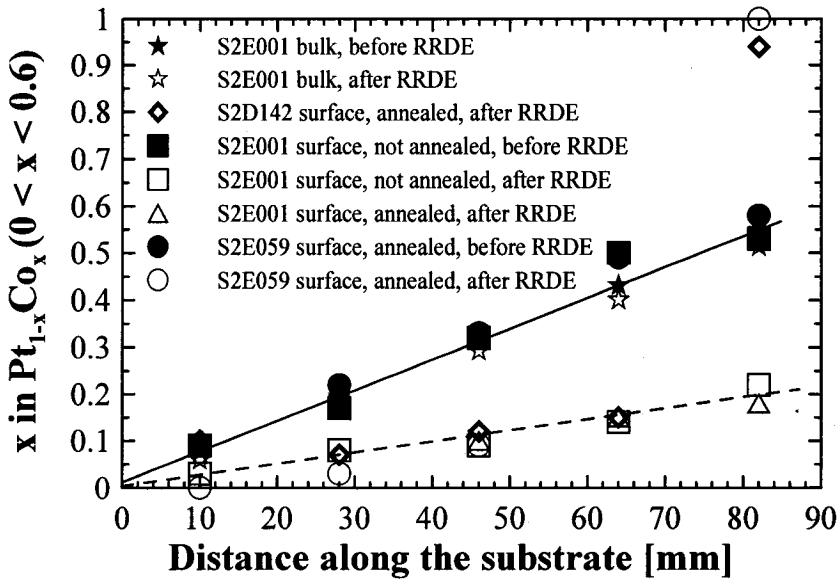

Figure 6.11 *Bulk and surface composition of $Pt_{1-x}Co_x$ ($0 \leq x_{initial} \leq 0.55$) films determined by electron microprobe and XPS respectively. After RRDE measurements, the surface Co content is no more than $x_{surface} = 0.1$ or so.*

6.2 $Pt_{1-x}Co_x$ ($0 \leq x \leq 0.5$) Films: ORR Activities

Figures 6.12a and b show the CVs of a library of as-deposited and annealed (750°C) Pt-Co films. The surface enhancement factor is reduced from 5 to 1.7 after annealing, which corresponds to growth of the grains. Note that for the as-deposited films, there is no correlation between the Co content and the ECSA. As explained in chapter 2, the current general understanding is that OH intermediate adsorption is too strong on Pt and lowering its adsorption energy (or essentially its coverage) increases the rate of ORR. Alloying of Pt with transition metals like Co or Ni reportedly shifts the onset of OH adsorption to higher potentials [177]. However, no significant OH shift was observed here.

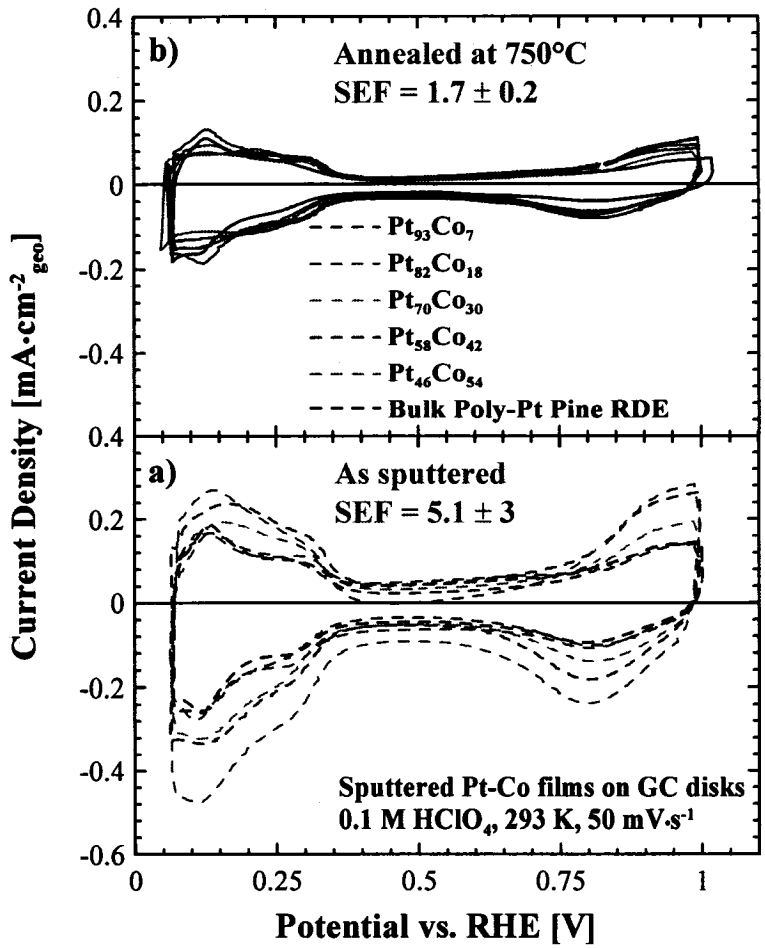

Figure 6.12 *Cyclic voltammograms of sputtered $Pt_{1-x}Co_x$ ($0 \leq x \leq 0.55$) are shown for as-sputtered (bottom) and annealed (top). The same scale is chosen in both panels to emphasize the reduction of ECSA after annealing.*

Figure 6.13 shows the ORR activities and H_2O_2 yield of the as-deposited and annealed samples. Note that all of these are geometric currents. With variable ECSAs, it becomes necessary to consider the ECSA normalized current densities in the kinetic region to judge the activities of Pt-Co samples. Nevertheless, Figure 6.13 shows features of ORR which are essentially identical to Pt: diffusion-limiting current densities of about 4.5 $mA \cdot cm^{-2}_{geo}$ and a $\%H_2O_2$ release, which is undetected for voltages higher than 0.6 V or so and gradually increasing towards the H^+ adsorption/desorption region.

Figure 6.14 shows kinetic current densities of several as-deposited and annealed Pt-Co compositions. The currents were normalized by ECSA and corrected for the non-Faradaic contributions.

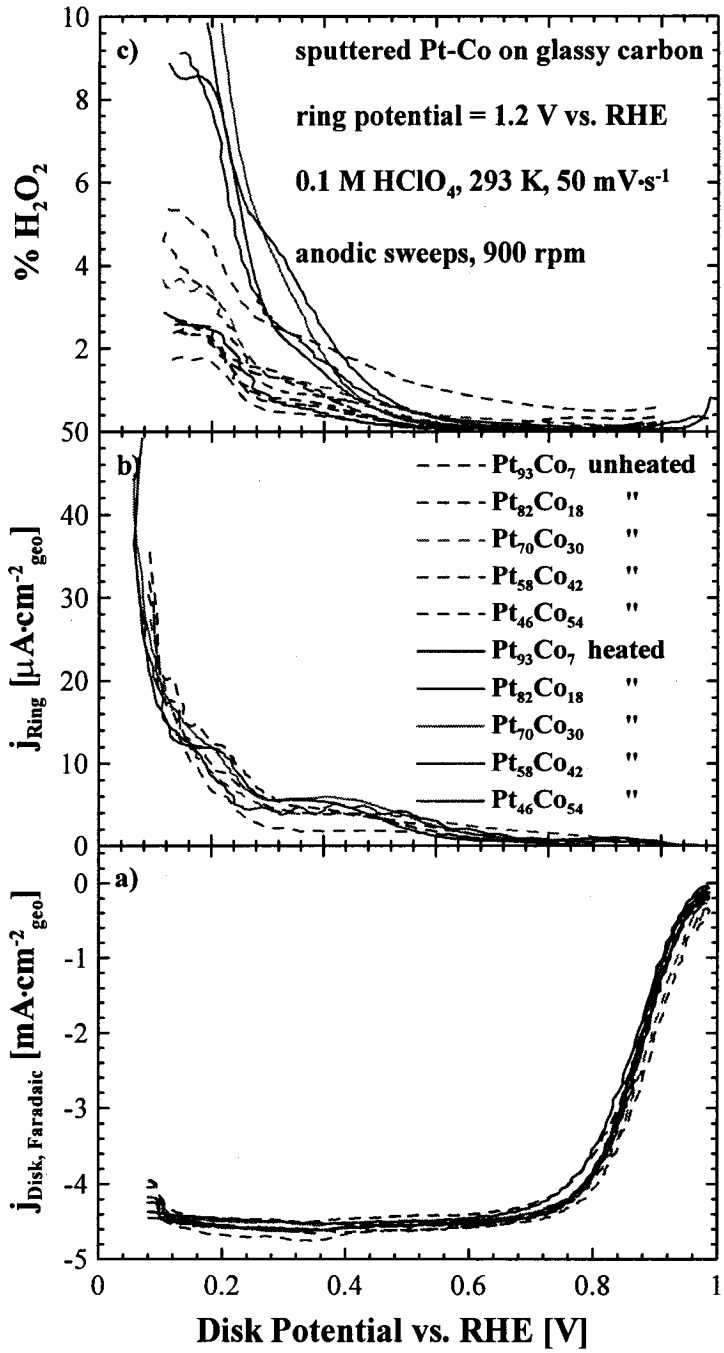

Figure 6.13 *a) Disk current densities for ORR of the sputtered $Pt_{1-x}Co_x$ ($0 \leq x \leq 0.55$) on GC disks in 0.1M $HClO_4$. b) The ring current densities and c) percentage H_2O_2 produced are shown.*

The Pt-Co Tafel lines fall into two groups: annealed (higher activity) and as-deposited (lower activity). In both cases the ORR activity is apparently insensitive to the Co content.

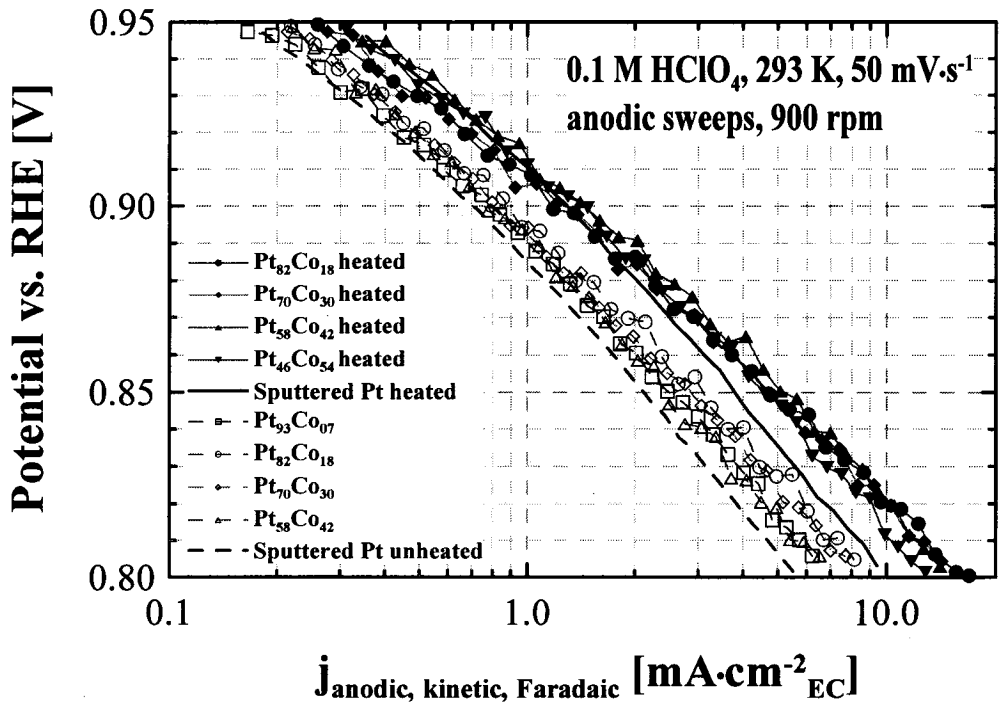

Figure 6.14 *Tafel region of the ORR of $Pt_{1-x}Co_x$ ($0 \leq x \leq 0.3$) shown for the anodic sweeps.*

In both cases, however, the activities are higher than the respective as-deposited and annealed Pt films on GC disks. This set of data corresponds to one single sputtered library. It is vital to show the repeatability and uncertainties of such measurements. For this reason, the kinetic current density (ECSA normalized) of all the prepared Pt-Co libraries at 0.85 V is plotted in Figure 6.15.

Figure 6.15 shows the Pt activity for both as-deposited and annealed samples. For comparison polycrystalline Pt data from LBNL is also shown. The error bars in Figure 6.15 represent averaging of current densities over several measured rotation rates and are in general indicative of the precision of measurement. The different data sets are intentionally not averaged and are shown individually to illustrate the variability of various sputter deposition experiments.

Figure 6.15 shows for the as-deposited Pt-Co samples, within the uncertainty of the measurements, there is no improvement of the ORR activity for any Co content. An activity gain is only observed when samples are annealed. The activity gain in these samples is at most 1.7×. The activity gain within the experimental uncertainties, is about $(1.4 \pm 0.1)\times$ for the Co contents between $0.2 < x < 0.5$. Increasing the Co content beyond

x = 0.55 is unlikely to increase the activity further. Figure 6.16 shows activity of as-deposited and heat-treated Pt-Co samples at 0.9 V.

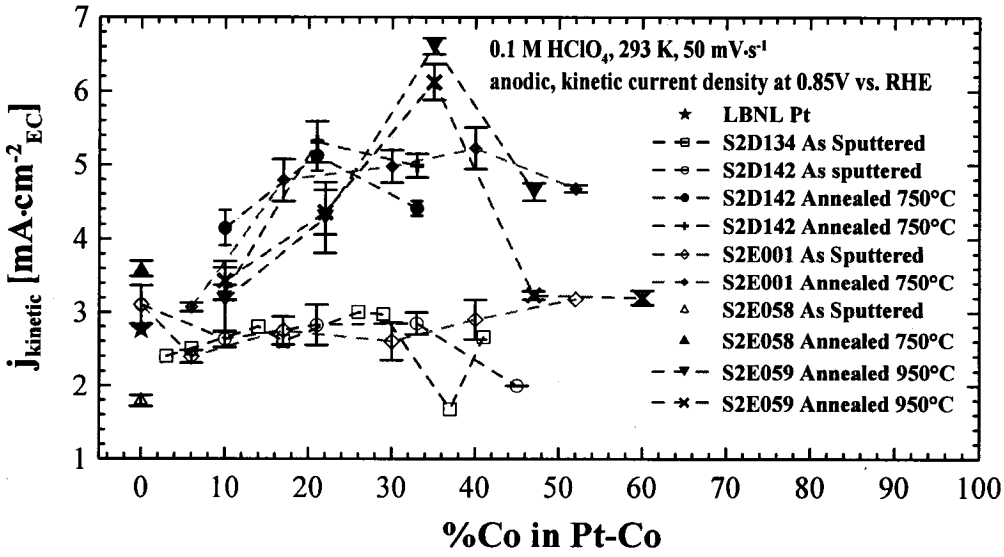

Figure 6.15 *Kinetic current density of ORR for $Pt_{1-x}Co_x$ ($0 \leq x \leq 0.55$) at 0.85 V versus RHE.*

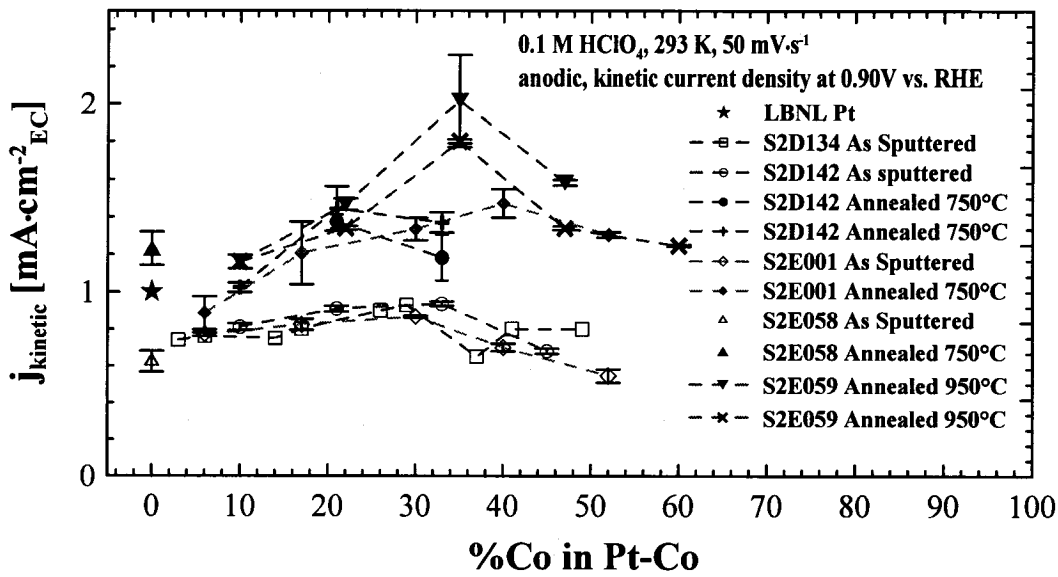

Figure 6.16 *Kinetic current density of ORR for $Pt_{1-x}Co_x$ ($0 \leq x \leq 0.55$) at 0.90 V versus RHE.*

The activity gains seen here are in general agreement with what is widely reported by various researchers for Pt-Co supported on carbon. Johnson Matthey [273] and GM [87], have reported activity gains of about 2× in PtCo alloys. However, activity gains reported

in some of the literature, like those of He and Toda discussed earlier, are not objective and are riddled with experimental errors.

6.3 Conclusions

For $x_{initial} > 0.2$, all samples of $Pt_{1-x}Co_x$ ($0 \leq x \leq 0.5$) showed a gain in the area-specific kinetic activity only after annealing. The gain was determined only after an objective measurement of Pt baseline activity was established. The surface Co content averaged over the first 2-3 nm surface layers after electrochemical measurements was less than about $x_{surface} = 0.1$ for all the initial values of x. When the stability of Pt-Co alloys on high surface area NSTF structures were studied, using 80°C acid treatment, significantly more dissolution of Co was observed.

In studies of Pt alloys for ORR, unless there is a clear and repeatable baseline standard measurement, results which indicate increased activity may be questionable. This is especially true for combinatorial studies where larger numbers of alloy electrocatalysts are produced and screened: simple comparisons to Pt or normalization of data to that of Pt is not sufficient. Sputtered films on flat surfaces do have variations in their roughness factors based on compositions and the angle of sputtering flux which need to be accounted for. Area-specific current densities, normalized by electrochemical surface areas should be used.

Chapter 7

Materials Science and Oxygen Reduction Activity of Sputtered Pt/NSTF and Pt-Co-Mn/NSTF

7.0 Introduction

The electrochemical results for Pt-based electrocatalysts on NSTF are presented in this chapter. The NSTF-based samples were prepared at 3M using magnetron sputtering and were mainly studied by RRDE as part of Dalhousie-3M collaborative work. The RRDE results are compared with the PEMFC measurements conducted at 3M Company.

7.1 ORR Activities of Pt and Pt-Mn-Co Sputtered onto NSTF Substrate

In the past few years, scientists at 3M's Fuel Cell Components Program have fabricated and tested over 100 different Pt alloys as PEMFC cathode electrocatalysts [226]. All of these samples have been prepared by magnetron sputtering onto 3M's NSTF substrate using a multi-target sputtering system. In summary, the 3M results show an approximate 5× and 2× increase in the area and mass specific activity of Pt/NSTF over Pt/C, respectively. For the ternary alloys (e.g. Pt-Co-Mn), a 2× increase the area specific activity has been observed over Pt-Co/C, which in turn is 2× more active than Pt/C. According to 3M, the best alloy composition, so far, has been Pt-Co-Mn. This has been repeatedly confirmed in 3M's PEMFC experiments.

How would NSTF alloy samples behave in solution cells? Do they exhibit a gain in activity in ORR performance just like carbon-supported Pt-alloys have shown [274]? Early measurements, done at LBNL and reported in a DOE report, showed no significant difference between Pt/NSTF and Pt-alloys/NSTF [275]. Figure 7.1 shows LBNL's Tafel measurements of Pt/NSTF and Pt-alloy/NSTFs reported in 2005 [275]. Although Pt/NSTF showed a significant increase in its area specific activity over Pt/C, all the Pt-alloy/NSTF measurements seemed to overlap each other. These results were contradictory to PEMFC results obtained at 3M, which persistently showed improvements in the Pt-alloy/NSTF samples. The discrepancy was not really understood

and was generally attributed to the fact that RRDE solution cells do not necessarily have the same environment as PEMFCs. This was a motivation for repeating the measurements on Pt and Pt-Co-Mn/NSTF samples. The experiments carried out at Dalhousie did show a difference between Pt/NSTF and Pt-Co-Mn/NSTF samples.

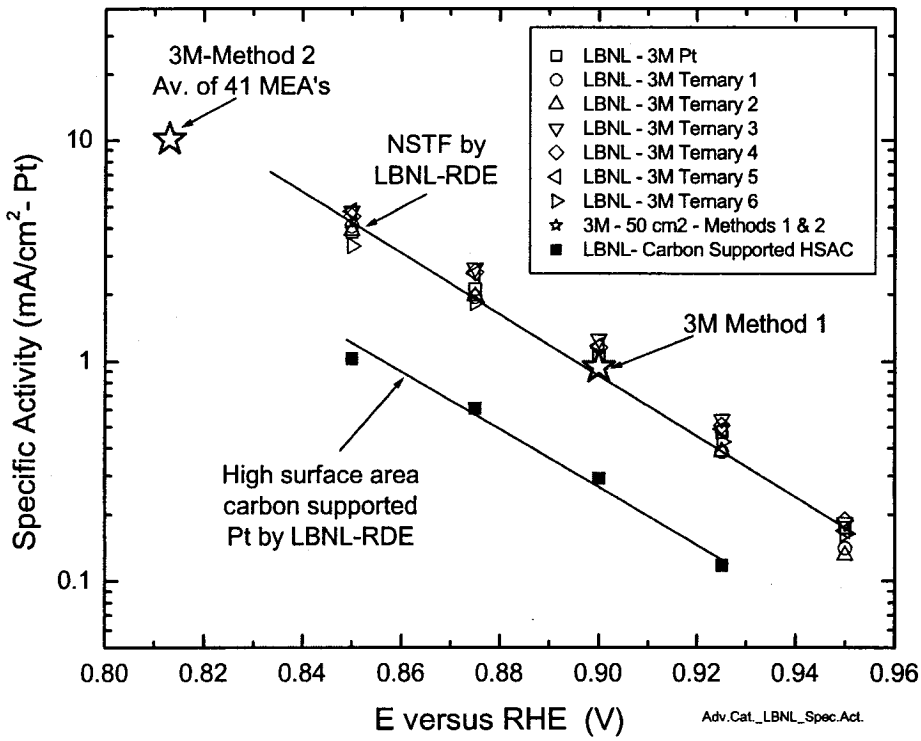

Figure 7.1 *Tafel kinetics of Pt/NSTF, Pt-alloy/NSTF and Pt/C showing the specific (Pt-area normalized) current densities. (Taken from reference [275])*

7.2 XRD and Electron Microprobe Analysis of the Samples

The depositions aimed to produce films of 0.15 $mg \cdot cm^{-2}$ of Pt and 0.17 $mg \cdot cm^{-2}$ of Pt-Co-Mn. The weight ratio of Pt : (Pt + Co + Mn) was about 88%, leading to a nominal chemical composition of $Pt_{0.68}[Co\text{-}Mn]_{0.32}$. The electron microprobe measurements of the Pt-Co-Mn samples showed a composition of $Pt_{0.68}Co_{0.32}Mn_{0.04}$, which is close to the nominal composition.

The XRD patterns of Pt/NSTF and Pt-Co-Mn/NSTF samples are shown in Figure 7.2. The lattice parameters were extracted from the (111) Bragg peaks. The addition of Mn and Co has contracted the lattice dimension, as is expected in these alloys. The fcc lattice constants of the Pt/NSTF and Pt-Co-Mn/NSTF samples are 3.92 and 3.86 Å, respectively. Average values of reported bulk lattice constants are about 3.79 ± 0.04 Å for fcc

$Pt_{0.5}Co_{0.5}$ and 3.83 Å for fcc $Pt_{0.75}Co_{0.25}$ [239, 241, 242]. The fcc lattice constant is much less sensitive to the Mn content as reported in the bulk Pt-Mn phases, where values of 3.90 to 3.89 Å are reported for phases with up to 25% Mn which are very close to 3.92 Å, the lattice constant of pure Pt [234, 244].

The average grain sizes of the Pt/NSTF and Pt-Co-Mn/NSTF films, obtained from the broadening of the (111) peak and accounting for the instrumental resolution, are about 11 and 8 nm, respectively.

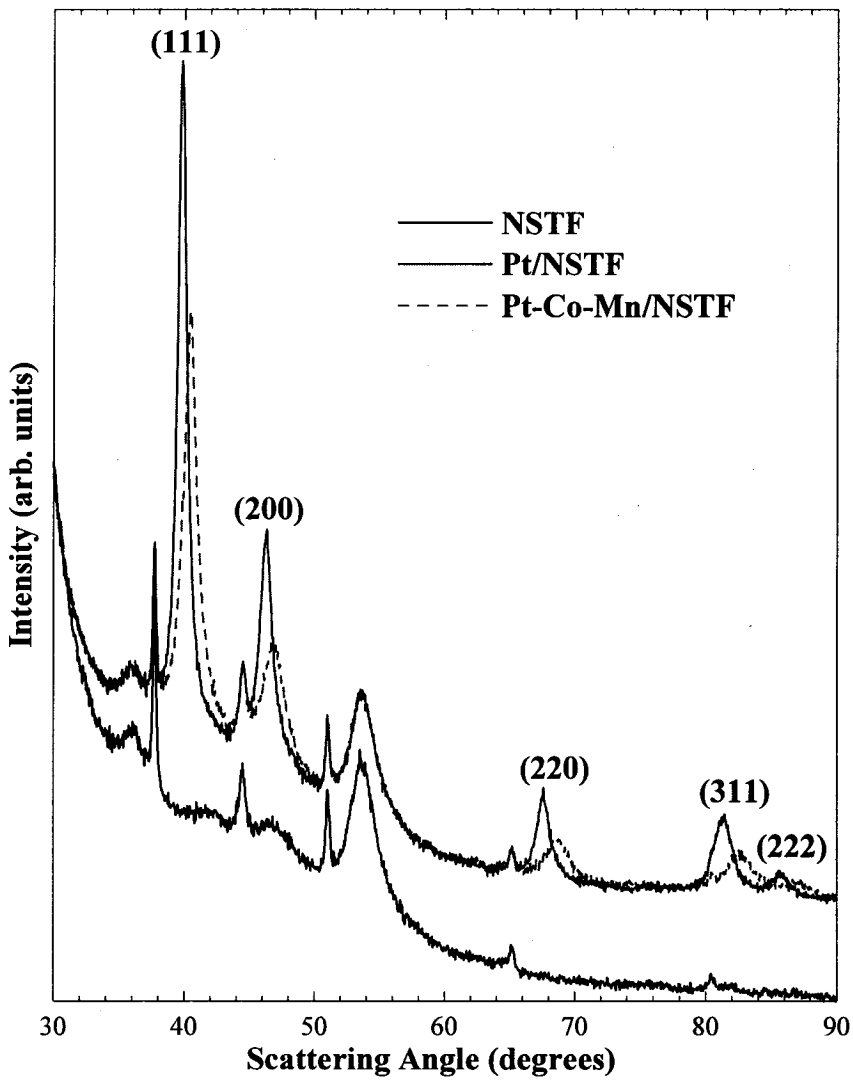

Figure 7.2 *XRD patterns of NSTF and as-sputtered Pt/NSTF and Pt-Co-Mn/NSTF. Lattice contraction in Pt-Co-Mn is evident by the movement of Bragg peaks to higher scattering angles. The background diffraction pattern of plain NSTF is also shown for clarity. All the fcc Miller indices are included on the patterns.*

7.3 RRDE Characterizations

The RRDE measurements were carried out with utmost care and results were carefully analyzed. Such treatment was necessary because the goal was to measure two rather well-studied samples and any difference observed between the two had to be very objective. As before, we ensured that the Pt measurements were in excellent agreement with the measurements reported by LBNL on polycrystalline Pt. Four slurries, each with a different concentration of catalysts were prepared for each electrocatalyst sample. Each slurry sample was studied in two simultaneous but independent RRDE cell setups. A picture of these two RRDE systems was shown earlier in chapter 3 (Figure 3.11). Experimental details are provided in the next sections.

7.4 Slurry Depositions

Figure 7.3 (a-e) shows slurry depositions on the tip of the GC electrodes for different loadings. Figure 7.3 (f) shows a higher magnification view of the individual whiskers on a GC disk. Depositions that were uniform to the eye and in a 40× optical microscope were always achieved.

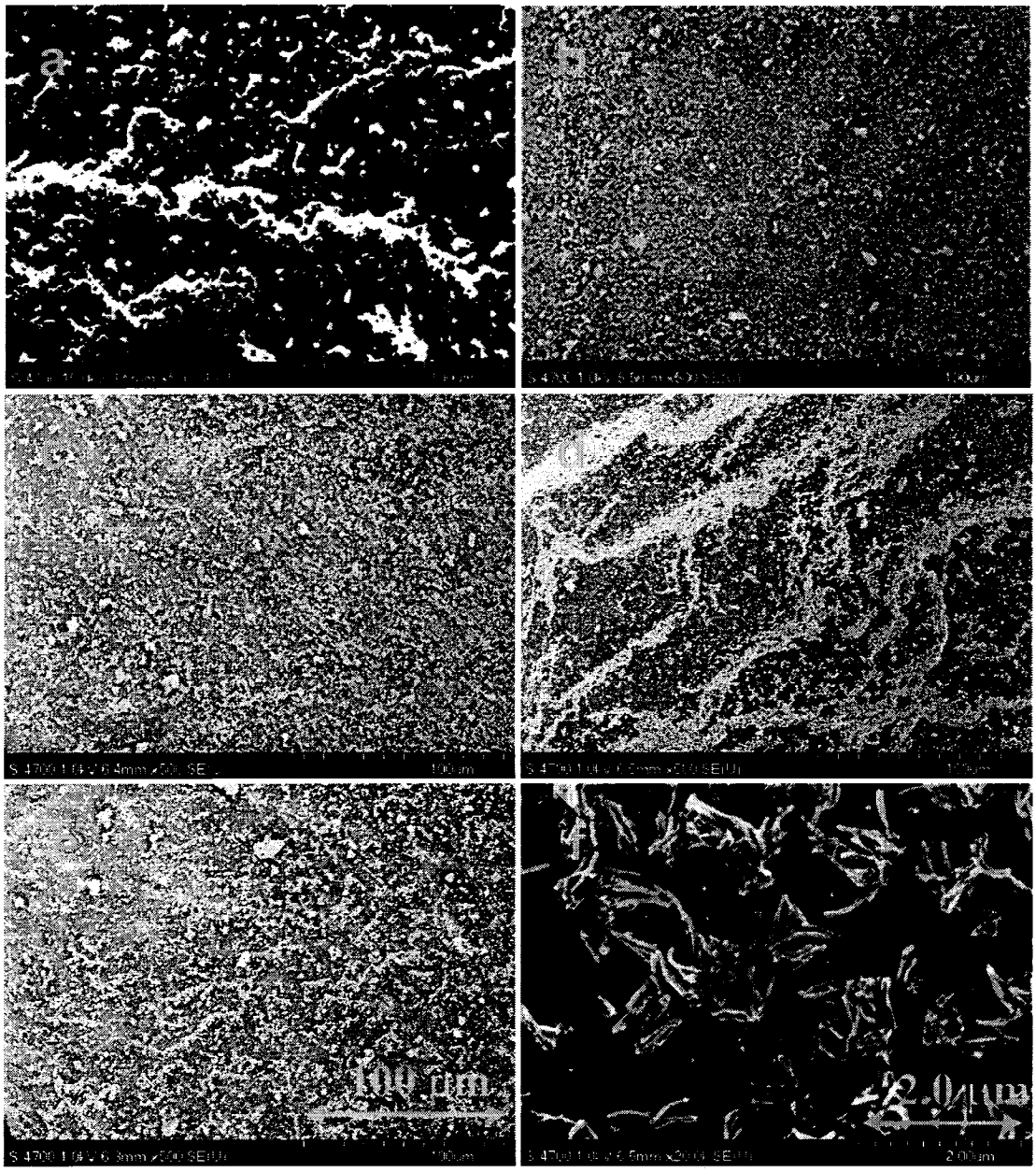

Figure 7.3 *Slurry deposition on the GC electrodes shown for 20 (a), 40(b), 60(c), 80(d), 100(e)* $\mu g_{Pt} \cdot cm^{-2}$. *f) A higher magnification image showing the individual whiskers 40* $\mu g_{Pt} \cdot cm^{-2}$.

7.5 RRDE Results

Detailed RRDE procedures that were used are outlined in Appendix A. Briefly, the sequence of measurements involved collecting Ar CVs with a stationary electrode, then performing the ORR measurements in flowing O_2 and at several rotation speeds, followed by a final Ar CV and finally a reference electrode calibration. Sample (disk)

and ring electrodes were always electrochemically cleaned by cycling them between 0.05 and 1.05 V (OCV potential) under Ar until stable voltammogram patterns were obtained.

7.5.1 Ar Cyclic Voltammograms

Cyclic voltammograms of Pt/NSTF and Pt-Co-Mn/NSTF taken at 50 $mV \cdot s^{-1}$ are shown in Figure 7.4. As loading increases, a gradual growth of the voltammogram peak is observed.

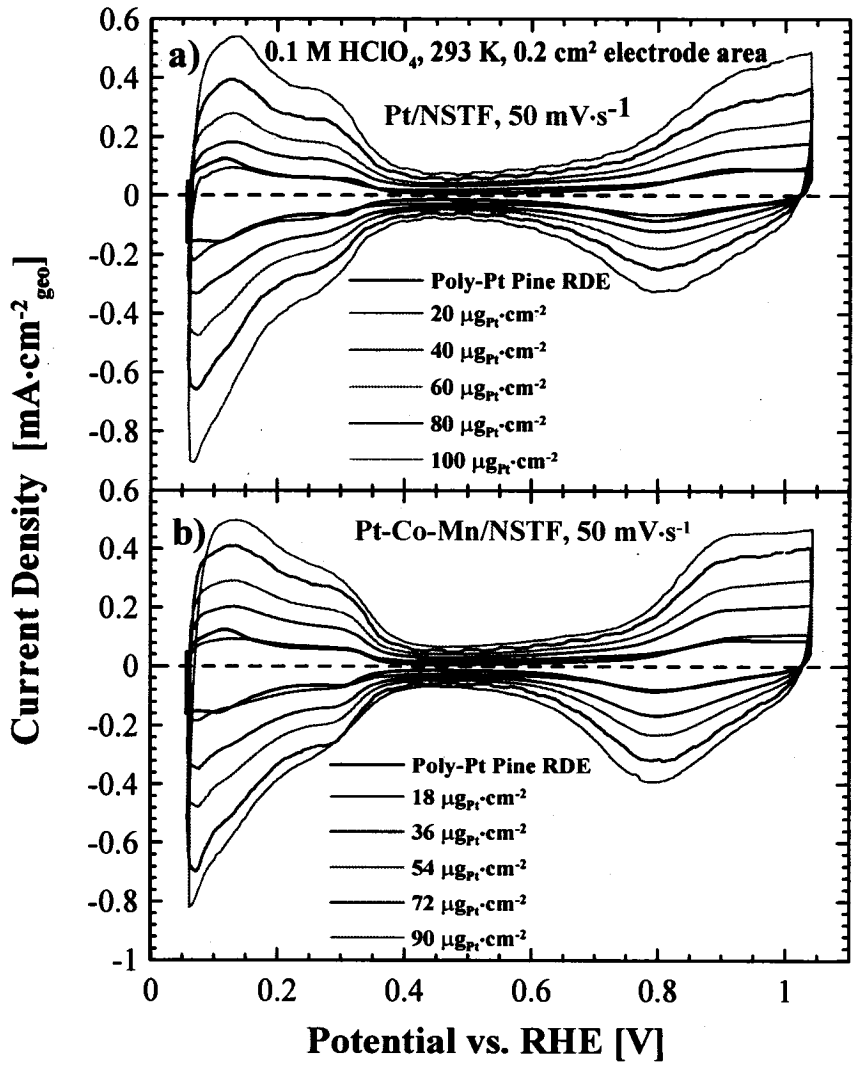

Figure 7.4 *Cyclic voltamograms of Pt/NSTF (a) and Pt-Co-Mn/NSTF (b) shown for various different loadings. The CV of a polycrystalline-Pt disk is also shown for comparison. Experimental parameters are indicated on the plot.*

Do we note any differences between the CV of Pt/NSTF and Pt-Co-Mn/NSTF in Figure 7.4? Figure 7.5 compares the CV of these two different catalysts on the same graph. Note that Pt-Co-Mn/NSTF has a better 'defined' or a larger OH_{ads} region.

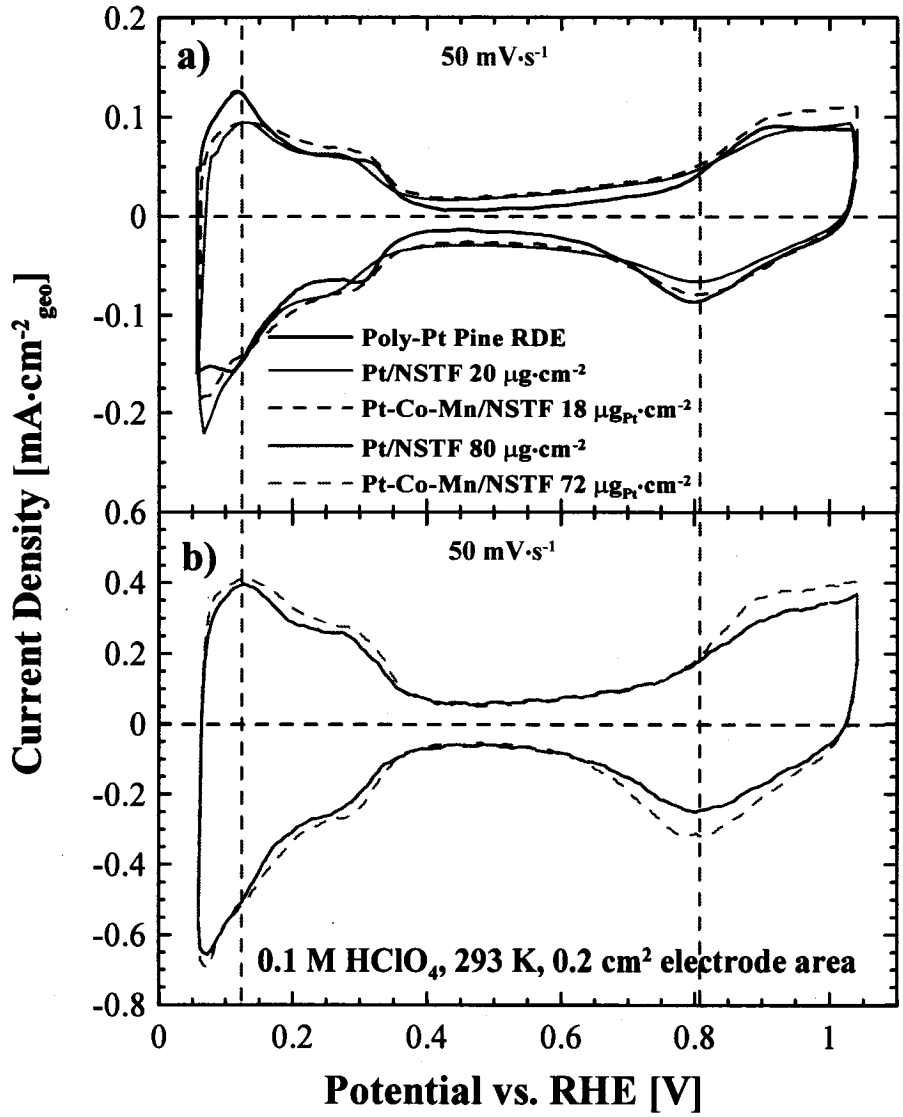

Figure 7.5 *CVs of Pt/NSTF and Pt-Co-Mn/NSTF samples are compared at two different loadings. The CV of poly-Pt is also shown for comparison. Experimental parameters are indicated on the plot.*

The 'onset' of OH adsorption in both Pt/NSTF and Pt-Co-Mn/NSTF is similar; i.e. in the case of the alloy the OH adsorption onset has not shifted to higher potentials. As mentioned in chapter two, a shift of the OH adsorption peak to higher potentials in single crystals of Pt-alloys has been observed and is thought to be reason for the enhanced ORR

activity in those alloys. Although both Pt/NSTF and Pt-Co-Mn/NSTF show similar OH adsorptions, this potential is higher than for Pt/C electrocatalysts [87, 249].

From the data and using eq. 3.12, the ECSA of the electrocatalyst particles was obtained. Surface enhancement factors (SEF) were obtained as mentioned in the previous section and are plotted versus the Pt mass loading for Pt/NSTF and Pt-Co-Mn/NSTF in Figure 7.6 (a). The SEF value of 10× at 0.1 $mg \cdot cm^{-2}$ is very close to values obtained from PEMFC data [226]. When the linear fits to both samples are considered, the difference in the SEF (or roughness factor) of the two samples can be obtained. The Pt-Co-Mn electrocatalyst has about 15% higher electrochemical surface area than the Pt/NSTF.

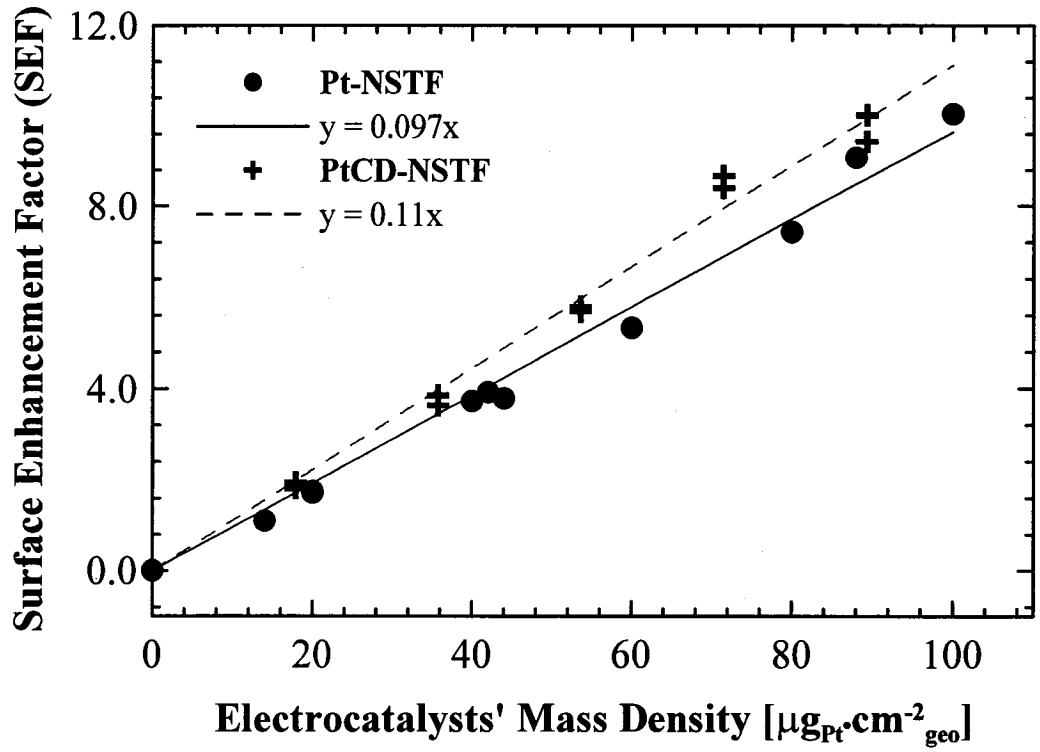

Figure 7.6 *Surface enhancement factors of Pt/NSTF and Pt-Co-Mn/NSTF as a function of Pt loading.*

7.5.2 ORR Activities of the Pt/NSTF and Pt-Co-Mn/NSTF Electrocatalysts

The oxygen reduction activity of Pt-NSTF at 900 rpm is shown in Figure 7.7 for several different loadings. Note that the data are essentially the same except that at lower loadings the expected theoretical diffusion-limited current is not reached. In the case of low loadings, it is the availability of the catalytic sites which presumably becomes a limiting factor in the observed current densities not the flow of oxygen.

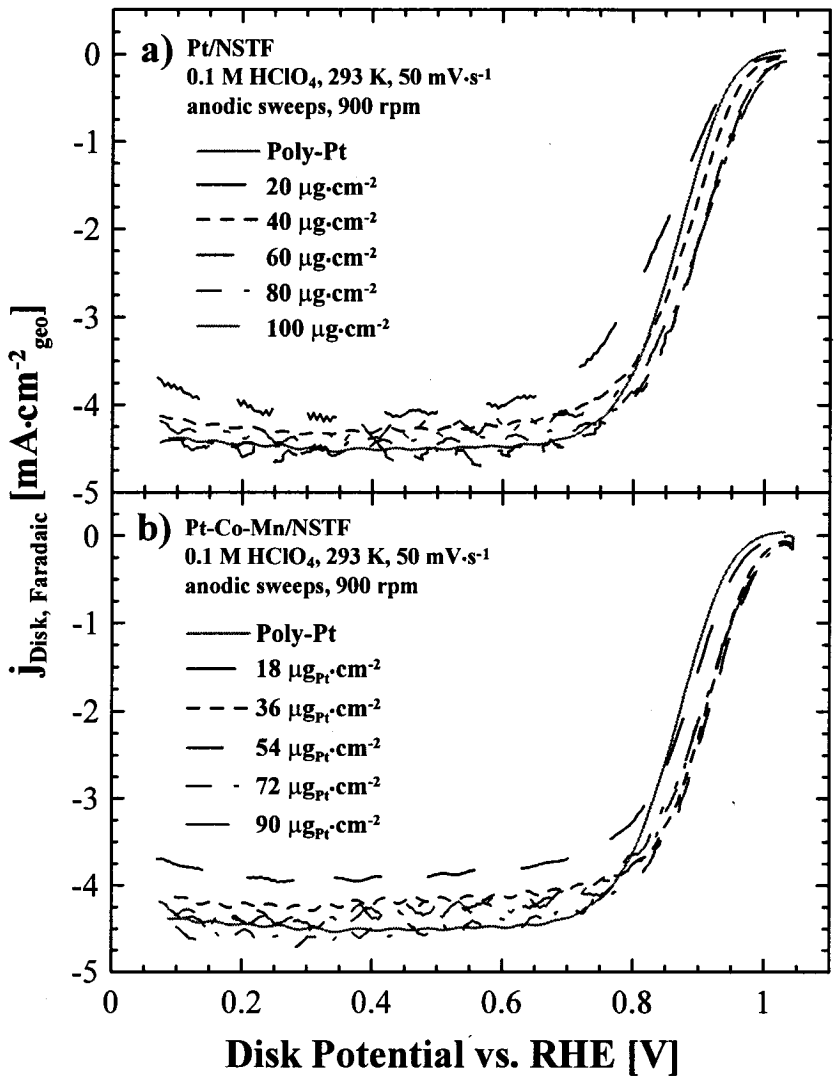

Figure 7.7 *Oxygen reduction curves of Pt/NSTF (a) and Pt-Mn-Co/NSTF (b) taken at 900 rpm and shown in the anodic direction.*

To analyze the kinetic activity of the Pt/NSTF and Pt-Co-Mn/NSTF electrocatalysts, we again consider the Tafel region. Figure 7.8 shows the Tafel region of Pt/NSTF where the kinetic current density, normalized by ECSA and corrected for the background non-Faradaic current, is plotted. Data for a polycrystalline Pt-disk is also shown for reference. Note that for the Pt/NSTF electrocatalyst all the Tafel lines fall on or below the Pt-disk baseline.

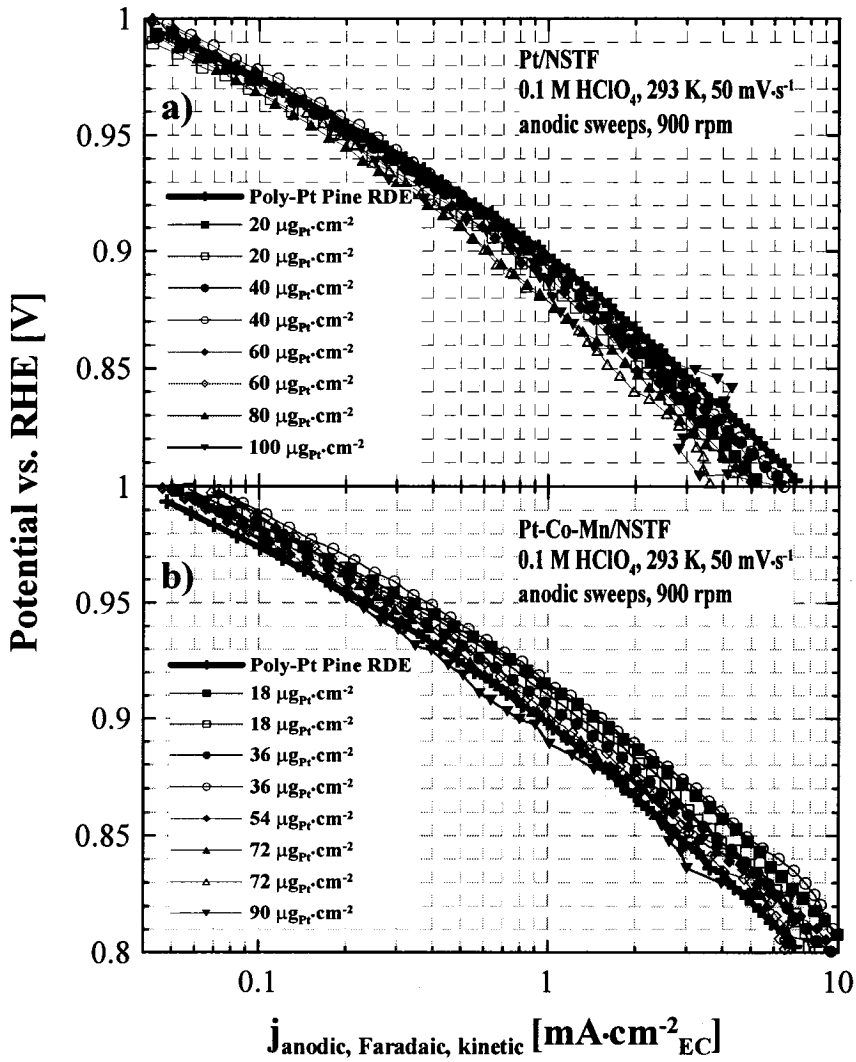

Figure 7.8 *Tafel behavior of Pt/NSTF (a) and Pt-Co-Mn/NSTF (b) showing the area specific activity. The current is normalized by the ECSA, corrected for double-layer effects and mass transfer limitations. All experimental parameters are indicated in the figure.*

Duplicate measurements are also shown to illustrate the repeatability of the measurements. The spread in the data is about 10 mV or so and activity seems to decrease with increasing loading, although the effect of loading has been considered by normalizing the data by ECSA. Figure 7.8 (b) shows Tafel kinetics of the Pt-Co-Mn/NSTF sample and again one can observe a spread in the data, where a decrease to lower potentials is seen when the loading on the GC disks increases. However, unlike the Pt-NSTF data, all these measurements fall on or above the Pt baseline, which is extremely significant. According to these measurements, Pt-Co-Mn/NSTF clearly shows an advantage over Pt/NSTF for ORR electrocatalysis.

From these data, two average sets from Pt/NSTF and Pt-Co-Mn/NSTF were chosen and are plotted in Figure 7.9, to compare the intrinsic activity of Pt/NSTF and Pt-Co-Mn/NSTF. The Tafel data of both Pt/NSTF and Pt-Co-Mn/NSTF can be fitted with two linear lines giving slopes of 70 and 135 $mV \cdot decade^{-1}$. These slopes are similar to that observed for sputtered Pt films (see chapter 5) and are close to what is generally observed for Pt in $HClO_4$ [166]. Fuel cell data provided by 3M, taken at two different oxygen pressures and corrected for the iR loss, are also shown for Pt-Co-Mn/NSTF samples. Extrapolation of the FC data to higher potentials seems to agree well with the data obtained from our RRDE measurements. More FC data are presented later in this chapter.

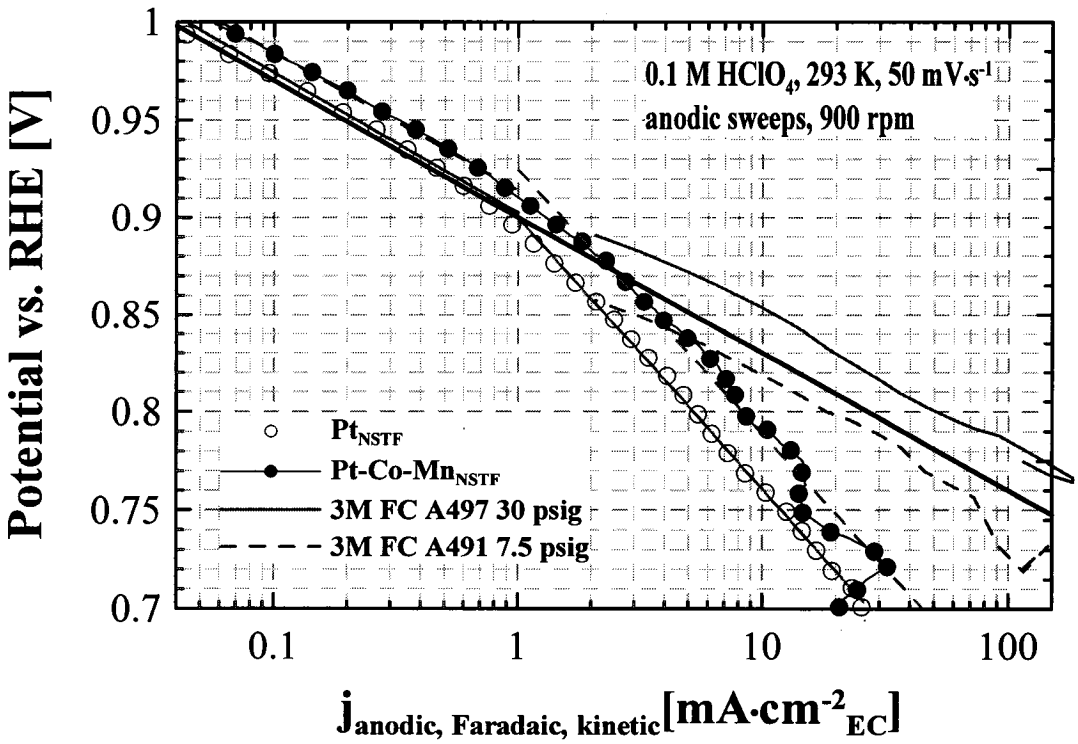

Figure 7.9 *Comparison of Pt/NSTF and Pt-Co-Mn ORR kinetics. The data show two slopes of 70 and 135 $mV \cdot decade^{-1}$. The black thick line is a Tafel line with a slope of 70 $mV \cdot decade^{-1}$ assuming 1 $mA \cdot cm^{-1}$ Pt at 0.9 V. 3M FC data for Pt-Co-Mn/NSTF are measurements done at H_2/O_2 with O_2 pressures of 7.5 (dashed) and 30 psig (solid) [226].*

The Pt-Co-Mn/NSTF catalyst shows an improved kinetic gain of about 20 mV or so. For a more quantitative comparison, we compare the kinetic current densities of the two respective electrocatalysts at 0.9 V and 0.85 V versus RHE, by averaging the current data. The kinetic current densities of Pt/NSTF at 0.9 and 0.85 (versus RHE) are 0.76 and

2.15 $mA \cdot cm^{-2}_{EC}$. The values for Pt-Co-Mn/NSTF are: 1.22 and 3.87 $mA \cdot cm^{-2}_{EC}$. Pt-Co-Mn/NSTF has a 1.8× gain in its intrinsic rate of ORR. This value is in agreement with the PEMFC evaluations.

Figure 7.10 shows the mass specific activity of Pt/NSTF and Pt-Co-Mn/NSTF. Again, an increase of about 2× in the current density of the latter is observed. Thus the RRDE data presented show that Pt-Co-Mn/NSTF has a clear advantage over Pt/NSTF.

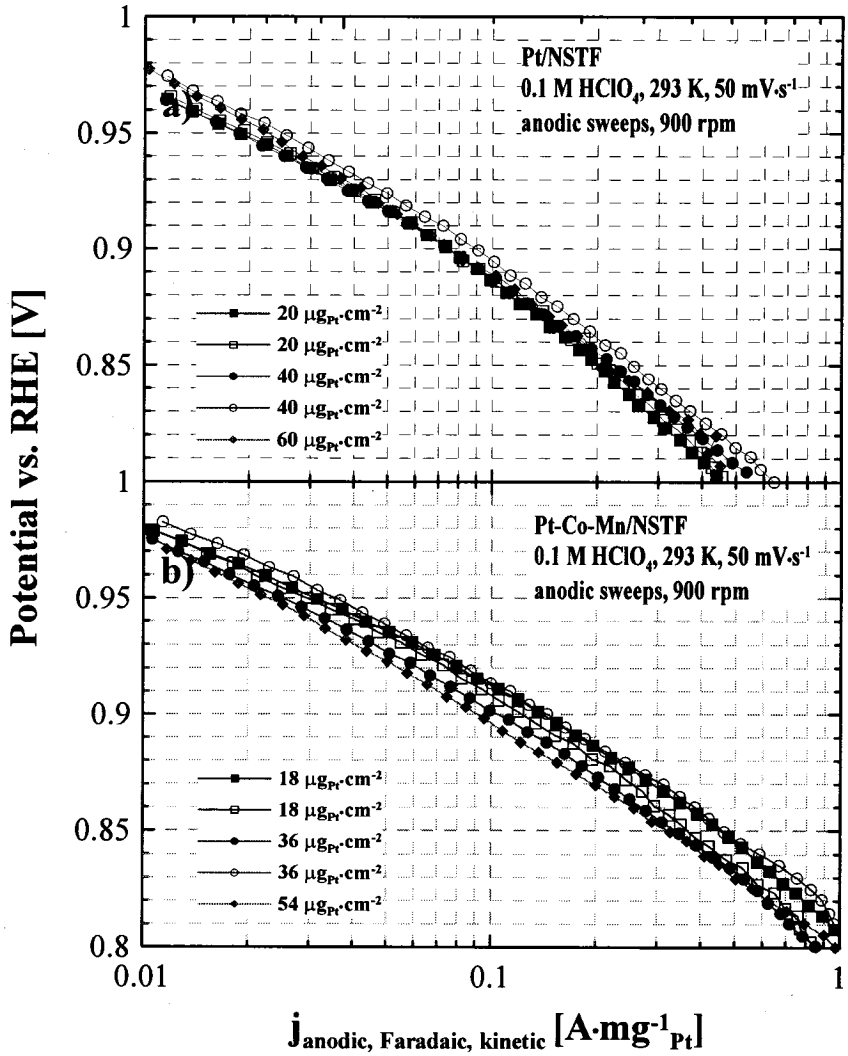

Figure 7.10 *Tafel behavior of Pt/NSTF a) and Pt-Co-Mn/NSTF b) showing the mass specific activity. The current is normalized by the mass of Pt, corrected for double-layer effects and mass transfer limitations. All experimental parameters are indicated in the figure.*

Why does Pt/NSTF show higher activity than Pt/C? As mentioned previously in chapters 2 and 5, OH adsorption plays a very important role in the rate of oxygen reduction. Mayerfoher *et al.* show that the onset of OH adsorption shifts to higher

potentials when the Pt particle size increases [249]. For example, Pt/NSTF catalysts show a higher potential than Pt/C, indicating that the OH coverage is lower in these catalysts than Pt/C; thus increasing the rate of ORR. For a more fundamental explanation, the authors also study the potential of zero charge ($E_{\sigma=0}$), as a function of Pt particle size and note a similar increase in $E_{\sigma=0}$. The potential of zero charge refers to a point on the potential scale where the surface is neutral. Above this potential, the surface becomes negatively charged and below it is positively charged [276, 277]. The reported results point towards $E_{\sigma=0}$, which is directly related to the work function, as a fundamental factor which apparently shows a size dependence. Generally $E_{\sigma=0}$-Φ correlations take the following form:

$$E_{\sigma=0} = \Phi + \Delta X + \text{const}, \qquad (6.1)$$

where ΔX and const account for the interfacial environment effects and the potential referencing, respectively [276]. The work function has two contributions, namely the chemical potential of the electrons, $E_{f\,\text{and}}$ a surface potential, χ:

$$\Phi = -E_f + \chi. \qquad (6.2)$$

According to Mayerhofer *et al.* it is the second term in equation (6.2), or the surface potential of Pt arising from electron spilling outside of the metal surface, which is different for different sized electrocatalyst particles. However, it must be stressed that there has been significant debate over the Φ–$E_{\sigma=0}$ correlations; moreover the $E_{\sigma=0}$ and Φ of poly-crystalline materials are difficult quantities to measure. Surface heterogeneities impact these measurements, thus making the quantities themselves questionable. Trasatti and Lust provide the most recent and extensive review of the potential of zero charge and discuss these difficulties in *Modern Aspects of Electrochemistry* (Vol. 33) [276].

A second possibility to explain the greater area specific activity of larger particles could be a smaller fraction of defect sites, like steps and edges, when the particle size is larger. The defects or the high energy sites could adsorb OH more strongly, which would hinder the ORR. Increased metal-adsorbate interactions at the defect sites could in some cases be a positive factor. A well known case is that of N_2 dissociation on Ru (0001) facets, where on the steps it is shown to occur about 9 orders of magnitude faster than on terraces [278]. The same properties of Pt/NSTF, i.e. larger grain size and contiguous

morphology in the polycrystalline film form, is thought to be largely responsible as well for the excellent corrosion stability of Pt/NSTF in this class of electrocatalysts [251].

A harder question to answer is the reason for higher activity of Pt-Co-Mn/NSTF over Pt/NSTF. OH adsorption arguments, which hold for Pt-alloys studied on carefully prepared surfaces, do not hold here, because we saw earlier in Figure 7.5 that the onset of OH adsorption in Pt/NSTF and Pt-Co-Mn/NSTF catalysts is similar.

7.5.3 H_2O_2 Yield of Pt/NSTF and Pt-Co-Mn/NSTF

The amount of H_2O_2 released into the electrolyte during the ORR of Pt/NSTF and Pt-Co-Mn/NSTF was obtained from the ring electrode and the results are shown in Figure 7.11. Both Pt/NSTF and Pt-Co-Mn/NSTF samples seem to produce equal amounts of H_2O_2 which is similar to amounts measured in bulk Pt samples.

Figure 7.11 shows the hydrogen peroxide yield of Pt/NSTF, Pt-Co-Mn/NSTF and a sputtered Pt film for comparison. The production of H_2O_2 on both samples having the same loading is essentially the same. What is interesting to note, however, is the increased amount of H_2O_2 observed in both cases when loading is at its lowest level. In the case of Pt/C electrocatalysts, Inaba *et al.* have reported an increasing amount of H_2O_2 when the loading on the GC disk decreased and/or the particle size was reduced [279]. The impact of catalyst loading on H_2O_2 formation for Pt-based and non-Pt based catalysts is discussed in chapter 8.

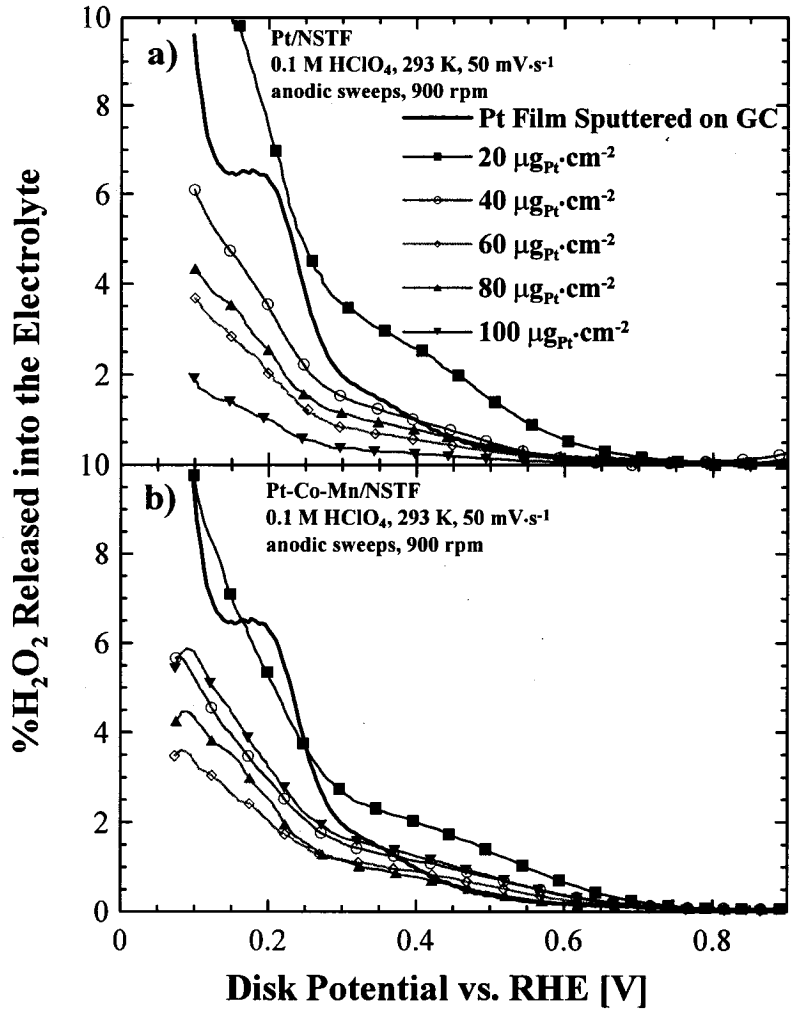

Figure 7.11 *H_2O_2 that is detected by the ring shown as a function of potential for a) Pt/NSTF b) and Pt-Co-Mn/NSTF. Data for a Pt film sputtered on GC are also shown for comparison.*

7.6 PEMFC Performance of Pt/NSTF and Pt-Co-Mn/NSTF

It is both interesting and useful to compare the RRDE measurements to those of PEMFC. The PEMFC data show the "real life" scenario for the performance of these (or any) electrocatalysts. The fuel cell measurements were made at 3M Company in typical 50 cm^2 electrode single cells operated at a temperature of 80°C, H_2/O_2 pressures of 150 kPa (abs). The area and mass specific activities were recorded at 0.9 V, after a 15-20 min stabilization period.

Figure 7.12 shows the specific activities of several different Pt loading Pt-Co-Mn/NSTF catalysts [226]. The loading refers to that of Pt only. At 0.9 V, a 1.5× gain in

the specific activities of Pt-Co-Mn/NSTF over Pt/NSTF is observed, which is close to that obtained in the RRDE measurements.

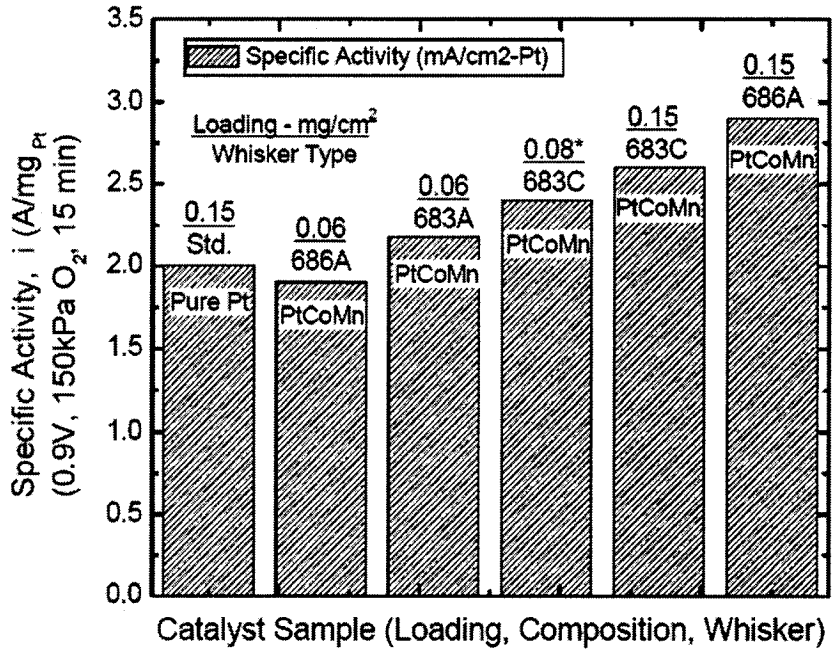

Figure 7.12 *Area-specific activity of Pt/NSTF versus Pt-Co-Mn/NSTF (various Pt loadings) shown at 0.9 V. (Taken from reference [226])*

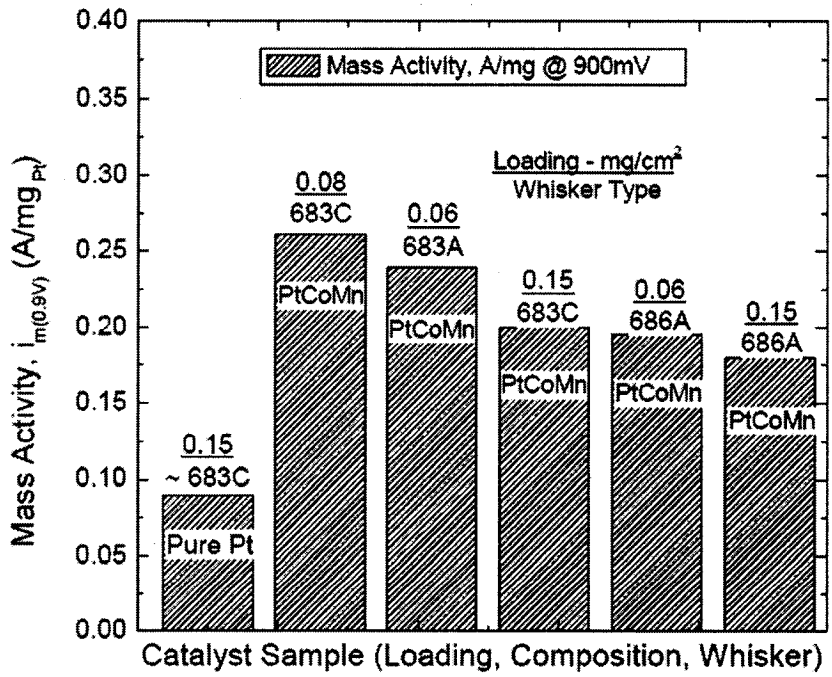

Figure 7.13 *Mass--specific activity of Pt/NSTF versus Pt-Co-Mn/NSTF (various Pt loadings) shown at 0.9 V. (Taken from reference [226])*

Figure 7.13 shows the mass specific activities of Pt/NSTF and various loadings of Pt-Co-Mn/NSTF. The loadings refer only to the Pt content. At a loading of 0.15 $mg_{Pt} \cdot cm^{-2}$, Pt-Co-Mn/NSTF provides a 2× gain in the mass specific kinetic activities.

Two important questions still remain to be answered. How important is the Mn content? The Mn content, as measured by electron microprobe, is only about 5%. As was shown in chapter 3, Mn is also more likely to corrode faster than Co. However, according to 3M, Pt-Co-Mn/NSTF does show an improvement over Pt-Co/NSTF catalysts. The exact bulk and surface composition and surface morphology of Pt-Co-Mn/NSTF catalysts are not known. Further understanding of these properties should help to explain the apparent higher activity observed in these catalysts.

Another question is more application-related than fundamental. How do kinetic gains at 0.9 V translate into improved current densities at 0.6 V, which is the working potential of PEMFCs? Does a 2× activity gain at 0.9 V translate into a 2× gain in the current density at 0.6 V? The answer is no. Figure 7.14 shows a complete polarization curve of Pt/NSTF versus that of Pt-Co-Mn/NSTF for very low loading (0.06 $mg_{Pt} \cdot cm^{-2}$) measured at identical conditions. At 0.6 V, the Pt-Co-Mn/NSTF catalyst shows at best a 10% gain in current densities. This is because iR and mass transfer losses are not important when activities are measured at 0.9 V. As was mentioned in the first chapter, the total activation losses at the cathode amount to about 400 mV (see Figure 1.13). A gain of 20 mV at 0.9, corresponds to a 5% reduction in activation losses. Thus at 0.6 V, where the FC is not under activation control, one expects to obtain a 5% or so gain in the current density.

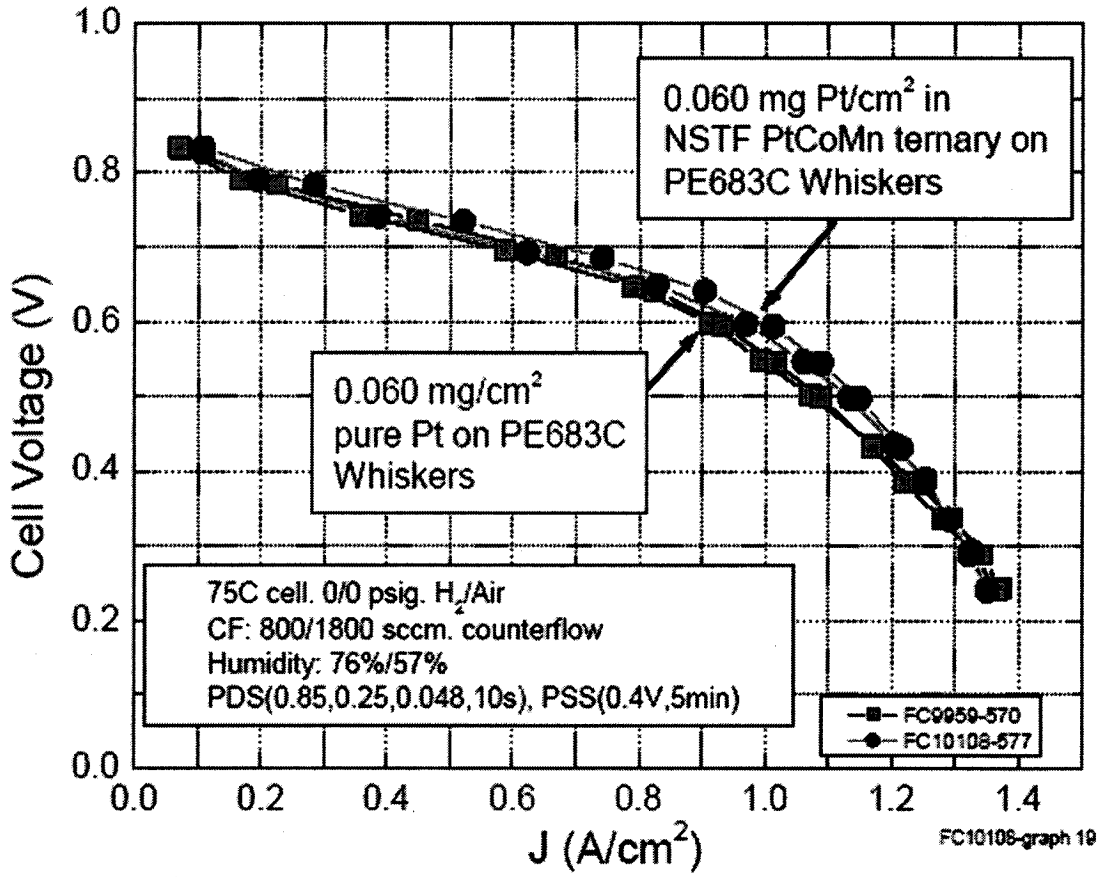

Figure 7.14 *PEMFC polarization measurements of Pt/NSTF and Pt-Co-Mn/NSTF electrocatalysts. Notice the higher current densities observed at 0.6 V – the operating potential of hydrogen FCs. The operating conditions are all indicated in the figure. (Taken from reference [226])*

7.7 Conclusions

The work presented here clearly shows that Pt-Co-Mn/NSTF has an advantage in its ORR activity over Pt sputtered on NSTF. The gain observed by RRDE cells is similar to the results of measurements made in PEMFCs. Further work on the RRDE of the electrocatalysts could include studies of different compositions, temperature effects and perhaps more importantly the effect of acid treatment on the electrocatalysts' activity.

Chapter 8

Impact of Electrocatalyst Loading in RRDE Experiments

8.0 Introduction

This chapter discusses the effects of catalyst loading in RRDE experiments. This is still an on-going project, however because of the importance of this subject, the data collected to-date are presented.

The diffusion-limited current as observed in RRDE experiments was discussed in chapter 3. When the reaction rate becomes mass-transfer limited, the current will not increase further even if the potential is lowered. In chapters 5, 6 and 7, diffusion-limited currents for ORR were reached on Pt (Figure 5.12), Pt-Co (Figure 6.12) and Pt-Co-Mn (Figure 7.7) electrocatalysts. Within the mass transfer region, the intrinsic turn-over frequency (TOF) of the electrocatalyst is not reached and increasing the rotation speed of the electrode increases the observed current because more O_2 reaches the electrode per unit time. However, in a situation where the electrocatalytic site density is low on the electrode tip, it may not be the oxygen flow rate (or the rotation speed) which is rate limiting, but the number of catalytic sites, or simply the catalyst loading. For sputtered films of Pt and Pt-alloys, such as Pt-Co, on GC disks, diffusion-limited currents were always reached at the practical rotation speeds. For $Pt_{1-x}Ta_x$ ($0.1 \leq x \leq 0.3$) samples (presented in chapter 5), however, diffusion-limited currents were not reached (Figure 5.19). Apparently the number of catalytic sites is greatly reduced when $x > 0.1$ in $Pt_{1-x}Ta_x$ samples.

A related observation is that H_2O_2 yield, as detected by the ring, also increases. What would be the behavior of the diffusion-limited current and levels of produced H_2O_2 for powdered samples like Pt/NSTF, where the amount of catalyst on the RRDE electrode tip can be rather easily and systematically varied? Inaba *et al.* have observed that when the amount of Pt/C on the RRDE electrode is reduced, diffusion-limited currents are not reached and H_2O_2 yields increase [279]. This loading effect is yet another very crucial

factor in RRDE measurements because it could lead to different fundamental and applied interpretations.

The data presented in this chapter were collected on two types of very different ORR catalysts: a) Pt/NSTF and b) non-noble metal catalysts (NNMC) in thin film and powder form.

8.1 RRDE Results for Pt/NSTF Electrocatalysts

Figure 7.7 showed that the lowest loading (20 $\mu g \cdot cm^{-2}$) for both Pt/NSTF and Pt-Co-Mn/NSTF electrocatalysts lead to the lowest diffusion-limited currents and the highest H_2O_2 levels. Figure 8.1 shows ORR curves for Pt/NSTF taken using even lower loadings. In general, lower loading leads to lower currents in the plateau region.

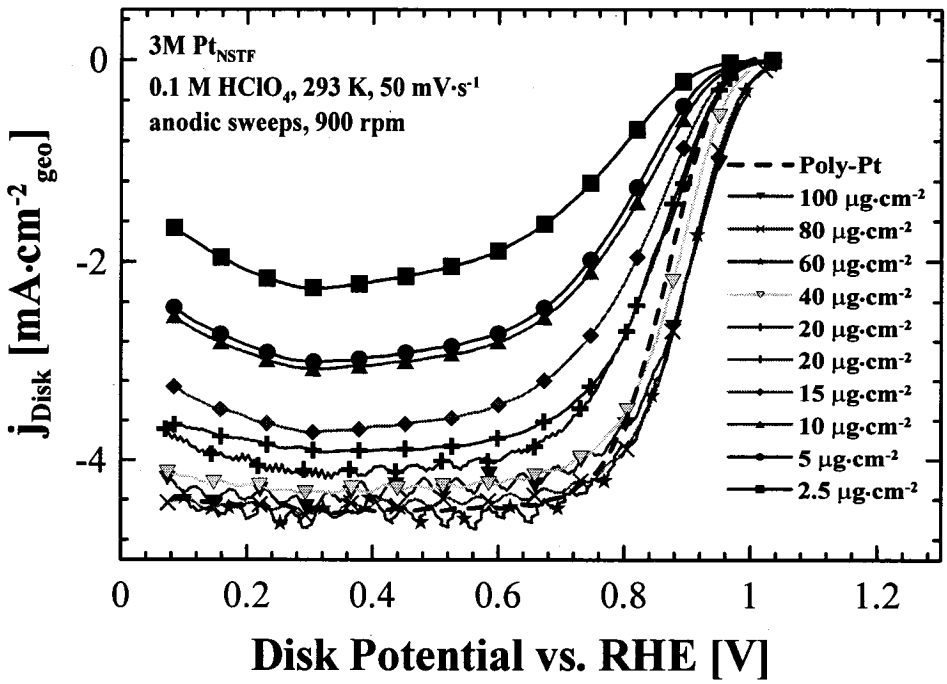

Figure 8.1 *ORR current densities for various different loadings of Pt/NSTF.*

Figure 8.2 shows the peroxide production measurements obtained from the RRDE measurements for different loadings. The trend is clear: lower electrocatalyst loadings lead to an increased amount of H_2O_2. As discussed in chapter 2 (Figure 2.6), the series pathway, that is reduction of oxygen to peroxide and then to water, is a possibility. When the catalyst concentration is low, there is a smaller chance of H_2O_2 breaking down. This can happen when a) impurities cover the Pt surface or b) the catalyst loading is low. Note

that in clean cells, peroxide levels increase when potential reaches the H_{ad} region (Figure 5.14). This happens because the surface gets covered with H_{ads} thus, there is a smaller chance for the dissociation of O_2. In this case, it is apparently more probable for an O_2 molecule to become protonated, form H_2O_2 and desorb, rather than go under dissociative chemisorption. Other impurities like Cl^-, Br^- and alcohols have the same effect, i.e. increased H_2O_2 production because of Pt surface contamination [170-172]. H_2O_2 could also adsorb at a different catalytic site to break down and form H_2O. If the catalyst concentration is low (low loading), there is a smaller probability for the H_2O_2 to reach a suitable site and decompose.

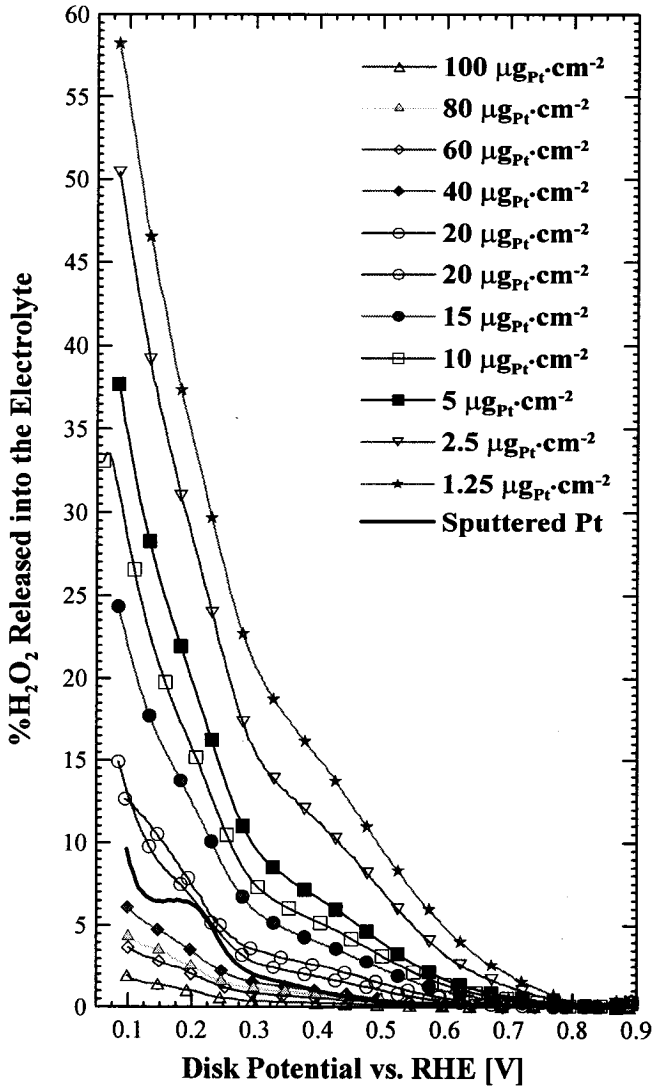

Figure 8.2 *$\%H_2O_2$ produced during the reduction of O_2 on Pt/NSTF in 0.1M $HClO_4$ at room temperature.*

8.2 RRDE Results for NNMC Electrocatalysts

Although no mention of non-noble metal based ORR electrocatalysts have been made so far in this thesis, some RRDE results for various loadings are reported here.

Very briefly, metal macrocyclic compounds such as N_4-metal (Fe, Co) macrocycles like porphyrins have long been known as oxygen reducing catalysts [280]. The exact nature of the catalytic sites and mechanisms are not really understood, partly because single crystalline samples like those of Pt and Pt-alloys are not available. What is currently known, however, is that carbon, nitrogen and a transition metal like Fe or Co is needed to produce activity for ORR [131, 132, 281-286]. Jean-Pol Dodelet provides a good review of these electrocatalysts [280]. Sputtered TM-C-N films on GC disks have been extensively studied in our research group over the past two years [285, 286]. After heat treatment these films become active towards oxygen reduction [287].

Figure 8.3 shows the ORR activity of several Fe-C-N film compositions sputtered on GC disks and treated at different temperatures. Figure 8.3 also includes literature data, reported by Dodelet's research group, showing that powdered NNMC catalysts reach diffusion-limited currents in ORR measurements made by RRDE.

Figure 8.4 shows the corresponding peroxide productions. A puzzling observation was that, although differences in the onset potentials were observed for the sputtered films, none of the ORR curves reached diffusion limited currents and the peroxide levels were usually much higher than any other Fe-C-N type catalyst reported in the literature [131, 288, 289].

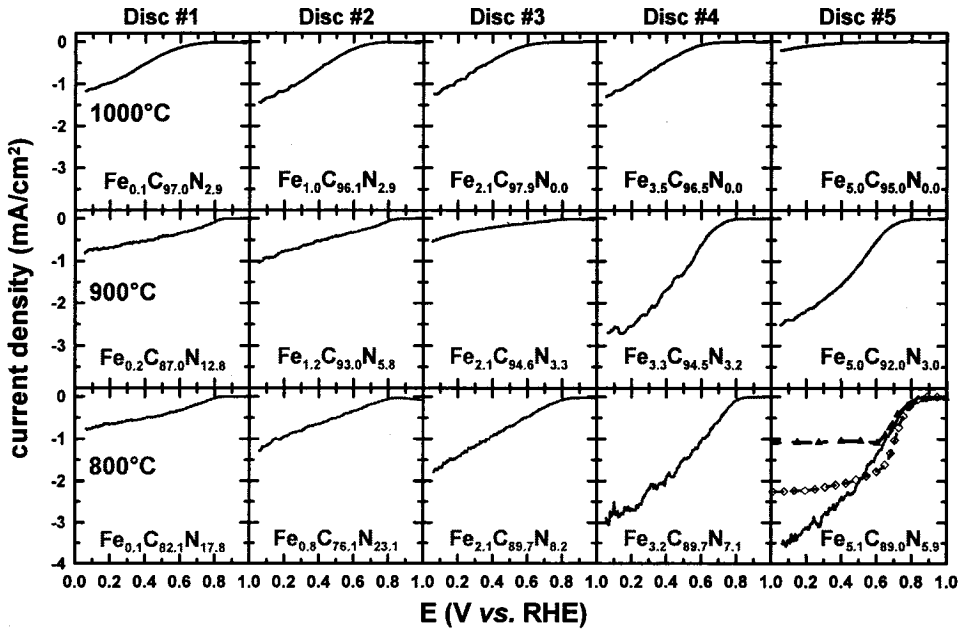

Figure 8.3 *Disc current densities for sputtered libraries annealed at 800, 900 and 1000°C. Measurements were made at a sweep rate of 5 $mV \cdot s^{-1}$ in O_2-saturated 0.1M $HClO_4$ at room temperature while the electrode was rotated at 900 RPM. The average composition of each disk is indicated in each panel. Also shown in the bottom-right panel is the activity reported by Dodelet's group for "II (0.2) FeAc(900)" at 100 RPM (triangles) [131] and "ClFeTMPP/ RC1" at 1500 RPM [290].*

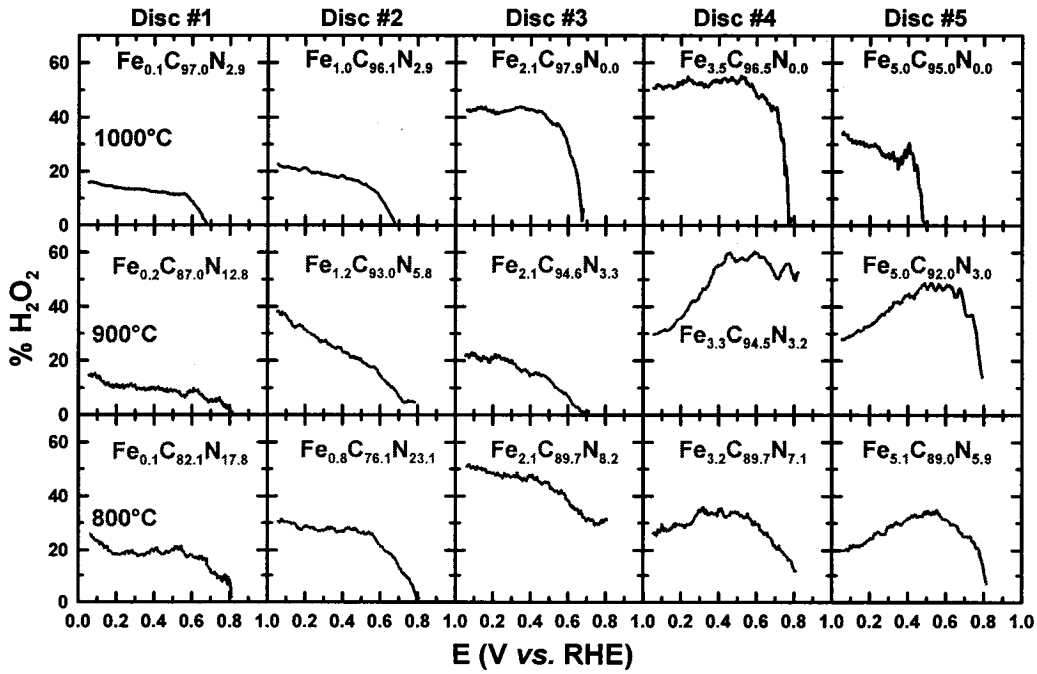

Figure 8.4 *% H_2O_2 produced as a function disc potential for sputtered libraries annealed at 800, 900 and 1000°C. Measurements were made at a sweep rate of 5 $mV \cdot s^{-1}$ in O_2-saturated 0.1M $HClO_4$ at room temperature while the electrode was rotated at 900 RPM. The average composition of each disk is indicated in each panel.*

Typical Fe-C-N powder samples were acquired from Dodelet's group at INRS and catalyst slurries with different concentrations were prepared as described earlier in chapter 3. All electrochemical measurements were performed as described earlier in Chapter 3. Figure 8.5 shows the ORR and peroxide production data for these samples. The trends in the ORR curves and peroxide production levels are very similar to those of Pt/NSTF. ORR curves are reduced and higher amounts of H_2O_2 are produced as the loading decreases. These measurements are in agreement with those made at INRS. NNMC films sputtered on flat surfaces like GC disks are equivalent to low loading powder samples. In both cases the number of catalytic sites is low, diffusion-limited currents are not reached and peroxide levels are high.

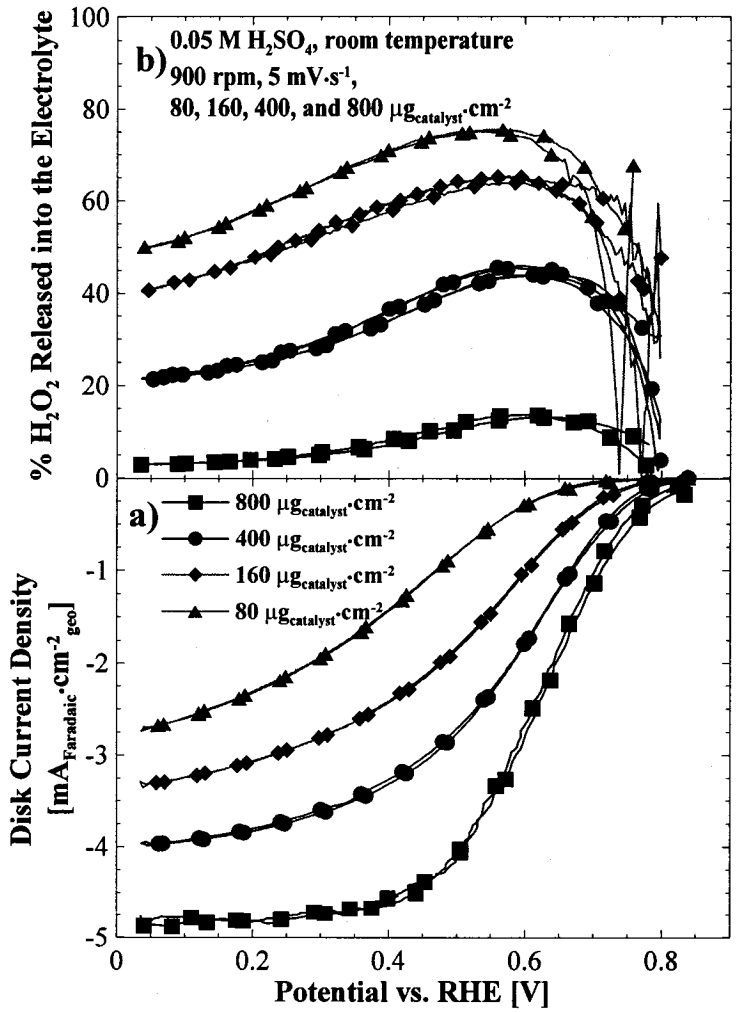

Figure 8.5 *a) ORR currents and b) $\%H_2O_2$ produced during the oxygen reduction reaction for various loadings of the same Fe-C-N-type electrocatalyst. Measurements were made in 0.05M H_2SO_4 and at room temperature.*

8.3 Conclusions

The implications of the data presented here are important for both mechanistic studies and applications. The reduction of Pt catalyst content could ultimately lead to an increased amount of peroxide produced in a PEMFC. Measurements made using the same catalyst (but a different recipe for the preparation of ink and a different lab standard) could lead to different interpretations. It is quite possible, as Inaba has argued, that the actual reduction on a single Pt/C particle goes through a H_2O_2 step first.

Chapter 9
Conclusions

9.0 Introduction

A brief summary of the various experiments presented in this thesis is given here. More detailed conclusions have been provided at the end of each chapter. Suggested further work in these related subject areas are outlined at the end.

9.1 Pt-Based Electrocatalysts Sputtered on NSTF

Extensive leaching studies of Pt-transition metal alloys showed that significant loss of transition metals occurs in the binary and ternary sputtered films of Pt-M and Pt-M-M' (M, M' = Ni, Fe, Mn, Co). These films were all sputtered onto nano-structured thin film supports, which are designed for direct use in PEMFCs. Similar loss of transition metals from these alloys occurs when they are subjected to the corrosive environments of hydrogen PEMFCs. Treatment in 0.5M H_2SO_4 at 80°C for a period of several days mimicked the acidic environment of hydrogen PEMFCs very well. In these Pt-alloy nano-grains (10-15 nm), transition metals are lost from the surface layer when the transition metal content is less than 60% and from the surface and the bulk when the transition metal content is greater than 60%. The leaching of transition metals is very important as it changes the composition of catalyst during use in a PEMFC and could contaminate the Nafion membrane used in the PEMFC. The exact impact of transition metal leaching on the catalytic activity of ORR is still not very well understood and there are contradictory conclusions at the moment. As far as Pt-alloy/NSTF electrocatalysts are concerned, there are alloys, such as Pt-Co-Mn, which maintain their activities even though dissolution of transition metals occurs. Figure 9.1 shows a scheme, which Antolini *et al.* have provided after reviewing the literature on the corrosion and ORR activity of Pt-alloys.

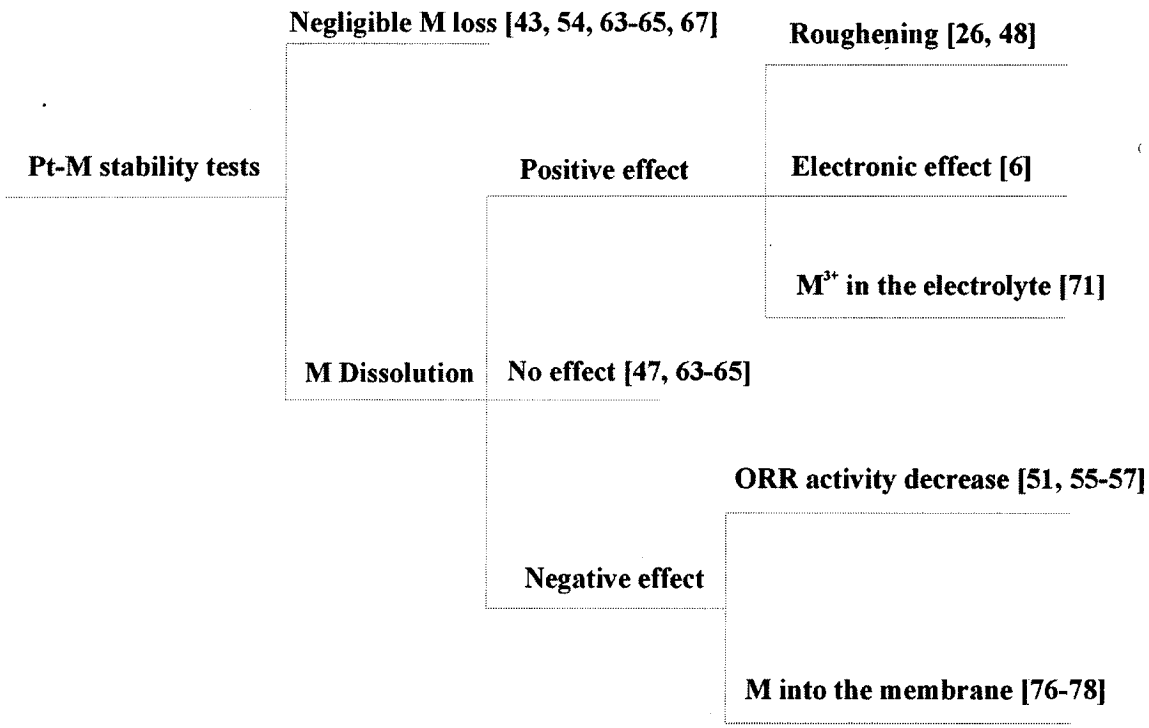

Figure 9.1 *A summary of transition metal corrosion in Pt-alloys and the reported impact on ORR. The numbers indicate references which can be found in [291].*

9.2 Electrocatalysts Sputtered on GC Disks

Several libraries of $Pt_{1-x}Co_x$ were studied for their ORR activity. The activity comparisons were made to an objectively established Pt baseline measurement. For $x > 0.2$, the maximum activity gain observed at 0.85 V was about 1.7× for the annealed alloys. No strong correlation between x and activity was observed over the range $0.2 \leq x \leq 0.5$. There are reports of 10× or so activity gain in alloys such as Pt-Co in the literature. These high activity gains usually stem from poor Pt baseline measurements.

9.3 Catalyst Loading in RRDE Experiments

Lowering the catalyst loading in RRDE experiments shows significant increase of H_2O_2 levels for both Pt and non-Pt based ORR electrocatalysts. A conclusion that can be drawn at this point is that oxygen reduction occurs primarily though the H_2O_2 pathway. When concentration of catalyst particles is high there are enough catalytic sites to reduce the H_2O_2. That is, H_2O_2 molecules can diffuse to neighboring sites and get reduced. Lowering the catalyst loading leads to a lower probability of H_2O_2 reduction because there are not enough catalytic sites and H_2O_2 away out into the solution. The findings are

important because H_2O_2 is known to cause membrane degradation in FCs. Thus, lowering the Pt loading (or reduction of catalyst layer thickness) can potentially lead to production of undesired H_2O_2 and this should be considered by the fuel cell researchers. Furthermore, such studies could help to further elucidate the ORR mechanism.

9.4 Future Work on Pt-Based ORR Electrocatalysts

As for future work, acid bath treatment of combinatorial libraries remains a fast, simple and accurate way of determining the stability of Pt-alloy/NSTF catalysts. More RRDE experiments on as-deposited and acid leached Pt-alloy/NSTF electrocatalysts could determine the impact of leaching on the ORR activity. The design of stable and more active electrocatalysts is not simple. A systematic study of Pt-alloys, incorporating Pourbaix-stable elements, using 'real' type electrocatalysts (i.e. sputtered on NSTF or produced on carbon supports) is needed. For corrosion studies, more XPS characterization (before and after acid) is desired, because XPS is more surface sensitive. Sample tilt angle and/or a different choice of photoelectron peaks could make the measurements more surface sensitive. By choosing higher binding energy photoelectrons (i.e. lower kinetic energy electrons), it would be possible to detect those electrons which are closer to the surface; however, the signal to noise ratio could be lower. Another important measurement is the grain size determination by XRD (preferably high resolution) upon acid treatment (or post FC testing). SEM and TEM work on acid treated samples is time consuming, but could be performed for a selected number of samples. Addition of acid-stable elements like Ta should be further investigated. It may be possible to incorporate up to 10% of elements like Ta or Nb, both of which are stable in acid, in ternaries like Pt-Ta-Ni without loss of activity. The fact that corrosion effects may or may not hinder the ORR activity implies that stability and activity of Pt-alloys needs to be investigated independently.

Combinatorial methods are very useful in these screening processes; however, to date and after several years of research by various research groups no reliable combinatorial report for ORR catalysts has been reported. The problems of achieving state-of-the-art Pt baseline performance have plagued combinatorial efforts using both FC and solution-cell approaches. Combinatorial fuel cell work using sputtered film NSTF substrates has a

great advantage over the flat film-based approach because real type catalysts, which capture the effects of particle size and high surface area, are used. Any improvement in this regard could be highly rewarding.

The corrosion of Pt itself is also known and widely reported in the literature. Pt corrosion occurs above 0.5 V and as potential increases its rate accelerates [253]. As discussed in chapter 4, the surface area and hence particle size of Pt particles, is especially important in determining the rate of corrosion. The design of Pt-based alloy electrocatalysts should be based on: maintaining (or increasing) the ORR activity and maintaining the stability. For these reasons a thorough study of particle size effects from 1 to 30 nm is highly recommended. Particular attention should be paid to the 1-15 nm range, where most variations are thought to occur. Pt providers and fuel cell catalyst manufacturers generally maintain that scarcity of Pt is not an issue because Pt can be recovered. Loss of Pt during FC operation, however, in addition to a performance loss also decreases the efficiency of Pt recovery. The NSTF based catalysts, with grain sizes of 10-15 nm, have shown higher specific (and mass) activity and much better stability than Pt/C type catalysts. To further reduce the amount of Pt, the logical solution is to replace the Pt atoms that reside in the core of grains by non-noble metals (a core-shell type catalyst). This approach is only useful if the stability of Pt is not jeopardized. Is a 2-5 monolayer Pt shell on a non-Pt core as stable as the grains where the entire composition is Pt? More research is needed.

More in depth studies of Pt nano-grain formation on NSTF are also desired. The size Pt grains is about 8-15 nm regardless of the deposition thickness. It is speculated that the sputtered Pt atoms are energetic enough to diffuse and form such grains on the NSTF substrate. Different morphologies, for instance smaller grain size, can be obtained by varying the sputtering conditions. Sputtering in higher plasma pressures would decrease the kinetic energy of Pt atoms impinging on the NSTF substrate; however, more Pt would be lost to the chamber walls during deposition. An alternative way of reducing the kinetic energy of Pt atoms could be achived by using a lower temperature substrate table.

On highly oxidized Pt surfaces, where Pt corrosion is minimized, and using highly pure acidic electrolytes, the thermodynamic potential of 1.23 V (at room temperature) can be achieved [292]. Although such oxidized Pt surfaces are most likely not stable upon

electrochemical cycling, ternary Pt-M-M'-O surfaces (where M = Ta or Nb; M' = Ni or Co), may be stable. Sputtering of these systems in oxygen plasma and thus introduction of oxygen in the final layers of sputtered catalysts thus may be investigated. Another idea in prevention of Pt corrosion is the use of capping agents to hinder the corrosion of Pt. Au nano-islands, for instance, are shown to improve the stability of Pt [293]. There are also reports of polyoxometalates which do have oxygen reduction activity and are reported to improve the activity of Pt catalysts when used as overlayers [120]. More research is needed here.

There is substantial amount of research on non-noble metal catalysts (NNMC) for ORR [280]. These catalysts are not mentioned here because they were not discussed in detail in the thesis. It is generally argued that a 100× fold increase in activity is needed in these materials before they become competitive versus Pt [87]. A simple idea is just to mix the two types of catalysts. Could a substantially lower loading of 0.01-0.02 mg_{Pt}/cm^2 (i.e. 10× lower than the current Pt loading) with large grain sizes (10-15 nm) mixed with NNMC (either during synthesizing NNMC or just by adding), lead to a positive synergy between the two types of catalysts? No work has been reported in this regard.

Almost all RRDE studies (reported here and elsewhere) use H_2SO_4 or $HClO_4$ electrolytes. Trifluoromethanesulfonic acid or CF_3SO_3H, however, may better resemble Nafion which is comprised of fluorinated backbone and sulfonic acid groups. Both are superacids, but Nafion is weaker by about three orders of magnitude. Another example of superacids includes fluorosulfuric acid (FSO_3H). In addition, the impact of humidity can also be studied in these acids [294].

RRDE testing protocols can also be expanded to include numerous different measurements which will yield useful information about ORR. A loading study of any catalyst, Pt-based or non-Pt based, is vital to demonstrate the impact of loading on H_2O_2 production. For durability tests, hour(s)-long cyclic voltammetry within the desired potential range, or hour(s)-long constant potential could reveal the loss of active ECSA of the catalysts. Measurement of ORR before and after these CVs would then show the impact of ECSA loss on ORR. For this purpose similar testing procedures which are used by industry for fuel cells could be mimicked. For the Pt-alloys or NNMC, these CV tests could also identify the effect of metal corrosion and the extent to which they would

impact the ORR. Post-mortem analysis of the catalysts is then needed to determine the stable compositions.

The impact of impurities on ORR can be easily and be accurately studied. Controlled amounts of impurities like cations, anions or alcohols can be added to the RRDE cell and their impact on ORR can be determined. Such measurements could also be included in the form of a standard ORR measurement protocol.

A further expansion of RRDE testing protocols could include higher (80°C) temperature measurements. Experimental setups, however, would be more difficult because of acid leakage in the RRDE.

Expansion of the exciting work on Pt_3Ni (111) single crystals, which show 15× higher activity over Pt [176], to real type, high surface area catalysts, is very appealing and challenging. Annealing of films is needed to create such surfaces and for this reason supports that can be annealed are needed. Carbon nano-tube support structures could be an option. There are also reports of controlling the shape of nanometric Pt crystallites using polymeric capping agents [295]. These approaches can also be pursued further.

As for discovery of new ORR electrocatalysts, films deposited on flat surfaces such as GC disks are not an ideal approach. The purity of RRDE and similar solution cell setups is generally not easy to achieve and contamination always remains a problem. Thus combinatorial methods using solution cells are most likely to suffer from these problems. Furthermore, films deposited on flat surfaces do not represent nano-sized electrocatalysts that are used in PEMFC applications. Both activity and stability of electrocatalysts are size dependent properties and in general there is no one-to-one correspondence between low surface area catalysts such as films deposited on GC or single crystals and high surface area Pt/NSTF or Pt/C catalysts. These factors are all very important facts which should be considered in the search for better ORR electrocatalysts.

For more fundamental studies, patterned electrodes where controlled nano-sized islands of Pt are deposited on the surface of a GC disk could be very useful. Nano-islands with different dimensions produced on GC disks could be used. The size of islands could vary, for example, from 5-50 nm in lateral dimensions and 5-50 nm in height. The island to island separation should also be studied. The author speculates that H_2O_2 production increases when the size of islands decreases and/or the separation

between the islands increases. A systematic study of this kind could shed more light on the crucial factor of catalyst scale in the reduction of H_2O_2 during oxygen reduction reaction. Studies of this kind may also allow one to drive the Pt catalyst to a limit where further increasing the rotation speed would not lead to further increase in current. One can then deduce a turn-over frequency for ORR on Pt, which would effectively be a catalytic limit measuring the number of water molecules produced per Pt site per second.

Bibliography

1. N. Lewis, *Plenary talk presented at the Annual Fall Meeting of the Electrochemical Society, Los Angeles, CA, Nov. 14-18, (See Also http://nsl.caltech.edu/energy.html, Last Accessed on: May 14 2007)*, (2005).

2. C. J. Campbell and J. H. Laherrere, *Scientific American*, **279**, 78-83 (1998).

3. http://en.wikipedia.org/wiki/Hubberts_peak, Last Accessed on: May 14 2007.

4. M. R. Simmons, *Twilight in the Desert: The Coming Saudi Oil Shock and the World Economy*, Wiley, (2006).

5. K. S. Deffeyes, *Hubbert's Peak: The Impending World Oil Shortage*, Princeton University Press, (2003).

6. K. S. Deffeyes, *Beyond Oil: The View from Hubbert's Peak*, Hill and Wang, (2005).

7. R. Heinberg, *Powerdown: Options and Actions for a Post-Carbon World*, New Society Publishers, (2004).

8. R. Heinberg, *The Party's Over: Oil, War and the Fate of Industrial Societies*, New Society Publishers, (2005).

9. J. H. Kunstler, *The Long Emergency: Surviving the End of Oil, Climate Change, and Other Converging Catastrophes of the Twenty-First Century*, Grove Press, (2006).

10. S. Leeb and G. Strathy, *The Coming Economic Collapse: How You Can Thrive When Oil Costs $200 a Barrel*, Warner Business Books, (2006).

11. P. Roberts, *The End of Oil: On the Edge of a Perilous New World*, Mariner Books, (2005).

12. D. Yergin, *The Prize : The Epic Quest for Oil, Money & Power*, Free Press, (1993).

13. G. Monbiot, *Heat: How to Stop the Planet from Burning*, South End Press, (2007).

14. http://www.ipcc.ch/, Last Accessed on: May 14 2007.

15. A. Gore, *An Inconvenient Truth*, Rodale, New York (2006).

16. E. Linden, *The Winds of Change: Climate, Weather, and the Destruction of Civilizations*, Simon & Schuster, New York (2006).

17. T. Flannery, *The Weather Makers : How Man Is Changing the Climate and What It Means for Life on Earth*, Harper Collins, Toronto (2006).

18. R. Gelbspan, *The Heat Is on: The Climate Crisis, the Cover-Up, the Prescription*, Perseus Books Group, Cambridge (1998).

19. C. D. Harvell, C. E. Mitchell, J. R. Ward, S. Altizer, A. P. Dobson, R. S. Ostfeld and M. D. Samuel, *Science*, **296**, 2158-2162 (2002).

20. O. Hoegh-Guldberg, *Mar. Freshw. Res.*, **50**, 839-866 (1999).

21. L. Hughes, *Trends Ecol. Evol.*, **15**, 56-61 (2000).

22. T. P. Hughes, A. H. Baird, D. R. Bellwood, M. Card, S. R. Connolly, C. Folke, R. Grosberg, O. Hoegh-Guldberg, J. B. C. Jackson, J. Kleypas, J. M. Lough, P. Marshall, M. Nystrom, S. R. Palumbi, J. M. Pandolfi, B. Rosen and J. Roughgarden, *Science*, **301**, 929-933 (2003).

23. P. D. Jones, M. New, D. E. Parker, S. Martin and I. G. Rigor, *Rev. Geophys.*, **37**, 173-199 (1999).

24. K. A. Kvenvolden, *Rev. Geophys.*, **31**, 173-187 (1993).

25. M. Oppenheimer, *Nature*, **393**, 325-332 (1998).

26. G. R. Walther, E. Post, P. Convey, A. Menzel, C. Parmesan, T. J. C. Beebee, J. M. Fromentin, O. Hoegh-Guldberg and F. Bairlein, *Nature*, **416**, 389-395 (2002).

27. J. Zachos, M. Pagani, L. Sloan, E. Thomas and K. Billups, *Science*, **292**, 686-693 (2001).

28. http://en.wikipedia.org/wiki/Renewable_energy, Last Accessed on: May 14 2007.

29. M. I. Hoffert, K. Caldeira, G. Benford, D. R. Criswell, C. Green, H. Herzog, A. K. Jain, H. S. Kheshgi, K. S. Lackner, J. S. Lewis, H. D. Lightfoot, W. Manheimer, J. C. Mankins, M. E. Mauel, L. J. Perkins, M. E. Schlesinger, T. Volk and T. M. L. Wigley, *Science*, **298**, 981-987 (2002).

30. J. Twidell, *Renewable Energy Resources*, Taylor & Francis, New York (2005).

31. A. V. da Rosa, *Fundamentals of Renewable Energy Processes*, Elsevier Academic Press, Burlington (2005).

32. N. S. Lewis and D. G. Nocera, *Proc. Natl. Acad. Sci. U. S. A.*, **103**, 15729-15735 (2006).

33. S. A. Kalogirou, *Prog. Energy Combust. Sci.*, **30**, 231-295 (2004).

34. P. G. Charalambous, G. G. Maidment, S. A. Kalogirou and K. Yiakoumetti, *Appl. Therm. Eng.*, **27**, 275-286 (2007).

35. http://en.wikipedia.org/wiki/Photovoltaics, Last Accessed on: May 14 2007.

36. Z. Ssen, *Prog. Energy Combust. Sci.*, **30**, 367-416 (2004).

37. T. Ackermann and L. Soder, *Renew. Sust. Energ. Rev.*, **4**, 315-374 (2000).

38. http://en.wikipedia.org/wiki/Windpower, Last Accessed on: May 14 2007.

39. A. D. Sahin, *Prog. Energy Combust. Sci.*, **30**, 501-543 (2004).

40. L. Landberg, L. Myllerup, O. Rathmann, E. L. Petersen, B. H. Jorgensen, J. Badger and N. G. Mortensen, *Wind Energy*, **6**, 261-271 (2003).

41. J. O. G. Tande, *Wind Energy*, **6**, 281-295 (2003).

42. S. Singh, T. S. Bhatti and D. P. Kothari, *J. Energy Eng.-ASCE*, **132**, 8-14 (2006).

43. M. A. Bolinger, *Renew. Sust. Energ. Rev.*, **9**, 556-575 (2005).

44. N. Lewis, *Plenary talk presented at the Annual Fall Meeting of the Electrochemical Society, Los Angeles, CA, Nov. 14-18, (See Also http://nsl.caltech.edu/energy.html Last Accessed: May 14 2007)*, (2005).

45. S. A. Sherif, F. Barbir and T. N. Veziroglu, *Sol. Energy*, **78**, 647-660 (2005).

46. J. I. Levene, M. K. Mann, R. M. Margolis and A. Milbrandt, *Sol. Energy*, **81**, 773-780 (2007).

47. G. Hooger, *Fuel Cell Technology Handbook*, CRC Press, Boca Raton (2002).

48. K. Kleiner, *Nature*, **441**, 1046-1047 (2006).

49. F. de Bruijn, *Green Chem.*, **7**, 132-150 (2005).

50. S. Srinivasan, *Fuel Cells: From Fundamentals to Applications*, Springer, New York (2006).

51. J. Larminie and A. Dicks, *Fuel Cell Systems Explained*, John Wiley & Sons, Ltd, Chichester (2000).

52. L. Carrette, K. A. Friedrich and U. Stimming, *ChemPhysChem*, **1**, 162-193 (2000).

53. H. Kohnke, in *Handbook of Fuel Cells: Fundamentals, Technology and Applications*, 1st ed., W. Vielstich, A. Lamm and H. A. Gasteiger, Edditors, p. 281, John Wiley & Sons, Chichester (2003).

54. J. M. King and H. R. Kunz, in *Handbook of Fuel Cells: Fundamentals, Technology and Applications*, 1st ed., W. Vielstich, A. Lamm and H. A. Gasteiger, Edditors, p. 287, John Wiley & Sons, Chichester (2003).

55. E. J. Cairns, in *Handbook of Fuel Cells: Fundamentals, Technology and Applications*, 1st ed., W. Vielstich, A. Lamm and H. A. Gasteiger, Edditors, p. 301, John Wiley & Sons, Chichester (2003).

56. A. Hamnett, in *Handbook of Fuel Cells: Fundamentals, Technology and Applications*, 1st ed., W. Vielstich, A. Lamm and H. A. Gasteiger, Edditors, p. 305, John Wiley & Sons, Chichester (2003).

57. C. Lamy and E. M. Belgsir, in *Handbook of Fuel Cells: Fundamentals, Technology and Applications*, 1st ed., W. Vielstich, A. Lamm and H. A. Gasteiger, Edditors, p. 323, John Wiley & Sons, Chichester (2003).

58. P. Holtappels and U. Stimming, in *Handbook of Fuel Cells: Fundamentals, Technology and Applications*, 1st ed., W. Vielstich, A. Lamm and H. A. Gasteiger, Edditors, p. 335, John Wiley & Sons, Chichester (2003).

59. E. Katz, A. N. Shipway and I. Willner, in *Handbook of Fuel Cells: Fundamentals, Technology and Applications*, 1st ed., W. Vielstich, A. Lamm and H. A. Gasteiger, Edditors, p. 381, John Wiley & Sons, Chichester (2003).

60. K. A. Adamson, A. Baker and D. Jollie, *Fuel Cell Systems: A Survey of worldwide activity*, Fuel Cell Today, (2004).

61. K. A. Adamson, *US Hydrogen and Fuel Cell R&D Targets and 2005 Funding*, Fuel Cell Today, (2005).

62. http://www.hydrogen.energy.gov/, Last Accessed on: May 14 2007.

63. http://www.nrel.gov/hydrogen/, Last Accessed on: May 14 2007.

64. T. Koppel *Powering the Future: The Ballard Fuel Cell and the Race to Change the World*, Wiley, New York (2001).

65. http://www.ballard.com/resources/powergen/MAN5100073.pdf, Last Accessed on: May 14 2007.

66. http://en.wikipedia.org/wiki/PEMFC, Last Accessed on: May 14 2007.

67. http://education.lanl.gov/RESOURCES/H2/gottesfeld/education.html., Last Accessed on: May 10 2004.

68. http://en.wikipedia.org/wiki/Nafion, Last Accessed on: May 14 2007.

69. S. Banerjee and D. E. Curtin, *J. Fluor. Chem.*, **125**, 1211-1216 (2004).

70. S. J. Hamrock and M. A. Yandrasits, *Polym. Rev.*, **46**, 219-244 (2006).

71. D. A. Schiraldi, *Polym. Rev.*, **46**, 315-327 (2006).

72. M. W. Perpall, D. W. Smith, D. D. DesMarteau and S. E. Creager, *Polym. Rev.*, **46**, 297-313 (2006).

73. A. M. Herring, *Polym. Rev.*, **46**, 245-296 (2006).

74. J. L. Zhang, Z. Xie, J. J. Zhang, Y. H. Tanga, C. J. Song, T. Navessin, Z. Q. Shi, D. T. Song, H. J. Wang, D. P. Wilkinson, Z. S. Liu and S. Holdcroft, *J. Power Sources*, **160**, 872-891 (2006).

75. J. Ihonen, F. Jaouen, G. Lindbergh, A. Lundblad and G. Sundholm, *J. Electrochem. Soc.*, **149**, A448-A454 (2002).

76. F. Jaouen, G. Lindbergh and G. Sundholm, *J. Electrochem. Soc.*, **149**, A437-A447 (2002).

77. A. A. Kulikovsky, *Electrochem. Commun.*, **4**, 845-852 (2002).

78. L. Ma, D. B. Ingham, M. Pourkashanian and E. Carcadea, *J. Fuel Cell Sci. Technol.*, **2**, 246-257 (2005).

79. J. B. Young, *Annu. Rev. Fluid Mech.*, **39**, 193-215 (2007).

80. N. B. Huang, B. L. Yi, M. Hou and P. W. Ming, *Prog. Chem.*, **17**, 963-969 (2005).

81. X. G. Li and M. Sabir, *Int. J. Hydrog. Energy*, **30**, 359-371 (2005).

82. H. Tawfik, Y. Hung and D. Mahajan, *J. Power Sources*, **163**, 755-767 (2007).

83. A. Weber, R. Darling, M. J. and J. Newman, in *Handbook of Fuel Cells: Fundamentals, Technology and Applications*, 1st ed., W. Vielstich, A. Lamm and H. A. Gasteiger, Edditors, p. 47, John Wiley & Sons, Chichester (2003).

84. R. von Helmolt and W. Lehnert, in *Handbook of Fuel Cells: Fundamentals, Technology and Applications*, 1st ed., W. Vielstich, A. Lamm and H. A. Gasteiger, Edditors, p. 134, John Wiley & Sons, Chichester (2003).

85. K. Scott, in *Handbook of Fuel Cells: Fundamentals, Technology and Applications*, 1st ed., W. Vielstich, A. Lamm and H. A. Gasteiger, Edditors, p. 70, John Wiley & Sons, Chichester (2003).

86. J. Goodisman, *Electrochemistry: Theoretical Foundations*, Wiley-Interscience Publication, New York (1987).

87. H. A. Gasteiger, S. S. Kocha, B. Sompalli and F. T. Wagner, *Appl. Catal. B-Environ.*, **56**, 9-35 (2005).

88. A. A. Kulikovsky, *Electrochem. Commun.*, **4**, 318-323 (2002).

89. J. Wolf, in *Handbook of Fuel Cells: Fundamentals, Technology and Applications*, 1st ed., W. Vielstich, A. Lamm and H. A. Gasteiger, Edditors, p. 89, John Wiley & Sons, Chichester (2003).

90. G. Sandrock, in *Handbook of Fuel Cells: Fundamentals, Technology and Applications*, 1st ed., W. Vielstich, A. Lamm and H. A. Gasteiger, Edditors, p. 101, John Wiley & Sons, Chichester (2003).

91. R. Funck, in *Handbook of Fuel Cells: Fundamentals, Technology and Applications*, 1st ed., W. Vielstich, A. Lamm and H. A. Gasteiger, Edditors, p. 83, John Wiley & Sons, Chichester (2003).

92. S. Suda, in *Handbook of Fuel Cells: Fundamentals, Technology and Applications*, 1st ed., W. Vielstich, A. Lamm and H. A. Gasteiger, Edditors, p. 9, John Wiley & Sons, Chichester (2003).

93. R. Wurster and J. Schindler, in *Handbook of Fuel Cells: Fundamentals, Technology and Applications*, 1st ed., W. Vielstich, A. Lamm and H. A. Gasteiger, Edditors, p. 62, John Wiley & Sons, Chichester (2003).

94. P. Hoffmann, *Tomorrow's Energy: Hydrogen, Fuel Cells, and the Prospects for a Cleaner Planet*, The MIT Press, Cambridge (2002).

95. E. Bilgen, *Sol. Energy*, **77**, 47-55 (2004).

96. http://en.wikipedia.org/wiki/Sulfur-iodine_cycle, Last Accessed on: July 15 2007.

97. K. Damen, A. Faaij, F. van Bergen, J. Gale and E. Lysen, *Energy*, **30**, 1931-1952 (2005).

98. K. Damen, M. van Troost, A. Faaij and W. Turkenburg, *Prog. Energy Combust. Sci.*, **32**, 215-246 (2006).

99. P. Hennicke and M. Fischedick, **34**, 1260-1270 (2006).

100. M. Hisschemoller, R. Bode and M. van de Kerkhof, **34**, 1227-1235 (2006).

101. W. McDowall and M. Eames, **34**, 1236-1250 (2006).

102. J. M. Ogden, *Annu. Rev. Energ. Environ.*, **24**, 227-279 (1999).

103. S. Ramesohl and F. Merten, *Energy Policy*, **34**, 1251-1259 (2006).

104. M. Wietschel, U. Hasenauer and A. de Groot, *Energy Policy*, **34**, 1284-1298 (2006).

105. J. Zhao and M. W. Melaina, *Energy Policy*, **34**, 1299-1309 (2006).

106. S. A. Sherif, F. Barbir and T. N. Veziroglu, *J. Sci. Ind. Res.*, **62**, 46-63 (2003).

107. E. J. Carlson, P. Kopf, J. Sinha and S. Sriramulu, *Cost Analysis of PEM Fuel Cell Systems for Transportation*, National Renewable Energy Laboratory, Cambridge, Massachusettts (2005).http://www.nrel.gov/hydrogen/pdfs/39104.pdf last accessed: July 15 2007.

108. P. J. Ferreira, G. J. la O, Y. Shao-Horn, D. Morgan, R. Makharia, S. Kocha and H. A. Gasteiger, *J. Electrochem. Soc.*, **152**, A2256-A2271 (2005).

109. K. Yasuda, A. Taniguchi, T. Akita, T. Ioroi and Z. Siroma, *Phys. Chem. Chem. Phys.*, **8**, 746-752 (2006).

110. Z. Siroma, A. Taniguchi, T. Akita, K. Yasuda, K. Ishii, M. Tanaka, M. Inaba and A. Tasaka, *Paper 1181 presented at the Electrochemical Society Meeting, Los Angeles, CA, Oct. 16-21*, ECS, Los Angeles (2005).

111. F. H. Garzon, J. Davey and R. Borup, *Paper 1179 presented at the Electrochemical Society Meeting, Los Angeles, CA, Oct. 16-21*, ECS, Los Angeles (2005).

112. D. A. Stevens and J. R. Dahn, *Carbon*, **43**, 179-188 (2005).

113. A. Bonakdarpour, J. Wenzel, D. A. Stevens, S. Sheng, T. L. Monchesky, R. Lobel, R. T. Atanasoski, A. K. Schmoeckel, G. D. Vernstrom, M. K. Debe and J. R. Dahn, *J. Electrochem. Soc.*, **152**, A61-A72 (2005).

114. A. Bonakdarpour, R. Lobel, R. T. Atanasoski, G. D. Vernstrom, A. K. Schmoeckel, M. K. Debe and J. R. Dahn, *J. Electrochem. Soc.*, **153**, A1835-A1846 (2006).

115. D. Thompsett, in *Handbook of Fuel Cells: Fundamentals, Technology and Applications*, 1st ed., W. Vielstich, A. Lamm and H. A. Gasteiger, Edditors, p. 467, John Wiley & Sons, Chichester (2003).

116. S. Mukerjee, S. Srinivasan, M. P. Soriaga and J. McBreen, *J. Phys. Chem.*, **99**, 4577-4589 (1995).

117. V. Stamenkovic, T. J. Schmidt, P. N. Ross and N. M. Markovic, *J. Phys. Chem. B*, **106**, 11970-11979 (2002).

118. J. Zhang, F. H. B. Lima, M. H. Shao, K. Sasaki, J. X. Wang, J. Hanson and R. R. Adzic, *J. Phys. Chem. B*, **109**, 22701-22704 (2005).

119. S. G. Neophytides, K. Murase, S. Zafeiratos, G. Papakonstantinou, F. E. Paloukis, N. V. Krstajic and M. M. Jaksic, *J. Phys. Chem. B*, **110**, 3030-3042 (2006).

120. P. J. Kulesza, K. Karnicka, K. Miecznikowski, M. Chojak, A. Kolary, P. J. Barczuk, G. Tsirlina and W. Czerwinski, *Electrochim. Acta*, **50**, 5155-5162 (2005).

121. M. S. El-Deab and T. Ohsaka, *Angew. Chem.-Int. Edit.*, **45**, 5963-5966 (2006).

122. P. Strasser, N. T. Hahn and S. Koh, in Proton Exchange Membrane Fuel Cells 6, T. Fuller et. al. Editors, PV 3-1, p. 139, The Electrochemical Society Transactions, Pennington, NJ (2006).

123. E. L. Brosha, M. Wilson, F. Garzon, C. Johnston and F. A. Uribe, in Proton Exchange Membrane Fuel Cells 6, Fuller et. al., T. Editors, PV 3-1, p. 319, The Electrochemical Society Transactions, Pennington, NJ (2006).

124. M. K. Debe, in *Handbook of Fuel Cells: Fundamentals, Technology and Applications*, 1st ed., W. Vielstich, A. Lamm and H. A. Gasteiger, Edditors, p. 576, John Wiley & Sons, Chichester, England (2003).

125. P. Zelenay, J. Choi, C. Johnston, D. Cao, P. Babu, A. Wieckowski and N. Alonso-Vante, in Proton Exchange Membrane Fuel Cells 6, Fuller et. al., T. Editors, PV 3-1, p. 171, The Electrochemical Society Transactions, Pennington, NJ (2006).

126. F. Jaouen, F. Charreteur and J. P. Dodelet, *J. Electrochem. Soc.*, **153**, A689-A698 (2006).

127. B. Wang, *J. Power Sources*, **152**, 1-15 (2005).

128. E. B. Easton, T. Buhrmester and J. R. Dahn, *Thin Solid Films*, **493**, 60-66 (2005).

129. N. Alonso-Vanter, in *Handbook of Fuel Cells: Fundamentals, Technology and Applications*, 1st ed., W. Vielstich, A. Lamm and H. A. Gasteiger, Edditors, p. 534, John Wiley & Sons, Chichester (2003).

130. J. B. Goodenough and B. L. Cushing, in *Handbook of Fuel Cells: Fundamentals, Technology and Applications*, 1st ed., W. Vielstich, A. Lamm and H. A. Gasteiger, Edditors, p. 520, John Wiley & Sons, Chichester (2003).

131. M. Lefevre and J. P. Dodelet, *Electrochim. Acta*, **48**, 2749-2760 (2003).

132. F. Jaouen, S. Marcotte, J. P. Dodelet and G. Lindbergh, *J. Phys. Chem. B*, **107**, 1376-1386 (2003).

133. P. Stonehart, *Ber. Bunsen-Ges. Phys. Chem. Chem. Phys.*, **94**, 913-921 (1990).

134. P. Stonehart, *J. Appl. Electrochem.*, **22**, 995-1001 (1992).

135. M. Watanabe, K. Tsurumi, T. Mizukami, T. Nakamura and P. Stonehart, *J. Electrochem. Soc.*, **141**, 2659-2668 (1994).

136. M. Bowker, *The Basis and Applications of heterogeneous Catalysis*, Oxford University Press, Oxford (1998).

137. K. W. Kolasinski, *Surface Science Foundations of Catalysis and Nanoscience*, John Wiley & Sons, Ltd., Chichester, New York (2002).

138. G. A. Somorjai, in *Treatise on Solid State Chemistry*, ed., Edditors, p. 1, Plenum Press, New York (1976).

139. A. Zangwill, *Physics At Surfaces*, Cambridge University Press, New York (1988).

140. I. Chorkendorff and J. W. Niemantsverdriet, *Concepts of Modern Catalysis and Kinetics*, John Wiley & Sons, Chichester, New York (2003).

141. K. J. Laidler, *Chemical Kinetics*, Harper Collins Publishers, London (1987).

142. G. A. Attard and C. Barnes, *Surfaces*, Oxford University Press, Oxford (1998).

143. B. Hammer and J. K. Norskov, in *Impact of Surface Science on Catalysis*, ed., Edditors, p. 71, Academic Press, San Diego (2000).

144. B. Hammer and J. K. Norskov, *Nature*, **376**, 238-240 (1995).

145. J. K. Norskov, T. Bligaard, A. Logadottir, J. R. Kitchin, J. G. Chen and S. Pandelov, *J. Electrochem. Soc.*, **152**, J23-J26 (2005).

146. F. Raimondi, G. G. Scherer, R. Kotz and A. Wokaun, *Angew. Chem.-Int. Edit.*, **44**, 2190-2209 (2005).

147. R. Meyer, C. Lemire, S. K. Shaikhutdinov and H. Freund, *Gold Bull.*, **37**, 72-+ (2004).

148. F. Besenbacher, I. Chorkendorff, B. S. Clausen, B. Hammer, A. M. Molenbroek, J. K. Norskov and I. Stensgaard, *Science*, **279**, 1913-1915 (1998).

149. S. U. M. Khan and J. O. M. Bockris, *Quantum Electrochemistry*, Plenum Press, New York (1979).

150. S. U. M. Khan and J. O. M. Bockris, *Surface Electrochemistry A Molecular Level Approach*, Plenum Press, New York (1993).

151. A. J. Appleby, in *Kinetics and Mechanisms of Electrode Processes*, 1st ed., B. E. Conway, J. O. M. Bockris, E. Yeager, S. U. M. Khan and R. E. White, Edditors, p. 173, Plenum Press, New York (1983).

152. R. R. Dogonadze and A. M. Kuznetsov, in *Kinetics and Mechanisms of Electrode Processes*, 1st ed., B. E. Conway, J. O. M. Bockris, E. Yeager, S. U. M. Khan and R. E. White, Edditors, p. 1, Plenum Press, New York (1983).

153. M. Enyo, in *Kinetics and Mechanisms of Electrode Processes*, 1st ed., B. E. Conway, J. O. M. Bockris, E. Yeager, S. U. M. Khan and R. E. White, Edditors, p. 241, Plenum Press, New York (1983).

154. L. I. Krishtalik, in *Kinetics and Mechanisms of Electrode Processes*, 1st ed., B. E. Conway, J. O. M. Bockris, E. Yeager, S. U. M. Khan and R. E. White, Edditors, p. 87, Plenum Press, New York (1983).

155. M. R. Tarasevich, A. Sadkowski and E. Yeager, in *Kinetics and Mechanisms of Electrode Processes*, 1st ed., B. E. Conway, J. O. M. Bockris, E. Yeager, S. U. M. Khan and R. E. White, Edditors, p. 301, Plenum Press, New York (1983).

156. S. Trasatti, in *Handbook of Fuel Cells: Fundamentals, Technology and Applications*, 1st ed., W. Vielstich, A. Lamm and H. A. Gasteiger, Edditors, p. 79, John Wiley & Sons, Chichester (2003).

157. A. J. Bard and L. R. Faulkner, *Electrochemical Methods : Fundamentals and Applications*, Wiley, New York (2000).

158. D. Pletcher, R. Greef, R. Peat, L. M. Peter and J. Robinson, *Instrumental Methods in Electrochemistry*, Horwood Publishing, Chichester (2001).

159. K. Kinoshita, *Oxygen Electrochemical Technology*, Wiley-Interscience, (1992).

160. J. P. Hoare, *The Electrochemistry of Oxygen*, Interscience, New York (1968).

161. M. Gattrell and B. MacDougall, in *Handbook of Fuel Cells: Fundamentals, Technology and Applications*, 1st ed., W. Vielstich, A. Lamm and H. A. Gasteiger, Edditors, p. 444, John Wiley & Sons, Chichester (2003).

162. S. Mukerjee and S. Srinivasan, in *Handbook of Fuel Cells: Fundamentals, Technology and Applications*, 1st ed., W. Vielstich, A. Lamm and H. A. Gasteiger, Edditors, p. 502, John Wiley & Sons, Chichester (2003).

163. U. A. Paulus, T. J. Schmidt and H. A. Gasteiger, in *Handbook of Fuel Cells: Fundamentals, Technology and Applications*, 1st ed., W. Vielstich, A. Lamm and H. A. Gasteiger, Edditors, p. 555, John Wiley & Sons, Chichester (2003).

164. P. N. Ross, in *Handbook of Fuel Cells: Fundamentals, Technology and Applications*, 1st ed., W. Vielstich, A. Lamm and H. A. Gasteiger, Edditors, p. 465, John Wiley & Sons, Chichester (2003).

165. R. Adzic, in *Electrocatalysis*, 1st ed., J. Lipkowski and P. N. Ross, Edditors, p. 197, Wiley-VCH, New York (1998).

166. N. M. Markovic and P. N. Ross, *Surf. Sci. Rep.*, **45**, 121-229 (2002).

167. V. Stamenkovic, T. J. Schmidt, P. N. Ross and N. M. Markovic, *J. Electroanal. Chem.*, **554**, 191-199 (2003).

168. V. R. Stamenkovic, B. S. Mun, M. Arenz, K. J. J. Mayrhofer, C. A. Lucas, G. F. Wang, P. N. Ross and N. M. Markovic, *Nat. Mater.*, **6**, 241-247 (2007).

169. N. M. Markovic, T. J. Schmidt, V. Stamenkovic and P. N. Ross, **1**, 105-116 (2001).

170. N. M. Markovic, H. A. Gasteiger, B. N. Grgur and P. N. Ross, *J. Electroanal. Chem.*, **467**, 157-163 (1999).

171. V. Stamenkovic and N. M. Markovic, *Langmuir*, **17**, 2388-2394 (2001).

172. V. Stamenkovic, N. M. Markovic and P. N. Ross, *J. Electroanal. Chem.*, **500**, 44-51 (2001).

173. S. Mukerjee, S. Srinivasan, M. P. Soriaga and J. McBreen, *J. Electrochem. Soc.*, **142**, 1409-1422 (1995).

174. J. L. Zhang, M. B. Vukmirovic, K. Sasaki, A. U. Nilekar, M. Mavrikakis and R. R. Adzic, *J. Am. Chem. Soc.*, **127**, 12480-12481 (2005).

175. J. L. Zhang, M. B. Vukmirovic, Y. Xu, M. Mavrikakis and R. R. Adzic, *Angew. Chem.-Int. Edit.*, **44**, 2132-2135 (2005).

176. V. R. Stamenkovic, B. Fowler, B. S. Mun, G. Wang, P. N. Ross, C. A. Lucas and N. M. Markovic, *Science*, **315**, 493-497 (2007).

177. V. Stamenkovic, B. S. Mun, K. J. J. Mayrhofer, P. N. Ross, N. M. Markovic, J. Rossmeisl, J. Greeley and J. K. Norskov, *Angew. Chem.-Int. Edit.*, **45**, 2897-2901 (2006).

178. J. J. Hanak, in *Combinatorial Materials Synthesis*, 1st ed., X. D. Xiang and I. Takeuchi, Edditors, p. Marcel Dekker, New York (2003).

179. H. Chang and I. Takeuchi, in *Combinatorial Materials Synthesis*, 1st ed., X. D. Xiang and I. Takeuchi, Edditors, p. Marcel Dekker, New York (2003).

180. T. X. Sun, in *Combinatorial Materials Synthesis*, 1st ed., X. D. Xiang and I. Takeuchi, Edditors, p. Marcel Dekker, New York (2003).

181. R. V. Belosludov, S. Takami, M. Kubo and A. Miyamoto, in *Combinatorial Materials Synthesis*, 1st ed., X. D. Xiang and I. Takeuchi, Edditors, p. Marcel Dekker, New York (2003).

182. S. I. Woo, K. W. Kim, H. Y. Cho, K. S. Oh, M. K. Jeon, N. H. Tarte, T. S. Kim and A. Mahmood, *QSAR Comb. Sci.*, **24**, 138-154 (2005).

183. R. B. van Dover and L. F. Schneemeyer, in *Combinatorial Materials Synthesis*, 1st ed., X. D. Xiang and I. Takeuchi, Edditors, p. Marcel Dekker, New York (2003).

184. R. J. Sanderson and K. C. Hewitt, *Physica C*, **425**, 52-61 (2005).

185. A. Hagemeyer, B. Jandeleit, Y. M. Liu, D. M. Poojary, H. W. Turner, A. F. Volpe and W. H. Weinberg, *Appl. Catal. A-Gen.*, **221**, 23-43 (2001).

186. J. R. Engstrom and W. H. Weinberg, *Chim. Oggi-Chem. Today*, **17**, 58-59 (1999).

187. X. D. Xiang and I. Takeuchi, *Combinatorial Materials Synthesis*, Marcel Dekker, In., New York (2003).

188. R. A. Potyrailo and E. J. Amis, *High-Throughput Analysis : A Tool for Combinatorial Materials Science*, Kluwer Academic, New York (2003).

189. R. A. Potyrailo and W. F. Maier, *Combinatorial and High-Throughput Discovery and Optimization of Catalysts and Materials (Critical Reviews in Combinatorial Chemistry)*, CRC Press, Boca Raton (2006).

190. A. Hagemeyer, P. Strasser and A. F. Volpe, *High-Throughput Screening in Chemical Catalysis : Technologies, Strategies and Applications*, John Wiley & Sons, Weinheim (2003).

191. P. Strasser, Q. Fan, M. Devenney, W. H. Weinberg, P. Liu and J. K. Norskov, *J. Phys. Chem. B*, **107**, 11013-11021 (2003).

192. E. Reddington, A. Sapienza, B. Gurau, R. Viswanathan, S. Sarangapani, E. S. Smotkin and T. E. Mallouk, *Science*, **280**, 1735-1737 (1998).

193. R. Z. Jiang, C. Rong and D. Chu, *J. Comb. Chem.*, **7**, 272-278 (2005).

194. S. Jayaraman and A. C. Hillier, *Meas. Sci. Technol.*, **16**, 5-13 (2005).

195. E. S. Smotkin and R. R. Diaz-Morales, *Ann. Rev. Mater. Res.*, **33**, 557-579 (2003).

196. E. S. Smotkin, J. H. Jiang, A. Nayar and R. X. Liu, *Appl. Surf. Sci.*, **252**, 2573-2579 (2006).

197. J. R. Dahn, S. Trussler, T. D. Hatchard, A. Bonakdarpour, J. R. Mueller-Neuhaus, K. C. Hewitt and M. Fleischauer, *Chem. Mat.*, **14**, 3519-3523 (2002).

198. V. Chevrier and J. R. Dahn, *Meas. Sci. Technol.*, **17**, 1339-1404 (2006).

199. M. D. Fleischauer, T. D. Hatchard, A. Bonakdarpour and J. R. Dahn, *Meas. Sci. Technol.*, **16**, 212-220 (2005).

200. T. Harchard, *Combinatorial Studies of Si-Based Alloy Negatives For Li-Ion Batteries*, PhD Thesis, Dalhousie University, Halifax (2004).

201. M. Fleischauer, *The Effect of Transition Metals on Amorphous Alloy Negative Electrode Materials for Lithium-Ion Batteries*, PhD Thesis, Dalhousie University, Halifax (2005).

202. V. Chevrier, *Production, Characterization and Visualization of Quaternary Combinatorial Thin Films*, MSc Thesis, Dalhousie University, Halifax (2006).

203. D. A. Stevens, J. M. Rouleau, R. E. Mar, R. T. Atanasoski, A. K. Schmoeckel, M. K. Debe and J. R. Dahn, *accepted for publication in Journal of the Electrochemical Society*,

204. D. A. Stevens, J. M. Rouleau, R. E. Mar, A. Bonakdarpour, R. T. Atanasoski, A. K. Schmoeckel, M. K. Debe and J. R. Dahn, *accepted for publication in Journal of the Electrochemical Society*,

205. D. M. Mattox, *Handbook of Physical Vapor Deposition (PVD) Processing*, Noyes Publications, Park Ridge (1998).

206. D. L. Smith, *Thin-Film Deposition: Principles and Practice*, McGraw-Hill Professional, Columbus (1998).

207. J. L. Vossen and W. Kern, *Thin Film Processes*, Academic Press, New York (1991).

208. J. E. Mahan, *Physical Vapor Deposition of Thin Films*, Wiley-Interscience, New York (2000).

209. K. Wasa and S. Hayakawa, *Handbook of Sputter Deposition Technology: Principles, Technology and Applications*, Noyes Publications, Park Ridge (1992).

210. K. Wasa, M. Kitabatake and H. Adachi, *Thin Films Material Technology: Sputtering of Compound Materials*, Springer, Heidelberg (2004).

211. A. Bonakdarpour, *Combinatorial Synthesis and Characterization of $Mo_{1-x}Sn_x$ Anode Materials for Li-ion Batteries*, MSc Thesis, Dalhousie University, Halifax (2002).

212. W. L. Bragg, *Proceedings of the Cambridge Philosophical Society*, **17**, 43-57 (1912).

213. R. Jenkins and R. L. Snyder, *Introduction to X-Ray Powder Diffractometry*, Wiley Interscience, New York (1996).

214. B. E. Warren, *X-Ray Diffraction*, Dover Publications, Mineola (1990).

215. H. Fuess, T. Hahn, H. Wondratschek, U. Muller, U. Shmueli, E. Prince, A. Authier, V. Kopský, D. B. Litvin, M. G. Rossmann, E. Arnold, S. Hall and B. McMahon, *International Tables for Crystallography*, Springer, Heidelberg (2006).

216. J. Goldstein, D. E. Newbury, D. C. Joy, C. E. Lyman, P. Echlin, E. Lifshin, L. C. Sawyer and J. R. Michael, *Scanning Electron Microscopy and X-ray Microanalysis*, Springer, Heidelberg (2003).

217. S. Hufner, *Photoelectron Spectroscopy: Principles and Applications*, Springer, Heidelberg (2003).

218. D. Briggs, *Handbook of X-ray and Ultraviolet Spectroscopy*, Heyden (1977).

219. D. Briggs and M. P. Seah, *Practical Surface Analysis*, Wiley Interscience, New York (1990).

220. http://srdata.nist.gov/xps/, Last Accessed on: May 17 2007.

221. P. M. S. Monk, *Fundamentals of Electro-Analytical Chemistry*, John Wiley & Sons, Chichester (2001).

222. M. A. Brett and A. M. O. Brett, *Electrochemistry Principles, Methods, and Applications*, Oxford University Press, Oxford (1993).

223. T. J. Schmidt and H. A. Gasteiger, in *Handbook of Fuel Cells: Fundamentals, Technology and Applications*, 1st ed., W. Vielstich, A. Lamm and H. A. Gasteiger, Edditors, p. 316, John Wiley & Sons, Chichester (2003).

224. http://www.pineinst.com/echem/viewproduct.asp?ID=45651, Last Accessed on: May 14 2007.

225. K. Kinoshita, *Carbon: Electrochemical and Physicochemical Properties*, Wiley-Interscience, New York (1988).

226. M. K. Debe, A. K. Schmoeckel, R. T. Atanasoski and G. D. Vernstrom,Paper 583 presented at the Fuel Cell Seminar, Honolulu, HI, Nov. 13-17, 2006.

227. N. G. Thompson, *DC Electrochemical Test Methods*, NACE International, Houston, Texas (1998).

228. M. Pourbaix, *Atlas of Electrochemical Equilibria in Aqueous Solutions*, NACE International, Houston, Texas (1974).

229. http://www.wellesley.edu/Chemistry/chem120/pour.html, Last Accessed on: May 14 2007.

230. http://en.wikipedia.org/wiki/Pourbaix_diagram, Last Accessed on: May 14 2007.

231. F. Lihl, H. Ebel and W. Baumgartner, *Zeitschrift fur Metallkunde*, **62**, (1971).

232. J. Crangle and J. A. Shaw, *Philos. Mag.*, **7**, (1962).

233. A. Menshiukov, T. Tarnoczi and E. Kren, *Phys. Status Solidi A*, **28A**, (1975).

234. K. H. Buschow, P. G. van Engen and R. Jongebreuer, *J. Magn. Magn. Mater.*, **38**, 1-22 (1983).

235. T. Toda, H. Igarashi, H. Uchida and M. Watanabe, *J. Electrochem. Soc.*, **146**, 3750-3756 (1999).

236. A. P. Miodownik, *J. Magn. Magn. Mater.*, **10**, 126-135 (1979).

237. L. Zwell, G. R. Speich and W. C. Leslie, *Metall. Trans.*, **4**, (1973).

238. U. Esch and A. Schneider, *Z. Elektrochem. Angew. Phys. Chem.*, **50**, 268-274 (1944).

239. C. Leroux, M. C. Cadeville, V. Pierron-Bohnes, G. Inden and F. Hinz, *J. Phys. F: Met. Phys.*, **18F**, 2033-2051 (1988).

240. J. C. Woolley, J. H. Phillips and J. A. Clark, *J. Less-Common Met.*, **6**, 461-471 (1964).

241. E. Gebhardt and W. Koster, *Z. Metallkd.*, **32**, 253-261 (1940).

242. A. H. Geisler and D. L. Martin, *J. Appl. Phys.*, **23**, 375 (1952).

243. B. van Laar, *J. Phys-Paris*, **25**, 600-603 (1964).

244. D. E. G. Williams and A. Jezierski, *J. Magn. Magn. Mater.*, **59**, 41-56 (1986).

245. E. Raub and W. Mahler, *Z. Metallkd.*, **46**, 282-290 (1955).

246. E. Kren, G. Kadar, L. Pal, J. Solyom, P. Szabo and T. Tarnoczi, *Phys. Rev.*, **171**, 574-585 (1968).

247. A. Bonakdarpour, J. Wenzel, D. A. Stevens, S. Sheng, T. L. Monchesky, R. Lobel, R. T. Atanasoski, A. K. Schmoeckel, G. D. Vernstrom, M. K. Debe and J. R. Dahn, *J. Electrochem. Soc.*, **152**, 1-12 (2005).

248. D. A. Jones, *Principles and Prevention of Corrosion*, Prentice Hall, Upper Saddle River, NJ (1996).

249. K. J. J. Mayrhofer, B. B. Blizanac, M. Arenz, V. R. Stamenkovic, P. N. Ross and N. M. Markovic, *J. Phys. Chem. B*, **109**, 14433-14440 (2005).

250. M. K. Debe, A. K. Schmoeckel, R. T. Atanasoski and G. D. Vernstrom, *Paper 64 presented at the Fuel Cell Seminar, Palm Springs, CA, Nov. 14-18*, (2005).

251. M. K. Debe, A. K. Schmoeckel, G. D. Vernstrom and R. T. Atanasoski, *J. Power Sources.*, **161**, 1002-1011 (2006).

252. Y. Shao-Horn, P. J. Ferreira and G. J. la O', *Paper 1182 presented at the Electrochemical Society Meeting, Los Angeles, CA, Oct. 16-21*, EDS, Los Angeles (2005).

253. K. Ota, Y. Koizumi, S. Mitsushima and N. Kamiya, in Proton Exchange Membrane Fuel Cells 6, Fuller et. al., T. Editors, PV 3-1, p. 619, The Electrochemical Society Transactions, Pennington, NJ (2006).

254. B. Merzougui and S. Swathirajan, *J. Electrochem. Soc.*, **153**, A2220-A2226 (2006).

255. M. K. Debe, S. K. Hendricks, A. K. Schmoeckel, R. T. Atanasoski, G. D. Vernstrom and G. M. Haugen,Paper 1170 presented at the Electrochemical Society Meeting, Los Angeles, CA, Oct. 16-21

256. A. Bonakdarpour, R. Lobel, S. Sheng, T. L. Monchesky and J. R. Dahn, *J. Electrochem. Soc.*, **153**, A2304-A2313 (2006).

257. A. A. El-Moneim, E. Akiyama, H. Habazaki, A. Kawashima, K. Asami and K. Hashimoto, *Corrosion Sci.*, **40**, 1491-1512 (1998).

258. K. Hashimoto, H. Habazaki, E. Akiyama, H. Yoshioka, J. H. Kim, P. Y. Park, A. Kawashima and K. Asami, *Sci. Rep. Res. Inst. Tohoku Univ. Ser. A-Phys. Chem. Metall.*, **42**, 99-105 (1996).

259. W. G. Moffatt, *The Handbook of Binary Phase Diagrams*, Genium Publishing Corporation, Schenectady, N.Y. (1976).

260. P. Villars and L. D. Calvert, *Pearson's Handbook of Crystallographic Data for Intermetallic Phases*, Asm International, Materials Park, OH (1991).

261. B. C. Giessen and N. J. Grant, *Acta Cryst.*, **17**, 615-616 (1964).

262. V. Sadagopan and H. C. Gatos, *Physica Status Solidi*, **13**, 423-7 (1966).

263. T. D. Hatchard, J. R. Dahn, S. Trussler, M. Fleischauer, A. Bonakdarpour, J. R. Mueller-Neuhaus and K. C. Hewitt, *Thin Solid Films*, **443**, 144-150 (2003).

264. O. Kerrec, D. Devilliers, H. Groult and P. Marcus, *Mater. Sci. Eng. B-Solid State Mater. Adv. Technol.*, **55**, 134-142 (1998).

265. K. Hashimoto, P. Y. Park, J. H. Kim, H. Yoshioka, H. Mitsui, E. Akiyama, H. Habazaki, A. Kawashima, K. Asami, Z. Grzesik and S. Mrowec, *Mater. Sci. Eng. A-Struct. Mater. Prop. Microstruct. Process.*, **198**, 1-10 (1995).

266. A. Kawashima, H. Habazaki and K. Hashimoto, *Mater. Sci. Eng. A-Struct. Mater. Prop. Microstruct. Process.*, **304**, 753-757 (2001).

267. H. Habazaki, T. Sato, A. Kawashima, K. Asami and K. Hashimoto, *Mater. Sci. Eng. A-Struct. Mater. Prop. Microstruct. Process.*, **304**, 696-700 (2001).

268. M. W. Ruckman and M. Strongin, *Phys. Rev. B*, **35**, 487-492 (1987).

269. N. M. Markovic, R. R. Adzic, B. D. Cahan and E. B. Yeager, *J. Electroanal. Chem.*, **377**, 249-259 (1994).

270. J. X. Wang, N. M. Markovic and R. R. Adzic, *J. Phys. Chem. B*, **108**, 4127-4133 (2004).

271. T. He, E. Kreidler, L. Xiong, J. Luo and C. J. Zhong, *J. Electrochem. Soc.*, **153**, A1637-A1643 (2006).

272. H. A. E. Hagelin-Weaver, G. B. Hoflund, D. A. Minahan and G. N. Salaita, *Appl. Surf. Sci.*, **235**, 420-448 (2004).

273. S. Ball, B. Theobald, D. Thompsett and S. Hudson, *Paper 1178 presented at the Electrochemical Society Meeting, Los Angeles, CA, Oct. 16-21*, ECS, Los Angeles (2005).

274. U. A. Paulus, A. Wokaun, G. G. Scherer, T. J. Schmidt, V. Stamenkovic, V. Radmilovic, N. M. Markovic and P. N. Ross, *J. Phys. Chem. B*, **106**, 4181-4191 (2002).

275. M. K. Debe and e. al., *2005 U.S. DOE Annual Merit Review Meeting, Arlington, VA*, (2005).

276. S. Trasatti and E. Lust, in *Modern Aspects of Electrochemistry*, 1st ed., R. E. White, J. O. M. Bockris and B. E. Conway, Edditors, p. Kluwer Academic / Plenum Publishers, New York (1999).

277. S. Trasatti, in *Handbook of Fuel Cells: Fundamentals, Technology and Applications*, 1st ed., W. Vielstich, A. Lamm and H. A. Gasteiger, Edditors, p. 71, John Wiley & Sons, Chichester (2003).

278. S. Dahl, A. Logadottir, R. C. Egeberg, J. H. Larsen, I. Chorkendorff, E. Tornqvist and J. K. Norskov, *Phys. Rev. Lett.*, **83**, 1814-1817 (1999).

279. M. Inaba, H. Yamada, J. Tokunaga and A. Tasaka, *Electrochem. Solid State Lett.*, **7**, A474-A476 (2004).

280. J. P. Dodelet, in *N_4-Macrocyclic Metal Complexes*, 1st ed., J. H. Zagal, F. Bedioui and J. P. Dodelet, Edditors, p. 83, Springer, New York (2006).

281. F. Jaouen, M. Lefevre, J. P. Dodelet and M. Cai, *J. Phys. Chem. B*, **110**, 5553-5558 (2006).

282. M. Lefevre, J. P. Dodelet and P. Bertrand, *J. Phys. Chem. B*, **104**, 11238-11247 (2000).

283. P. H. Matter, L. Zhang and U. S. Ozkan, *J. Catal.*, **239**, 83-96 (2006).

284. P. H. Matter and U. S. Ozkan, *Catal. Lett.*, **109**, 115-123 (2006).

285. E. B. Easton, A. Bonakdarpour and J. R. Dahn, *Electrochem. Solid State Lett.*, **9**, A463-A467 (2006).

286. R. Z. Yang, A. Bonakdarpour, E. B. Easton, P. Stoffyn-Egli and J. R. Dahn, *J. Electrochem. Soc.*, **154**, A275-A282 (2007).

287. E. B. Easton, R. Z. Yang, A. Bonakdarpour and J. R. Dahn, *Electrochem. Solid State Lett.*, **10**, B6-B10 (2007).

288. M. Lefevre, J. P. Dodelet and P. Bertrand, *J. Phys. Chem. B*, **106**, 8705-8713 (2002).

289. M. Lefevre, J. P. Dodelet and P. Bertrand, *J. Phys. Chem. B*, **109**, 16718-16724 (2005).

290. C. Medard, M. Lefevre, J. P. Dodelet, F. Jaouen and G. Lindbergh, *Electrochim. Acta*, **51**, 3202-3213 (2006).

291. E. Antolini, J. R. C. Salgado and E. R. Gonzalez, *J. Power Sources*, **160**, 957-968 (2006).

292. N. Watanabe and M. A. V. Devanathan, **111**, 615-619 (1964).

293. R. R. Adzic, J. Zhang, M. Shao, K. Sasaki, M. B. Vukmirovic and F. A. Uribe,The Electrochemical Society Transactions

294. V. S. Murthi, R. C. Urian and S. Mukerjee, *J. Phys. Chem. B*, **108**, 11011-11023 (2004).

295. T. S. Ahmadi, Z. L. Wang, T. C. Green, A. Henglein and M. A. ElSayed, *Science*, **272**, 1924-1926 (1996).

Appendix A

XPS Transmission Function

The transmission function of the VG Microtech Multilab XPS instrument is given below. The transmission function appears as T(E) in the sensitivity factor calculations (equation 3.6). The recommended procedure for obtaining T(E) is to measure the intensity of a standard (Ag $3p_{3/2}$) at various pass energies. A polynomial fit is made to y = Log_{10} [peakArea/PassEnergy] versus x = Log_{10} [Kinetic Energy/Pass Energy]. The transmission function at a given kinetic energy of KE and pass energy of PE is then given by

$$T(KE,PE) = 10^{y\left(\log_{10}\left(\frac{KE}{PE}\right)\right)} \times PE, \qquad \text{A.1}$$

where y is the polynomial given in Figure A.1.

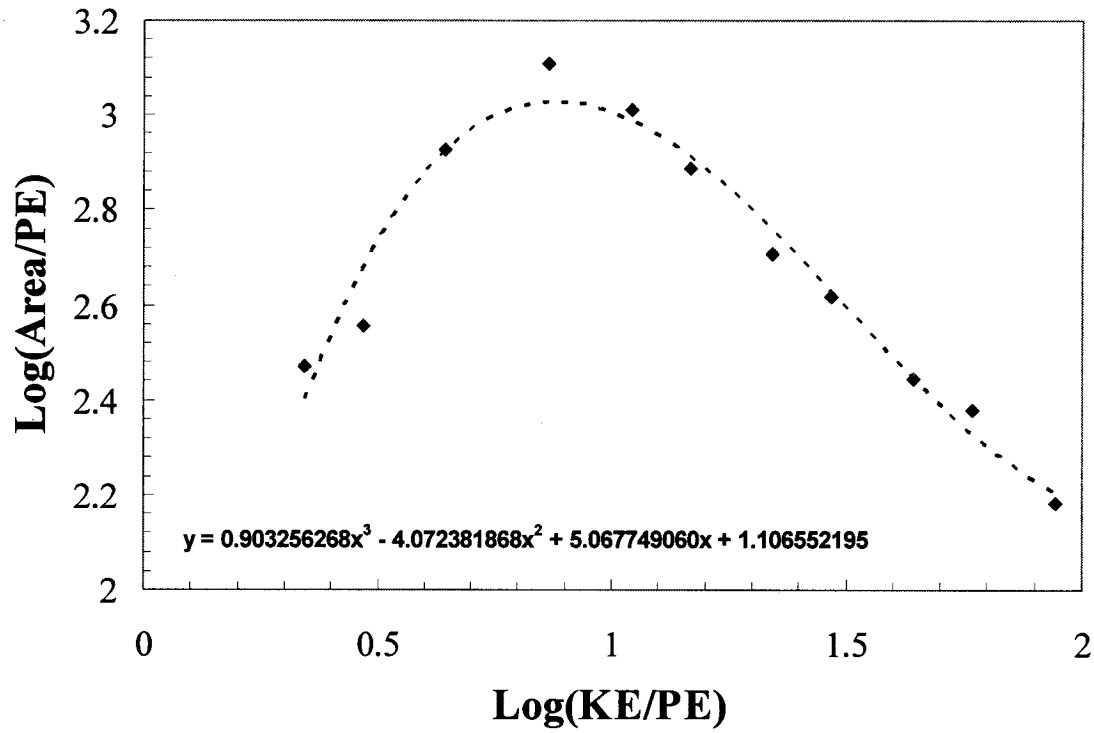

Figure A.1 *Transmission function of the VG Microtech Multilab XPS.*

Appendix B

RRDE Preparations

Measurements in surface electrochemistry, like electrocatalytic properties, are tedious and require a lot of care and attention. The reason for this is that surfaces are very prone to contamination and minute amounts of impurities (ppm) present at very low levels could have a pronounced impact on the results of experiments and on their subsequent interpretation. In particular, the electrocatalytic properties of Pt and Pt-based materials in reactions like the oxygen reduction reaction can easily be influenced by the presence of impurities (anions like Cl^- or hydrocarbons) in the cell setup. Fundamental measurements of Pt crystals are conducted with a very high degree of scrutiny and with meticulous experimental preparation. The reader is referred to literature sources for more information [166]. The procedures that were developed during the course of this thesis are outlined below:

1) Only dedicated glassware; normally brand new glassware, was used
2) Clean the glassware in a saturated KOH bath (water/ethanol in 4:1 ratio) overnight
3) Rinse glassware with a few times with hot tab water
4) Rinse with nano-pure water a few times
5) Boil in nano-pure water, for at least 0.5 hours and then dry in air
6) Wrap the glassware in paper towel and keep them in a clean plastic box for later use
7) Glassware was always handled with gloves, even the outside
8) 4L beakers, which are cleaned beforehand, were used for boiling the glassware used for the experiments
9) Prior to any measurement, the cell and cells parts (Teflon stoppers, counter electrode and fitted tubes) were also boiled. (see Appendix C).

10) All the cell parts and RRDE electrodes were handled with care and with gloves. The RRDE electrode parts were also cleaned with nano-pure water and always kept in Ziploc bags when not in use.

Appendix C

RRDE Measurement Procedures

The procedures below were used in measurements of Pt, Pt-Ta and PtCo films and for the Pt/NSTF samples. They form a good guideline for RRDE experiments. The cell setup, disassembly and reference electrode calibration is common for all different measurements. For Pt/NSTF samples we used 1-compartment and 2-compartment cells, no significant difference was observed.

Procedure for Pine Platinum Electrode Standard

A) **Set-up of the Cell (Gloves worn at all times):**

1. Boil the cell (already stored in the nano-pure water beaker) once in 4 L beaker of nano-pure water (NPW) for approximately 1 hour. Make sure the water level is high enough to cover the entire cell.
2. Boil cell parts (glass frit, counter electrode and Teflon pieces) once in NPW.
3. Rinse the cell once with 0.1M $HClO_4$. Once rinsed, fill the cell with 125 mL 0.1M $HClO_4$.
4. Connect the gas glass frit to the gas line and purge all NPW out of the frit.
5. Assemble cell parts and cell in proper orientation. Starting with the left most neck and moving counter-clockwise: Teflon stopper, gas glass frit, counter electrode, and reference electrode (with Teflon piece inserted previously).
6. Connect the counter and reference electrode to the proper wires, red and black respectively.
7. Rinse the electrode with a minimal amount of EtOH followed by lots of NPW.
8. Polish the electrode using 5 μm followed by 0.05 μm polishes. Once polished, rinse it with warm NPW.
9. Install the electrode in the rotator and then lower it into the cell.
10. Make sure only the disk wire (yellow) is connected.
11. Make sure there are no bubbles on the electrode.
12. Make sure the electrode is not touching the neck of the glass cell and can rotate freely.

Counter Electrode: Platinum
Reference Electrode: MMS (Mercury/Mercury Sulfate) 0.1M $HClO_4$
Working Electrode: Pine Platinum RDE
Cell Type: Single Compartment

B) **Electrochemical Cleaning of the Electrode:**

1. Purge Ar gas into the cell for 15 min.
2. While still purging Ar, run the following cleaning CV:
   Sweep Rate: 500 mV/s
   Potential Range: (-700 mV, 500 mV)
   # Of Sweeps: 200
3. Repeat the cleaning CV if necessary.

C) **Study of CV (Cyclic Voltammetry) Features:**

1. While still purging Ar, run the following CVs:
   I. **Sweep Rate:**100 mV/s
      Potential Range: (-635 mV, 350 mV)
      # Of Sweeps: 4
   II. **Sweep Rate:** 50 mV/s
      Potential Range: (-635 mV, 350 mV)
      # Of Sweeps: 4
   III. **Sweep Rate:**10 mV/s
      Potential Range: (-635 mV, 350 mV)
      # Of Sweeps: 4

CVs will tell if you have a clean electrode and/or setup or not. The H and OH regions will develop after potential cycling and should reach a steady state. The CVs should not be 'sloped' – otherwise there is a leak in the electrode and the Teflon U-Cups must be changed! The leakage could be a serious issue as it degrades the electrode. Avoid it at all costs.

D) **Study of Oxygen Activity During ORR (Oxygen Reduction Reactions):**

1. Purge oxygen gas for 5 min.
2. While still purging oxygen, run the following ORRs:
   I. **Sweep Rate:** 50 mV/s
      Potential Range: (-635 mV, 350 mV)
      # Of Sweeps: 4
      Rotation Speed: 400 rpm
   II. **Sweep Rate:** 10 mV/s
      Potential Range: (-635 mV, 350 mV)
      # Of Sweeps: 4
      Rotation Speed: 400 rpm
3. Repeat step 2, changing the rotation speed to 1600 rpm.

E) **Calibration of the Reference Electrode vs. RHE (Reversible Hydrogen Electrode):**

1. Purge Ar gas for 10 min.
2. Start purging hydrogen gas then immediately start the following run:
   I. **Sweep Rate:** 100 mV/s
      Potential Range: (-800 mV, 0 mV)
      # Of Sweeps: 2
      Rotation Speed: 1600 rpm

*Only purge hydrogen gas when needed. Otherwise, make sure it is shut off.

F) **Disassembly of the Cell:**

1. Once completing all desired runs remove the electrode from the solution and rotator. Disassemble the electrode, rinse off the RRDE and wrap the pieces in Kimwipe and store them in a Ziploc bag.
2. Place the cell and cell parts back in their original beakers with fresh NPW.

Procedure for 3M Pt-NSTF Samples

Counter Electrode: Platinum
Reference Electrode: MMS (Mercury/Mercury Sulfate) 0.1M $HClO_4$
Working Electrode: 1. Glassy Carbon RDE or
2. Platinum Ring Glassy Carbon Disk RRDE
Cell Type: 1. Single Compartment or
2. Double Compartment

*Measured each sample twice. Once using the glassy carbon RDE with the single compartment cell, then again using the old platinum ring and glassy carbon disk RRDE with the double compartment cell. No significant difference was observed.

A) **Slurry Preparation (Gloves worn at all times):**

1. Scrape desired amount of whiskers off the film.
2. Weigh desired amount of whiskers and add to desired amount of nano-pure water (NPW) to make slurry of desired concentration.
3. Sonicate the slurry before use to ensure the slurry is homogeneous. 0.5 hour sonication, followed by 5-10 minutes of shaking by hand. No Nafion was used.

B) **Set-up of the Cell (Gloves worn at all times):**

1. Boil the cell once in 4 L beaker of NPW for approximately 1 hour. Make sure the water level is high enough to cover the entire cell.
2. Boil cell parts (glass frit, counter electrode and Teflon pieces) once or twice in NPW (depending on the time since last run and the materials used in the last run).
3. Rinse the cell once with 0.1M $HClO_4$. Once rinsed, fill the cell with 125 mL 0.1M $HClO_4$.
4. Connect the gas glass frit to the gas line and purge all NPW out of the frit.
5. Assemble cell parts and cell in proper orientation. Starting with the left most neck and moving counter-clockwise: Teflon stopper, gas glass frit, counter electrode, and reference electrode (with Teflon piece inserted previously).
6. Connect the counter and reference electrode to the proper wires, red and black respectively.
7. Rinse the electrode with a minimal amount of EtOH followed by lots of NPW.
8. Polish the electrode using 5 μm followed by 0.05 μm polishes. (Polish the old platinum ring and glassy carbon disk RRDE with only the indicated 0.05 μm polish.) Once polished, heat the electrode in fresh NPW.

9. Using a micropipette, add desired amount of slurry (prepared above) to the disk of the electrode. Allow the slurry to dry. Ar may be used to facilitate the drying process. Generally about 15 μL is put on the RRDE. The concentration of slurry depends on the desired loading.
10. Install the electrode in the rotator and then lower it into the cell.
11. Make sure only the disc wire is connected to the RDE. Both wires should be connected normally for the RRDE.
12. Make sure there are no bubbles on the electrode.
13. Make sure the electrode is not touching the neck of the glass cell and can rotate freely.

C) **Study of Oxygen Activity During ORR (Oxygen Reduction Reaction) Before Electrochemical Cleaning:**

1. Purge oxygen gas for 5 min.
2. While still purging oxygen, run the following ORR:
   I. **Sweep Rate:** 50 mV/s
   Potential Range: (-635 mV, 350 mV)
   # Of Sweeps: 4
   Rotation Speed: 400 rpm

Note: the OCV is not exceeded in these CVs!!

D) **Electrochemical Cleaning of the Electrode:**

1. Purge Ar gas into the cell for 15 min.
2. While still purging Ar, run the following cleaning CV:
   I. **Sweep Rate:** 500 mV/s
   Potential Range: (-700 mV, 350 mV)
   # Of Sweeps: 200
3. Repeat the cleaning CV if necessary.

Note: the OCV is not exceeded in these CVs!!

CVs will show if you have a clean electrode and/or setup or not. The H and OH regions will develop after potential cycling and should reach a steady state. The CVs should not be 'sloped' – otherwise there is a leak in the electrode and the Teflon U-Cups must be changed! The leakage could be a serious issue as it degrades the electrode. Avoid it at all costs.

E) **Study of CV (Cyclic Voltammetry) Features:**

1. While still purging Ar, run the following CVs:
   I. **Sweep Rate:** 50 mV/s
   Potential Range: (-635 mV, 350 mV)
   # Of Sweeps: 4
   II. **Sweep Rate:** 10 mV/s
   Potential Range: (-635 mV, 350 mV)
   # Of Sweeps: 4

Note: the OCV is not exceeded in these CVs!!

F) **Study of Oxygen Activity During ORR After Electrochemical Cleaning:**

1. Purge oxygen gas for 5 min.
2. While still purging oxygen, run the following ORRs:
   I. **Sweep Rate:** 50 mV/s
      Potential Range: (-635 mV, 350 mV)
      # Of Sweeps: 4
      Rotation Speed: 400 rpm
   II. **Sweep Rate:** 10 mV/s
      Potential Range: (-635 mV, 350 mV)
      # Of Sweeps: 4
      Rotation Speed: 400 rpm
3. Repeat step 2 another 3 times, changing the rotation speed to 900, 1600 and 2500 rpm.
   Note: the OCV is not exceeded in these CVs!!

G) **Study of CV Features After Oxygen Measurements:**

1. Purge Ar gas into the cell for 15min.
2. While still purging Ar, run the following CVs:
   I. **Sweep Rate:** 50 mV/s
      Potential Range: (-635 mV, 350 mV)
      # Of Sweeps: 4
   II. **Sweep Rate:** 10 mV/s
      Potential Range: (-635 mV, 350 mV)
      # Of Sweeps: 4
      Note: the OCV is not exceeded in these CVs!!

H) **Calibration of the Reference Electrode vs. RHE (Reversible Hydrogen Electrode):**

1. Start purging hydrogen gas then immediately start the following run:
   I. **Sweep Rate:** 100 mV/s
      Potential Range: (-800 mV, 0 mV)
      # Of Sweeps: 2
      Rotation Speed: 1600 rpm
      Use both disk and ring electrodes as working electrode.

*Only purge hydrogen gas when needed. Otherwise, make sure it is shut off.

I) **Disassembly of the Cell:**

3. Once completing all desired runs remove the electrode from the solution and rotator. Disassemble the electrode, rinse off the RRDE and wrap the pieces in Kimwipe and store them in a Ziploc bag.
4. Place the cell and cell parts back in their original beakers with fresh NPW.

Appendix D

RRDE Collection Efficiency Measurements

The collection efficiency of the ring electrode is determined by reduction and oxidation of the ferrocyanide ions at the disk and ring electrodes, respectively. Gasteiger *et al.* describe this procedure in more detail elsewhere [223]. The calibration includes measurements of the disk and ring currents using a deaerated solution of 3 mmol $K_3[Fe(CN)_6]$ in 0.5M K_2SO_4. The disk potential is swept from 1 to 0 V at 10 $mV \cdot s^{-1}$ and ring is kept constant at 1.2 V. During this experiment Fe^{3+} reduces to Fe^{2+} and the opposite reaction occurs at the ring. The collection efficiency is obtained from the ratio of ring to disk currents: $N = -I_{ring}/I_{disk}$.

Based on the geometry of the electrodes and their dimensions, the collection efficiency, or N, is expected to be about 0.2 or 20%. However, variations in N can occur due to differences in the catalyst thickness and electrode rotation rates. Figure C.1 shows the collection efficiency obtained for sputtered Pt on a GC disk at different rotation speeds. A polynomical fit to the data is then made which allows one to interpolate N for intermediate rotation speeds.

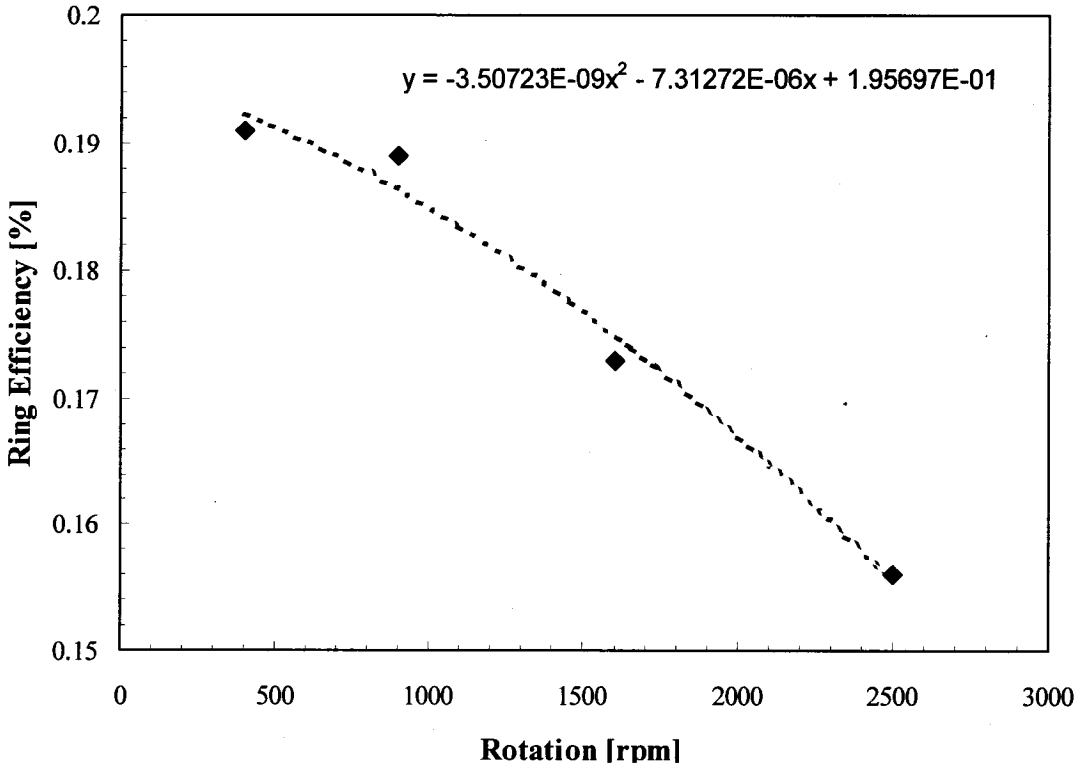

Figure D.1 *Collection efficiency of the Pine RRDE electrode.*

Appendix E

List of Samples and Characterizations Made

Table E.1 summarizes all the samples that were studied in this thesis. The listed numbers under each measurement column correspond to the respective figure number.

Table E.1 *Summary of all the samples studied and the characterizations made.*

ID	Composition	XRD Si	XRD NSTF	XRD NSTF after acid	XRD GC	EM Si	EM NSTF	EM NSTF after acid	EM after FC	EM GC
SPI4	$PtMn_x$, $(0 \le x \le 3)$	4.27 4.29	4.30 4.34, 4.36			4.24.6	4.26	4.37	4.37	
SPI84	$Pt_{1-x}Ni_x$, $(0 \le x \le 1)$	4.9, 4.10, 4.11	4.36			4.5		4.13, 4.14, 4.37	4.37	
SPI44	$Pt_{1-x}Fe_x$, $(0 \le x \le 1)$	4.6, 4.7,4.8	4.18, 4.36	4.19, 4.20, 4.21		4.5		4.13, 4.16, 4.17, 4.37	4.37	
SPI24	$Pt_{1-x}[Mn_{0.375}Fe_{0.625}]_x$, $(0 \le x \le 0.75)$		4.30, 4.34 4.36			4.24	4.26	4.38	4.38	
SPI40	$Pt_{1-x}[Mn_{0.167}Fe_{0.833}]_x$, $(0 \le x \le 0.75)$							4.39	4.39	
SPI42	$Pt_{1-x}[Mn_{0.5}Ni_{0.5}]_x$, $(0 \le x \le 0.75)$							4.40	4.40	
SPI139	$Pt_{0.7}[Co_{1-y}Ni_y]_{0.3}$ $(0 \le y \le 1)$		4.30, 4.32 4.36						4.41	
SPI134	$Pt_{0.5}[Co_{1-y}Ni_y]_{0.5}$ $(0 \le y \le 1)$		4.30, 4.32 4.36							

ID	Composition	XRD Si	XRD NSTF	XRD NSTF after acid	XRD GC	EM Si	EM NSTF	EM NSTF after acid	EM after FC	EM GC
SPI133	$Pt_{0.3}[Co_{1-y}Ni_y]_{0.7}$ $(0 \le y \le 1)$	4.28, 4.29	4.30, 4.31 4.32, 4.36					4.42	4.42	
SPI140	$Pt_{0.7}[Co_{1-y}Mn_y]_{0.3}$ $(0 \le y \le 1)$		4.30, 4.33 4.35, 4.36						4.41	
SPI141	$Pt_{0.5}[Co_{1-y}Mn_y]_{0.5}$ $(0 \le y \le 1)$		4.30, 4.33 4.35, 4.36			4.24	4.26		4.41	
SPI143	$Pt_{0.3}[Co_{1-y}Mn_y]_{0.7}$ $(0 \le y \le 1)$		4.30, 4.33 4.35, 4.36			4.24	4.26	4.42	4.42	
S2A137	Pt: 0→1, Ni: 0→1 in orthogonal directions					4.43		4.44, 4.45	4.45	
S2A15	$Pt_{1-x}Ta_x$ (0<x<1)	5.2				5.1 5.6		5.3		
S2D077	$Pt_{1-x}Ta_x$ (0<x<0.3)					5.16				
S2E058	Pt (0→300nm)				5.8					
S2D134	$Pt_{1-x}Co_x$ (0<x<0.5)	6.4, 6.5					6.3			6.3
S2D142	$Pt_{1-x}Co_x$ (0<x<0.5)									
S2E001	$Pt_{1-x}Co_x$ (0<x<0.5)									6.1 1
S2E059	$Pt_{1-x}Co_x$ (0<x<0.5)			6.8	6.8		6.7	6.7		6.6
PE4130	Pt		7.2							
PE4131	Pt-Co-Mn		7.2							

ID	Composition	XPS alumina	XPS NSTF	XPS NSTF after acid	XPS GC	XPS GC after RRDE	RRDE	FC	AA	SEM
SPI4	$PtMn_x$ ($0 \le x \le 3$)									
SPI84	$Pt_{1-x}Ni_x$ ($0 \le x \le 1$)		4.22, 4.23	4.22, 4.23						
SPI44	$Pt_{1-x}Fe_x$ ($0 \le x \le 1$)								4.15	
SPI24	$Pt_{1-x}[Mn_{0.375}Fe_{0.625}]_x$, ($0 \le x \le 0.75$)									
SPI40	$Pt_{1-x}[Mn_{0.167}Fe_{0.833}]_x$, ($0 \le x \le 0.75$)									
SPI42	$Pt_{1-x}[Mn_{0.5}Ni_{0.5}]_x$, ($0 \le x \le 0.75$)									
SPI139	$Pt_{0.7}[Co_{1-y}Ni_y]_{0.3}$ ($0 \le y \le 1$)									
SPI134	$Pt_{0.5}[Co_{1-y}Ni_y]_{0.5}$ ($0 \le y \le 1$)									
SPI133	$Pt_{0.3}[Co_{1-y}Ni_y]_{0.7}$ ($0 \le y \le 1$)	4.28								
SPI140	$Pt_{0.7}[Co_{1-y}Mn_y]_{0.3}$ ($0 \le y \le 1$)									
SPI141	$Pt_{0.5}[Co_{1-y}Mn_y]_{0.5}$ ($0 \le y \le 1$)					4.26	4.26			
SPI143	$Pt_{0.3}[Co_{1-y}Mn_y]_{0.7}$ ($0 \le y \le 1$)					4.26	4.26			
S2A137	Pt: 0→1, Ni: 0→1 in orthogonal directions									
S2A15	$Pt_{1-x}Ta_x$ ($0<x<1$)	5.4, 5.5, 5.6, 5.7								
S2D077	$Pt_{1-x}Ta_x$ ($0<x<0.3$)				5.22	5.22	5.17, 5.19, 5.20, 5.21			5.18

ID	Composition	XPS alumina	XPS NSTF	XPS NSTF after acid	XPS GC	XPS GC after RRDE	RRDE	FC	AA	SEM
S2E058	Pt (0→300nm)						5.10, 5.11, 5.12, 5.13, 5.14, 5.15			5.9
S2D134	$Pt_{1-x}Co_x$ (0<x<0.5)						6.15, 6.16			
S2D142	$Pt_{1-x}Co_x$ (0<x<0.5)				6.11	6.11	6.15, 6.16			
S2E001	$Pt_{1-x}Co_x$ (0<x<0.5)				6.11	6.11	6.12, 6.13, 6.14, 6.15, 6.16			
S2E059	$Pt_{1-x}Co_x$ (0<x<0.5)				6.9, 6.11	6.11	6.15, 6.16			
PE4130	Pt						7.4, 7.5, 7.7, 7.8, 7.9 7.10, 7.11, 8.1, 8.2	7.14		7.3
PE4131	Pt-Co-Mn						7.4, 7.5, 7.7, 7.8, 7.9 7.10, 7.11	7.9, 7.14		